INVESTIGATION OF OPTIMISED ELECTROMAGNETIC FIELDS IN SRF CAVITIES FOR THE ILC

A Thesis submitted to The University of Manchester for the degree of

Doctor of Philosophy

in the Faculty of Engineering and Physical Sciences

2011

Nawin Juntong

Manchester Accelerator Physics Group

School of Physics and Astronomy

Contents

List of Tables

List of Figures

Total word count 64,771

Abstract

The International Linear Collider (ILC) project aims at colliding electrons and positrons at an initial centre of mass energy of 500 GeV with high luminosity, and thus will allow scientists to probe new energy regimes. A general consensus within the accelerator physics and particle physics community has been made to utilise superconducting technology rather than normal conducting technology. A superconducting radio frequency (SRF) cavity will be used to accelerate bunches of particle beams to the design energy before delivering them to the collision point. The major financial cost of the ILC lies in the area of the main linacs. These linacs consist of nine-cell cavities and are based on the TESLA design. An option being considered to reduce the overall footprint and project cost is to enhance the cavity gradient. This research concerns itself with my new cavity design with a view to reaching higher gradients. This design is focussed on minimising the surface electromagnetic fields and maximising the bandwidth of the accelerating mode. This new shape, which is referred to as the New Low Surface Field (NLSF) design, bears a similarity to the current Ichiro and Reentrant designs. A design of a complete nine-cell cavity, including power couplers and higher order mode damping couplers is presented. An equivalent circuit model theory is applied to represent the radio frequency (rf) mode properties of the cavity for both the fundamental accelerating mode and higher order modes. This represents an almost complete design, including HOM damping, for a unique high gradient superconducting cavity.

Declaration and Copyright Statement

No portion of the work referred to in this thesis has been submitted in support of an application for another degree or qualification of this or any other university or institute of learning.

The author of this thesis (including any appendices and/or schedules to this thesis) owns certain copyright in it (the Copyright) and s/he has given The University of Manchester certain rights to use such Copyright, including for administrative purposes.

Copies of this thesis, either in full or in extracts and whether in hard or electronic copy, may be made **only** in accordance with the Copyright, Designs and Patents Act 1988 (as amended) and regulations issued under it or, where appropriate, in accordance with licensing agreements which the University has from time to time. This page must form part of any such copies made.

The ownership of certain Copyright, patents, designs, trade marks and other intellectual property (the Intellectual Property) and any reproductions of copyright works in the thesis, for example graphs and tables (Reproductions), which may be described in this thesis, may not be owned by the author and may be owned by third parties. Such Intellectual Property and Reproductions cannot and must not be made available for use without the prior written permission of the owner(s) of the relevant Intellectual Property and/or Reproductions.

Further information on the conditions under which disclosure, publication and commercialisation of this thesis, the Copyright and any Intellectual Property and/or Reproductions described in it may take place is available in the University IP Policy, in any relevant Thesis restriction declarations deposited in the University Library, The University Library's regulations and in The University's policy on presentation of Theses.

Dedication

To the memory of my father,

the pride of my mother,

and for my family

Acknowledgements

During my PhD, I had opportunity to get involve with many people and I wish to take this opportunity to thank all those people. I wish I could mention them individually and apologise for not doing so.

Firstly, my thanks go to my supervisor Dr. Roger Michael Jones for his patient guidance and suggestions throughout my work. Under his guidance I learned not only academic contents, but also the way to present your achievement and the way to handle your stress when you were down. I also thank my advisors Prof. Roger Barlow and Prof. Fred Loebinger for their support in every issues. Secondly, Thanks to Dr. Ian Shinton for his patient guidance on various RF solvers simulation and discussions of work. I also want to thank my colleagues, namely Narong Chanlek, Vasim Khan, Chris Glasman, Mike Salt and Sam Tygier who participated in various discussions and activities.

My thanks goes to international colleagues, Vyacheslav Yakovlev for his kindly give me the couplers geometry of TESLA cavity and suggestions on calculation. This is also the permission to use his SLANS code. Valery Shemlin for his patient guide through SLANS simulation. I also thank Igor Zagorodnov for the permission to use his ECHO code. Thanks goes to Karl Bane for a fruitful discussion on wakefield. I also thank Nicoleta Baboi for her hospitality while I was at DESY.

I also want to acknowledge CAS school and ILC school for providing a high level training in accel-

erator physics, which I have broaden my knowledge and made many friends.

I would like to thank directorate staff, who are responsible for my various conferences and workshops, namely Anne Morrow from the University of Manchester; Liz Kennedy, Sue Waller, Marie White and Leanne Fletcher from the Cockcroft Institute.

My sincere thanks goes to my mother, Somjai, my grand mother, my grand father, and my sister for their tremendous moral support. In particular, my wife Jiraporn deserves a special mention for her patient and everyday life support. We come to this point together.

Finally, I wish to devote my last word to my father, Sawing, who can not be here with me. Thanks dad, I will always remember you!

The Author

The author was educated at Chaing Mai University, Chiang Mai, Thailand with electrical engineering as major subject. I then joined the Synchrotron Light Research Institute (Public Organisation), after 5-year working in the Seagate company (Thailand). I received joint support from the Royal Thai Government and the Synchrotron Light Research Institute to pursue PhD study in the Manchester Accelerator Physics Group, School of Physics and Astronomy at The University of Manchester. The work presented here was undertaken at Manchester and the Cockcroft Institute of Accelerator Science and Technology (Daresbury).

Chapter 1

Introduction

The focus of this research is on optimisation of the superconducting radio frequency (SRF) cavities and the couplers for the linacs of the ILC. This chapter provides an overview of the essential details of the ILC, the main linac cavities and the couplers. Chapter 2 outlines a basic concept of electromagnetic (e.m.) fields inside a cavity, a figures of merit of a cavity and the concept of a wakefields. Chapter 3 provides an overview of a research in a high gradient cavities. A concept of circuit model theory for an accelerating cavity is introduced in Chapter 4. A study on the TESLA cavity to validate the study's methodology and a circuit model theory is presented in Chapter 5. My optimisation to obtain the NLSF cavity is discussed in Chapter 6 and rf properties of the NLSF cavity are presented in Chapter 7, along with the results of applying a circuit model. The wakefields of the NLSF cavity are presented in Chapter 8. The penultimate chapter outlines the rf power coupler design and the HOM coupler for the NLSF cavity. Some concluding remarks and suggestions for further work are presented in the final chapter.

1.1 Why is a Linear Collider Desirable?

The development of the Standard Model has been a success of 20th century particle physics. The Standard Model includes a third component beyond particles and forces that has not yet been veri-fied, in particular the Higgs mechanism that gives mass to the particles. It is anticipated fundamental new physics will be discovered at a few hundred GeV of energy.

In the past, lepton and hadron colliders have been built as storage rings. In a storage ring, the par-ticles are accelerated many times through the same accelerating cavities. Dipole magnets, located between the cavities, are used to bend the trajectory of the particles. Particles gain energy from the accelerating field at each turn and this requires a higher magnetic field to maintain the same trajectory. The Large Electron Positron collider (LEP), the largest electron positron storage ring, closed down in November 2000, represented an energy limit beyond which energy losses due to synchrotron radiation becomes prohibitively large.

The power radiated by an accelerated charged particle is given by Larmor's formula [1]:

$$P = \frac{1}{4\pi\epsilon_0} \frac{2e^2\dot{v}^2}{3c^3} \tag{1.1}$$

For a linear accelerator, the power radiated is [1]:

$$P = \frac{1}{4\pi\epsilon_0} \frac{2e^2}{3c^3 m^2} \left(\frac{dp}{dt}\right)^2 \tag{1.2}$$

where p is the momentum and m is the rest mass of particle. The rate of change of momentum is equal to the force exerted on the particle in the direction of acceleration (z-direction), which in turn

equals the change in the energy, E, of the particle per unit distance. Consequently,

$$P = \frac{1}{4\pi\epsilon_0} \frac{2e^2}{3c^3m^2}\left(\frac{dE}{dz}\right)^2 \tag{1.3}$$

Thus, in a linear accelerator the radiated power depends on the external force acting on the particle, and not on the actual energy or momentum of the particle. It is clear from the above formula that electrons radiate more than heavier particles such as protons. The ratio of power radiated to the power supplied by the external sources is:

$$\frac{P}{dE/dt} = \frac{1}{4\pi\epsilon_0} \frac{2e^2}{3mc^2mc\upsilon}(\frac{dE}{dz}) \simeq \frac{e^2}{4\pi\epsilon_0mc^2} \frac{2}{3mc^2}(\frac{dE}{dz}) = \frac{2r_e}{3mc^2}(\frac{dE}{dz}) \tag{1.4}$$

where $r_e = 2.82 \times 10^{-15}$ m is the classical radius of an electron. It is clear from the above expression that the radiation losses in an electron linear accelerator are negligible unless the gain in energy is of order $m_ec^2 = 0.511$ MeV in a distance of $2r_e/3 = 1.88 \times 10^{-15}$ metres. That is 2.72×10^{14} MeV/m (9.20×10^{20} MeV/m for proton).

In circular accelerators the momentum $\vec{p}$ changes rapidly in direction as the particle rotates, but the change in energy per revolution is small. Furthermore, the direction of acceleration is always perpendicular to the direction of motion. With the bending radius ρ and $\omega = \beta c/\rho$, the radiated power loss becomes [1]:

$$P = \frac{2}{3}\frac{r_0}{mc}\gamma^2\omega^2|\vec{p}|^2 = \frac{\beta^4 cC_\gamma}{2\pi}\frac{E^4}{\rho^2} \tag{1.5}$$

where r_0 is the classical radius of the particle, m is the rest mass and $C_\gamma = 4\pi r_0/3(mc^2)^3$, which is $8.85 \times 10^{-5} m/GeV^3$ for electrons and $7.78 \times 10^{-18} m/GeV^3$ for protons. The radiative energy loss per revolution of a circular accelerator becomes:

$$\triangle E_\gamma = P_\gamma T_{rev} = \beta^3 C_\gamma \frac{E^4}{\rho} \tag{1.6}$$

For example in the electron positron collider, LEP [2, 3], at an energy of 100 GeV the energy loss per turn is 2.86 GeV. Also, for the Cornell Electron-positron Storage Ring (CESR) [4], an electron-positron collider, the energy loss is 1.2 MeV per turn at the energy of 5.3 GeV. The SRS at Daresbury Laboratory [5], 2 GeV energy with bending radius of 8.6 m, the energy loss is 0.25 MeV per turn. While at CERN's Large Hadron Collider (LHC) [6], the 7 TeV proton collider, the energy loss per turn is 6.66 keV. Therefore, when accelerating leptons to higher energies linear colliders become a necessity.

1.2 Key Parameters of a Collider

The two important key parameters for a high energy collider are the centre of mass energy and the beam luminosity.

1.2.1 Centre of Mass Energy

The total centre of mass energy E_{cm} of collision represents the energy available for high energy reactions to create new particles. It depends on the kinematic parameters of the colliding particles, which can be defined as the expression:

$$E_{cm}^2 = \left(\sum_i E_i \right)^2 - \left(\sum_i cp_i \right)^2 \tag{1.7}$$

with $E_i = \gamma_i m_i c^2$ and $p_i = \gamma_i m_i \beta_i c$, the relation become:

$$E_{cm}^2 = \left(\sum_i \gamma_i m_i c^2 \right)^2 - c^2 \left(\sum_i \gamma_i m_i \beta_i c \right)^2 \tag{1.8}$$

For head on collisions of two particles having the same energy, velocity and mass ($m_1 = m_2 = m, \gamma_1 = \gamma_2 = \gamma, \beta_1 = -\beta_2 = \beta,$), the total centre of mass energy is simply twice the energy of each

of the particles:

$$E_{cm} = 2\gamma mc^2 = 2E \tag{1.9}$$

The situation is different in a fixed target collision, for the particle with energy E_b and the target mass m_t the total collision energy in this mode is:

$$E_{cm} = \sqrt{2m_t c^2 E_b} \tag{1.10}$$

This demonstrates that the centre of mass energy after collision is lower for a fixed target collision. For example, consider the LHC accelerating 7 TeV protons beams to produce a total collision centre of mass energy of 14 TeV, compared to 115 GeV centre of mass energy produced if a fixed target mode is considered.

1.2.2 Luminosity

In addition to the centre of mass energy of the beam, luminosity (L) is the second key parameter for linear colliders [7]:

$$L = \frac{n_b N_e^2 f_{rep} H_D}{4\pi \sigma_x^* \sigma_y^*}. \tag{1.11}$$

Here n_b is number of bunches per pulse, N_e is number of electrons (positrons) per bunch, f_{rep} is pulse repetition frequency, $\sigma_{x(y)}^*$ is horizontal (vertical) beam size at the interaction point (IP), and H_D is disruption enhancement factor. This assumes that particle bunches have a Gaussian distribution in both the horizontal and vertical plane.

Introducing the average beam power $P_b = E_{cm} n_b N_e f_{rep}$, the luminosity can be written as

$$L = \frac{P_b}{E_{cm}} \frac{N_e}{4\pi \sigma_x^* \sigma_y^*} H_D \tag{1.12}$$

By choosing $\sigma_x^*/\sigma_y^* \gg 1$, L becomes effectively independent of the horizontal beam size and the luminosity can be increased by making σ_y^* as small as possible. Since $\sigma_y^* = \sqrt{\gamma\epsilon_y^*\beta_y^*}$ [1], where $\gamma\epsilon_y^*$, β_y^* is normalised emittance and beta function at the IP respectively, this is achieved by using both a small vertical beta function and a small normalised vertical emittance at the IP.

The other method to increase the luminosity is operating at the high beam power, P_b. This can be achieved by increasing the pulse repetition rate or number of particles in bunch or number of bunches per pulse. L can also be increased by operating at higher beam energies. This is obtained by increasing the pulse repetition rate or by operation in multi bunch mode.

1.3   The International Linear Collider

LHC will investigate physics at the TeV energy scale and is anticipated to be the discovery machine for the Higgs particle. The ILC is a complementary machine in that it is expected to play a central role in the precise measurement and exploration for physics beyond the Standard Model. The ILC is designed to collide electrons and their antiparticle, positrons, at an initial centre of mass energy of 500 GeV with an option to upgrade to 1 TeV. In contrast to the LHC where collision between protons at a centre of mass energy of 14 TeV, the ILC will provide good signal to background ratio, which will allow precision measurement of the physics of the interaction.

A Reference Design Report (RDR) was published in August, 2007 [8]. These documents provide details of technical requirements for a machine to reach a centre of mass energy of 500 GeV with a peak luminosity of $2 \times 10^{34} cm^{-2} s^{-1}$. As listed in Table 1.1 and schematic, shown in Fig. 1.1 the ILC machine will be approximately 31 kilometres in length. The major subsystems of the ILC are electron and positron sources, the damping rings, the ring to main linacs, the main linacs, the beam delivery systems, and the detectors at the Interaction Point (IP). The beam parameters at the IP for

500 GeV energy are listed in Table 1.2. The vertical normalised emittance and beta function are very small compare to that of the horizontal. There are three advantage points for using a flat beam instead of a round beam [9]: first, the small emittance allows for small spot sizes at the IP which is needed to achieve the high luminosity as discussed in previous section. Second, flat beams take advantage of the natural asymmetry of the damping ring based sources and of the final focus; quadrupole focusing is asymmetric and a flat beam final focus is easier to design than a round beam final focus. Third, for a given cross sectional area and charge, flat beams generate less beamstrahlung than round beams. The beamstrahlung increases the energy spread and causes detector backgrounds.

Table 1.1: Global parameters for the ILC at 500 GeV [8]

Parameter	Value	Unit
Centre of mass energy range	500	GeV
Peak luminosity	2×10^{34}	$cm^{-2}s^{-1}$
Availability	75	%
Repetition rate	5	Hz
Duty cycle	0.5	%
Main linacs		
Average accelerating gradient in cavities	31.5	MV/m
Length of each main linac	11	km
Beam pulse length	969	μs
Average beam current in pulse	9.0	mA
Damping rings		
Beam energy	5	GeV
Circumference	6.7	km
Length of BDS (2 beams)	4.5	km
Total site length	31	km
Total site power consumption	230	MW

Starting from the gun, a short description of the ILC machine is now given. Electrons from the electron gun will be focused into a bunches and accelerated up to an energy of 5 GeV before injection into a damping ring. Positrons do not exist naturally on earth. They will be created by
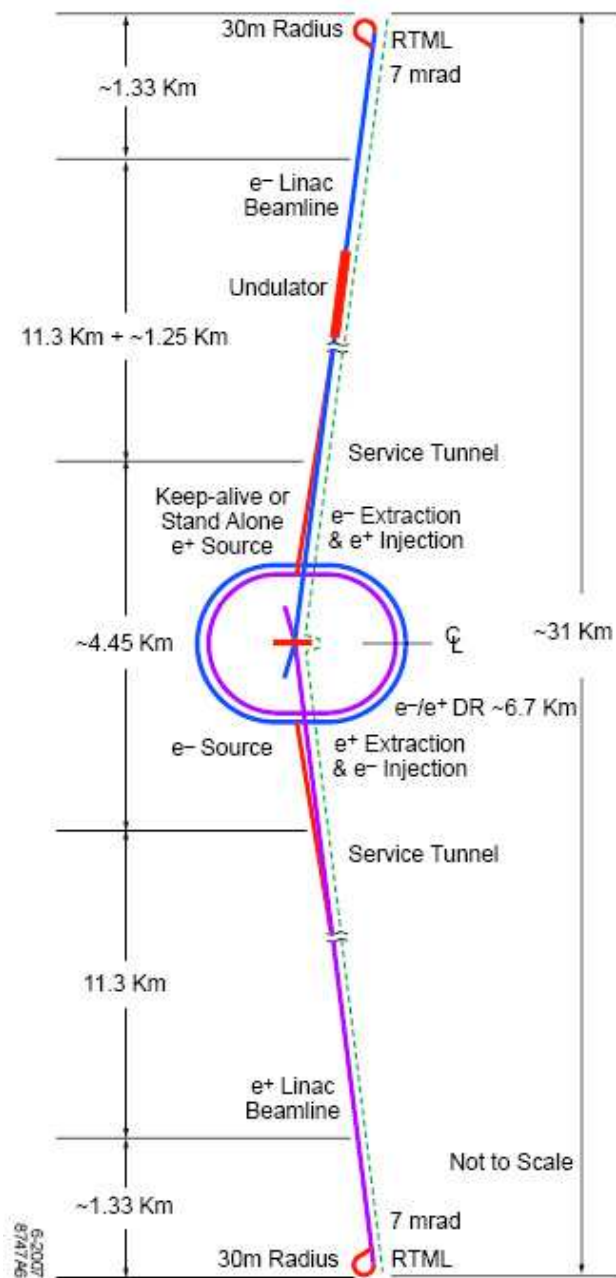
Figure 1.1: A schematic layout of ILC for 500 GeV centre-of-mass energy [8]

Table 1.2: Beam and IP parameters for the ILC at 500 GeV [8]

Parameter	Symbol/Units	Value[*]
Repetition rate	f_{rep} (Hz)	5
Number of particles per bunch	N (10^{10})	2
Number of bunches per pulse	n_b	2625
Bunch interval in the main linac	t_b (ns)	369.2
in units of RF buckets		480
Average beam current in pulse	I_{ave} (mA)	9.0
Normalised emittance at IP	$\gamma\epsilon_x^*$ (mm $\cdot$ mrad)	10
Normalised emittance at IP	$\gamma\epsilon_y^*$ (mm $\cdot$ mrad)	0.04
Beta function at IP	β_x^* (mm)	20
Beta function at IP	β_y^* (mm)	0.4
RMS beam size at IP	σ_x^* (nm)	639
RMS beam size at IP	σ_y^* (nm)	5.7
RMS bunch length	σ_z (μm)	300
Disruption parameter	D_x	0.17
Disruption parameter	D_y	19.4
Beamstrahlung parameter	Υ_{ave}	0.048
Energy loss by beamstrahlung	δ_{BS}	0.024
Number of beamstrahlung photons	n_γ	1.32
Luminosity enhancement factor	H_D	1.71
Geometric luminosity	L_{geo} ($10^{34}/cm^2/s$)	1.20
Luminosity	L ($10^{34}/cm^2/s$)	2

[*] *This values are nominal based on beam current 9.0 mA, beam pulse length*
970 μs, and RF pulse length 1.56 ms [8]

sending high-energy electron beam into a helical undulator. This undulator will cause electrons to emit photons. After the undulator the electrons and photons are separated. The photons will be sent to strike a titanium-alloy target which produces pairs of electrons and positrons. The positrons will be collected and accelerated up to an energy of 5 GeV before injection into a damping ring.

The damping rings are used to produce electron and positron bunches compact enough for a high luminosity collision. There are two damping rings, one for electrons and one for positrons, each of which is 6.7 kilometres circumference operating at a beam energy of 5 GeV as listed in Table 1.1. In each ring the bunches will travel through a series of wigglers that cause the beam to emit photons. This repeated process makes the bunches more compact (9 mm bunch length).

The ring to main linacs (RTML) transport the beam from damping ring to main linacs and compress bunch length into the short bunches required by main linac. The RTML will compress bunches from 9 mm at 5 GeV at the entrance to 0.3 mm at 15 GeV at the exit and deliver these beams into main linacs.

The main linacs, one for electrons and one for positrons, accelerate beams from their injected energy of 15 GeV to the final energy of 250 GeV over a total length of 23 kilometres. The purpose of these linacs is to accelerate the beams, whilst preserving the emittance and maintain the beam energy within the design requirement of a $\sim 0.1\%$ energy spread at the IP.

The beam delivery system (BDS) is responsible for transporting electron and positron beams from the main linacs, focusing them to the size required at the IP, bringing them into collision, and then transporting the spent beams to the main beam dumps.

1.4 Room Temperature or Superconducting Accelerators?

Normal conducting (NC) accelerating structures have been used worldwide over several decades and we refer to these as a warm accelerators. NC accelerators are fabricated from copper and are water cooled during operation. Superconducting (SC) accelerating structures, which we refer to as a cold accelerators, have the advantage of low electrical resistance. This low loss allow almost 100% of rf power transfer to particle beams. However, in practise a finite time is required to fill the cavities and this affects the efficiency adversely. The drawbacks of using SC is the power needed to cool the structure to 2 K, the superconducting state. The rf input power is calculated from:

$$P_{rf} = E_a L_c I_b \tag{1.13}$$

where E_a is the loaded accelerating gradient of the cavity with effective length L_c and beam current I_b. The beam current is calculated from the bunch charge, $Q_b = Nq$, divided by the bunch spacing ($I_b = Q_b/t_b$). In practise the rf input will be provided from klystrons through the distribution network. For the ILC 26 cavities are fed per klystron (with 9, 8, and 9 cavities in each cryomodule, respectively). The baseline design of the ILC requires an average accelerating gradient of 31.5 MV/m over a cavity effective length 1.038 m with a beam current of 9 mA. The required klystron power is:

$$P_{kly} = P_{rf} N_{cav} \eta_d \eta_{to} = 31.5 \cdot 9 \cdot 1.038 \cdot 26 \cdot 1/0.93 \cdot 1/.84 \approx 10\text{MW} \tag{1.14}$$

here η_d is distribution losses efficiency and η_{to} is the tuning overhead factor. The accelerating cavity needs to be filled with rf power before introducing the beam into it. The standing wave cavity fill time is calculated from $T_{fill} = 2ln2 \cdot Q_e/\omega \sim 0.6$ms [10] and the bunch train length or beam pulse length is obtained from the product of the bunch spacing and the number of bunches, $T_b = n_b t_b \sim 1$ms. Then the rf pulse length, T_{rf}, is the summation of these two. The rf to beam efficiency is obtained

from the ratio of beam pulse to the rf pulse length:

$$\eta_{rf} = \frac{T_b}{T_{rf}} 100\% \tag{1.15}$$

From the ILC-RDR, the rf to beam efficiency is 62% compared to 28% for CLIC [11]. This rf to beam efficiency is more than a factor of two larger. However, once all losses are taken into account, the overall efficiency of these two accelerators are comparable. This efficiency is calculated from the total power consumption of the accelerators. For the ILC, the average beam power is given by,

$$P_b = E_{cm} n_b N_e f_{rep} = 500 \cdot 10^9 \cdot 1.6 \cdot 10^{-19} \cdot 2625 \cdot 2 \cdot 10^{20} \cdot 5 = 21 \text{MW} \tag{1.16}$$

From Table 1.1 the total site power P_{tot} is 230 MW. The overall wall plug to beam efficiency is:

$$\eta_{tot} = \frac{P_b}{P_{tot}} 100\% = \frac{21}{230} 100\% = 9.13\% \tag{1.17}$$

Table 1.3 provides a comparison of NC versus SC colliders. The overall efficiency of the SC collider is no more than $\approx 2\%$ higher than that of the high gradient NC collider.

1.5   The ILC Accelerator

The ILC accelerator is based on 1.3 GHz SRF accelerating cavities. More than 17,000 of these cavities are needed for the ILC. The use of SRF technology was recommended by the International Technology Recommendation Panel (ITRP) in August 2004 [12]. The ILC SRF linac technology was pioneered by the TESLA collaboration in a proposal for a 500 GeV centre of mass energy linear collider in 2001 [7]. The current baseline assumes an average accelerating gradient of 31.5 MV/m - requiring a minimum of 35 MV/m gradient during mass production vertical testing. Cavity design parameters are listed in Table 1.4 and an example of the 1.3 GHz TESLA nine-cell cavity is shown

Table 1.3: Main parameters comparison between LC at 500 GeV

	NLC	ILC	CLIC
Total luminosity($10^{34}cm^{-2}s^{-1}$)	2	2	2.3
Repetition rate (Hz)	120	5	50
Loaded gradient (MV/m)	50	31.5	80
Main linac frequency (GHz)	11.4	1.3	12
Number of particles/bunch(10^9)	7.5	20	6.8
Number of bunch/pulse	192	2625	354
Bunch separation (ns)	1.4	369	0.5
Beam pulse (ns)	400	969000	177
Normalised horizontal emittance (nm mrad)	3.6	10	2.4
Normalised vertical emittance (nm mrad)	0.040	0.040	0.025
Horizontal beta function at IP (mm)	8	20	8
Vertical beta function at IP (mm)	0.11	0.4	0.1
RMS Horizontal beam size at IP (nm)	243	639	202
RMS Vertical beam size at IP (nm)	3	5.7	2.3
RMS bunch length (μm)	10	300	72
Over all two linac length (km)	14	22	9.26
Proposed site length (km)	18	31	13
Beam power (MW)	14	21	10
Total site AC power (MW)	195	230	130
RF to beam efficiency (%)	29	61.7	27.7
Wall-plug to beam efficiency (%)	7.2	9.1	7.7

in Fig. 1.2. As mentioned, operation at high luminosity requires the use of high power and small emittance beams. The low loss in SRF cavities allows long rf pulse length to be used. The choice of gradient is an important cost and performance parameter as it affects the length of the linac, while the cavity quality factor (Q_0) relates to the required cryogenic cooling power.

Figure 1.2: TESLA nine-cell SRF cavity (adapted from [13]).

Alternative cavity shapes and materials are being studied in order to reduce the cost of fabrication and to achieve higher gradients. Higher gradients can be reached by changing the shape of cavity cell walls in such a way that the magnetic flux on the wall is reduced and the electric field is also reduced to acceptable levels. The magnetic field causes heat dissipation on the surface of the cavity which can lead to a quench, a rapid change state from SC to resistive. So far only a single cell of the new alternative cavity designs have been tested and achieved high gradients up to 50 MV/m. At Cornell this has been experimentally tested with a Reentrant (RE) shape [14]. At DESY it has been achieved with a Low loss (LL) shape, and at KEK with a Ichiro shape [15]. However, it still remains a challenge to mass produce cavities which will achieve the desired yield for nine-cell cavities of 35 MV/m gradient.

Table 1.4: ILC nine-cell SRF cavity design parameters [8].

Parameter	Value	Unit
Type of accelerating structure	Standing Wave (SW)	
Accelerating mode	TM_{010}, π mode	
Fundamental frequency	1.300	GHz
Average installed gradient	31.5	MV/m
Qualification gradient	35.0	MV/m
Installed quality factor	$\geq 1 \times 10^{10}$	
Quality factor during qualification	$\geq 0.8 \times 10^{10}$	
Average Q_e	3.5×10^6	
Active length	1.038	m
Number of cells	9	
Cell to cell coupling	1.87%	
Iris diameter	70	mm
R/Q	1036	Ω
Geometry factor	270	Ω
E_{peak}/E_{acc}	2.0	
B_{peak}/E_{acc}	4.26	$mT MV^{-1} m^{-1}$
Tuning range	± 300	kHz
$\Delta f / \Delta L$	315	kHz/mm
Fill time	596	μs
Cavity resonance width	370	Hz
Number of HOM couplers	2	

1.5.1 SRF Cavity

The ILC cavity is made from high purity niobium sheets. The parameter which used to indicate the purity of SC materials is the Residual Resistivity Ratio (RRR) value:

$$\text{RRR} = \frac{\rho_{300\text{K}}}{\rho_{4.2\text{K}}}, \tag{1.18}$$

the ratio of the room temperature resistivity (300 K) to the normal residual resistivity state of the material at liquid helium temperature (4.2 K) [10]. High RRR values indicate a high purity material, the theoretical limit is 35,000 [10]. ILC cavities are based on Nb sheet whit a RRR value of 300. These properties for various materials are shown in Table 1.5.

Table 1.5: Typical properties of a 300-RRR Nb for use in the ILC cavities [8].

Element	Impurity content in ppm (wt)	Property	Value
Ta	≤ 500	RRR	≥ 300
W	≤ 70	Grain size	≈ 50μm
Ti	≤ 50	Yield strength	50 MPa
Fe	≤ 30	Tensile strength	100 MPa
Mo	≤ 50	Elongation at break	30%
Ni	≤ 30	Vickers hardness	
H	≤ 2	HV10	≤ 50
N	≤ 10		
O	≤ 10		
C	≤ 10		

The nine-cell cavity, consists of 7 identical middle cells and 2 end cells. A parameterised cell is sketched in Fig. 1.3. The current baseline design for the ILC uses TESLA-style cavities [8] and it is illustrated in Fig. 1.2. Each cell is composed of a circular equator ($A = B$) in which each iris is connected to the equator at a positive angle with respect to the line transverse to the cavity axis (refer to Fig. 1.3 in which $\theta > 0$). The cell geometries are listed in Table 1.6. There are three main
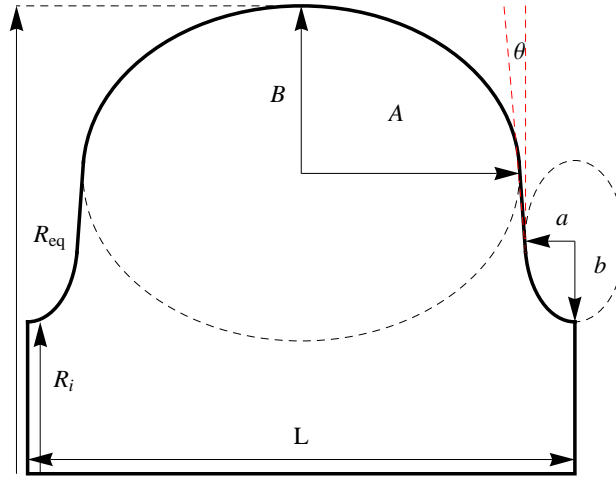
Figure 1.3: A sketch of a general cavity's geometry.

alternative designs to the TESLA cavity: Ichiro, Low loss and Reentrant. All of these design enable

high accelerating gradient to be used. The former two are based on an elliptical ($A \neq B$) equator

and the latter is also elliptical but it also tilts inwards ($\theta < 0$) with respect to the vertical line. This

thesis presents a new design, NLSF (New Low Surface Fields), which will allows operation of high

gradient with a large bandwidth.

Table 1.6: The geometry parameters of the three cell shapes of a TESLA cavity (units in mm) [16].

Parameter	middle cell	end cell 1	end cell 2
Iris radius (R_i)	35.0	39.0	39.0
Equator radius (R_{eq})	103.3	103.3	103.3
Half cell length ($L/2$)	57.7	56	57
Curvature at			
equator ($A = B$)	42.0	40.3	42.0
iris horizontal axis (a)	12.0	10.0	9.0
iris vertical axis (b)	19.0	13.5	12.8

The SRF cavity has to be carefully designed to minimise the collective effects from the wakefields,

these effects are considered small in one cavity but these effects will be accumulated in a long linac.

There are two types of wakefields: short-range and long-range wakefields. The former is the wake within a bunch itself. The long-range wake is experienced by subsequent trailing bunches.

The wakefields have the longitudinal and transverse components. The longitudinal wakefield can enhance the energy spread of the beam. Transverse wakefield can kick the beam off axis and this can lead to emittance dilution and also to a beam breakup (BBU) instability. These wakefields depend on cavity design, orientation of rf couplers, and the operating frequency.

Table 1.7: A comparison between frequency scaling of normal and superconducting cavities.

Parameter	Super conducting	Normal conducting
Cavity dimension (b)	ω^{-1}	ω^{-1}
Surface resistance (R_s)	ω^2	$\omega^{1/2}$
Power dissipation (P_d')	ω^1	$\omega^{-1/2}$
Stored energy (U')	ω^{-2}	ω^{-2}
Quality factor (Q_0)	ω^{-2}	$\omega^{-1/2}$
Shunt impedance (R')	ω^{-1}	$\omega^{1/2}$
Geometric factor (G)	ω^0	ω^0
R over Q (R'/Q_0)	ω^1	ω^1
Longitudinal lost factor (k_L')	ω^2	ω^2
Transverse kick factor (k_T')	ω^3	ω^3

As derived in Appendix A, and summarised in Table 1.7, the longitudinal and transverse wakefields depend on the operating frequency as ω^2 and ω^3, respectively. This is a strong component in the choice of linac operating frequency. The SC cavity is preferred to be operated at low frequency because at the low frequency the effect from wakefields and the heat on surface will be small and the stored energy, quality factor, and shunt impedance will be large. However, for NC linacs $R' \propto \omega^{1/2}$ and hence high frequency operation is preferred.

1.5.2   Fundamental Power Coupler

The fundamental power coupler is the connecting part between the waveguide systems and the SRF cavity, transferring rf power into the cavity. Two types of couplers can be used: waveguide or coaxial. Both have some advantages and disadvantages in terms of design, power handling capacity, and multipacting. The two are compared in Table 1.8 [17, 18].

Table 1.8: Advantages and disadvantages of waveguide and coaxial type couplers.

Type	Advantages	Disadvantages
Waveguide	· Simple design · Better power-handling capacity · Easier to cool · Higher pumping speed	· Large size · Bigger heat leak · Difficult to make tuning
Coaxial	· Compact · Smaller heat leak · Easier to make tuning · Easy to modify multipacting power levels	· More complicated design · Worse power-handling capacity · Difficult to cool · Smaller pumping speed

A choice of coupler is made on the basis of operating frequency, source power, and simplicity of design. At lower frequencies the waveguide is quite large and it is cumbersome to accommodate it in the cryostat, while a coaxial type will be compact. On the other hand because of its large size, external cooling is readily provided by brazing on cooling channels on the waveguide coupler design. A coaxial type will be used in the ILC because it has a compact size and it can easily be fitted inside the cryomodule. Furthermore, the external quality factor (Q_e) tuning is more flexible. This coupler will be operated in pulsed mode at frequency of 1.3 GHz.

A recent design based on the TTF-III type coupler is shown in Fig. 1.4. It consists of a cold and a warm section. All parts are cleaned and assembled in a class 10 clean room [1] in which the contam-

---

[1]No more than 10 particles of 0.5 microns in size are allowed in a cubic foot of air.

ination is carefully controlled. The coupler has two cylindrical ceramic windows, cold and warm
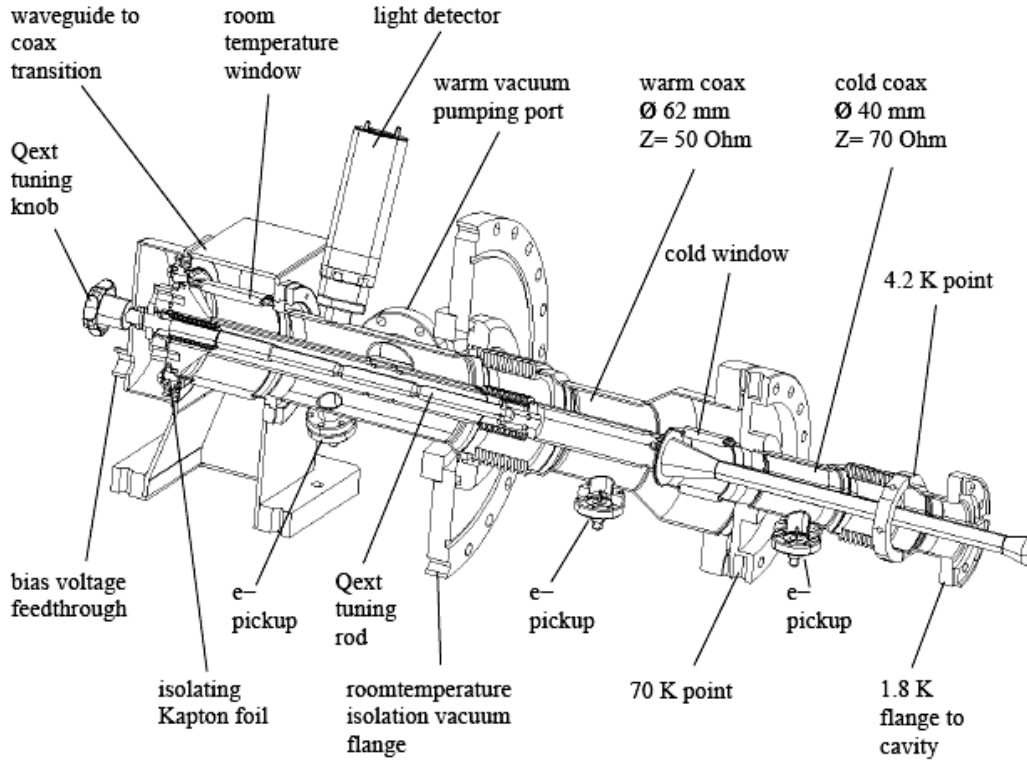
Figure 1.4: A cut view of a TTF-III power coupler (adapted from [19]).

windows, for protection of the cavity against contamination during mounting in the cryomodule, and against a window fracture during linac operation. The two ceramic windows are made from aluminum oxide (Al_2O_3) which is insensitive to multipacting resonances, and are coated with titanium nitride (TiN) to reduce the secondary electron emission coefficient. The inner conductor is biased with dc voltage to suppress multipacting resonances.

Inside the coupler there are a set of bellows to allow a few mm of movement when the cavities are cooled from room temperature to the operating temperature. To achieve a low heat load and a low thermal conductivity, stainless steel pipes and bellows with 10-20 μm copper plating are used. Heat loads of 6W at 70K, 0.5W at 5K and 0.06W at 2K have been designed.

The inner conductor of the coaxial line can be adjusted to vary the Q_e in the range of 1×10^6 - 6×10^6. This coupler has been tested at the TESLA test facility (TTF) at DESY and was able to transmit rf power up to 1.5 MW operating in the travelling wave mode [7].

1.5.3 Higher Order Mode Coupler

When intense electron bunches travel through a cavities they excite electromagnetic waves at a host of frequencies. This may result in multibunch instabilities and beam breakup. These higher order frequency components must be properly damped by extracting the stored energy via the higher order mode (HOM) couplers. The cross section of the HOM coupler is shown in Fig. 1.5. The SC pickup antenna is cooled and is insensitive to γ radiation and electron bombardment. A fundamental mode (1.3 GHz) notch filter is used to suppress extracting the energy of the accelerating mode.
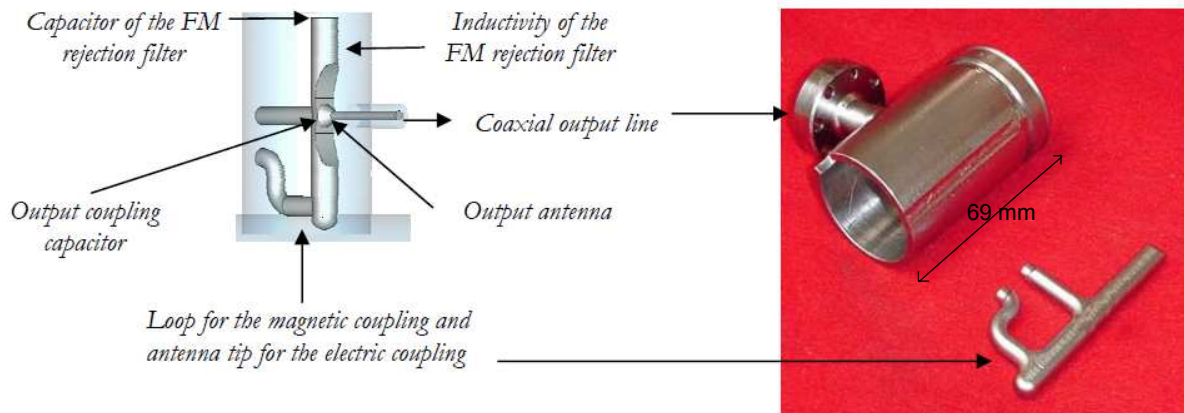
Figure 1.5: The cross section of the HOM coupler (adapted from [20]).

A problem can arise if 'trapped modes' are found concentrated in the centre cell and have low field amplitude in the end cells of the cavity. These can not be extracted via the HOM couplers. Trapped modes can be extracted by using an alternate shape of the end half cells in such a way that one can

boost the amplitude of a higher order mode frequency at one end cell and then use the HOM coupler to extract the energy.

The fundamentals of e.m. fields in a cavity are described in the next chapter. Wakefields are also discussed, together with beam dynamics considerations.

Chapter 2

Fundamentals of Wakefields and Beam Dynamics

This chapter outlines how the fields inside a cavity are defined in terms of a multi-pole expansion. This leads to an interpretation of the fields in terms of wakefields. Quantities fundamental to accelerating cavities are defined in detailed. In particular the following cavity figures of merit are discussed: loss factor, kick factor, cavity quality factor, shunt impedance, and R/Q. The implications of wakefields on beam dynamics issues are discussed and means to cure instabilities are also delineated.

2.1   Electromagnetic Modes in a Cavity

Here we consider a cylindrical waveguide with the e.m. wave propagated in the z direction. A cavity is a partially or fully closed waveguide. The harmonic component of the e.m. fields is given by:

$$\mathbf{E}(r, \phi, z, t) = \tilde{\mathbf{E}}(r, \phi, z)\, e^{-i\omega t}$$

$$\mathbf{B}(r, \phi, z, t) = \tilde{\mathbf{B}}(r, \phi, z)\, e^{-i\omega t}$$

(2.1)

Here we utilise cylindrical polar coordinates (r, ϕ, z). The $\tilde{\mathbf{E}}(r, \phi, z)$ and $\tilde{\mathbf{B}}(r, \phi, z)$ fields, in a cavity with cylindrical symmetry, can be written by expanding into a series of modes, *i.e.* a multi-pole expansion [16, 21], as

$$\tilde{\mathbf{E}}(r, \phi, z) = \sum_m \left(E_r^{(m)}(r, z) \cos(m\phi) \, \mathbf{e_r} + E_\phi^{(m)}(r, z) \sin(m\phi) \, \mathbf{e_\phi} + E_z^{(m)}(r, z) \cos(m\phi) \, \mathbf{e_z} \right)$$

$$\tilde{\mathbf{B}}(r, \phi, z) = \sum_m \left(B_r^{(m)}(r, z) \sin(m\phi) \, \mathbf{e_r} + B_\phi^{(m)}(r, z) \cos(m\phi) \, \mathbf{e_\phi} + B_z^{(m)}(r, z) \sin(m\phi) \, \mathbf{e_z} \right)$$

(2.2)

where $m = 0, 1, 2, ...$, corresponds to the monopole, dipole, quadrupole modes, and etc.

In the plane $\phi = 0$ we have only longitudinal and radial electric fields and azimuthal magnetic field components

$$\tilde{\mathbf{E}}(r, 0, z) = \sum_m \left(E_r^{(m)}(r, z) \, \mathbf{e_r} + E_z^{(m)}(r, z) \, \mathbf{e_z} \right)$$

$$\tilde{\mathbf{B}}(r, 0, z) = \sum_m \left(B_\phi^{(m)}(r, z) \, \mathbf{e_\phi} \right)$$

(2.3)

From Maxwell's equation: $\nabla \times \tilde{\mathbf{E}}(r, \phi, z) = i\omega \tilde{\mathbf{B}}(r, \phi, z)$ we can write the magnetic field component as

$$B_\phi^{(m)}(r, z) = \frac{-i}{\omega} \left(\frac{\partial}{\partial z} E_r^{(m)}(r, z) - \frac{\partial}{\partial r} E_z^{(m)}(r, z) \right)$$

(2.4)

Also with Maxwell's equation: $\nabla \cdot \tilde{\mathbf{E}}(r, \phi, z) = 0$ for all modes, we can find the azimuthal component of the electric field for $m > 0$ mode from the longitudinal and radial components as

$$E_\phi^{(m)}(r, z) = \frac{-1}{m} \left[E_r^{(m)}(r, z) + r \left(\frac{\partial}{\partial r} E_r^{(m)}(r, z) + \frac{\partial}{\partial z} E_z^{(m)}(r, z) \right) \right]$$

(2.5)

The electric field at the plane $\phi = 0$ is sufficient to reconstruct the complete electric and magnetic field patterns of the mode. To accelerate a charged particle, the longitudinal component of $\tilde{\mathbf{E}}$ must be present at the beam axis. The TM_{010} mode is usually chosen for acceleration because it has the lowest eigenfrequency and has a large field amplitude on beam axis hence a large acceleration.

2.2   Cavity Figures of Merit

Assuming a charged particle travels on the axis of a cavity along the z direction at speed of light (c). This particle always sees a field pointing in a direction which can provide an accelerating force. For an electron-positron accelerator, we use the electric field of the TM_{010} mode, which has maximum field amplitude on the beam axis. We define the accelerating voltage (V_c) for a cavity as the magnitude of the line integral of $\mathbf{E}_z$ seen by charged particles

$$V_c = \left| \int_z \mathbf{E}_z(r = 0, z)\, e^{-i\omega z/c + i\varphi}\, dz \right| \tag{2.6}$$

where $\mathbf{E}_z$ is a complex field and φ is some arbitrary phase.

This accelerating voltage is often quoted as the average accelerating field gradient, E_a, or the cavity gradient, defined as

$$E_a = \frac{V_c}{L}, \tag{2.7}$$

where L is the cavity length. The maximum gradient which a cavity can operate at is limited by the surface e.m. fields it can sustain. The maximum surface magnetic field (B_s) is important for a SC cavity because it defines the value beyond which the cavity will quench and hence will no longer be superconducting. On the other hand for a NC cavity, large values of B_s cause a rise in the cavity surface temperature which can lead to irreparable cavity damage. Increasing the surface electric field (E_s) eventually leads to field emission of electrons near the surface of cavity walls. Thus, in designing any cavity with a view to maximising the accelerating gradient, it is crucial to minimise both the peak surface electric and magnetic field.

2.2.1 Power Dissipation and Quality Factor

The total energy stored within a cavity (U) includes that contained in the electric and magnetic fields:

$$U = \frac{1}{4}\left(\int_V \epsilon_0 |\mathbf{E}|^2 dv + \int_V \mu_0 |\mathbf{H}|^2 dv\right) \tag{2.8}$$

At resonance, the time-averaged energy in the electric field equals that in the magnetic field:

$$U = \frac{1}{2}\int_V \epsilon_0 |\mathbf{E}|^2 dv = \frac{1}{2}\int_V \mu_0 |\mathbf{H}|^2 dv \tag{2.9}$$

When the cavity is filled with an e.m. field, there will be a flow of a surface current on the walls and it is where the energy is dissipated. This loss can be characterised by the surface resistance (R_s), which is the power dissipated per unit area:

$$\frac{dP_d}{ds} = \frac{1}{2}R_s|\mathbf{H}|^2 \tag{2.10}$$

For example, R_s is $O(n\Omega)$ for a well-prepared niobium cavity and $O(m\Omega)$ for a copper cavity.

The power dissipated is given by:

$$P_d = \frac{1}{2}R_s\int_S |\mathbf{H}|^2 ds. \tag{2.11}$$

The ratio of the stored energy to the power dissipated in the cavity wall per rf cycle is defined as the quality factor (Q_0) of the cavity:

$$Q_0 = \frac{\omega_0 U}{P_d} \tag{2.12}$$

where ω_0 is the accelerating frequency. From eq. 2.9 and 2.11 we find

$$Q_0 = \frac{\omega_0\mu_0 \int_V |\mathbf{H}|^2 dv}{R_s \int_S |\mathbf{H}|^2 ds}. \tag{2.13}$$

This is written as

$$Q_0 = \frac{G}{R_s} \tag{2.14}$$

where we define

$$G = \frac{\omega_0 \mu_0 \int_V |\mathbf{H}|^2 dv}{\int_S |\mathbf{H}|^2 ds} \tag{2.15}$$

as the geometrical constant of the cavity. This constant depends on the cavity shape but not its size and its surface resistance. It is useful for comparing different cavity shapes. The quality factor depends on the cavities size due to the frequency dependence of R_s (seen in Appendix A).

2.2.2   Shunt Impedance and R/Q

To characterise a cavity, we define the shunt impedance (R) by the ratio:

$$R = \frac{V_c^2}{P_d} \tag{2.16}$$

in unit of Ohms. This shunt impedance can be defined in unit of Ohms per unit length, where $P'_d = P_d/L$ denotes the power dissipated per unit length. Similarly, the ratio of the shunt impedance and the quality factor can be regarded as an another important parameter as

$$\frac{R}{Q_0} = \frac{V_c^2}{\omega_0 U} \tag{2.17}$$

The R/Q is independent of the cavity size and proportional to the operating frequency.

The efficiency of supplying rf power to an accelerated beam is directly related to the shunt impedance. It is important to maximise the shunt impedance in order to ensure the majority of power supplied goes into accelerating the charged particle beam, rather than into heating the cavity walls.

2.3   Fundamental of Beam Loading and Loss Factor

Consider a point charge moving on axis through a cylindrically symmetric cavity. Only monopole modes can be excited by charges moving on axis because other modes have no longitudinal electric field on axis. This charge will induce surface charges on the cavity walls and a beam-induced voltage within the cavity. Considering two equal charges q, each with kinetic energy W, that are separated by half wavelength of cavity mode: the first charge q travels through the initially unexcited cavity, this charge then generates a voltage:

$$V_c = -V_{bq} \tag{2.18}$$

The induced voltage seen by the first charge is

$$V_q = fV_{bq} \tag{2.19}$$

where f is the unknown fraction of the total beam-induced voltage that acts on the charge that produced it. The energy loss for the first charge q is

$$\Delta W_1 = -qfV_{bq} \tag{2.20}$$

We define the induced stored energy by

$$U = \alpha V_{bq}^2 \tag{2.21}$$

where α is a proportional constant. From the conservation of energy:

$$U = \alpha V_{bq}^2 = -\Delta W_1 = qfV_{bq} \tag{2.22}$$

so

$$V_{bq} = \frac{qf}{\alpha} \tag{2.23}$$

This implies that the induced voltage is proportional to the charge that produced it. The trailing charge enters the cavity a half period later. The voltage induced by the first charge has its phase changed by π so now it is an accelerating voltage $+V_{bq}$. The second charge also induces a voltage $-V_{bq}$, so these two voltages added to leave the total cavity voltage as $V_c = V_{bq} - V_{bq} = 0$ when the second charge has left the cavity. This makes the cavity stored energy to be zero.

The energy change for second charge is

$$\Delta W_2 = -qfV_{bq} + qV_{bq} = qV_b(1 - f) \tag{2.24}$$

since these charges are identical and the cavity is lossless. With the energy conservation we have

$$\Delta W_1 + \Delta W_2 = -qfV_{bq} - qfV_{bq} + qV_{bq} = qV_b(1 - 2f) = 0 \tag{2.25}$$

which implies that $f = 1/2$. This means that the induced voltage seen by the first charge is equal to the half of the induced voltage that the charge leaves in the cavity

$$V_q = \frac{V_b}{2} \tag{2.26}$$

This equation is called the fundamental theorem of beam loading. This result is valid for both relativistic and non-relativistic charges.

Let us define the loss parameter $k_n = 1/4\alpha$ for each cavity mode n, so that the energy loss of a point charge q into an empty cavity mode is

$$U = \alpha V_{bq}^2 = \alpha \left(\frac{fq}{\alpha} \right)^2 = \frac{q^2}{4\alpha} = k_n q^2 \tag{2.27}$$

Because $f = 1/2$, the total induced voltage by the point charge q is $V_b = 2k_n q$. However, the charge itself will see half of this voltage, $V_q = k_n q$. On the other hand, this loss factor, in terms of the cavity voltage and the stored energy, can be written as

$$U = \alpha V_b^2 = \frac{V_b^2}{4k_n}$$

$$k_n = \frac{V_b^2}{4U} \quad , \text{or} \quad k_n = \frac{V_c^2}{4U} \tag{2.28}$$

and can also be expressed in terms of R/Q_0 as

$$k_n = \frac{\omega_n}{4} \frac{R}{Q_0} \tag{2.29}$$

The fundamental of beam loading is important as it indicates that the potential experienced by the charged particle itself is half of that experienced by the trailing particles. The next section describes the scattered fields, the wakefields. These are generated when a charged particle passes through discontinuities in the beam pipe or the structural components.

2.4 Beam-Induced Wakefields in RF Cavities

Consider an ultrarelativistic charged particle travelling along the axis of a cylindrically symmetric and perfectly conducting pipe; since the charged particle is travelling very close to the speed of light, its fields are almost entirely perpendicular to the direction of motion. Thus trailing charged particles moving behind on the same or parallel path, at the same velocity, do not experience any force from the fields produced by the leading particle. However, the electromagnetic fields of the charged particle can be scattered as a result of a discontinuities in the beam pipe or the structural components and this will affect the trailing charged particles. These scattered fields are known as wakefields. In the case of a conductor, resistive losses present in the wall of a cavity can also cause wakefields - known as resistive-wall wakefields.

Wakefields can be described as the sum of all resonant modes excited within the structure. The components which have their frequencies synchronous with the beam will have strong interaction with the beam. The highest frequency component of the wakefields may affect the particles in the same bunch but do not remain localised; this is because their frequencies are higher than the cut off frequency of the pipe, so they propagate along it. The lower frequency modes remain local to where they are generated and may act on particles in trailing bunches.

Wakefields are classified as either short-range or long-range wakefields. For ultra-relativistic bunches, short-range wakefields generated by particles at the head of the bunch affect the trailing particles in the same bunch. This causes energy loss and leads to a distortion in the shape of the bunch. The long-range wakefields generated by a leading bunch affect subsequent trailing bunches. If the deflecting modes are strongly excited by the beam, they may cause a BBU instability both for single bunch and for trailing bunches. This can also give rise to emittance growth when averaged over time.

Wakefields also affect the operation of the cavity in terms of additional rf power required to compensate for the beam energy extracted by the wakefields. This extracted power represents additional power dissipation through ohmic losses in the walls or power delivered to some external load. In a superconducting linac, this causes additional power on the refrigeration load unless the power is coupled out to a load at a higher temperature by a specially designed higher order mode coupler.

2.4.1   Wakefields from a Point Charge

Considering a point charge q_1 moving parallel to the axis of a cylindrical cavity at an offset $\mathbf{r}_1$ and a trailing charge q_2 travelling at a constant distance s behind q_1 at an offset $\mathbf{r}_2$ as shown in Fig. 2.1.
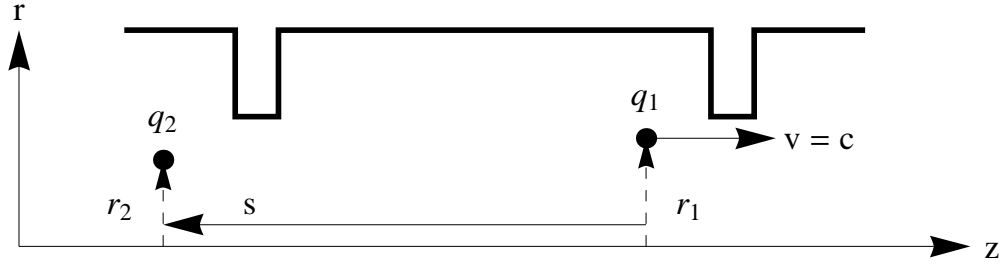
Figure 2.1: Illustration of drive and witness charges passing through a cylindrical cavity.

The longitudinal and transverse induced wakefields on a trailing charge are given by [22, 23]:

$$w_z(\mathbf{r}_2, \mathbf{r}_1, s) = \frac{-1}{q_1} \int_{z_1}^{z_2} [E_z(\mathbf{r}_2, z, t)]_{t=(z+s)/c} dz \tag{2.30a}$$

$$w_\perp(\mathbf{r}_2, \mathbf{r}_1, s) = \frac{1}{q_1} \int_{z_1}^{z_2} [\mathbf{E}_\perp + c(\mathbf{e}_z \times \mathbf{B})]_{t=(z+s)/c} dz \tag{2.30b}$$

where $\mathbf{e}_z$ is unit vector in direction of motion. The driving charge is assumed to enter the cavity at $z, t = 0$ and leave the cavity at $z = L$. The test charge enters and leaves the cavity at z_1, $t = (z + s)/c$ and z_2, respectively. The momentum kick on a trailing charge is:

$$c\Delta p_z(\mathbf{r}_2, \mathbf{r}_1, s) = -q_2 q_1 w_z(\mathbf{r}_2, \mathbf{r}_1, s) \tag{2.31a}$$

$$c\Delta p_\perp(\mathbf{r}_2, \mathbf{r}_1, s) = q_2 q_1 w_\perp(\mathbf{r}_2, \mathbf{r}_1, s) \tag{2.31b}$$

for longitudinal and transverse momentum changes, respectively.

These wakefields result from point-like charges and are effectively the Green's functions of the cavity. Once they have been calculated the wakefields for an arbitrary bunch distribution can be obtained by convolving them over the particular distribution.

2.4.2 Wakefields in a Symmetric Structure

A field parameter analysis allows the wakefields to be decomposed in terms of a summation over the modal numbers [24]. This representation is used here. In a cylindrically symmetric structures, a point charge q_1 traverses the cavity at coordinate (r_1, ϕ_1) and the test charge q_2 is travelling behind at position (r_2, ϕ_2). These offsets r_1 and r_2 can be normalised with respect to the radius of the tubes (a). The structure will have modes that are represented by an azimuthal m-pole dependence. The longitudinal wake potential is given by a sum over the longitudinal n-modes of the structure

$$w_{zm} = \left(\frac{r_1}{a}\right)^m \left(\frac{r_2}{a}\right)^m \cos m(\phi_2 - \phi_1) \sum_{n=0}^{\infty} 2k_{mn}(r_2 = a) \cos \frac{\omega_{mn} s}{c} \Theta(s) \qquad (2.32)$$

and

$$w_{\perp m} = m\left(\frac{r_1}{a}\right)^m \left(\frac{r_2}{a}\right)^{m-1} (\cos m(\phi_2 - \phi_1)\, \mathbf{e}_r - \sin m(\phi_2 - \phi_1)\, \mathbf{e}_\phi) \sum_{n=0}^{\infty} \frac{2k_{mn}(r_2 = a)}{\omega_{mn} a/c} \sin \frac{\omega_{mn} s}{c} \Theta(s) \quad (2.33)$$

for transverse wake potential, which is nonzero for $m > 0$. Where $\Theta(s)$ is the Heaviside step function. Causality requires both wake potentials to be zero for $s < 0$ (ahead of source). The mode loss factor k_{mn} is defined as in eq. 2.29.

The total wake potential is obtained by summing over m and n. For small offsets (compared to radius a), the dominant term for the longitudinal wake potential is the monopole term ($m = 0$) and the dipole term ($m = 1$) for the transverse wake potential. So we can approximate wake potentials as

$$w_z \simeq w_{z0} = \sum_{n=0}^{\infty} 2k_{0n} \cos \frac{\omega_{0n} s}{c} \Theta(s) \qquad (2.34a)$$

$$w_\perp = w_{\perp 1} = \frac{r_1}{a} \mathbf{e}_x \sum_{n=0}^{\infty} \frac{2k_{1n}}{\omega_{1n} a/c} \sin \frac{\omega_{1n} s}{c} \Theta(s) \qquad (2.34b)$$

where $\mathbf{e}_x$ is the direction of the source charge displacement. The transverse wake potential is proportional to the offset of the source charge, and independent of the transverse coordinates of the test charge. The longitudinal wake potential is independent of the transverse position of both charges. For the transverse wake potential it is convenient to define kick factors as

$$k_{\perp n} = \frac{k_{1n}(r = a)}{\omega_{1n}a^2/c} \tag{2.35}$$

where k_{1n} is the dipole loss factor. In this manner the kick factor is independent of charge offset.

Applying the fundamental theorem of beam loading, the source charge at $s = 0$ will see half of the longitudinal wake potential that is induced. Finally we can summarise:

$$w_z(s) = \begin{cases} \sum_{n=0}^{\infty} 2k_{0n} \cos \frac{\omega_{0n}s}{c} & s > 0 \\ \sum_{n=0}^{\infty} k_{0n} & s = 0 \\ 0 & s < 0 \end{cases} \tag{2.36}$$

for longitudinal wake potential and

$$w_{\perp}(s) = \begin{cases} \frac{r_1}{a} \mathbf{e}_x \sum_{n=0}^{\infty} \frac{2k_{1n}}{\omega_{1n}a/c} \sin \frac{\omega_{1n}s}{c} & s > 0 \\ 0 & s = 0 \\ 0 & s < 0 \end{cases} \tag{2.37}$$

for transverse wake potential.

The energy lost by the source charge is

$$\Delta U = q_1^2 w_z(0) = q_1^2 \sum_{n=0}^{\infty} k_{0n} = q_1^2 k_{tot} \tag{2.38}$$

with k_{tot} defined as the total loss factor, and the power dissipated from the wakefields can be calculated using the quality factors of the modes as

$$\Delta P = \frac{\omega \Delta U}{Q} = q_1^2 \sum_{n=0}^{\infty} \frac{\omega_{0n} k_{0n}}{Q_{0n}} \tag{2.39}$$

Up until this stage, the analysis has been for a point charge. The next section extends this to include realistic charge distributions.

2.4.3 Wakefields from a Charged Particle Bunch

For an ultra-relativistic charged bunch, with a line charge density ρ, an element of charge $dq = \rho(z_1)\, dz_1$ will produce a potential at z either longitudinal or transverse as

$$dV(z) = w(s)dq = w(s)\rho(z_1)dz_1 \tag{2.40}$$

The bunch wake potential at z is the convolution over all source charges ahead of z, divided by the total charge in the bunch Q_t

$$W(z) = \frac{1}{Q_t} \int_{-\infty}^{z} w(z - z_1)\rho(z_1)dz_1. \tag{2.41}$$

We can write this in terms of the distance behind the source charge ($s = z - z_1$) as

$$W(z) = \frac{-1}{Q_t} \int_{-\infty}^{0} w(s)\rho(z - s)ds = \frac{1}{Q_t} \int_{0}^{\infty} w(s)\rho(z - s)ds \tag{2.42}$$

The energy lost from the bunch is equal to the work done by the wakefields on the bunch, which can be expressed in terms of the longitudinal wake potential $W_z(z)$ as

$$\Delta U = Q_t \int_{-\infty}^{\infty} \rho(z)W_z(z)dz \tag{2.43}$$

then the total bunch loss factor is defined as

$$k_{tot} = \frac{\Delta U}{Q_t^2} = \frac{1}{Q_t} \int_{-\infty}^{\infty} \rho(z) W_z(z) dz \tag{2.44}$$

As mentioned earlier, causality ensures the wake potential is zero ahead of the bunch, i.e. $w_z(s) = 0$, for $s < 0$. For a current source, $I = \rho c$, then eq. 2.42 can be written as

$$W_z(z) = \frac{1}{cQ_t} \int_{-\infty}^{\infty} w_z(s) I(z-s) ds \tag{2.45}$$

Considering a harmonic component of this source current at a frequency ω, $I(z_1) = I_0 e^{j\omega z_1/c}$ where $z_1 + s = z$. We have

$$I(z-s) = I_0 e^{j\omega(z-s)/c} = I_0 e^{j\omega z/c} e^{-j\omega s/c} = I(z) e^{-j\omega s/c} \tag{2.46}$$

then

$$W_z(z) = \frac{I(z)}{cQ_t} \int_{-\infty}^{\infty} w_z(s) e^{-j\omega s/c} ds \tag{2.47}$$

This is the longitudinal wake potential $W_z(z)$, as a result of a source current $I(z)$. The voltage response is $V(\omega) = Q_t W_z(\omega)$, and this defines the beam-coupling impedance as

$$Z_z(\omega) = \frac{V(\omega)}{I(\omega)} = \frac{1}{c} \int_{-\infty}^{\infty} w_z(s) e^{-j\omega s/c} ds \tag{2.48}$$

This impedance is the Fourier transform of the δ-function wake potential. If we know the beam-coupling impedance, then on taking the Inverse Fourier transform we get the δ-function wake potential as

$$w_z(\mathbf{r}_\perp, s) = \frac{1}{2\pi} \int_{-\infty}^{\infty} Z_z(\mathbf{r}_\perp, \omega) e^{j\omega s/c} d\omega \tag{2.49}$$

In a similar fashion, applied to the transverse components, we get

$$Z_\perp(\mathbf{r}_\perp, \omega) = \frac{1}{jc} \int_{-\infty}^{\infty} w_\perp(\mathbf{r}_\perp, s) e^{-j\omega s/c} ds \tag{2.50}$$

$$w_\perp(\mathbf{r}_\perp, s) = \frac{j}{2\pi} \int_{-\infty}^{\infty} Z_\perp(\mathbf{r}_\perp, \omega) e^{j\omega s/c} d\omega \tag{2.51}$$

where $\mathbf{r}_\perp$ is the transverse coordinate. These transverse and longitudinal impedances are related by the Panofsky-Wenzel theorem [25] as

$$\frac{\omega}{c} Z_\perp(\mathbf{r}_\perp, \omega) = \nabla Z_z(\mathbf{r}_\perp, \omega) \tag{2.52}$$

2.4.4   Parasitic Energy Loss and Energy Spread

The wakefields act on the beam, and this causes the beam to lose energy. This effect is called parasitic energy loss. By increasing the rf voltage, we can compensate for this lost energy. Wakefield energy is also dissipated to the structure walls; the average power loss can be calculated from

$$P = \Delta U(L) f_R = \frac{f_R k_{tot} L (eN)^2}{l_c} \tag{2.53}$$

where f_R is bunch repetition rate, L is cavity effective length, l_c is cavity cell length, e is an electron charge, and N is number of particles per bunch.

For example, considering the parameters of the ILC linac; which has $N = 2 \times 10^{10}$ electrons per bunch, cell length $l_c = 115.4\,\text{mm}$, bunch repetition rate $f_R = 5\,\text{Hz}$, cavity length $L = 1.038\,\text{m}$, and a total loss factor $k_{tot} = 9 \times 10^{12}\,\text{V/C}$, we obtain $P = 4\,\text{mW/m}$.

An energy spread across the beam can be caused by the wakefields generated by the head acting

along the rest of the bunch. By considering a longitudinal wake potential that increases linearly with respect to distance s, $W_z(s) = sW_z'$, along the bunch, the approximate energy loss over the structure length, L, is

$$\Delta W(s, L) = -\frac{eQ_t s W_z' L}{l_c} \tag{2.54}$$

If we neglect wakefields energy lost at the head, $s = 0$, the total energy spread across the beam is

$$\delta W(L) = -\frac{eQ_t l_b W_z' L}{l_c} \tag{2.55}$$

where l_b is the bunch length.

2.4.5 Beam Breakup

Beam breakup instabilities can affect high current linacs if the higher order modes induced in the cavity are not damped. Beam breakup is caused by deflecting modes -the dipole mode is the dominant term.

The fundamental mechanism of the instability can be understood from a straightforward two particle model - which can be extended to an N-particle model [26]. To begin, consider two charged particles travelling down a linac subjected to focusing in a FODO [1] lattice, q_1 at offset x_1 and q_2 at offset x_2, separated by distance s. The leading particle q_1 faces external focusing forces, and as a result it will experience transverse oscillations (betatron oscillation) about the beam axis. The position of the leading particle is approximated as a simple harmonic oscillation, $x_1 = X \cos \omega_\beta t$, with frequency ω_β. If we neglect the transverse wakefields induced by the leading particle, the tailing particle performs the same motion as the leading particle. From the relation of force and the change of momentum

$$\Delta p_\perp c = F_w l_c = q_2 q_1 w_\perp(s) \tag{2.56}$$

the average wakefields force, F_w, arising due to q_1 acting over a cell length, l_c, can be written as

$$F_w = \frac{q_2 q_1}{l_c} \left[\frac{w_\perp(s)}{x_1/a} \right] \frac{x_1}{a} \tag{2.57}$$

In a constant-energy beam, the equation of motion for a tailing particle can be written as

$$m\gamma \ddot{x}_2 = -m\gamma \omega_\beta^2 x_2 + F_w \tag{2.58}$$

with some algebraic rearrangement:

$$\ddot{x}_2 + \omega_\beta^2 x_2 = \frac{q_2 q_1}{m\gamma l_c a} \left(\frac{w_\perp}{x_1/a} \right) X \cos \omega_\beta t \tag{2.59}$$

The general solution of this driven oscillator equation of motion for the trailing particle is

$$\frac{x_2(t)}{X} = \cos \omega_\beta t + \frac{q_2 q_1 t}{2m\gamma l_c a \omega_\beta} \left(\frac{w_\perp}{x_1/a} \right) \sin \omega_\beta t \tag{2.60}$$

The second term is the response to the wake force, in which the amplitude growth is proportional
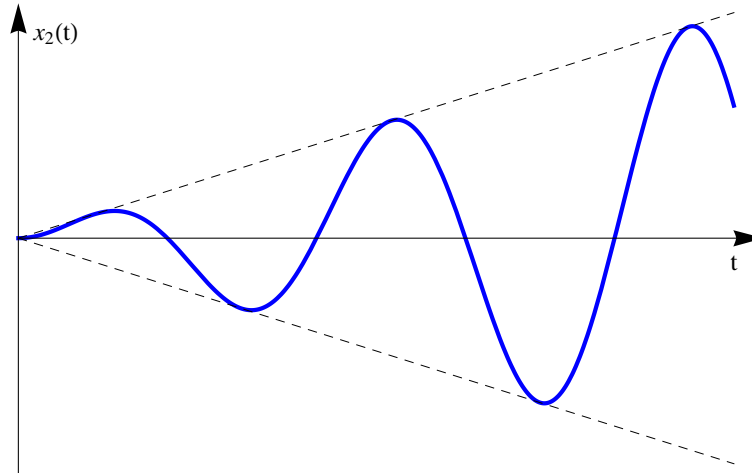
Figure 2.2: Offset position growth of the trailing charge relative to the leading charge.

to the time t, as can be seen from Fig. 2.2. As mentioned previously, when the term $w_\perp = 0$, the motion of the trailing charge approximates a simple harmonic oscillation like the leading charge with the betatron frequency ω_β.

Applying a two particle model to the bunch by dividing the bunch into two macro-particles which each contains half of the bunch population. Here, we calculate the effect of a charge $q_1 = eN/2$ at the head on an electron with charge $q_2 = e$ in the tail. The displacement equation for the tail of the bunch is then

$$\frac{x_2(t)}{X} = \cos \omega_\beta t + \frac{e^2 Nt}{4m\gamma l_c a \omega_\beta}\left(\frac{w_\perp}{x_1/a}\right)\sin \omega_\beta t \tag{2.61}$$

The relative displacement of the tail with respect to the head of the bunch over a cavity length L is

$$A(s) = \frac{e^2 NLc}{4(\gamma mc^2)l_c a \omega_\beta}\frac{w_\perp}{x_1/a} \tag{2.62}$$

When this bunch passes through the linac, the shape of the bunch resembles a banana at the particular time during the oscillation when the tail has swung away from the path of the head. This results in transverse emittance growth. If the amplitude grows large enough, the tail particles will be lost on the walls, referred to as single bunch beam breakup. The amplitude growth can be reduced by strong focusing, taking into consideration the ω_β factor.

The long-range wakefields, which often are dominated by a few dipole modes, can lead to a multibunch beam breakup instability which affect the intensity. Multibunch beam breakup can be initiated from a small transverse modulation of the bunches at the deflecting mode frequency, which can excite a small excitation of the deflecting mode. The deflecting mode will act on the following bunches to drive them off axis, which reinforces the excitation of the deflecting mode. From these we can group the growth mechanism into two mechanisms, regenerative and cumulative beam breakup.

The regenerative mechanism occurs in a single multi-cell linac structure, while a cumulative mechanism occurs in a linac consisting of an array of electromagnetically independent cavities. In the regenerative case the deflecting mode excitation from the beam-cavity interaction is carried from one cell to the next by the strong electromagnetic coupling of the cells, while in the cumulative case, the effect is coupled by the beam from earlier to later cavities.

Good alignment of the beam to the axis, using strong magnetic focusing, detuning of the deflecting mode frequencies from cavity to cavity, and damping the deflecting modes through the HOM couplers will reduce the effects of cumulative beam breakup.

2.4.6 BNS Damping of Beam Breakup

One method of reducing the emittance growth effect from single bunch beam breakup is called Balakin Novokhatsky Smirnov (BNS) damping [27]. This can be understood by considering a bunch with a head and tail of differing betatron frequencies. Referring to the two particle model in the previous section. Starting from the oscillator driven equation of motion of the tailing particle:

$$\ddot{x}_2 + \omega_{\beta 2}^2 x_2 = \frac{e^2 N}{2m\gamma l_c a} \left(\frac{w_\perp(s)}{x_1/a} \right) X \cos \omega_{\beta 1} t \tag{2.63}$$

where $\omega_{\beta 1}$ and $\omega_{\beta 2}$ are the betatron frequencies at the head and tail, respectively and with the initial conditions, $x_2(0) = x_1(0)$ and $\dot{x}_2(0) = \dot{x}_1(0)$. The solution for the tail displacement is

$$x_2(t) = X \cos \omega_{\beta 2} t + \frac{F_0(s)}{\omega_{\beta 2}^2 - \omega_{\beta 1}^2} (\cos \omega_{\beta 1} t - \cos \omega_{\beta 2} t) \tag{2.64}$$

where

$$F_0(s) = \frac{e^2 N X}{2m\gamma l_c a} \left(\frac{w_\perp(s)}{x_1/a} \right) \tag{2.65}$$

Minimising the difference between the displacement of the tail and head leads to a decrease of transverse emittance.

$$x_2(t) - x_1(t) = 2X \left[\frac{F_0(s)}{(\omega_{\beta 2}^2 - \omega_{\beta 1}^2)X} - 1 \right] \left[\sin \frac{(\omega_{\beta 2} + \omega_{\beta 1})t}{2} \sin \frac{(\omega_{\beta 2} - \omega_{\beta 1})t}{2} \right] \qquad (2.66)$$
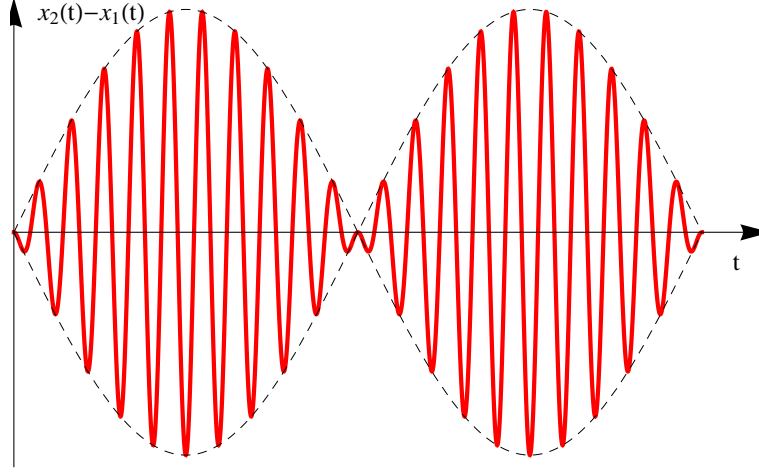
Figure 2.3: Beat pattern describing the displacement position growth of the trailing charge relative to the leading charge.

The difference between head and tail displacement is displayed graphically in Fig. 2.3. If we make $\omega_{\beta 2} > \omega_{\beta 1}$ and $\frac{F_0(s)}{(\omega_{\beta 2}^2 - \omega_{\beta 1}^2)X} = 1$, the displacement amplitude will be zero. This condition can be achieved with the small difference of the betatron frequency, $\Delta \omega_\beta = \omega_{\beta 2} - \omega_{\beta 1}$, of

$$\Delta \omega_\beta = \frac{F_0(s)}{2\omega_{\beta 1}X} \qquad (2.67)$$

In practise, there are several ways to create a betatron frequency difference: one involves using magnetic focusing, where the focusing force increases at lower momentum; another involves choosing to accelerate the beam off crest, so that particles in the tail see a smaller accelerating field than those of the head. This method is often adopted to minimise the effect of the short-range wakefield. The

long-range wakefield must be explicitly damped however.

The next chapter provides an overview of the current status of research in high gradient SC cavities. This serves as a prelude to the chapters following, which form the body of this thesis in which optimisation of e.m. fields in a SC cavity is explored.

Chapter 3

Review of High Gradient Cavities for the

ILC

The TESLA cavity has been chosen as the baseline design for the ILC project. However, several new cavities shapes have recently also been designed. The performances of a SC cavity is limited by the maximum surface electric (E_s) and magnetic (B_s) fields which can be sustained on the walls. The ratios: E_s/E_a and B_s/E_a form an important criterion and are dependant on the cavity geometry, surface morphology, and vacuum conditions.

The intrinsic rf critical magnetic field (B_c) is the limit of B_s. It is at the point the material looses its superconductivity. The limit of E_s is determined from the field emission within the cavity. For a niobium cavity B_c lays in the range 180 mT to 230 mT [28] and the E_s restricted to $\sim$ 100 MV/m [29–32]. Single cell cavities have achieved larger surface fields [14] than the current multi-cell cavity values. The maximum allowable gradient E_a^m can be written as:

$$E_a^m = \frac{B_c}{B_s/E_a} \tag{3.1}$$

This equation describes the theoretical maximum gradient obtainable in an ideal cavity. A more general form of equation for realistic experimental cavities can be written as:

$$E_a^m = \frac{r \cdot B_c}{\beta_{MAG} \cdot B_s/E_a} \tag{3.2}$$

where r (≤ 1) is a dimensionless factor representing the reduction due to impurities, lattice defects etc. in the rf penetration depth. β_{MAG} (≥ 1) is a dimensionless quantity representing the enhancement of B_s due to local geometric imperfections. For an ideal cavity both are equal to one and eq. 3.2 reduces to eq. 3.1. The maximum obtainable gradient from the limitation of E_s can be obtained in the similar fashion.

From eq. 3.1, there are two way to improve the maximum gradient. B_c can be increased by using different materials (Nb_3Sn) or B_s/E_a can be reduced by changing the cavity geometry. The two approaches have different advantages.

Reshaping the cell geometry has been a subject of investigation over the past decade. There are two current designs which result in reduced surface fields compared to TESLA, the reentrant [31, 33] and low loss [34–36] cavity. Another recent design is the LSF shape [37]. I have also introduced my own design which in addition to reducing the surface fields also results in an enhanced bandwidth of the accelerating mode.

The next section describes these cavity shapes and their influences of the e.m. fields in the cavity.

3.1   Reentrant Cavity

Cornell University has been conducting research on a reentrant cavity shape. This optimised shape was based on reducing B_s/E_a to achieve a higher potential gradient. The reentrant shape consists of two conjugated elliptical arcs. This shape is displayed in Fig. 3.1, along with other designs. This
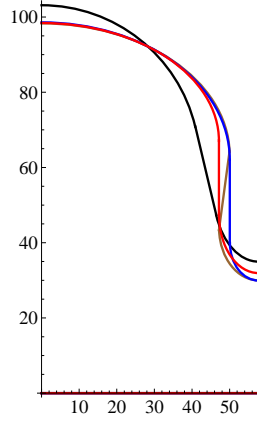
Figure 3.1: Half-cell geometry comparison of four designs: TESLA (black), Reentrant (brown), Low loss (blue) and NLSF (red), where dimension is in mm.

shape has the potential to trap water in the reentrant pocket during the cleaning process. However, it is expected that this can be solved by vigorous shaking between the high pressure rinse cycles. The reentrant shape initially was designed with an iris radius of 35mm and has a 13 % reduction in B_s/E_a compared to the TESLA shape [38]. However, subsequent designs opted for a 30mm iris radius and this reduced the bandwidth of the monopole mode, $\kappa_c \approx (\omega_\pi - \omega_0)/\omega_{\pi/2}$). The bandwidth determines the sensitivity of the cavity cell fabrication errors as the separation of the next nearest mode to the accelerating mode is given by [39]:

$$\triangle\overline{\omega} = \frac{\omega_\pi - \omega_{(1-N^{-1})\pi}}{\omega_{\pi/2}} \approx (\frac{\pi}{2N})^2\kappa_c \tag{3.3}$$

here N=9 for ILC cavities. A higher κ_c, implies a larger separation of modes. This single cell cavity has achieved a record gradient of 52 MV/m with a Q_0 of 2×10^{10} operating in a CW mode [14, 31].

The surface B_s and E_s are 197.1 mT and 114 MV/m, respectively [40].

Other shapes have been investigated. The half-reentrant shape [41, 42], for example, which consists of half a reentrant cell sandwiched with a TESLA-like half cell, has reached 51 MV/m. However, these have not received as much attention as the reentrant and low loss design. The low loss design is discussed in the next section.

3.2   Low Loss and Ichiro Cavity

A low loss shape was initially proposed in 2002 for the 12 GeV upgrade of the CEBAF cavities [34]. This shape has been optimised to increase both the R/Q and the geometrical factor G. The cavity has less stored energy and dissipates less power in the walls at a given accelerating gradient. The power dissipation to cavity walls (P_d) for a given cavity voltage (V_c) is inversely proportional to the product of R/Q and Q as

$$P_d = \frac{V_c^2}{R_a} = \frac{V_c^2}{Q_0 \cdot (R_a/Q_0)} = \frac{V_c^2}{(R_s \cdot Q_0)(R_a/Q_0)/R_s} = \frac{V_c^2 \cdot R_s}{G \cdot (R_a/Q_0)} \propto \frac{1}{G \cdot (R_a/Q_0)} \qquad (3.4)$$

where R_s and R_a are the surface resistance and shunt impedance of the cavity, respectively. The dissipated power is considered as the cryogenic load of the SC cavity cooling systems.

The approach has also been explored for cavity shape for the ILC. The 1.3 GHz low loss cavity was first reported at the first ILC workshop in 2004 and results were published in 2005 [35]. This shape consisted of an elliptical equator and elliptical iris connected by a straight segment, almost perpendicular to the beam axis (as shown in Fig. 3.1). This radius is 5 mm smaller than in the TESLA cavity and consequently the wakefields are larger. The initial 1.3 GHz single cell low loss cavity reached 47 MV/m with Q_0 of 1.2×10^{10} at KEK in 2005 [40]. Enhanced surface treatments enabled

a single cell obtain a gradient of 51 MV/m [14].

KEK has been conducting experimental studies on a single-cell and also on multi-cell 1.3 GHz cavities since 2004. KEK has built and tested a nine-cell low loss cavity, referred to as Ichiro. At the end of 2008, eight nine-cell Ichiro cavities had been fabricated. However, none of these Ichiro cavities reach more than 37 MV/m [43].

3.3 Low Surface Field and NLSF Cavity

In 2008 Li and Adolphsen proposed another optimised scheme for a high gradient cavity, referred to as a Low Surface Field (LSF) cavity [37]. The radius of 30 mm corresponds to that of the low loss design. However, this is 5 mm smaller than the TESLA design. The iris and equator elliptical parameters were optimised to achieve 11% reduction of B_s/E_a compared to that of TESLA and 15% less E_s/E_a than low loss design. The monopole bandwidth is however 18% narrower than that of the low loss, so this design is more sensitive to the cell errors and has significantly larger dimensional tolerance.

My design, the New Low Surface Field (NLSF) cavity was first presented in 2009 [44]. In addition to reducing the surface e.m. fields, the bandwidth is also increased. The cell geometry is sketched out in Fig. 3.1. It has the same iris thickness as that of the LSF shape. The iris radius is larger than the LSF, but 3 mm smaller than the TESLA design. The benefits of having a slightly larger iris are an increased bandwidth. The transverse kick is also decreased. The ellipticity of the iris and equator were optimised to minimise the surface fields and maximise the bandwidth. This resulted in a 8.5% reduction in the B_s/E_a ratio compared to TESLA shape and a 13% reduction in E_s/E_a compared to the LL design. In addition the bandwidth is 26.5% wider than the LSF design. This design has the potential to achieve an accelerating gradient of 47 MV/m to 60 MV/m for a surface magnetic

Table 3.1: RF parameters comparison of the TESLA shape and the new shapes (adapted from [14])

Parameter (Unit)	TESLA	Reentrant 35 mm iris	Reentrant 30 mm iris	Half reentrant	Low loss	Ichiro	LSF	NLSF
Frequency (MHz)	1300	1300	1300	1300	1300	1300	1300	1300
Iris radius (mm)	35	35	30	29	30	30	30	32
B_p/E_a (mT/(MV/m))	4.15	3.78	3.54	3.51	3.61	3.62	3.72	3.83
E_p/E_a (-)	1.98	2.40	2.28	2.40	2.36	2.37	2.06	2.11
$G \cdot R/Q$ (Ω^2)	30,840	33,762	41,208	39,363	37,970	37,914	-	35,186
k_c (%)	1.90	2.38	1.57	1.52	1.52	1.54	1.25	1.59

field B_s of 180 mT and 230 mT, respectively. The maximum E_s will be in the range 98 MV/m to 126 MV/m. Additional studies have been extended on the the reentrant shape [45]. Detailed designs and properties of these NLSF shapes will be discussed later. A comparison of rf parameters of the TESLA shape and the new shapes are summarised in Table3.1.

In addition to the SC materials and the cavity shape, cavity fabrication, surface treatment and processing also affect the ability of the cavity to sustain high accelerating fields. These effects are included in eq. 3.2. Their are many effects concerning from the choice of sheet niobium, cell shaping process, cell joining, surface treatment, cleaning procedures, low temperature bake out and the cleanliness of work environment. These all must be carefully controlled to obtain the full benefits from the new shapes and to reach high accelerating field gradients.

A circuit model representation of the cavity allows rapid computation of the rf properties of cavities and is presented in the next chapter. This is an important design tool.

Chapter 4

Coupled Circuit Models Applied to Accelerating Cavities

In order to ascertain the fields present in accelerating cavities finite difference and finite element codes may be used. However, these computer codes suffer from being computationally expensive: both in terms of the time and memory required. Circuit models can also be used to obtain the electromagnetic fields and eigenfrequencies of the cavities. These models focus on the physics of a particulars set of modes and hence are very efficient. Circuit models allows complete multi-cell accelerator cavities to be modelled rapidly and hence serve as an essential design tool. In this work both the monopole and dipole modes are analysed using a circuit model. The monopole mode is analysed using a single chain of coupled RLC circuits. This rapidly facilitates a design and enables fabrication errors in the cavities to be understood. This approach is explained in the next section and applied to the accelerating "π - mode".

4.1 Single Chain Circuit Model

A cavity consists of a string of resonant cells. This system can be represented by a chain of RLC resonant circuits as shown in Fig. 4.1. This method has been developed by many contributors [39, 46–50]. Circuit models have been used to understand and predict the rf quantities of, and the behaviour of standing waves and travelling waves in coupled accelerator cavities. This method assumes a next neighbouring coupling between cells and that each iris is thin. The resonant frequency of a cell is represented by the angular frequency $\omega_r = \sqrt{1/LC}$ and the coupling between cells is represented by the mutual inductance factor $M = \kappa L$.
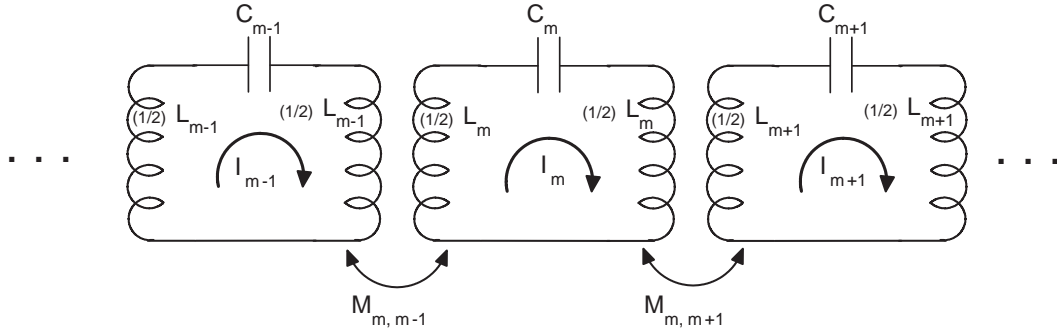
Figure 4.1: Schematic of a single chain of coupled cells represented by LC circuits.

The fundamental mode in a standing wave cavity is the monopole transverse magnetic (TM) mode. The single chain coupled circuit model illustrated in Fig. 4.1 has adequate information to describe the coupling between the cells of a TM -like structure. I use inductive coupling of cells and assume no losses in the cavity structure, i.e. no resistors in the circuit model. A loop of m chains represents m cells in the cavity structure. Using Kirchhoff's voltage law at the mth loop, one can obtain the following.

$$(j\omega L_m + \frac{1}{j\omega C_m})I_m + \frac{j\omega M_{m,m-1}}{2}I_{m-1} + \frac{j\omega M_{m,m+1}}{2}I_{m+1} = 0 \qquad (4.1)$$

one can simplify the above equation to:

$$(1 - \frac{\omega_m^2}{\omega^2})I_m + \frac{\kappa_{m-\frac{1}{2}}}{2}I_{m-1} + \frac{\kappa_{m+\frac{1}{2}}}{2}I_{m+1} = 0 \tag{4.2}$$

where ω is the resonant frequency of the chain, $\omega_m (= (L_m C_m)^{-1/2})$ is the resonant frequency of the mth cell and coupling constant is defined as:

$$\kappa_{m\pm\frac{1}{2}} = \frac{M_{m,m\pm1}}{L_m} \tag{4.3}$$

Here, the 1/2 factor refers to the coupling from the centre of one cell to the centre of an adjacent cell.

Eq. 4.2 is an eigensystem problem with corresponding eigenvectors I_m and eigenvalues ω^{-2}. In solving this eigensystem we need to specify boundary conditions. Two boundary conditions are possible for this problem [49]. First, N full cells with the end cells connected to beam tubes. This boundary condition is described as:

$$I_0 = I_1, \ I_{N+1} = I_N, \ \kappa_{\frac{1}{2}} = k_1, \ \kappa_{N+\frac{1}{2}} = \kappa_N \tag{4.4}$$

Using this boundary condition the π mode is not a solution of the problem and the phase advance of the pth mode is given by:

$$\phi_p = \frac{(p-1)\pi}{N} \quad , \quad p = 1, 2, ..., N \tag{4.5}$$

The other possible boundary condition is for $N-2$ full cells closed by two half cells (at either end). In this case the boundary condition is given as:

$$I_0 = I_2, \ I_{N+1} = I_{N-1}, \ \kappa_{\frac{1}{2}} = \kappa_{\frac{3}{2}}, \ \kappa_{N+\frac{1}{2}} = \kappa_{N-\frac{1}{2}} \tag{4.6}$$

The phase advance of the pth mode for this boundary condition is:

$$\phi_p = \frac{(p-1)\pi}{N-1} \quad , \quad p = 1, 2, ..., N. \tag{4.7}$$

The advantage of this boundary condition is that it admits both the 0 and π as solutions.

Considering an identical periodic structure (i.e. the cell resonant frequencies and coupling constants are same for N cells, hence $\omega_m = \omega_r$ and $\kappa_{m\pm\frac{1}{2}} = \kappa$), the periodic solution of eq. 4.2 can be written as $I_m = I_0 e^{jm\phi}$, i.e. a change in phase. This infinite periodic structure has a corresponding dispersion relation:

$$(1 - \frac{\omega_r^2}{\omega^2}) + \kappa \cos\phi = 0 \tag{4.8}$$

The resonant frequency and coupling constant ω_r and κ are obtained from the 0 and π phase advance frequencies using the relation:

$$\omega_r = \sqrt{\frac{2\omega_\pi^2 \omega_0^2}{\omega_\pi^2 + \omega_0^2}} \tag{4.9a}$$

$$\kappa = \frac{\omega_\pi^2 - \omega_0^2}{\omega_\pi^2 + \omega_0^2} \tag{4.9b}$$

The single chain circuit model (detailed by Bane and Gluckstern [49] and can also be seen in Appendix B) allows the coupled mode kick factors to be obtained for mode p:

$$K_p = \frac{|\sum_{n=1}^{N} I_n^{(p)} \sqrt{K_s^{(n)}(\omega_s^{(n)}/2\pi)} e^{jn\varphi_p}|^2}{N(\omega_p/2\pi)|I^{(p)}|^2} \tag{4.10a}$$

$$\varphi_p = \frac{\omega_p L}{c} \tag{4.10b}$$

where $I^{(p)}$ is the eigenvector and $\omega_p/2\pi$ is the eigenfrequency of pth mode respectively and $K_s^{(n)}$ is the kick factor of the nth cell at the synchronous frequency $\omega_s^{(n)}/2\pi$ of that cell.

In next section the extension of this single chain model to include a coupling from next nearest neighbouring cell is discussed. This model is used to accurately represent higher order monopole modes excited in the cavity.

4.2 Extension of the Single Chain Circuit Model to Include Next Nearest Coupling

The previous section relies on nearest neighbour coupling. One can extend this representation to include next nearest neighbour coupling, i.e. cell m coupled to not only cell $m \pm 1$ but also cell $m \pm 2$. In similar fashion to the previous section, at loop m we write:

$$(j\omega L_m + \frac{1}{j\omega C_m})I_m + \frac{j\omega M_{m,m-1}}{2}I_{m-1} + \frac{j\omega M_{m,m+1}}{2}I_{m+1} + \frac{j\omega M_{m,m-2}}{2}I_{m-2} + \frac{j\omega M_{m,m+2}}{2}I_{m+2} = 0$$

(4.11)

and then simplify this to:

$$(1 - \frac{\omega_m^2}{\omega^2})I_m + \frac{\kappa_{1,m-\frac{1}{2}}}{2}I_{m-1} + \frac{\kappa_{1,m+\frac{1}{2}}}{2}I_{m+1} + \frac{\kappa_{2,m-\frac{1}{2}}}{2}I_{m-2} + \frac{\kappa_{2,m+\frac{1}{2}}}{2}I_{m+2} = 0$$

(4.12)

where $\omega_m = 1/\sqrt{L_m C_m}$ is the resonant frequency of cell m, ω is the resonant frequency of the system and the two coupling constants defined as

$$\kappa_{1,m\pm\frac{1}{2}} = \frac{M_{m,m\pm1}}{L_m} \quad , \quad \kappa_{2,m\pm\frac{1}{2}} = \frac{M_{m,m\pm2}}{L_m}.$$

(4.13)

This eigensystem can be solved with suitable boundary conditions similar to the previous section and results in eigenvectors I_m and eigenvalues ω^{-2}.

To obtain the Brillouin diagram we specialise to an infinite periodic chain of cavity cells with a Floquet condition of constant phase shift between neighbouring cells and a current variation of $e^{j\omega t}$:

$$I_{m\pm 1} = i_{m\pm 1}e^{-j\omega t} = I_0 e^{\pm j\phi}e^{-j\omega t} \quad , \quad I_{m\pm 2} = i_{m\pm 2}e^{-j\omega t} = I_0 e^{\pm j2\phi}e^{-j\omega t}. \tag{4.14}$$

This allows eq. 4.12 to be simplified and the dispersion relation to be obtained

$$\omega(\phi) = \frac{\omega_r}{\sqrt{1 + \kappa_1 \cos\phi + \kappa_2 \cos 2\phi}}. \tag{4.15}$$

This equation can be solved to obtain the resonant frequency ω_r and coupling constants, κ_1 and κ_2, by calculating three pairs of frequencies and phase advances with finite element or finite difference computer codes. One can also extend this method further than next nearest coupling, although in the cavity modelled in this work it was not found to be necessary. Further details on enhancements to next nearest coupling are found in [51, 52].

Monopole modes in the cavity can be accurately described using the single chain coupled circuit model. However, for dipole modes the single chain circuit model does not provide enough information to correctly describe the properties of fields inside cavity. This is because a dipole mode is inherently a mixture of TM and transverse electric (TE) modes. In order to properly represent this mode a double chain of LC circuits is required. As will be seen, without this model the dispersion relation is poorly represented. This double chain model is described in the next section.

4.3 Double Chain Circuit Model

The hybrid characteristics of dipole e.m. fields are described by a double chain coupled circuit model. This consists of two chains of resonant circuits: one represents the TM wave behaviour and

the other represents the TE wave behaviour. This circuit model is illustrated in Fig. 4.2. In this case
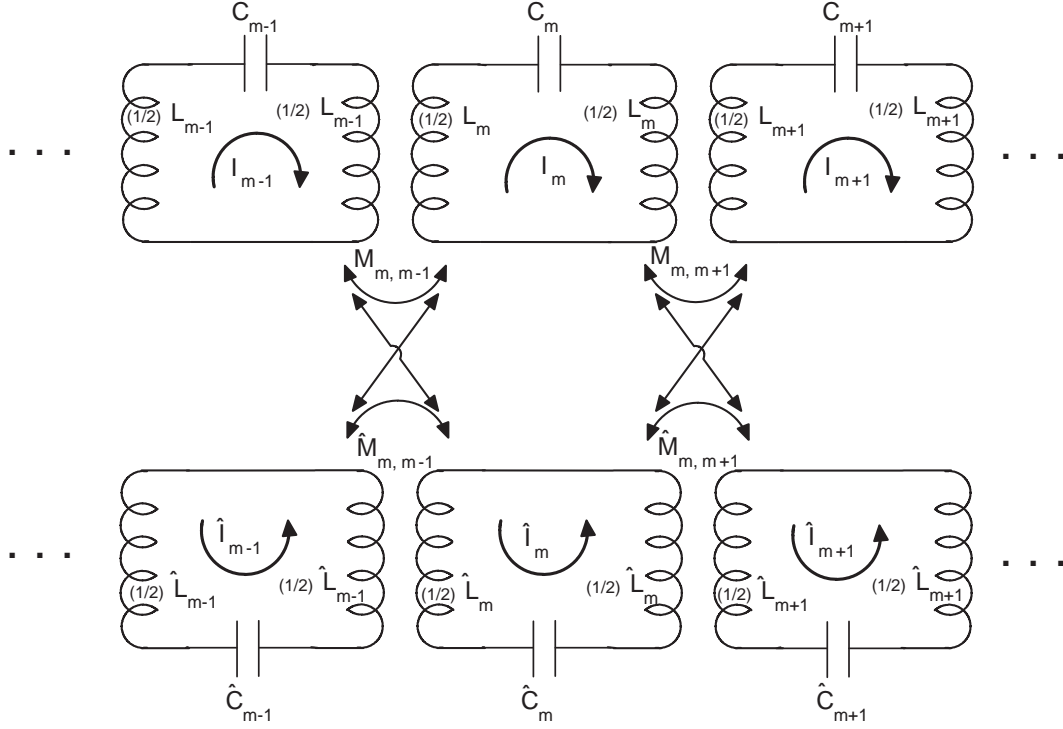
Figure 4.2: Schematic of a double chain of coupled cells represented by LC circuits.

$\hat{I}, \hat{L}, \hat{C}, \hat{M}$ refers to the TE wave and I, L, C, M to the TM, where the subscript m represents the mth cell of the cavity. In a similar fashion to the single chain circuit model, we use Kirchhoff's voltage law to derive the relationship between both chains at the mth loop. We apply this method for both the TM and TE chains.

For TM chain we obtain:

$$(j\omega L_m + \frac{1}{j\omega C_m})I_m - \frac{j\omega M_{m,m+1}}{2}I_{m+1} - \frac{j\omega M_{m,m-1}}{2}I_{m-1} = -\frac{j\omega \hat{M}_{m,m+1}}{2}\hat{I}_{m+1} + \frac{j\omega \hat{M}_{m,m-1}}{2}\hat{I}_{m-1} \quad (4.16)$$

and for the TE chain:

$$(j\omega \hat{L}_m + \frac{1}{j\omega \hat{C}_m})\hat{I}_m + \frac{j\omega \hat{M}_{m,m+1}}{2}\hat{I}_{m+1} + \frac{j\omega \hat{M}_{m,m-1}}{2}\hat{I}_{m-1} = +\frac{j\omega M_{m,m+1}}{2}I_{m+1} - \frac{j\omega M_{m,m-1}}{2}I_{m-1} \quad (4.17)$$

It is convenient to use normalised variables a_m ($= I_m \omega_m \sqrt{L_m}$) and $\hat{a}_m$ ($= \hat{I}_m \hat{\omega}_m \sqrt{\hat{L}_m}$) and thus allows eq. 4.16 and eq. 4.17 to be rewritten.

The TM chain becomes:

$$(1 - \frac{\omega_m^2}{\omega^2})a_m - \frac{\eta_{m+\frac{1}{2}}}{2}a_{m+1} - \frac{\eta_{m-\frac{1}{2}}}{2}a_{m-1} = -\frac{\sqrt{\eta_{m+\frac{1}{2}}\hat{\eta}_{m+\frac{1}{2}}}}{2}\hat{a}_{m+1} + \frac{\sqrt{\eta_{m-\frac{1}{2}}\hat{\eta}_{m-\frac{1}{2}}}}{2}\hat{a}_{m-1} \quad (4.18)$$

and the TE chain becomes:

$$(1 - \frac{\hat{\omega}_m^2}{\omega^2})\hat{a}_m + \frac{\hat{\eta}_{m+\frac{1}{2}}}{2}\hat{a}_{m+1} + \frac{\hat{\eta}_{m-\frac{1}{2}}}{2}\hat{a}_{m-1} = +\frac{\sqrt{\eta_{m+\frac{1}{2}}\hat{\eta}_{m+\frac{1}{2}}}}{2}a_{m+1} - \frac{\sqrt{\eta_{m-\frac{1}{2}}\hat{\eta}_{m-\frac{1}{2}}}}{2}a_{m-1} \quad (4.19)$$

Where $\eta_{m\pm\frac{1}{2}} = \frac{M_{m,m\pm1}}{\sqrt{L_m L_{m\pm1}}}$, $\hat{\eta}_{m\pm\frac{1}{2}} = \frac{\hat{M}_{m,m\pm1}}{\sqrt{\hat{L}_m \hat{L}_{m\pm1}}}$, $\omega_m = \frac{1}{\sqrt{L_m C_m}}$, $\hat{\omega}_m = \frac{1}{\sqrt{\hat{L}_m \hat{C}_m}}$ and a_m, $\hat{a}_m$ are eigenvectors with eigenvalues ω^{-2}.

In a similar manner to the single chain model, there are two possible boundary conditions. One is N full cells in which we define the boundary conditions as:

$$a_0 = a_1, \; a_{N+1} = a_N, \; \eta_{\frac{1}{2}} = \eta_1, \; \eta_{N+\frac{1}{2}} = \eta_N \quad (4.20a)$$

$$\hat{a}_0 = -\hat{a}_1, \; \hat{a}_{N+1} = -\hat{a}_N, \; \hat{\eta}_{\frac{1}{2}} = \hat{\eta}_1, \; \hat{\eta}_{N+\frac{1}{2}} = \hat{\eta}_N \quad (4.20b)$$

The other is $N - 2$ full cells terminated by two half cells:

$$a_0 = a_2, \ a_{N+1} = a_{N-1}, \ \eta_{\frac{1}{2}} = \eta_{\frac{3}{2}}, \ \eta_{N+\frac{1}{2}} = \eta_{N-\frac{1}{2}} \tag{4.21a}$$

$$\hat{a}_0 = 0, \ \hat{a}_{N+1} = 0, \ \hat{\eta}_{\frac{1}{2}} = \hat{\eta}_{\frac{3}{2}}, \ \hat{\eta}_{N+\frac{1}{2}} = \hat{\eta}_{N-\frac{1}{2}} \tag{4.21b}$$

Specialising to a uniform structure subjected to infinite periodic boundary conditions with $\omega_m = \omega_r$, $\hat{\omega}_m = \hat{\omega}_r$, $\eta_m = \eta_{m\pm\frac{1}{2}} = \eta$, $\hat{\eta}_m = \hat{\eta}_{m\pm\frac{1}{2}} = \hat{\eta}$ yields:

$$\left(\frac{1 - \eta\cos\phi}{\omega_r^2} - \frac{1}{\omega^2}\right)\left(\frac{1 + \hat{\eta}\cos\phi}{\hat{\omega}_r^2} - \frac{1}{\omega^2}\right) - \frac{\bar{\eta}^2}{\omega_r^2\hat{\omega}_r^2}\sin^2\phi = 0. \tag{4.22}$$

Here the Floquet condition has been applied in the form $a_m = a_0 e^{jn\phi}$, $\hat{a}_m = \hat{a}_0 e^{jn\phi}$, and $\bar{\eta} = \sqrt{\eta\hat{\eta}}$.

All other parameters η, $\hat{\eta}$, ω_r, and $\hat{\omega}_r$ are obtained by subjecting a single cell to periodic boundary conditions with a suitable finite difference or finite element computer code. The frequencies at which the 0 and π phase are taken needs to be carefully selected, so that both η and $\hat{\eta}$ are positive values, i.e. here TE is a forward wave ($\hat{\omega}_\pi > \hat{\omega}_0$) and TM is a backward wave ($\omega_\pi < \omega_0$). These frequencies are chosen based on the observed field pattern from the numerical simulations. It is straightforward to solve eq. 4.22 for all four parameters:

$$\omega_r = \sqrt{\frac{2\omega_\pi^2\omega_0^2}{\omega_\pi^2 + \omega_0^2}} \quad \text{and} \quad \eta = \frac{\omega_0^2 - \omega_\pi^2}{\omega_\pi^2 + \omega_0^2} \tag{4.23a}$$

$$\hat{\omega}_r = \sqrt{\frac{2\hat{\omega}_\pi^2\hat{\omega}_0^2}{\hat{\omega}_\pi^2 + \hat{\omega}_0^2}} \quad \text{and} \quad \hat{\eta} = \frac{\hat{\omega}_\pi^2 - \hat{\omega}_0^2}{\hat{\omega}_\pi^2 + \hat{\omega}_0^2} \tag{4.23b}$$

In [49] and also shown in appendix B the coupled mode kick factors are obtained for the dipole

mode in a double chain model:

$$K_p = \frac{\left| \sum_{n=1}^{N} a_n^{(p)} \sqrt{\epsilon^{(n)} K_s^{(n)}(\omega_s^{(n)}/2\pi)} e^{jn\varphi_p} \right|^2}{N(\omega_p/2\pi)(|a^{(p)}|^2 + |\hat{a}^{(p)}|^2)}.$$ (4.24)

In which $\varphi_p = \omega_p L/c$ is the phase shift per cell and $\epsilon^{(n)}$ is a fitting parameter which is given by $1 + (|\hat{a}^{(p)}|^2/|a^{(p)}|^2)$, where p is the mode nearest the synchronous point. $\epsilon^{(n)}$ determines the amplitude ratio of the TE to TM wave. Note that only the TM eigenvectors appears in the numerator of eq. 4.24, since only the TM component of the fields will kick the beam.

The double chain model has been validated with commercial software, and it has been found to be a very good prediction of frequencies and kick factors [51]. This model can be modified to represent not only the two lowest dipole modes but also the higher order dipole modes in the cavity. This has been analysed in [53]. Details on this will be discussed in a later chapter. Details on the application of these circuit models to the TESLA cavity are provided in the next chapter. This design is particularly important as at present it forms the baseline cavity for current ILC design.

Chapter 5

Circuit Models Applied to the TESLA Cavity

This chapter presents results from simulations of a TESLA cavity structure using the finite element code HFSS Ansoft[©]. HFSS is a computer code that numerically solves Maxwell's equations based on a finite element algorithm [54]. The first part of the chapter presents results on the monopole and dipole modes for single-cell and a nine-cell structures with beam pipes. Both the mode frequencies and kick factors are calculated and they are accurately represented using circuit models. This is presented in the second part of this chapter. It is important to accurately calculate these parameters as they have the potential to significantly dilute the luminosity of the beam.

5.1 Simulation Method and Results

5.1.1 Single-Cell Structure

The single-cell simulations presented here are carried out using periodic boundary conditions. The frequency within a band is a continuous function of phase advance of fields across a single cell. Simulations were performed for the resonant frequency as a function of phase advance. A single cell is cylindrically symmetric and hence for the monopole mode it is sufficient to simulate a $10°$

sector of the cell.
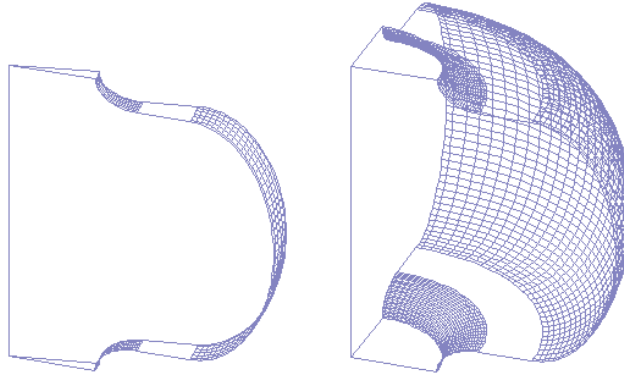
Figure 5.1: Single-cell input geometry for monopole (left) and dipole (right) simulations.

The TESLA mid-cell geometry in Table 1.6 is used in the simulations. For the monopole mode (TM_{010}), the electric field has a pattern parallel to the cavity axis and the magnetic field is perpendicular to the cavity axis. This is illustrated in Fig. 5.1, with magnetic field boundary conditions applied on either side of the slice. A 90° slice of cavity is also shown on the right of Fig. 5.1, with an electric symmetry plane on one side and a magnetic symmetry plane on the other. This is used to obtain dipole modes. Sextupole modes also exist for this set of boundary conditions.
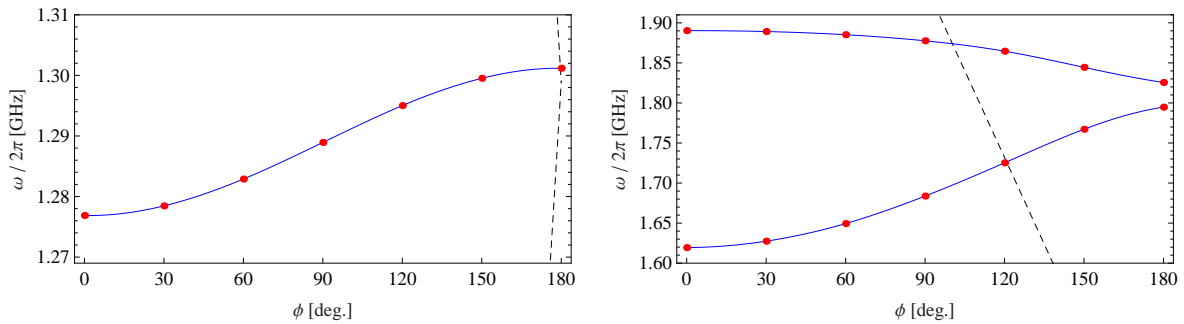
Figure 5.2: Dispersion curves of monopole (left) and dipole (right) bands of a single-cell structure. The light line is indicated by the dashed line. Dots are the results of HFSS simulations. Solid lines are cubit spline fits to the data.

The dispersion curve displayed in Fig. 5.2 was obtained using a 30° sampling in phase advance per cell, for both the first monopole mode and for the first two dipole bands. Note that the slope of the dispersion curve determines the group velocity of the mode. In these dispersion curves, the light line is a straight line which indicates modes with a phase velocity equal to the velocity of light. The point at which the cavity dispersion curves intersect with the light line is referred to as the synchronous point. This is the point at which the beam has a strong interaction with the cavity fields.
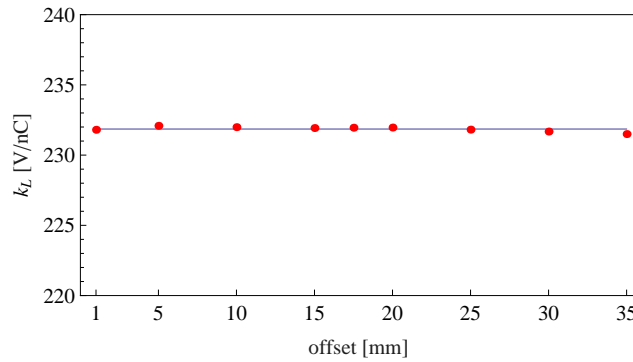
Figure 5.3: Loss factor of a monopole mode of a single-cell structure.
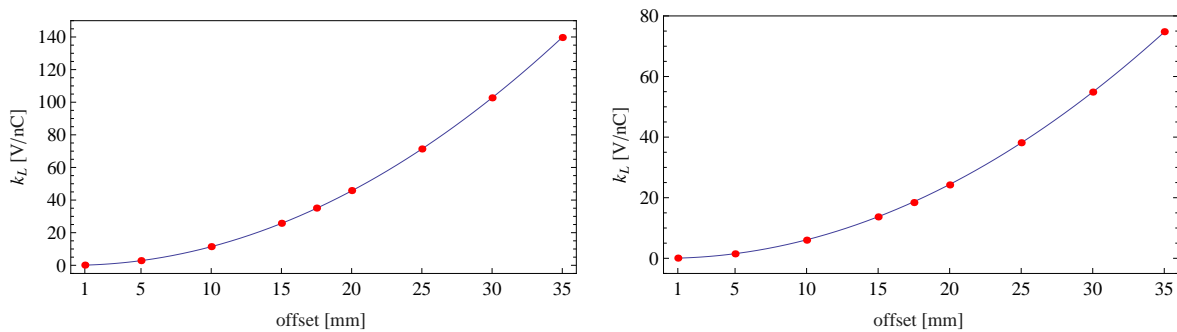
Figure 5.4: Quadratic fit to the loss factor of a first (left) and second (right) dipole modes of a single-cell structure.

The loss factor is calculated from e.m. fields, obtained from the simulation, using eq. 2.28. From these calculations, the loss factor of the monopole mode is independent of the offset from the cavity axis. However, the loss factor of the dipole mode is proportional to the offset squared (r^2) as shown

in Fig. 5.3 and 5.4. In this case it is evident that there is little influence of other higher order multipoles.

5.1.2 Nine-Cell Structure

In similar fashion to the single-cell structure, symmetry properties are invoked and a quarter section of the cavity is used to obtain dipole and also sextupole modes. The nine-cell cavity also includes beam pipes on both ends. The beam pipe cutoff frequency (approximately 2.5 GHz [16]) is higher than all bands under consideration. Thus all modes will be localised within each cavity.

As a realistic nine-cell cavity is terminated with end cells and beam tubes we can not assume the infinite periodic condition to obtain the phase of the structure. We define the phase using the Floquet condition. In the middle of the structure the field is that of an infinite periodic structure.

$$E_z(r, z + L) = E_z(r, z)e^{i\phi} \tag{5.1}$$

Thus, from eq. 5.1 the phase advance per cell is obtained by by taking the field at three points
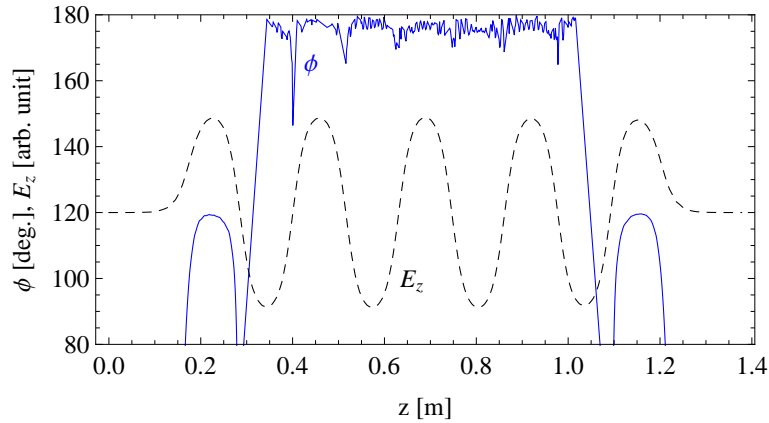
Figure 5.5: Floquet phase along the structure according to Eq.5.2 and the electric field E_z of the mode (dashed line).

$(z - L, z, z + L)$:

$$\phi(z) = \cos^{-1}\left[\frac{E_z(r, z + L) + E_z(r, z - L)}{2E_z(r, z)}\right] \tag{5.2}$$

However this method is strictly accurate only in the region of identical cells as illustrated in Fig. 5.5.

In these simulations, the nine-cell cavity is treated as one element and thus there are two choices for boundary conditions at the ends of the beam pipe: magnetic or electric planes. Fig. 5.6 illustrates the monopole and the dipole dispersion curves obtained from the nine-cell simulation with a magnetic-magnetic (MM) boundary conditions and the phase advance per cell calculation using eq. 5.2 compared to that of the single cell simulations. It can be observed that both the nine-cell and the single-cell frequencies lie on the same curve, which is as expected, because the single-cell simulation represents an infinite periodic structure as mentioned in the previous section.
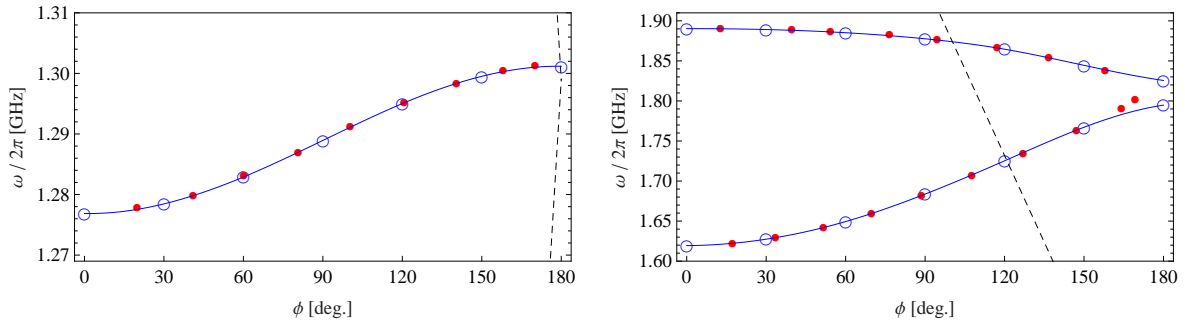
Figure 5.6: Dispersion curves of monopole (left) and dipole (right) bands of a nine-cell structure with beam pipes (red dots) compare to single cell simulations results (blue circles). Light line is indicated by the dashed line.

These dispersion curves can also be obtained using the circuit model representation method and this is discussed in the next section. In addition, the loss factors and kick factors are also calculated in a similar fashion to the single-cell structure.

5.2   Circuit Model Analysis

In the previous section, it was demonstrated that it is possible to estimate the properties of a nine-cell structure using single-cell parameters through the use of a circuit model as detailed in chapter 4. In this section, the results of a circuit model representation of a nine-cell structure is presented.

5.2.1   Frequency Prediction

A single chain circuit model requires two input frequencies, at 0 and π phase advance per cell, to construct the eigensystem matrix. For the nine-cell cavity with beam pipe attached, the proper boundary conditions are N-2 cells for MM boundary condition and N cells for an electric-electric (EE) boundary condition according to the boundary conditions at the beam pipes. In this case, the eigensystem matrix will be a 9x9 matrix for a single chain circuit model and only the cell-to-cell coupling constant (κ_c) and the resonant frequency ($\omega_r/2\pi$) will be inserted in the matrix. Simulations obtained using HFSS indicate that the TESLA cavity has a bandwidth (κ_c) of 1.87%.

From the solution of the eigensystem, the eigenvectors represent the fields inside the structure and the eigenvalues are the mode frequencies of the structure. Fig. 5.7 illustrates the results from this single chain circuit model compared to the simulation from HFSS on single-cell and nine-cell structures.   The circuit model dispersion curve is obtained from the characteristic curve of the eigensystem as stated in eq. 4.8. The discrepancy between the single chain circuit model and the first monopole band frequency from simulations is less than 1% for both single-cell and nine-cell structure.

A double chain circuit model was developed to represent the behaviour of the coupled dipole modes in the structure. It requires two input frequencies, at 0 and π phase advance per cell, from each dipole band to construct the eigensystem 2Nx2N matrix, where N is the number of cells in the struc-
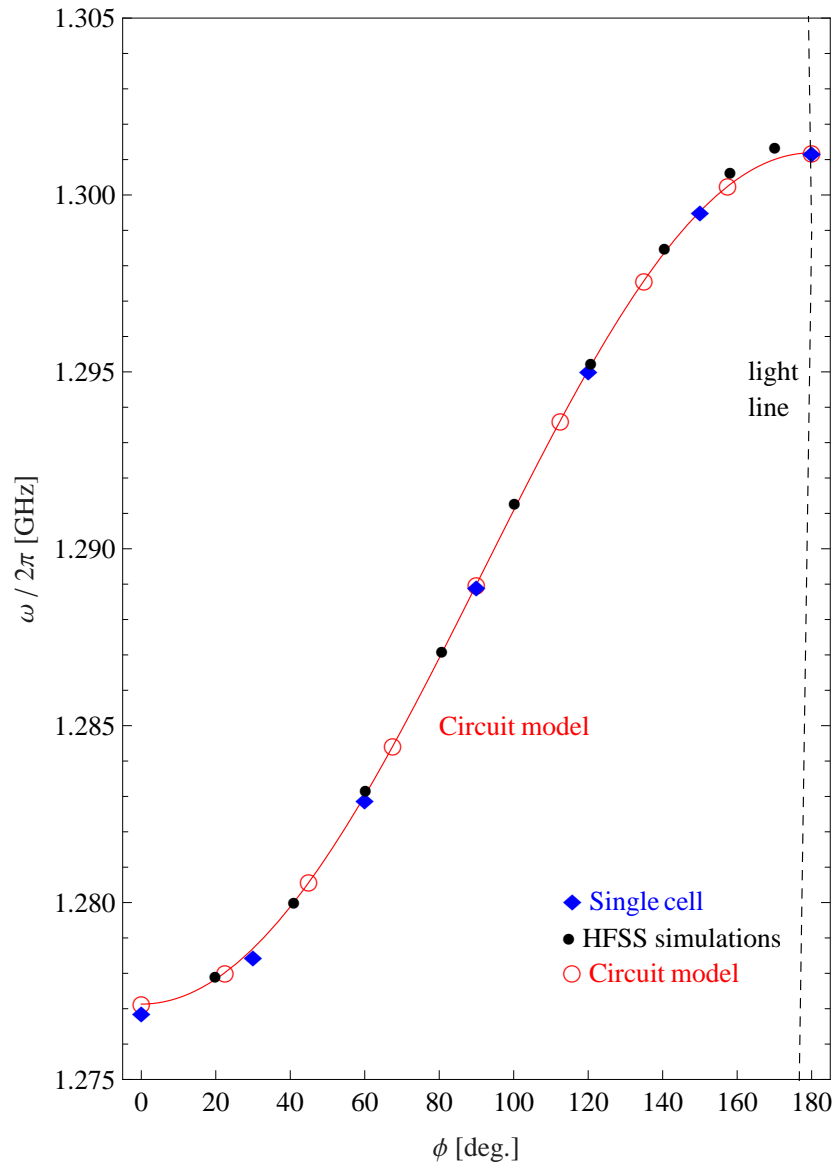
Figure 5.7: Circuit model results for the monopole band of a nine-cell structure with beam pipes. Red lines and circles are circuit model results, blue diamonds are an infinite periodic single-cell simulation results, and black dots are a nine-cell HFSS simulation results. The light line is indicated by a dashed line.
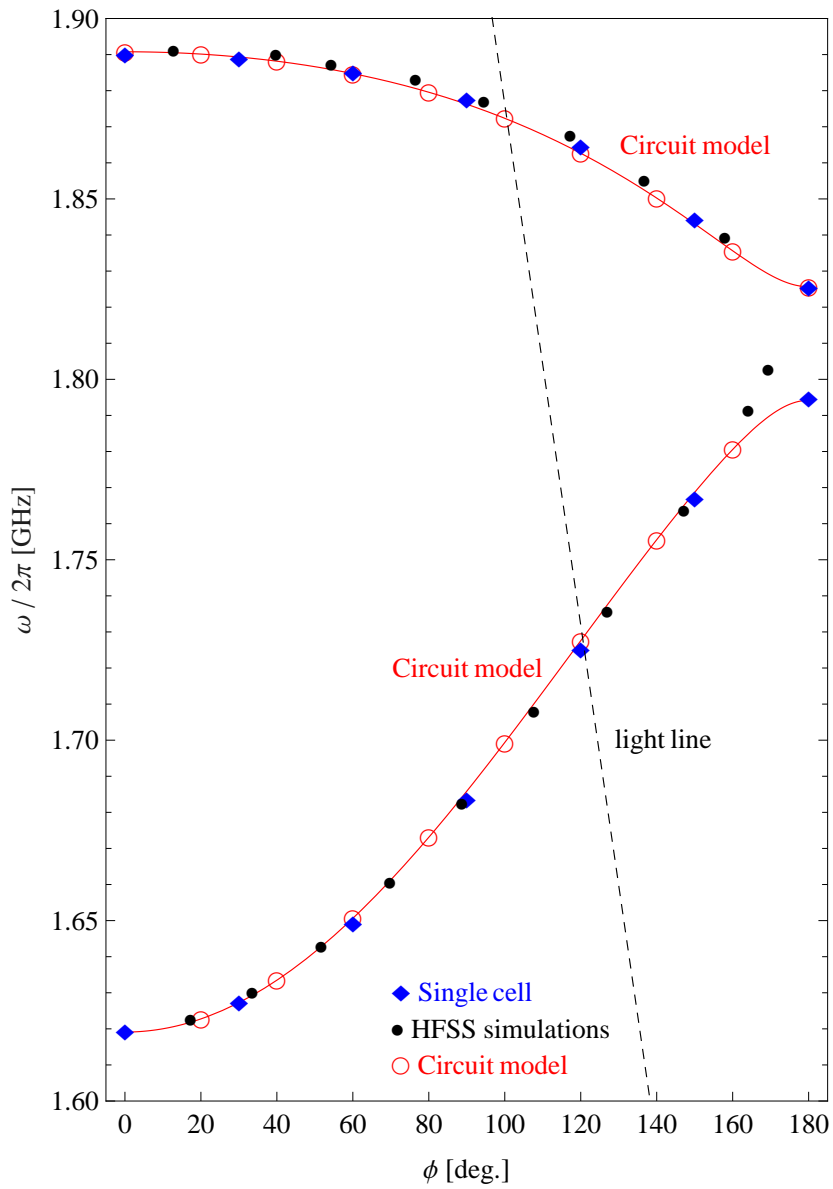
Figure 5.8: Circuit model results for the first two dipole bands of a nine-cell structure with beam pipes. Red lines and circles are circuit model results, blue diamonds are an infinite periodic single-cell simulation results, and black dots are a nine-cell HFSS simulation results. The light line is indicated by a dashed line.

ture. The parameters included in the eigensystem matrix are the coupling coefficients and resonant frequencies. This involves careful selection of the 0 and π frequencies of each band. In performing the analysis it is important to pay attention to the modal characteristic of each band.

Performing HFSS simulations on TESLA mid-cells, the coupling coefficients are found to be 5.24% and 11.95% for TM and TE modes respectively. Fig. 5.8 illustrates results from this double chain circuit model, compared to single-cell and nine-cell simulation results. N-2 full cells are used for the MM simulations. Single-cell results are overlaid on a dispersion curve, which is the solution of eq. 4.22, with a discrepancy of less than 5% . There is a small deviation for the nine-cell results; these differences are as a result of the non-identical cell geometry (end-cell geometries are different from mid-cell) and the perturbative influence of the beam pipe. They also result from the numerical noise of the Floquet phase calculation, which demonstrates non-smooth behaviour in Fig. 5.5. These effects will be encapsulated within the circuit model in the following section, in which we tune the circuit model parameters.

5.2.2   Kick Factor and Parameters Tuning

Initial tests were made using a simplified version of the TESLA nine-cell structure in which all the cells in the structure were assigned to those of the mid-cell (as indicated in Table 1.6). In order to estimate the kick factor, additional frequencies and kick factors from single-cell simulations are needed. These can be done by simulation with a particular phase setting from the synchronous phase of each band. The results of this initial study for both the first monopole and first two dipole pass bands kick factors are presented in Fig. 5.9. It can be observed that the results of the circuit model compare well to that of the full nine-identical cells structure simulation.

In the actual structure, which consists of non-identical cells together with attached beam pipes, the
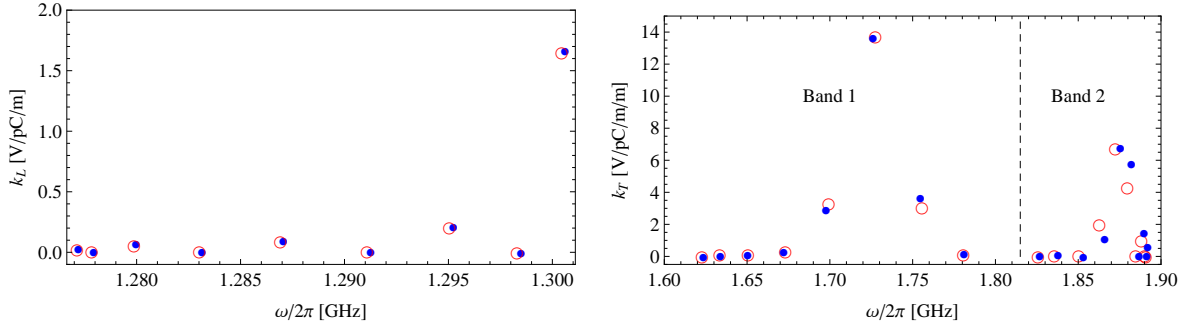
Figure 5.9: Loss and Kick factor comparisons for a nine-identical cells with the MM boundary condition (red circles) and a circuit model with the N-2 cells boundary condition (blue dots). Monopole on the left and dipoles on the right of the picture.

mode frequencies and mode kick factors will be modified. This deviation can be accounted for by changing the parameters of the end cells in the circuit model. The cell-to-cell coupling factors of the end cells needs to be changed in the circuit model to reflect the flattened field profiles of the structure. The system matrix was reconstructed after tuning these parameters.

In all eigenmode calculations a Mathematica [55] code was implemented. The eigensystem was solved and the mode frequencies and kick factors are obtained. The error between the current model and HFSS simulations is minimised by changing the end cell couplings.
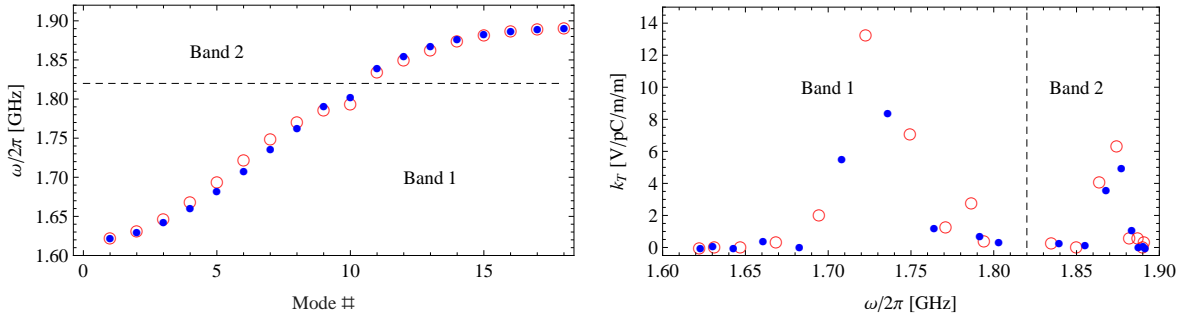
Figure 5.10: Mode frequencies and kick factors of the TESLA nine-cell structure from a circuit model with the N-2 cells boundary condition (red circles) and HFSS simulation with the MM boundary condition (blue dots). This is prior to tuning the end cells.

The frequencies and kick factors are displayed in Fig. 5.10 prior to tuning the end cells. There is an average discrepancy in frequency of about 5.2 MHz and 0.47 V/pC/m/m for the kick factors. The tuning algorithm relies on modifying four end-cell frequencies and four end-cell kick factors. Adding the end cell kick factor as an optimisation parameter was necessary in order to obtain an adequate prediction of the global kick factors. The result of this algorithm is the optimum point between the output frequency and kick factor therefore an average frequency difference of 1.78 MHz and the average difference of kick factor is 0.47 V/pC/m/m between the circuit model and the numerical HFSS, as shown in Fig. 5.11.
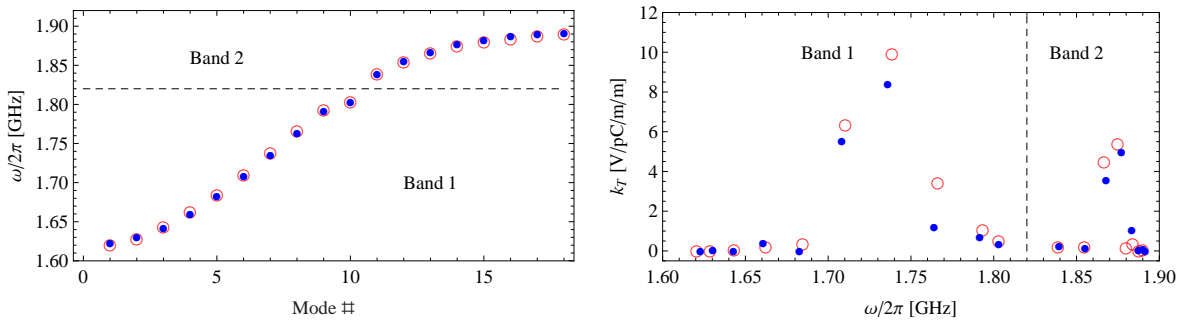
Figure 5.11: Mode frequencies and kick factors of a tuned circuit (frequencies and coupling constants) of the TESLA nine-cell structure (red circles) compared to HFSS simulations (blue dots). Half end cells are used.

These results indicate that the method can provide a reasonable prediction of the frequencies and kick factors. This has been presented in [51]. The circuit model allows fabrication errors to be rapidly implemented. Once all parameters have been implemented and verified, the circuit model allows the eigensystem to be calculated.

The next chapter presents my optimisation to obtain a new SRF cavity shape, which has both minimised surface fields and also has a looser tolerance to cavity cell fabrication errors. My new cavity design is a potential candidate for the ILC main accelerator linac.

Chapter 6

SRF Cavity Optimisation Towards a New Low Surface Field Cavity

The design of the main accelerating section of the ILC project is based on the TESLA cavity shape. The baseline design aims for an average accelerating gradient of 35 MV/m - although they will operate at 31.5 MV/m. Several new cavity designs have been proposed. The maximum allowable value of the surface magnetic and electric fields for a given accelerating electric field is a fundamental limitation on the cavities. The ratios: E_s/E_a and B_s/E_a are important design criteria. Another criteria is the fractional bandwidth of the accelerating mode $\kappa_c \approx (\omega_\pi - \omega_0)/\omega_{\pi/2}$. This represents the sensitivity of the cavity mode frequency to cell fabrication errors. In this chapter, the influence of the cell geometry on the design criterion is discussed.

The generic geometry for a SRF cavity cell is shown in Fig. 6.1. The ILC main accelerator is designed to operate at an rf frequency of 1.3 GHz with a π phase advance of the e.m. fields per cell. This operating point determines the cell length. When a cavity is excited with rf power, in principle an infinite number of modes are excited. However, the beam interacts strongly with those modes whose phase velocity is close to or equal to that of the ultrarelativistic beam. The beam is essentially
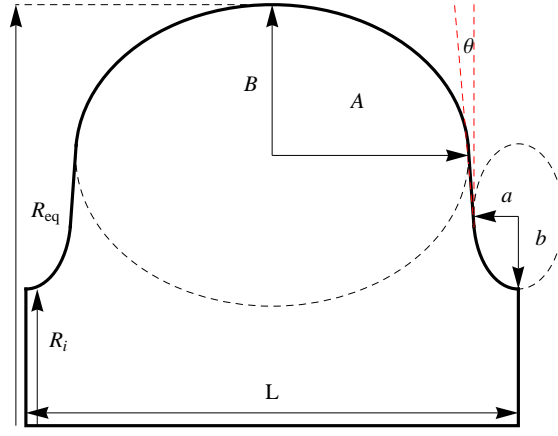
Figure 6.1: A generic SRF cavity's geometry.

travelling at the velocity of light:

$$c = v_{ph} = \frac{\omega}{k_z} = \frac{2\pi f L}{\phi}, \text{or} \quad L = \frac{\phi}{2\pi} \frac{c}{f} \tag{6.1}$$

where k_z is the longitudinal wave number, the cavity length L and the phase advance per cell is $\phi = k_z L$. These modes are known as the synchronous modes. In conventional linear accelerators, the accelerating mode is the lowest synchronous mode (TM_{010} cavity). In this case, for the π mode the cavity gap length is fixed at 115.304 mm. Others geometrical parameters (R_{eq}, R_i, A, B, a, b, and θ) can be varied in order to optimise various features of the cavity. A new design, the New Low Surface Fields (NLSF) structure is described here. This forms a major component of the unique results presented in this work. Prior to a discussion of this cavity the sensitivity of the field profile on various geometrical parameters is investigated.

6.1   Influence of Cell Geometry

6.1.1   Influence of Iris Aperture on E.M. Fields

The first geometrical parameter considered is the aperture of the iris (R_i). A larger iris aperture results in a weaker accelerating field along the beam axis. When the iris aperture is wider the cavity shunt impedance becomes smaller. Fig. 6.2 illustrates a sketch of an accelerating field near the beam axis. It is evident that as the iris size is increased more field leaks out and hence the shunt impedance is reduced correspondingly. It is important to obtain as high a shunt impedance as possible as this impacts the overall efficiency of coupling rf power to the beam. A numerical 2D rf solver code, SuperFish [56], is utilised to study this influence. Two cells with different iris radii are simulated.
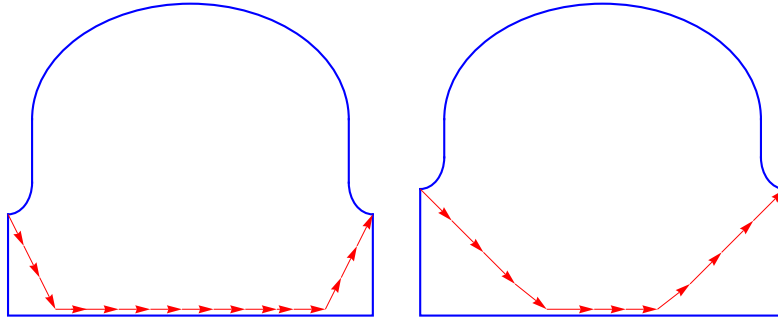
Figure 6.2: The influence of an iris opening on the accelerating field along the beam axis.

The geometry of the iris also affects the fundamental mode bandwidth. Clearly the bandwidth is reduced as the iris radius decreases. This behaviour can be observed from the summary of the 1.3 GHz ILC cavities with different iris radii in Table 6.1. A cavity with a small bandwidth (κ_c) will be very sensitive to fabrication errors (eq. 3.3). In addition the field flatness ($\Delta A/A$) or uniformity of the cavity depends on three quantities: the relative error of cell frequency $\Delta f/f$, the coupling

constant κ_c, and the cavity length N, as

$$\frac{\Delta A}{A} \propto \frac{\Delta f}{f}\frac{1}{\kappa_c}N^p \tag{6.2}$$

where $p \sim 2$, for a π mode cavity [46] [57].

Table 6.1: Fundamental mode bandwidths for different iris radii for the 1.3 GHz ILC cavities.

Iris radius (mm)	Bandwidth (MHz)
30 (LSF)	16.7
30 (LL, Ichiro)	19.7
31	18.3
32 (NLSF)	20.7
33	23.2
35 (TESLA)	24.3
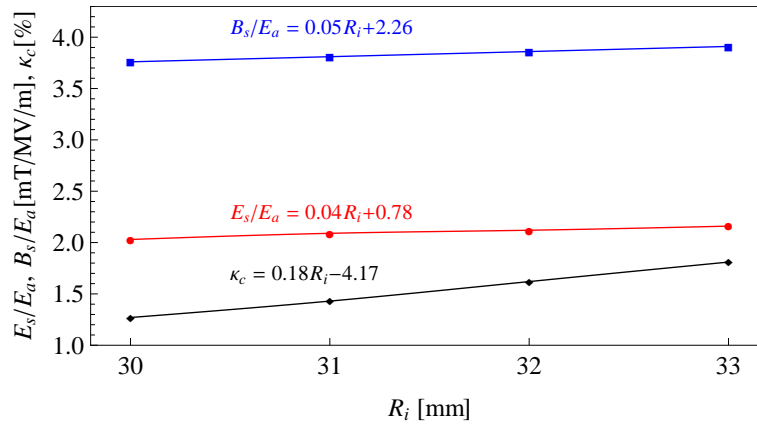
Figure 6.3: Three figures of merit; B_s/E_a, E_s/E_a, κ_c, versus an iris radius for the 1.3 GHz shape.

The change in iris aperture influences surface fields as aperture radius increases both the surface magnetic and electric field increases. These effects can be seen from an exploration on parameter regions for the ILC cavity as illustrated in Fig. 6.3. The relationship between the three figures of merit and an iris radius is also presented.

From a beam dynamics perspective, the short-range wakefields of the cavities are also very sensitive to the iris radius. The longitudinal and transverse components of the short-range wakefields are proportional to the square of the iris radius and to the forth power of the iris radius, respectively. The explicit dependence of these longitudinal and transverse wakefield are [58, 59]:

$$
\begin{aligned}
W_L(s) &= \frac{Z_0 c}{\pi a^2} e^{-\sqrt{s/s_{00}}} \\
W_T(s) &= \frac{4 Z_0 c s_{00}}{\pi a^4} \left[1 - \left(1 + \sqrt{\frac{s}{s_{00}}} \right) e^{-\sqrt{s/s_{00}}} \right]
\end{aligned}
\tag{6.3}
$$

where a is an iris radius, s is the distance behind the bunch, $Z_0 = 377\Omega$ the vacuum impedance, and s_{00} is a constant parameter which depends on cell geometry. The longitudinal component of the wakefields must be minimised to reduce the beam energy spread. The transverse component must be contained within limits to avoid emittance dilution and to avoid the potential of a beam breakup instability.

Once the iris radius has been fixed, the detailed geometry of the iris also has an impact on the surface fields. This is considered in the next section.

6.1.2   Influence of Iris Shape on E.M. Fields

The accelerating mode in the cells is TM_{010} in nature. In this mode, the accelerating field is maximum at the electrical centre of the cavity [60]. The maximum surface electric field is located in the vicinity of an iris. The iris ellipticity ($r = b/a$) can be varied to optimise the surface electric field. A study has been carried out to find the influence of this iris ellipticity on the three figures of merit of the 1.3 GHz cavity cells, and results are presented in Fig. 6.4. We observed that the surface magnetic field and the bandwidth increase when the iris ellipticity increases, but the surface electric

field has a minimum point when this ratio changes.
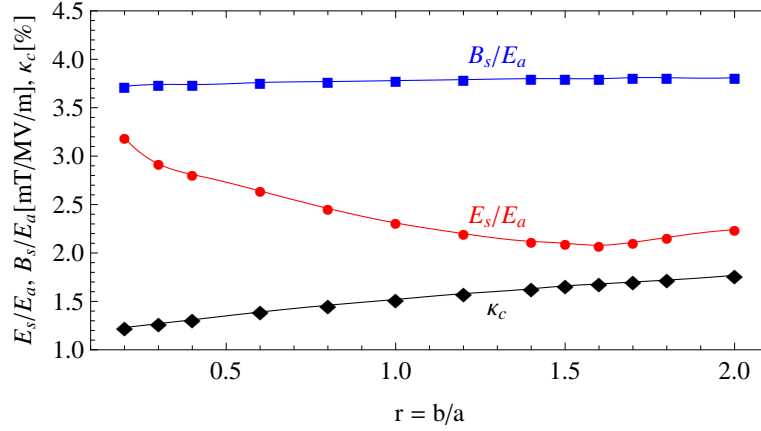
Figure 6.4: Surface e.m. fields and bandwidth versus iris ellipticity ($R_i = 32$ mm, $R = B/A = 0.67$, $\theta = 0$ and $\omega_c/2\pi = 1.3$ GHz).
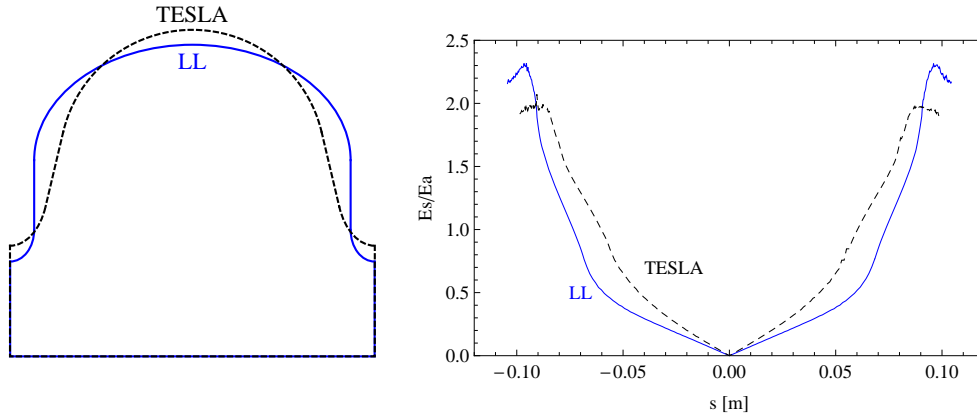
Figure 6.5: Cavity geometry (left) and E_s/E_a along the cavity surface (right) between the TESLA (black dash) and the low loss (blue line) shape, where s is the distance along the surface contour from centre of the equator.

Changing the ellipticity of the iris modifies the surface area on the cell's nose. This affects the field distribution on an iris surface and location of the peak field. Fig. 6.5 illustrates the surface electric field ratio along the surface of the TESLA and the low loss cavity cell. The TESLA cavity has a large surface area in the vicinity of an iris compared to the low loss and thus it has a lower surface

electric field. For a given shape, either the electric or magnetic field may reach its minimum, but the other is far from its minimum. In practise a trade off must be made between minimising the electric and magnetic surface fields.

Another aspect of the cavity that needs to be considered is the geometry of the equator as the cavity frequency is tuned by modifying the radius and shape of the equator. The equator shape also has influence on surface e.m. fields. This is described in the next section.

6.1.3 Influence of Equator Shape on E.M. Fields

The equator radius (R_{eq}) is an important parameter in the cell frequency tuning as the cutoff frequency of the TM_{010} mode of the circular cylindrical cavity with radius R_c is $2.405c/2\pi R_c$ [Hz]. The equator ellipticity of the cavity illustrated in Fig. 6.1 is defined according to B/A. Using the SuperFish solver, we study this influence on three figures of merit. In this study we seek to minimise
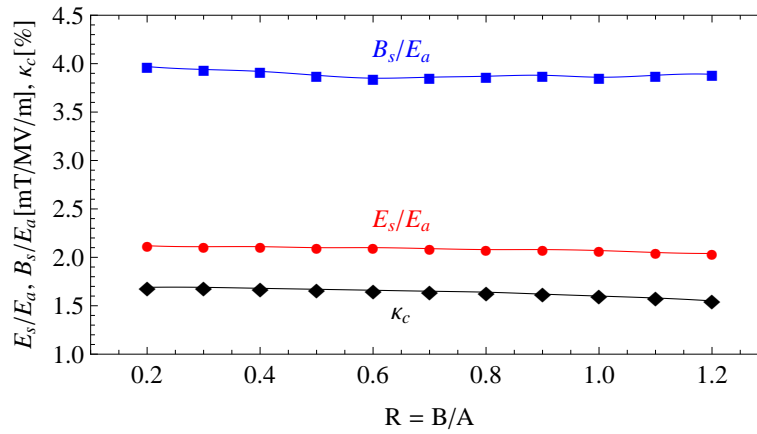
Figure 6.6: Sensitivity of surface e.m. fields and monopole bandwidth to cavity ellipticity (here $R_i = 32$ mm, $r = b/a = 1.5$, $\theta = 0$ and $\omega_c/2\pi = 1.3$ GHz).

these surface e.m. fields whilst minimising the impact on the bandwidth (κ_c). Fig. 6.6 represents initial results of the study which indicates that the surface magnetic field is slightly more sensitive

to equator elliptical compared to the other parameters.

Once R_{eq} has been fixed, the cell frequency can be tuned by changing the volume of the cell, i.e. changing A and B. A study has been carried out in SuperFish to find the relationship between the elliptical parameter B of the equator and the cell resonant frequency. Small changes in B allows a linear relationship to be obtained on the cavity resonant frequency. This is illustrated in Fig. 6.7.
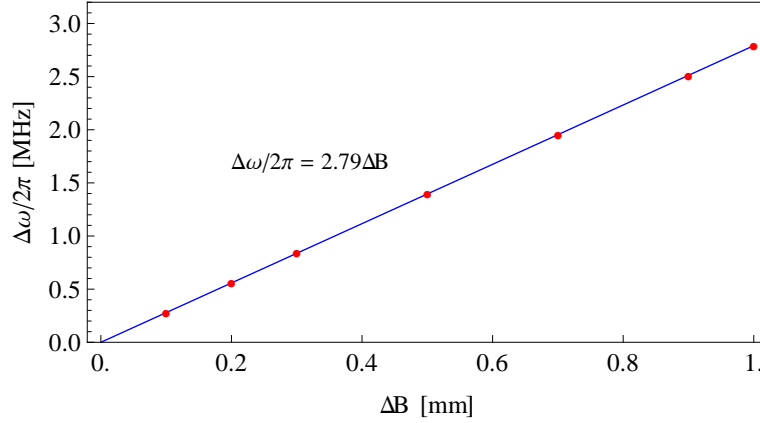
Figure 6.7: Frequency change versus elliptical parameter B for fixed values of $r = b/a = 1.3$, $A = 47.152$ mm, $\theta = 0$ and $R_{eq} = 98.14$ mm.

The shape of the equator strongly influences the surface magnetic field as the field has a maximum value in the vicinity of the equator. A cavity with a large volume means there is less magnetic field density on the equator surface compared to the cavity with a small volume, therefore, a large-volume cavity has a lower surface magnetic field for a given frequency. This was validated by simulation for the TESLA and the low loss cavity shapes and is illustrated in Fig. 6.8. It is evident that the low loss shape, which has a larger volume, has a lower surface magnetic field compared to that of the TESLA shape.

The final aspect of the cavity that needs to be considered is the slope of the cavity wall.
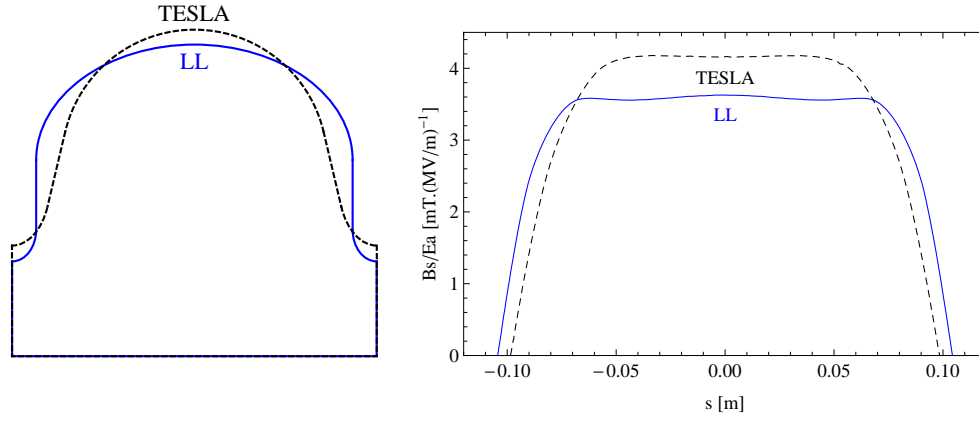
Figure 6.8: Cavity geometry (left) and B_s/E_a along the surface (right) for two different cavity profiles (where s is the distance along the surface contour from centre of the equator).

6.1.4 Influence of Cavity Slope on E.M. Fields

The slope of the cavity wall (θ) is also an important geometrical parameter that needs to be considered when designing the cavity. The change in θ affects both the electric and magnetic surface field. In Fig. 6.1 the cavity wall slope is defined as: $\theta = 0$ for a vertical line, $\theta > 0$ for a negative wall slope, and $\theta < 0$ for a positive wall slope. A study is carried out on the 1.3 GHz cavity with different wall angles. The results are summarised in Fig. 6.9. Increasing the wall angle decreases both the bandwidth and the surface electric field, but it also enhances the surface magnetic field. By increasing θ the surface area in the vicinity of an iris can be increased. Hence the surface electric field can be reduced, but in this process the surface area in the vicinity of an equator is decreased and hence the surface magnetic field increases.

In practise, cavities are designed with a small slope in the wall in order to make the process of surface cleaning easier. This small slope helps in allowing liquid to flow during the cleaning and rinsing process. Fig. 6.9 indicates that if the angle is negative the surface magnetic field tends to decrease. This geometry is referred to as the reentrant shape. If the optimisation extends into the region of a negative angle, the electric and magnetic surface fields can be minimised. This reentrant
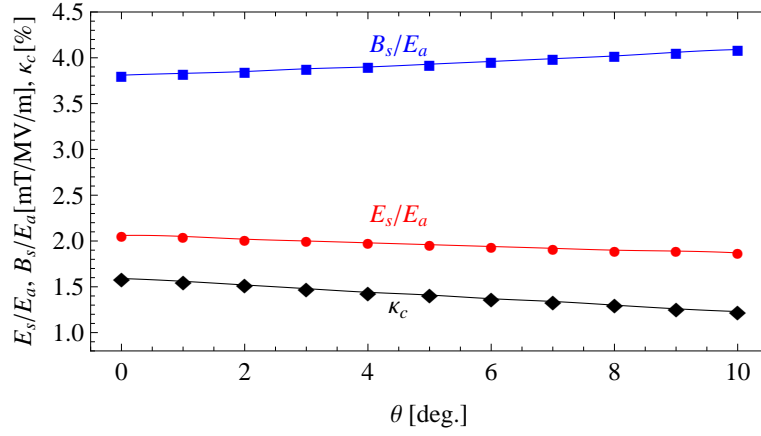
Figure 6.9: Surface e.m. fields and bandwidth versus wall angle ($R_i = 32$ mm, $R = B/A = 0.7$, $r = b/a = 1.5$, and R_{eq} is varied to tune the frequency to 1.3 GHz).

shape has lower losses and has the potential to reach a higher accelerating gradient. The reentrant design has been pursued at Cornell university and has resulted in single-cell gradients in excess of 50 MV/m [31].
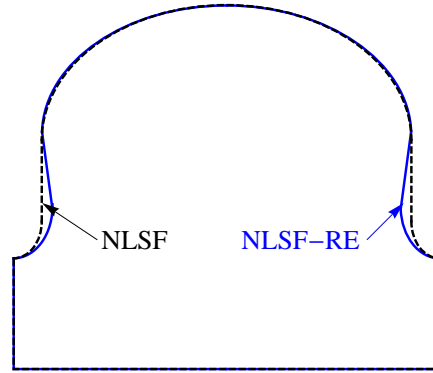
Figure 6.10: Geometry sketch of a NLSF (black dashed) and NLSF-RE shape (blue solid line).

I have conducted detailed studies on my own version of the reentrant cavity. This has allowed a further reduction in the surface fields compared to the standard shape. This shape, known as NLSF-RE is presented in [45]. Fig. 6.10 illustrates the NLSF-RE design. The surface fields are plotted in

Fig. 6.11.
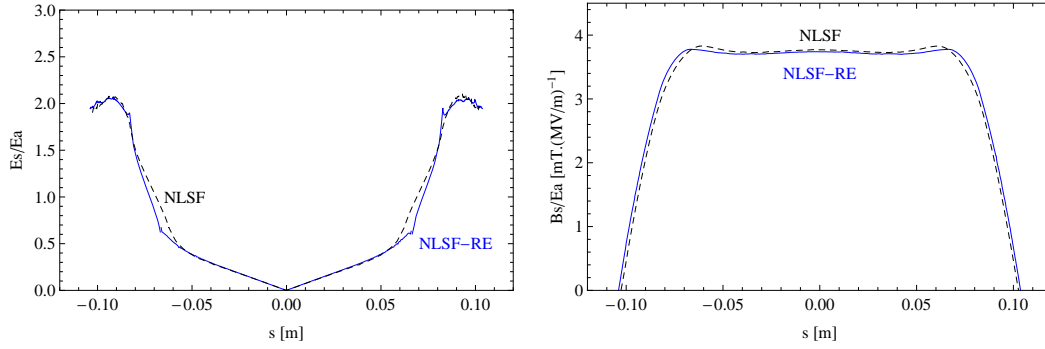
Figure 6.11: Surface fields ratios along the cavity surface comparison between the NLSF (black dash) and the NLSF-RE (blue line) shape, where s is the distance along the surface contour from centre of the equator.

It is important to note that the reentrant shape presents a challenge to current surface treatments, such as chemical etching and high pressure rinsing. This negative wall angle type cavity is also mechanically weaker than the positive wall angle cavity.

The focus of my work has been on an optimised design with $\theta = 0$. The procedure, necessary to obtain the NLSF cavity, is described in the next section.

6.2   NLSF Cavity Optimisation

The NLSF cavity is designed to optimise the surface fields and has a slightly larger bandwidth compared to existing cavity designs for the ILC. This section provides detailed optimisation of this cavity. SuperFish was used as a main field solver for calculating the accelerating frequency and the surface fields. The finite element code HFSS was used to validate the optimised designs. To expedite the simulation procedure, a Mathematica code was written to provide a frontend to the SuperFish simulations.

6.2.1 Tool Validation

A Mathematica frontend controls SuperFish to obtain the cell geometry and figures of merit. These geometries were also simulated in HFSS in order to validate the results. The simulation results obtained using SuperFish are within $\pm 1.5\%$ of the HFSS simulation results, as the rms of the error in κ_c is less than 0.5% , 7% and 1.5% for E_s/E_a and B_s/E_a respectively. These validation results are shown comparison in Table 6.2. This frontend was modified further to explore various cavity geometries. This is described in the next section.

6.2.2 Frequency Tuning Algorithm

A Mathematica code was written to explore various cavity geometries to input to SuperFish. The algorithm for the vertical line wall ($\theta = 0$) with a given equator radius is displayed as a flowchart in Fig. 6.12. The script generates input files, executes SuperFish and the post processor, reads output files for the desired parameters and then calculates the figures of merit. This algorithm explores parameters with different iris radii and iris elliptical shapes. For a given iris thickness(a), the equator parameter(A) is fixed at $(L/2) - a$. Varying the equator parameter B, the desired accelerating frequency is obtained within ± 5 kHz for a given equator radius. Once the cell geometry is tuned, then the other rf properties are calculated using the SuperFish post processor. The optimised cavity shape is obtained from analysing the rf properties in a large region of cavity shapes. This is discussed in the next section.

6.2.3 Choice of an Iris Aperture

The iris radius R_i, determines the concentration of the accelerating field along the cavity axis and hence the efficiency of the cavity. The present Low loss and Ichiro shape is designed with a 30 mm iris radius whereas the iris radius of the TESLA shape is 35 mm. Both the Low loss and Ichiro shape have higher R/Q and lower surface magnetic field than the TESLA shape; on the other hand, they

Table 6.2: Three figures of merit for proposed high gradient ILC cavities.

Parameters	TESLA		LL		Ichiro		NLSF		NLSF-RE	
	HFSS	SF	HFSS	SF	HFSS	SF	HFSS	SF	HFSS	SF
κ_c [%]	1.89	1.89	1.53	1.53	1.54	1.54	1.59	1.59	1.66	1.66
E_s/E_a	2.18	2.02	2.42	2.30	2.37	2.29	2.11	2.07	2.07	2.08
B_s/E_a [mT/(Mv/m)]	4.18	4.17	3.64	3.61	3.62	3.61	3.83	3.83	3.78	3.78
f_π [MHz]	1301.16	1301.06	1300.08	1299.97	1300.40	1300.31	1300.23	1300.11	1299.91	1300.00
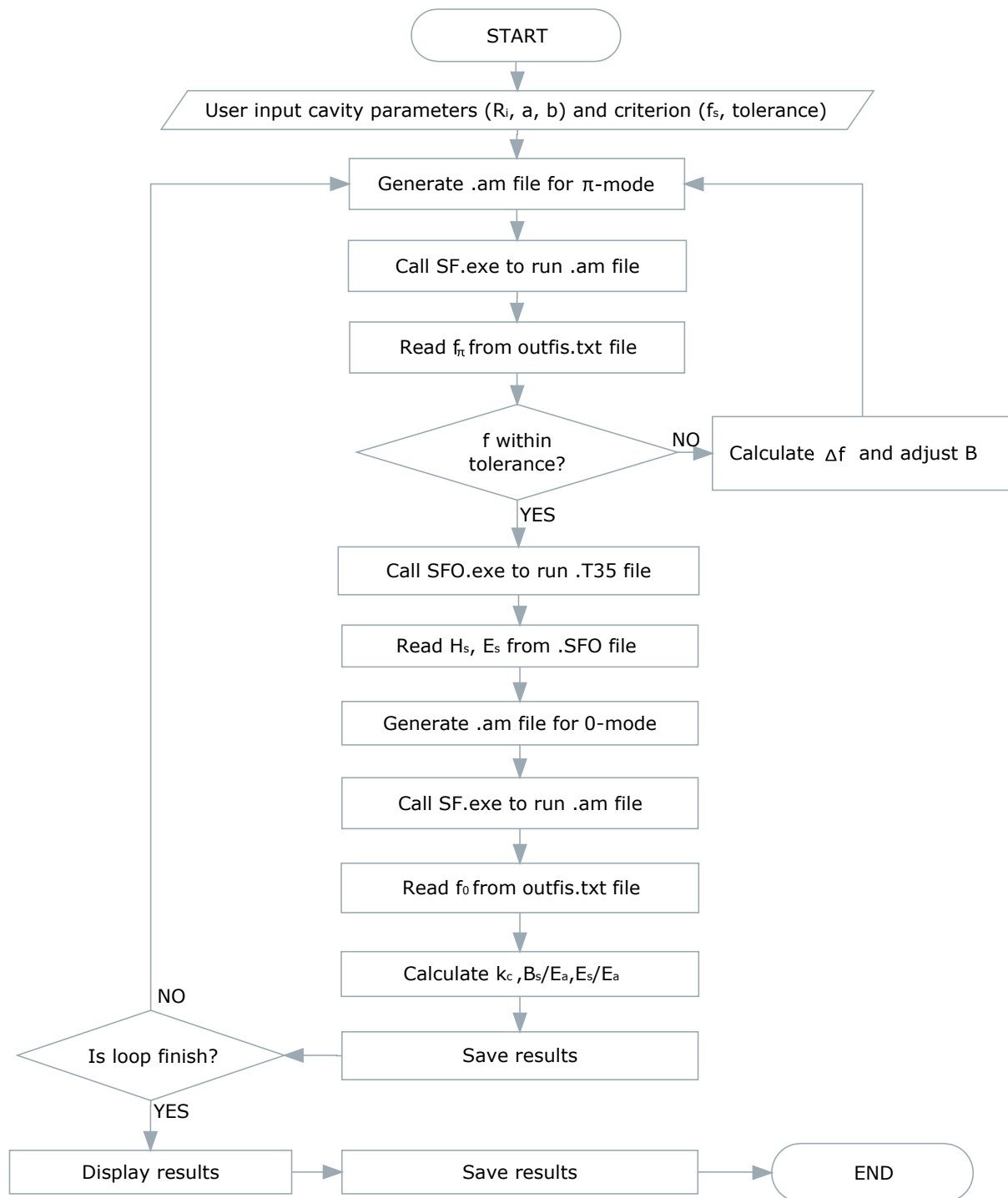
Figure 6.12: Frequency tuning algorithm for the NLSF shape.

have a higher surface electric field and a narrower bandwidth.
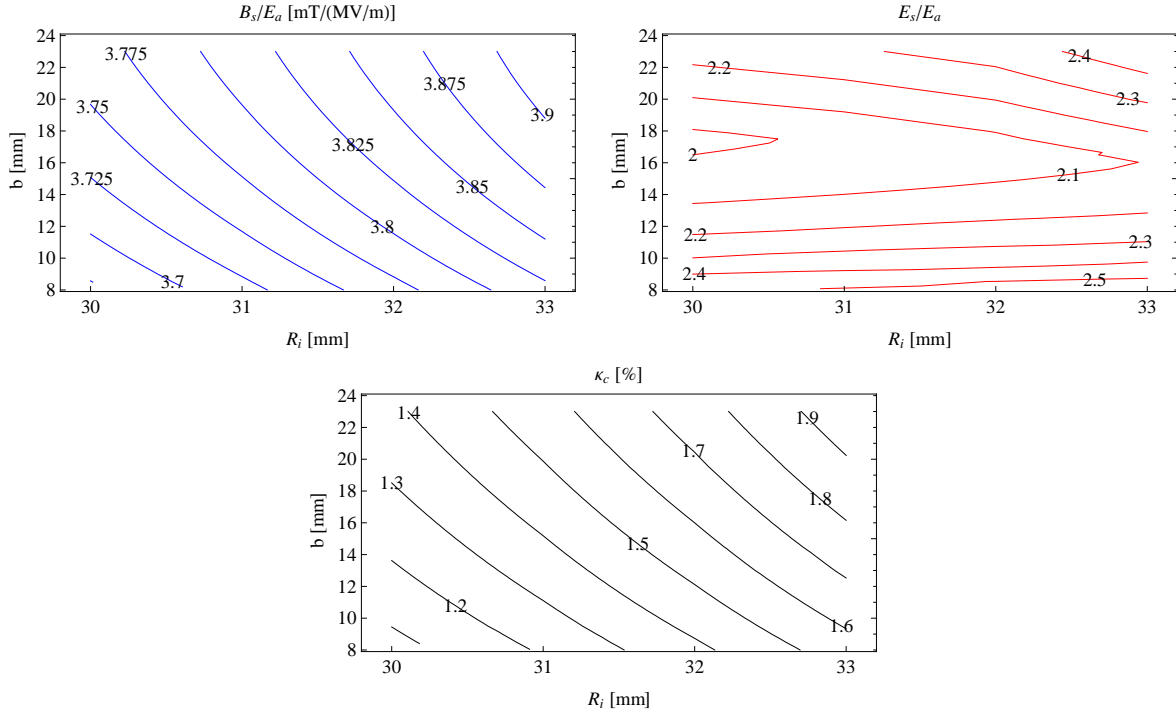
Figure 6.13: Three figures of merit versus the variation in iris radius R_i and iris elliptical parameter b at a fixed $a = 10.5$ mm

Various cavity geometries were explored to understand how the variation in the iris radius affects the cavity figures of merit. Fig. 6.13 shows these effects at a fixed iris thickness, $a = 10.5$ mm. It is clearly seen from these results that all figures of merit show a tendency to increase with increasing iris aperture. This can be seen from the selected points plotted at a fixed iris elliptical parameter $b = 15.5$ mm in Fig. 6.14.

In NLSF design I selected the optimum point for all three figures of merit at an iris radius of 32 mm. A comparison of the NLSF optimum bandwidth with the other designs is presented in Table 6.1.
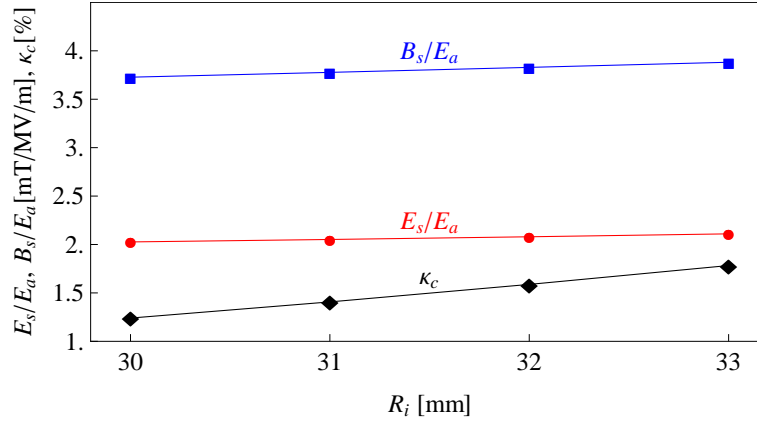
Figure 6.14: Three figures of merit; blue squares - B_s/E_a, red dots - E_s/E_a, black diamonds - κ_c, versus variation in iris radius for a NLSF shape with a given $a = 10.5$ and $b = 15.5$ mm.

The next cavity parameter to be considered is the shape of the iris. This is discussed in the next section.

6.2.4 Iris Shape Optimisation

For a given iris radius (R_i), its thickness (a) and shape (ellipticity $r = b/a$) are also the important parameters. These parameters are strongly related to the surface electric field and the cell-to-cell coupling constant, the latter involves the cavity field uniformity and the sensitivity to mechanical deformation. The thickness of the iris may lead to trapping of the HOMs inside the cavity. For a given iris radius, the cell-to-cell coupling constant and surface electric field tend to decrease whilst the surface magnetic field increases as iris thickness increases. With my Mathematica frontend to SuperFish, extensive simulations were carried out for various shapes. Various contours illustrating these results with $R_i = 32$ mm are shown in Fig. 6.15.

From these explorations, the selected optimum points of each iris thickness are plotted in comparison to present design shapes in Fig. 6.16. These reflect the behaviour of all three figures of merit as discussed above.
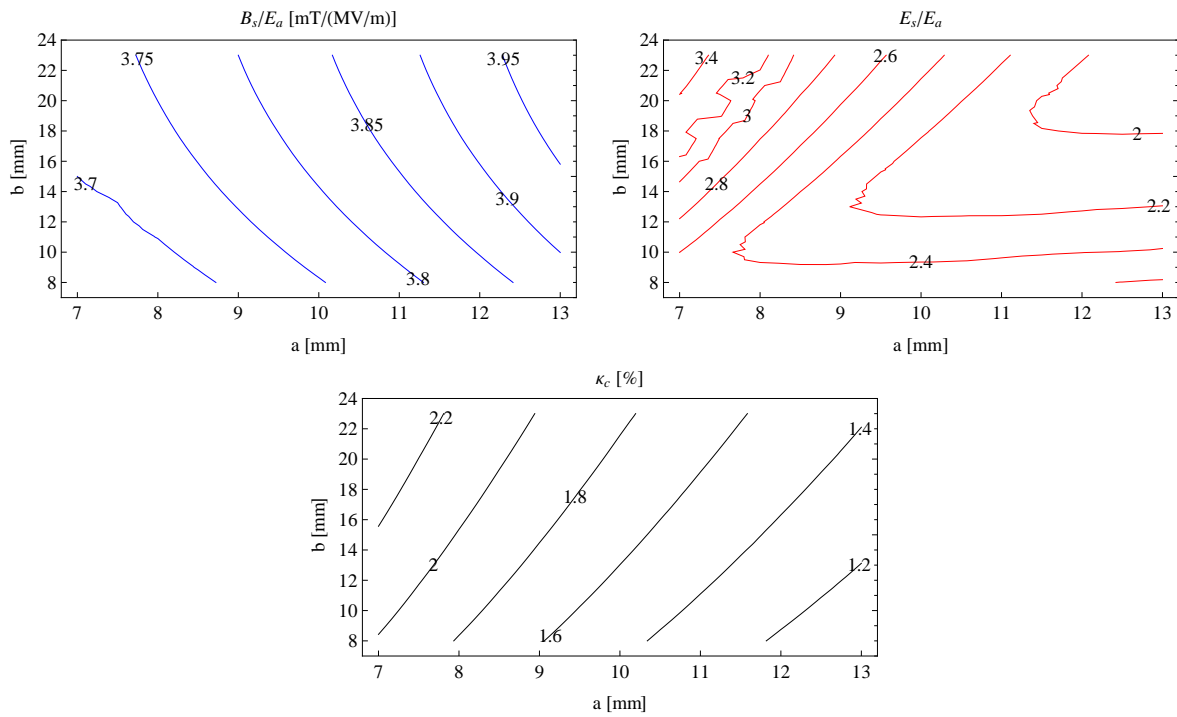
Figure 6.15: Three figures of merit versus the variation in iris shape a, b at a fixed $R_i = 32$ mm.
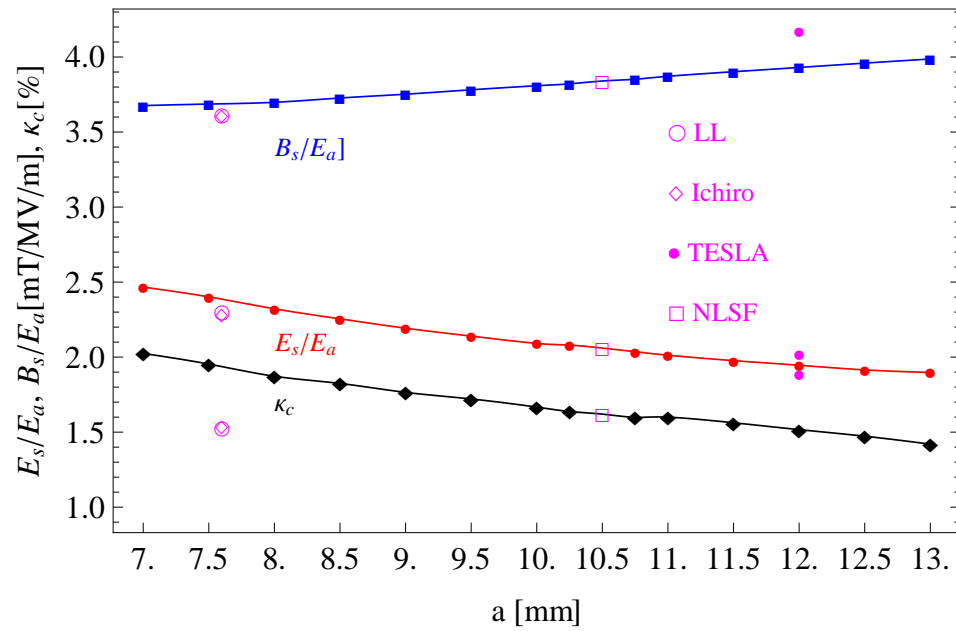
Figure 6.16: Three figures of merit versus variation in iris thickness for a NLSF shape with a given $R_i = 32$ mm, compared to present designs

My NLSF shape is selected at the optimum point of an iris parameter $a = 10.5$ and $b = 15.5$ mm. This design has ~ 8.5% lower B_s/E_a field compared to the TESLA, and a E_s/E_a 13% lower compared to the low loss design. Both ratio E_s/E_a and B_s/E_a are comparable to the LSF design. However the bandwidth is superior, as it is 26.5% wider. The surface field ratios of this shape are plotted in comparison with others in Fig. 6.17 and 6.18.
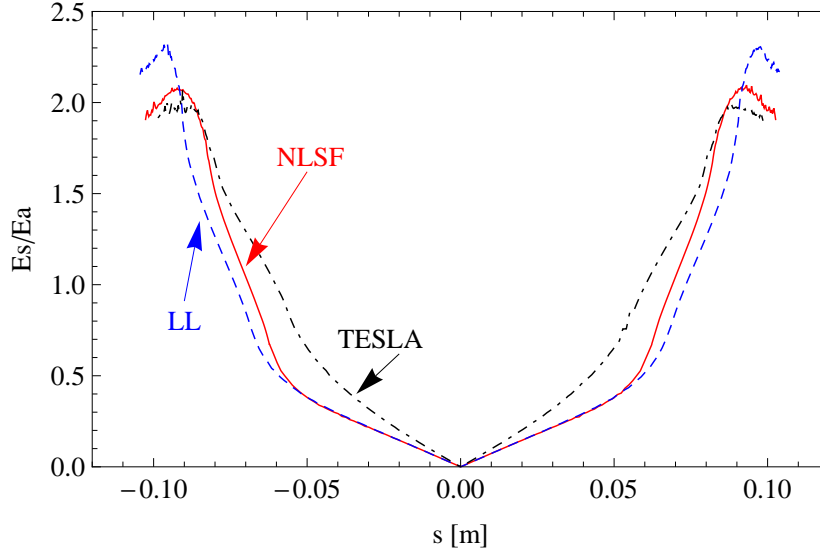
Figure 6.17: Surface electric field ratio along the cavity surface comparison between the NLSF (red line) and other designs; the TESLA (black dot-dashed line), the Low Loss (blue dashed line) shape, where s is the distance along the surface contour from centre of the equator.

Table 6.3 summarises the results of an optimisation study of an alternative design shape for the ILC. A comparison of the fields in each of these structures is presented in Fig. 6.19. The NLSF shape has slightly inferior parameters compared to the NLSF-RE shape. Despite this, we nevertheless opted for this shape for a full design study as, in fabricating the cavity, surface cleaning is considerably simpler for this shape.
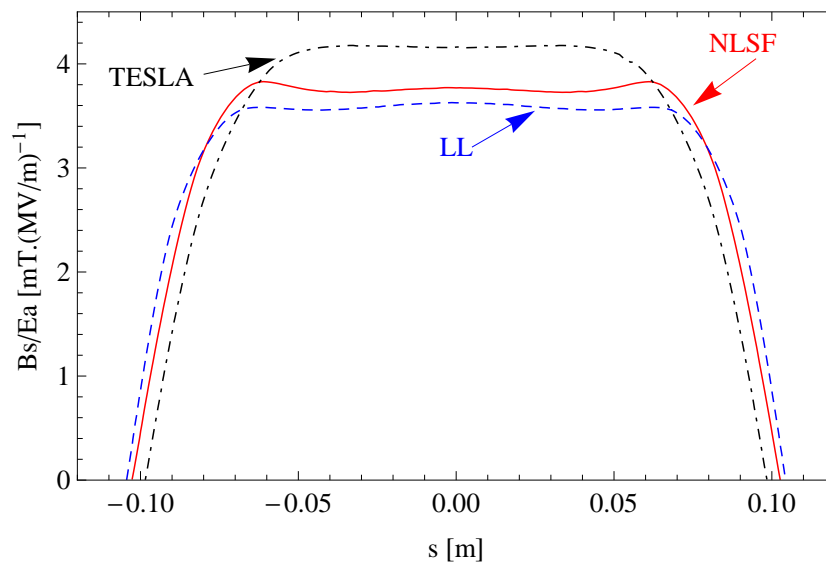
Figure 6.18: Surface magnetic field ratio along the cavity surface comparison between the NLSF (red line) and other designs; the TESLA (black dot-dashed line), the Low Loss (blue dashed line) shape, where s is the distance along the surface contour from centre of the equator.
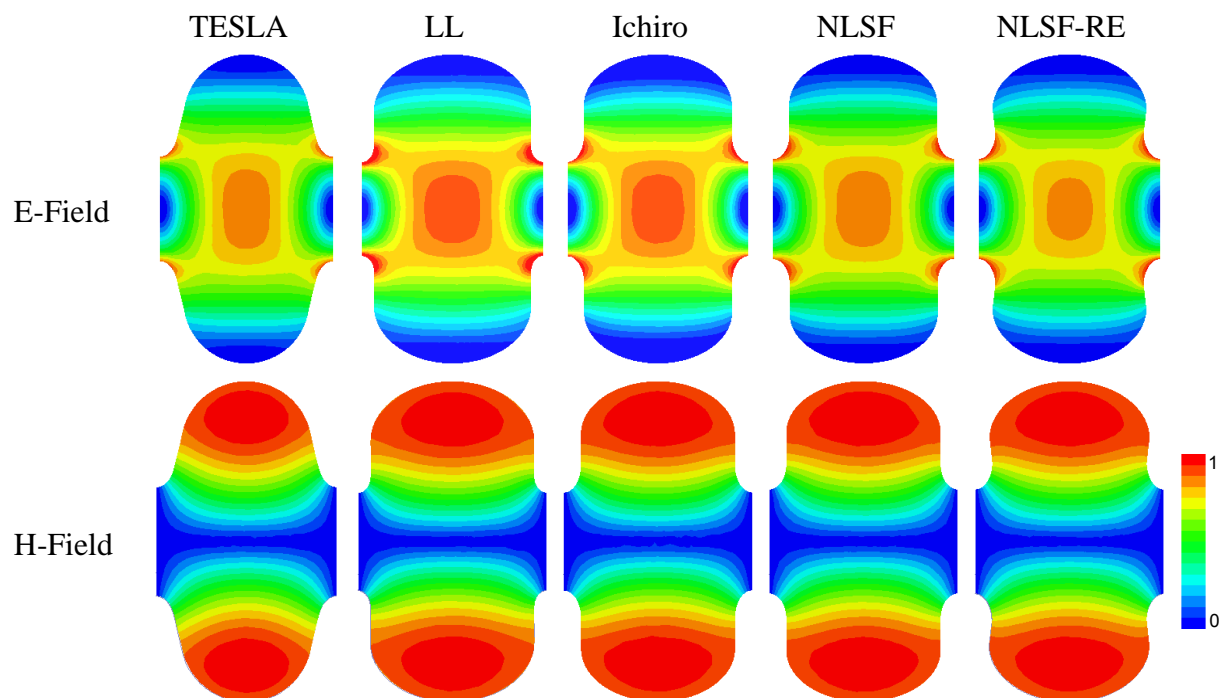
Figure 6.19: Comparison of the accelerating mode relative electric and magnetic fields for a range of potential ILC cavity shapes. All modes are computed at 1.3 GHz.

Table 6.3: Comparison of various optimised high gradient cavity designs.

Parameter	TESLA	LL	Ichiro	NLSF	NLSF-RE
R_i [mm]	35	30	30	32	32
R_{eq} [mm]	103.3	98.58	98.14	98.58	98.58
A [mm]	42	50.052	50.052	47.152	49
B [mm]	42	36.50	34.222	31.35	35.30
a [mm]	12	7.6	7.6	10.5	10.5
b [mm]	19	10	9.945	15.5	17
f_π [MHz]	1301.16	1300.08	1300.40	1300.23	1299.91
k_c [%]	1.89	1.53	1.54	1.59	1.66
E_s/E_a	2.18	2.42	2.37	2.11	2.07
B_s/E_a [mT/(Mv/m)]	4.18	3.64	3.62	3.83	3.78

Once the single cell has been designed, the end cells also need to be carefully designed in order to allow smooth connection of the fields between the cavity and beam pipes. This is described in the next section.

6.3 End Cell Design

We focused on a design for the NLSF cavity. The dimensions of the end cells were chosen to ensure a flat accelerating field along a multi-cell cavity and to allow a good match between the cavity and the HOM coupler region. The radius of the HOM beam pipes connecting successive cavities to one another was chosen to be that of the Low loss design, namely 38 mm, The lowest order mode that can propagate in this beam pipe is a TE_{11} mode, cutoff at approximately 2.3 GHz. Thus, the first two dipole modes (which are below 2.3 GHz) are contained within the cavity and can be damped with suitably designed couplers. Higher order dipole modes can propagate out of the cavity and in this case are partially damped with the HOM couplers. Firstly, we have focused our end cell design process on the NLSF shape. This was subsequently extended to the NLSF-RE shape for the sake of completeness.

Another Mathematica code was written to control SuperFish and hence facilitate a rapid variation of the parameters. An important parameter is the field flatness defined as:

$$\zeta = \left(1 - \frac{\sigma_p}{\mu_p}\right) \times 100 \, \%$$

(6.4)

where σ_p and μ_p is the standard deviation and the average value of the peak accelerating fields along the cavity axis in each cell respectively. These are illustrated in Fig. 6.20.
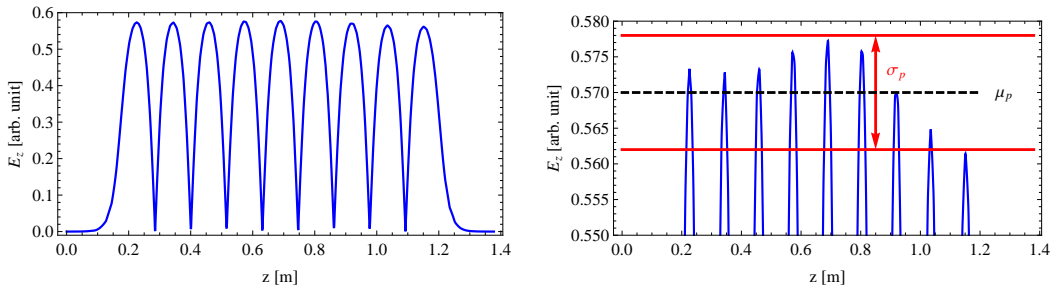
Figure 6.20: Accelerating field along a cavity axis of a 9-cell NLSF structure with beam pipes (left). The peaks are emphasised to the right.

The distance between two successive cavities was selected to be approximately similar to the configuration of the TESLA Test Facility (TTF) cryomodule, which has spacing of about $3\lambda/2$ between cavities. I used a beam pipe length of 170 mm which is approximately $3\lambda/4$.

Firstly, I tuned the end cell geometry with SuperFish. These results were validated with HFSS. The optimised NLSF cavity has a resonant frequency which is within 0.02% of the 1.3 GHz operating frequency and is 99% flat according to eq. 6.4. The field distribution is illustrated in Fig. 6.20. It is to be noted that this optimised end cell is very similar in shape to the middle cells, except for a slight difference in the iris and equator elliptical parameters ($a = 9.5$, $b = 12.5$, $A = 48.152$

and $B = 30.5$ mm). The NLSF cavity consists of seven identical middle cells and two identical end cells.

Table 6.4: Optimal NLSF and NLSF-RE cavities.

Parameters	NLSF		NLSF-RE1		NLSF-RE2	
	Mid cell	End cell	Mid cell	End cell	Mid cell	End cell
R_i [mm]	32	38	32	38	32	38
R_{eq} [mm]	98.58	98.58	98.58	98.58	98.58	98.58
A [mm]	47.152	48.152	49	50	49	49.5
B [mm]	31.35	30.5	35.30	35	35.30	35
a [mm]	10.5	9.5	10.5	10	10.5	10.5
b [mm]	15.5	12.5	17	15	17	13.5
ζ [%]	99.78		99.63		99.34	

Having designed a NLSF-RE shape, for the sake of completeness, the end cell tuning algorithm was then extended to the reentrant shape. Applied in a similar fashion to the NLSF cavity, two potential designs were obtained for a NLSF-RE cavity with symmetrical end cells. These are summarised in Table 6.4.

A detailed study on the NLSF modes and means to damp these modes is presented in the next chapter. If these modes are not suitably damped, the projected emittance of the bunch train can be diluted.

Chapter 7

Dipole and Higher Order Modes in the NLSF Cavity

The broad features of the surface e.m. fields and bandwidth of the monopole mode of the NLSF cavity were explained in the previous chapter. Here a detailed analysis of the e.m. fields present in a complete nine-cell cavity are explained. In particular, the properties of the dipole modes are studied.

7.1 Single-Cell Structure

In order to ascertain the transverse momentum kick imparted to the beam, the eigenvalues and eigenvectors of a full nine-cell cavity are calculated. Prior to analysing a full nine-cell cavity, a single cell is considered. For the sake of completeness, the dispersion curves for a single cell subjected to infinite periodic boundary conditions is shown in Fig. 7.1. Here the first six dipole bands are displayed, also included are quadrupole, sextupole, and octupole bands. The corresponding loss factors and kick factors are collected in Table 7.1.

The iris radius of this NLSF single cell is 32mm, which corresponds to a 2.75 GHz cutoff frequency
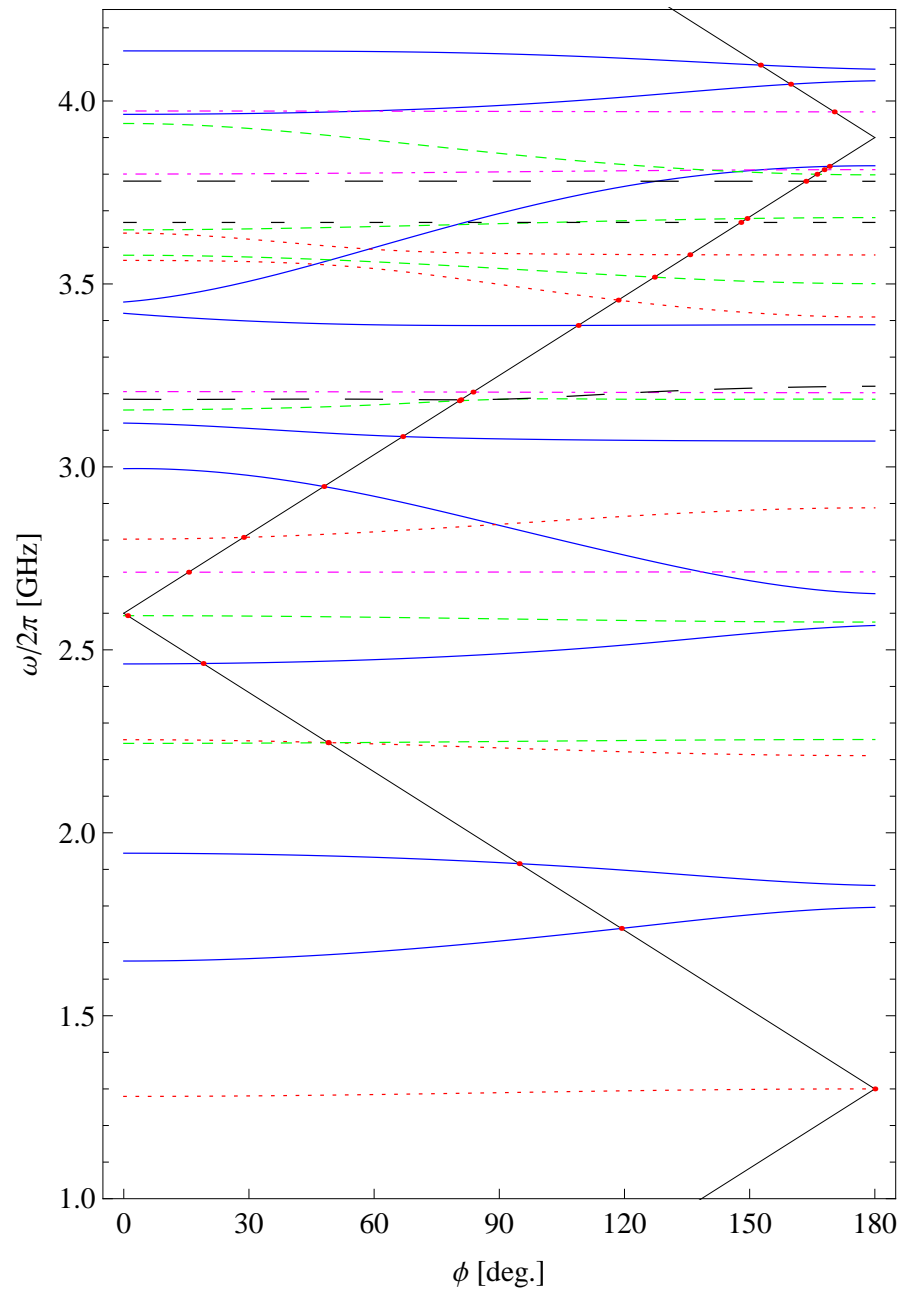
Figure 7.1: Dispersion curves for the monopole (red dotted line), dipole (blue solid line), quadrupole (green dashed line), sextupole (magenta dot-dashed line), octupole (black long-dashed line) and decapole (black short-dashed line) passbands with a light line (black zig-zag line) and synchronous points (red dot).

of the TE_{11} mode in a circular waveguide. The modes that have frequencies above 2.75 GHz can propagate through this waveguide and this is reflected in the dispersion curves - shown in Fig. 7.1. This will have important ramifications when considering coupling of many cavities.

Table 7.1: Loss factor of the monopole (M) modes and kick factor of the dipole (D) modes. The loss factors of the dipole modes are all calculated at a 1.5 cm offset.

Type	Band No.	$\omega_s/2\pi$ [GHz]	ϕ_s [deg.]	k_l [V/pC/m]	$k_\perp$ [V/pC/m^n/m]*
M	1	1.30021	180	2.25	0.083
M	2	2.24658	49	1.30	0.028
M	3	2.80736	29	0.05	0.001
M	4	3.45578	118	0.03	0.000
M	5	3.57978	136	0.49	0.006
D	1	1.73956	120	0.14	17.67
D	2	1.91546	95	0.21	23.00
D	3	2.46255	19	0.40	34.03
D	4	2.95240	45	0.01	0.37
D	5	3.08291	67	0.03	1.77
D	6	3.38650	109	0.03	2.13
D	7	3.81223	169	0.00	0.05
D	8	4.04637	160	0.08	3.96
D	9	4.09679	153	0.00	0.05

* $n = 0$ *for monopole and* $n = 1$ *for dipole.*

A detailed study of a nine-cell cavity is included in the next section.

7.2   Nine-Cell NLSF Structure

The nine-cell NLSF cavity consists of seven middle cells and two end cells. The geometrical parameters are collected in Table 6.4. A detailed study of a nine-cell NLSF cavity with beam pipe is discussed in this section. The study begins with the monopole and dipole modes.

Firstly, a quarter symmetrical section of a nine-cell NLSF cavity was used in the simulation with a set of boundary conditions, which admits only monopole, quadrupole and some higher order modes. By observing the electric field pattern of each resonant mode inside the cavity, the eigenfrequencies can be demarcated. The Floquet periodic condition was used to calculate the phase advance per cell of each mode and the dispersion relation of each passband.

A mode that has a frequency below the cutoff frequency of a beam pipe - 2.3 GHz and 3.0 GHz for TE and TM modes, respectively - remains locally within one cavity. When a mode possesses a frequency higher than the cutoff frequency, the mode can propagate from one cavity to another, creating a multicavity mode. In this case it is difficult to discriminate between other modes excited. Terminated boundary conditions at both ends of the beam pipe can accommodate these multicavity modes. In practise magnetic or electric field boundary conditions are used at each end of the beam pipes. Simulations are carried out with two separate sets of a terminating boundary conditions. These are either electric-electric (EE) or magnetic-magnetic (MM) boundary conditions.

Secondly, the boundary conditions were modified at the symmetry plane to satisfy the dipole, sextupole and higher order modes. A quarter section was simulated. The dispersion relations were obtained in a similar fashion to the monopole bands. Monopole and dipole dispersion curves are illustrated together in Fig. 7.2. Quadrupole and sextupole dispersion curves are plotted in Fig. 7.3.

In the monopole band, the terminations at the beam pipe does not affect the eigenfrequencies inside the cavity. When the mode frequency is higher than the cutoff frequency, the termination conditions at the beam pipes have an influence on the eigenfrequencies. This corresponds to a multicavity mode. This can be observed in the fourth and fifth monopole band dispersion curves in Fig. 7.2. The eigenfrequencies are not identical for different boundary conditions. This also applies to the
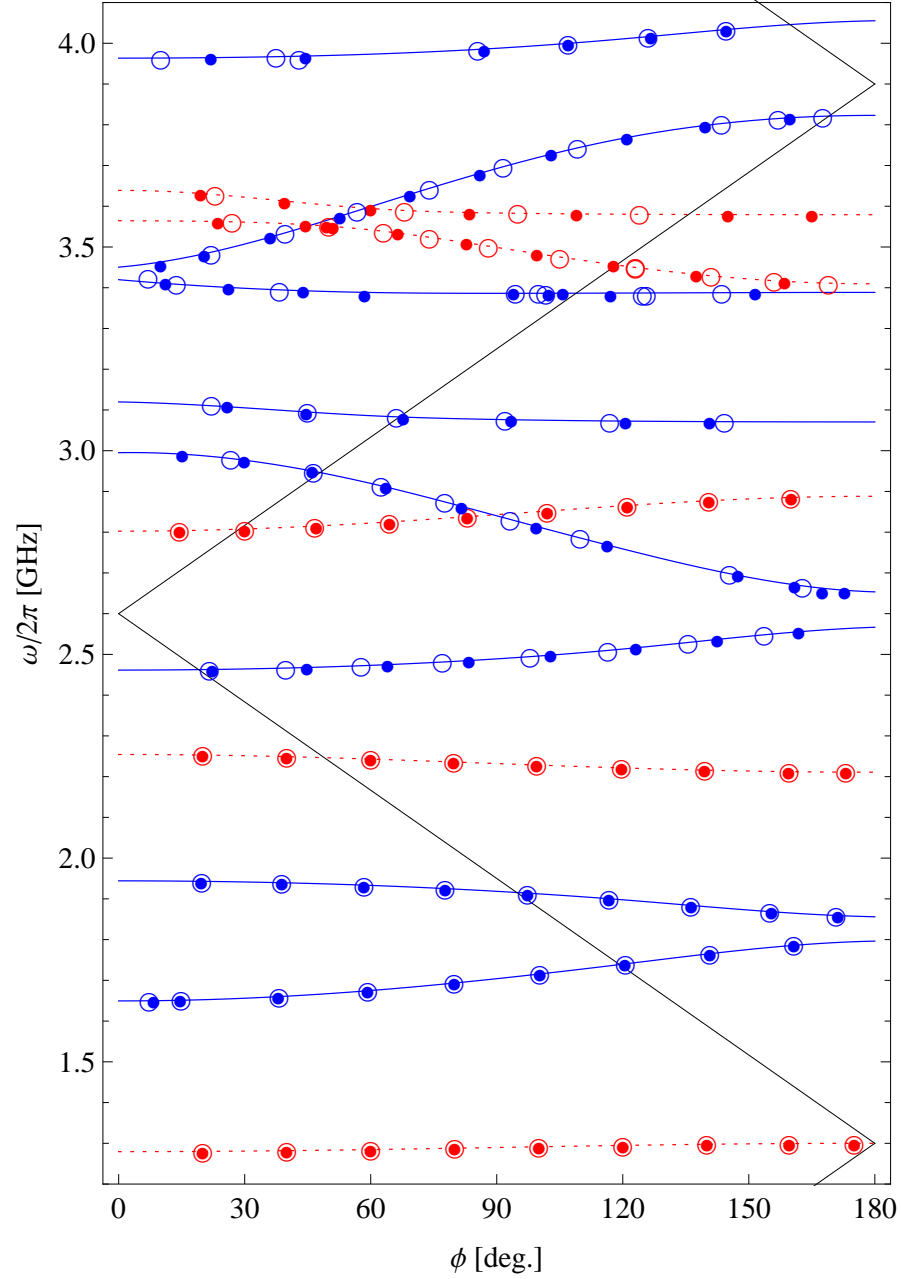
Figure 7.2: Monopole (red) and dipole (blue) dispersion curves of a nine-cell NLSF cavity. Dot indicates the results with MM boundary condition and circle represents those of the EE boundary condition. Cells subjected to an infinite periodic structure are indicated by the lines.
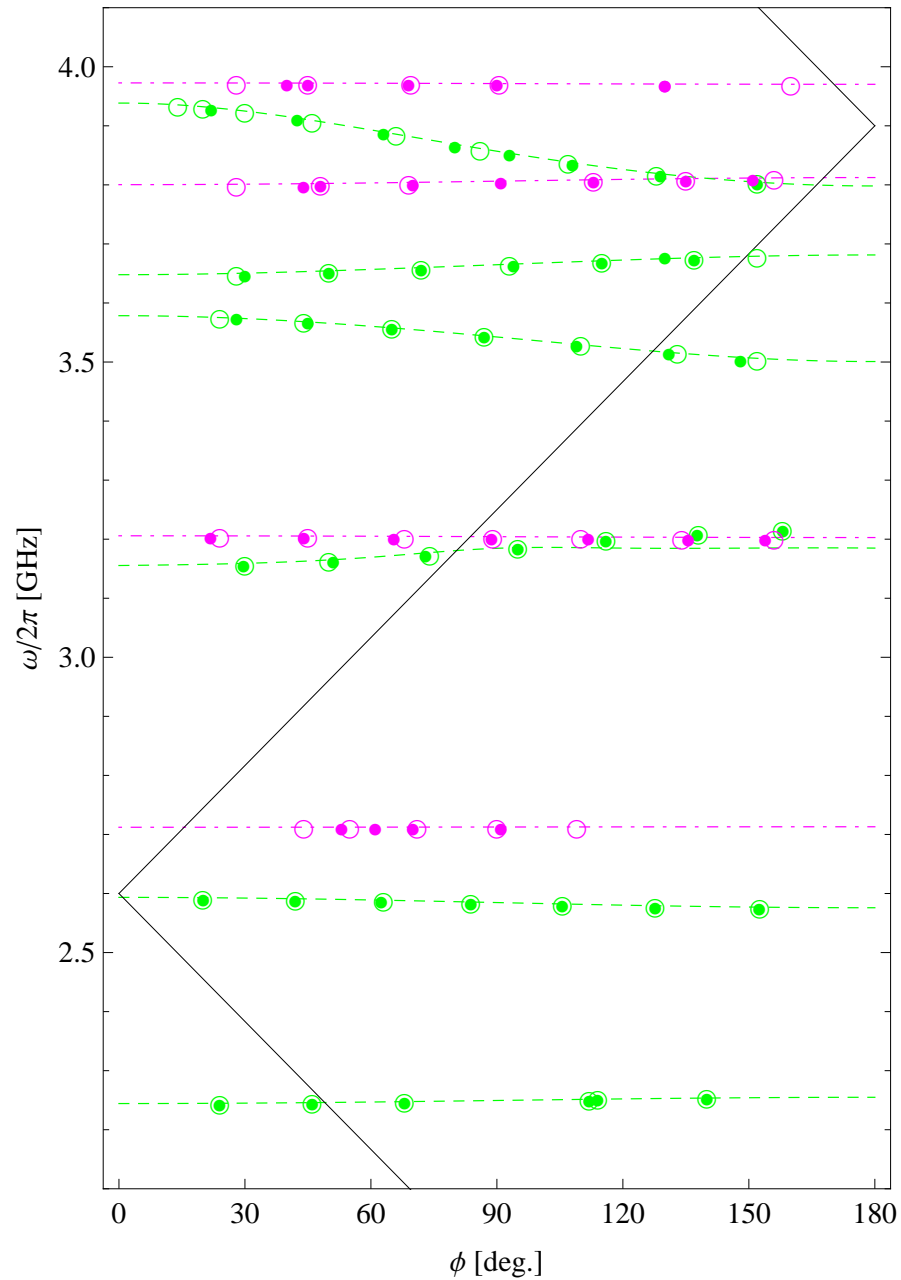
Figure 7.3: Quadrupole (green) and sextupole (magenta) dispersion curves of a nine-cell NLSF cavity. Dot indicates the results with MM boundary condition and circle represents those of the EE boundary condition. Cells subjected to an infinite periodic structure are indicated by the lines.

Table 7.2: R/Qs of the three lowest monopole bands; comparing the MM boundary conditions and the EE boundary conditions at the beam pipe.

MM bc.		EE bc.	
$\omega/2\pi$ [GHz]	R/Q [Ω]	$\omega/2\pi$ [GHz]	R/Q [Ω]
1.27906	0.00	1.27906	0.00
1.28082	0.01	1.28082	0.01
1.28351	0.03	1.28351	0.03
1.28684	0.03	1.28684	0.03
1.29039	0.07	1.29039	0.07
1.29375	0.03	1.29375	0.03
1.29651	0.01	1.29651	0.01
1.29830	0.01	1.29830	0.01
1.29894	**1126.78**	**1.29894**	**1126.78**
2.21015	1.39	2.21015	6.98
2.21146	6.17	2.21146	6.16
2.21508	4.06	2.21508	4.07
2.22066	9.52	2.22066	9.51
2.22759	10.74	2.22759	10.74
2.23510	28.66	2.23510	28.64
2.24227	**186.53**	**2.24227**	**186.53**
2.24824	**133.07**	**2.24824**	**133.09**
2.25217	7.96	2.25217	7.96
2.80154	0.01	2.80154	0.01
2.80555	0.41	2.80555	0.35
2.81276	**1.04**	**2.81275**	**1.03**
2.82305	0.05	2.82304	0.09
2.83573	0.40	2.83572	0.36
2.84965	0.10	2.84964	0.15
2.86334	0.10	2.86333	0.07
2.87504	0.06	2.87504	0.07
2.88302	0.01	2.88302	0.00

quadrupole band.

In the case of the dipole band, the eigenfrequencies of the lowest two bands are below the TE mode cutoff frequency, hence they are independent of the boundary condition at the beam pipe. The others are located above the cutoff frequency. Hence changing the boundary condition at the beam pipe gives different eigenfrequencies. This also applies to the sextupole band.

In order to ascertain the modes with the largest influence on beam dynamics the R/Q (= $V^2/\omega U$) is calculated. Table 7.2 lists the R/Qs of the monopole up to the third band. The mode frequencies and R/Q values are relatively independent of the boundary conditions. A graphical comparison is illustrated in Fig. 7.4.
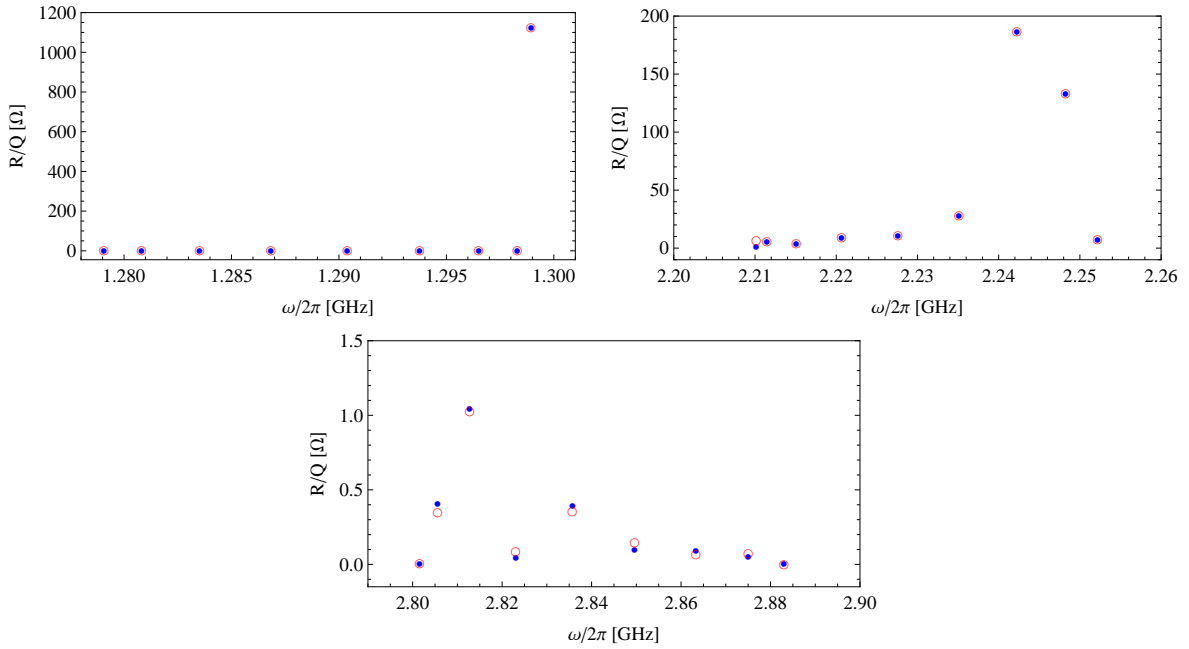
Figure 7.4: Monopole mode R/Qs for a nine-cell NLSF cavity for the three lowest monopole bands; comparing the results for the MM boundary conditions (blue dots) and those of the EE boundary conditions (red circles).

Table 7.3: R/Qs of the three lowest dipole bands; illustrating a comparison between the MM boundary conditions and the EE boundary conditions at the beam pipe.

MM bc.		EE bc.	
$\omega/2\pi$ [GHz]	R/Q [Ω/cm^2]	$\omega/2\pi$ [GHz]	R/Q [Ω/cm^2]
1.64789	0.09	1.64788	0.09
1.65026	0.37	1.65024	0.37
1.65925	0.12	1.65925	0.12
1.67353	0.61	1.67353	0.61
1.69245	0.08	1.69244	0.08
1.71491	4.59	1.71490	4.59
1.73952	**10.89**	**1.73951**	**10.89**
1.76432	2.56	1.76432	2.56
1.78583	0.09	1.78583	0.09
1.85668	0.17	1.85655	0.17
1.86699	1.52	1.86690	1.53
1.88293	0.12	1.88290	0.12
1.89877	**8.10**	**1.89878**	**8.14**
1.91251	**15.95**	**1.91255**	**16.00**
1.92359	**7.40**	**1.92366**	**7.38**
1.93203	0.21	1.93211	0.22
1.93787	0.26	1.93795	0.25
1.94133	0.02	1.94143	0.02
2.46161	**22.68**	**2.46121**	**24.33**
2.46600	**11.50**	**2.46470**	**15.84**
2.47317	0.11	2.47081	0.05
2.48350	1.60	2.48003	1.79
2.49727	0.07	2.49254	0.18
2.51451	0.46	2.50837	0.37
2.53480	0.12	2.52691	0.33
2.55493	0.05	2.54651	0.00

Mode frequencies and R/Qs of the first three dipole bands are listed in Table 7.3 and a graphical comparison between the MM and EE boundary condition is illustrated in Fig. 7.5. The modes in the third dipole are mixed between cavity modes and multicavity modes.

From this detailed study the accelerating mode R/Q is ∼ 1127 ohms. Also, the largest R/Q of the second monopole band is one sixth of the fundamental mode, and the third monopole band has a very small R/Q compared to the fundamental mode. From the perspective of beam dynamics it probably the case that no more than the first three monopole bands need to be considered. However, a detailed beam dynamics study is needed to confirm this postulate, and is a potential subject for further study. Similarly for the first three dipole bands. A mode compendium, presented in Appendix D, indicates the mode distribution and serves as a guide for considering means to suppress the modes.
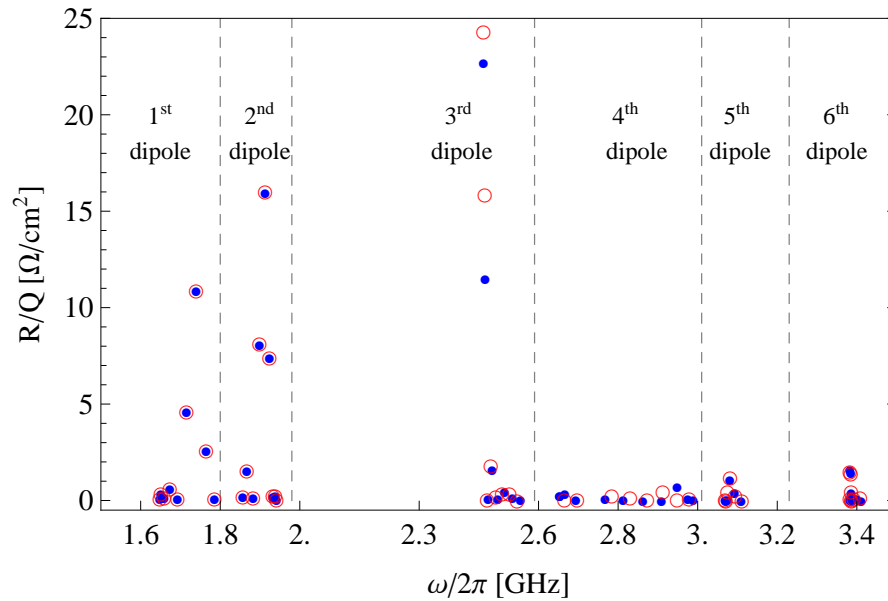
Figure 7.5: Dipole mode R/Qs; comparing the MM boundary conditions (blue dots) and the EE boundary conditions (red circles) for a nine-cell NLSF cavity.

The infinite periodic structure results, of the previous section, are in good agreement with a nine-

cell structure results. The next section entails constructing a circuit model in order to facilitate rapid calculation of the mode frequencies and kick factors.

7.3 Circuit Model Analysis

A circuit model provides approximate rf cavity properties which can be rapidly computed. A circuit model has been applied to the NLSF cavity. The methodology and results will be discussed and presented in the next section.

7.3.1 Circuit Model: The Monopole

A single chain circuit model, which was developed to represent the behaviour of the accelerating mode of the cavity, has been successfully employed to a TESLA cavity as discussed in chapter 5. Only two single-cell simulations are required to obtain the complete first monopole band. An additional simulation at the synchronous mode is required to estimate the dominant R/Qs of the band.

Table 7.4: Frequency discrepancy between a circuit model and a single cell with results for the lowest monopole.

ϕ [deg.]	$\omega/2\pi$ [GHz]		$\Delta\omega/2\pi$ [MHz]	$\Delta\omega/2\pi$ [%]
	Single cell	Circuit model		
0	1.27957	1.27957	0.00	0.00
30	1.28091	1.28092	0.00	0.00
60	1.28461	1.28460	0.01	0.001
90	1.28970	1.28970	0.01	0.001
120	1.29485	1.29485	0.01	0.001
150	1.29866	1.29866	0.00	0.00
180	1.30006	1.30006	0.00	0.00

Firstly, a single chain circuit model is applied to the lowest monopole band. In this case the maximum discrepancy with HFSS simulations is no more than 10 kHz. Similarly for a realistic nine-cell cavity the maximum discrepancy is 1.1 MHz for the first monopole. The nine-cell structure R/Qs are also well represented by the model. The results of this study are listed in Table 7.4 and Table 7.5. The R/Qs, illustrated in Fig. 7.6 as a function of frequency, are shifted in frequency with respect to each other. The eigenfrequencies from a circuit model and a nine-cell simulation are not at the same phase advance per cell, but they are placed on the same dispersion curve. This makes the R/Q plot display differently.

Table 7.5: Frequency discrepancy between a circuit model and nine-cell results for the lowest monopole.

ϕ [deg.]	$\omega/2\pi$ [GHz]		$\Delta\omega/2\pi$ [MHz]	$\Delta\omega/2\pi$ [%]
	Nine-cell	Circuit model		
20	1.27906	1.28018	1.11	0.09
40	1.28082	1.28192	1.10	0.09
60	1.28351	1.28460	1.09	0.08
80	1.28684	1.28792	1.08	0.08
100	1.29039	1.29148	1.09	0.08
120	1.29375	1.29485	1.10	0.08
140	1.29651	1.29761	1.11	0.09
160	1.29830	1.29941	1.10	0.09
175	1.29894	1.30002	1.08	0.08

The single chain circuit model has been extended to represent the higher monopole bands. We observed that the model represents the bands well up to the cutoff frequency as the discrepancy of frequency is less than 1 %. Higher order effects dominate as the frequency of the modes increases. The discrepancy between the circuit model and finite element simulations are expected to be exacerbated in this case. This is illustrated in Fig. 7.7 and Fig. 7.8.
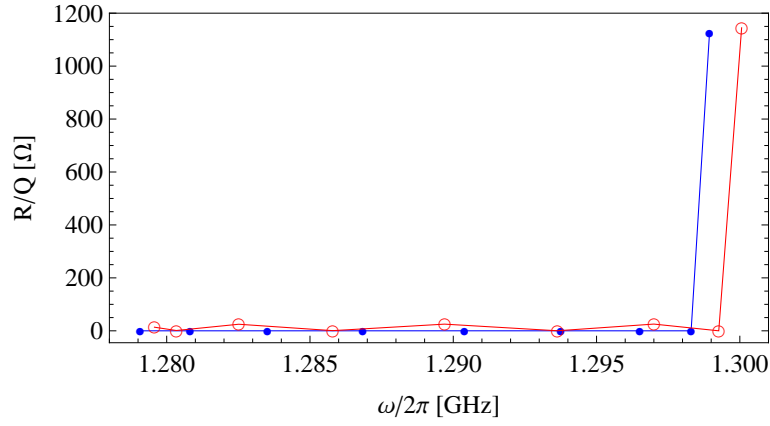
Figure 7.6: Comparison R/Qs of the first monopole between a circuit model (red circles) and a nine-cell cavity (blue dots) results.

In order to improve the model, next nearest neighbour coupling of cells is considered, in addition to the usual nearest neighbour coupling. This enhanced model has been applied to the fourth and the fifth monopole bands. The discrepancy is reduced in this case. This can be clearly observed from the dispersion diagram in Fig. 7.9. The model has a slight effect on the R/Qs - it improves the prediction of the circuit model. These comparisons are illustrated in the R/Qs plots in Fig. 7.10.

In the next section a double chain circuit model is used to represent the dipole modes of a NLSF cavity.

7.3.2 Double Band Circuit Model of Dipole Bands

Dipole cavity modes are inherently a mixture of TE and TM waves. In order to adequately represent this hybrid behaviour, a double chain circuit model is necessary. One chain represents the TE wave behaviour and the other represents the TM wave. The dipole bands are coupled together. The first is coupled to the second dipole; the third to the fourth dipole; the fourth to the fifth dipole; the sixth to the seventh dipole; and the eighth to the ninth dipole.
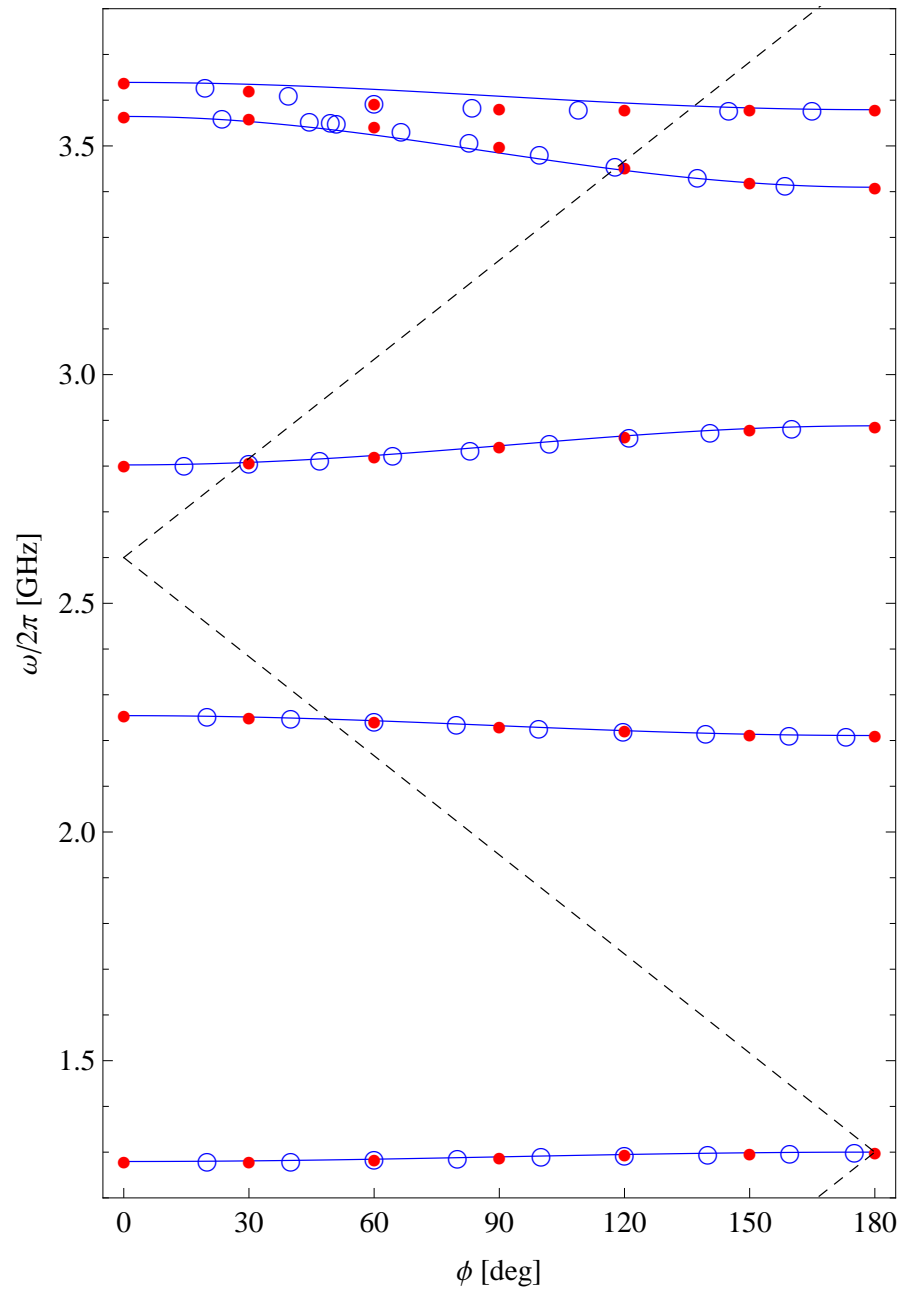
Figure 7.7: Circuit model dispersion curves (blue line) up to the fifth monopole band; comparing the results from an infinite periodic structure simulation (red dots) with a nine-cell cavity simulation (blue circles).
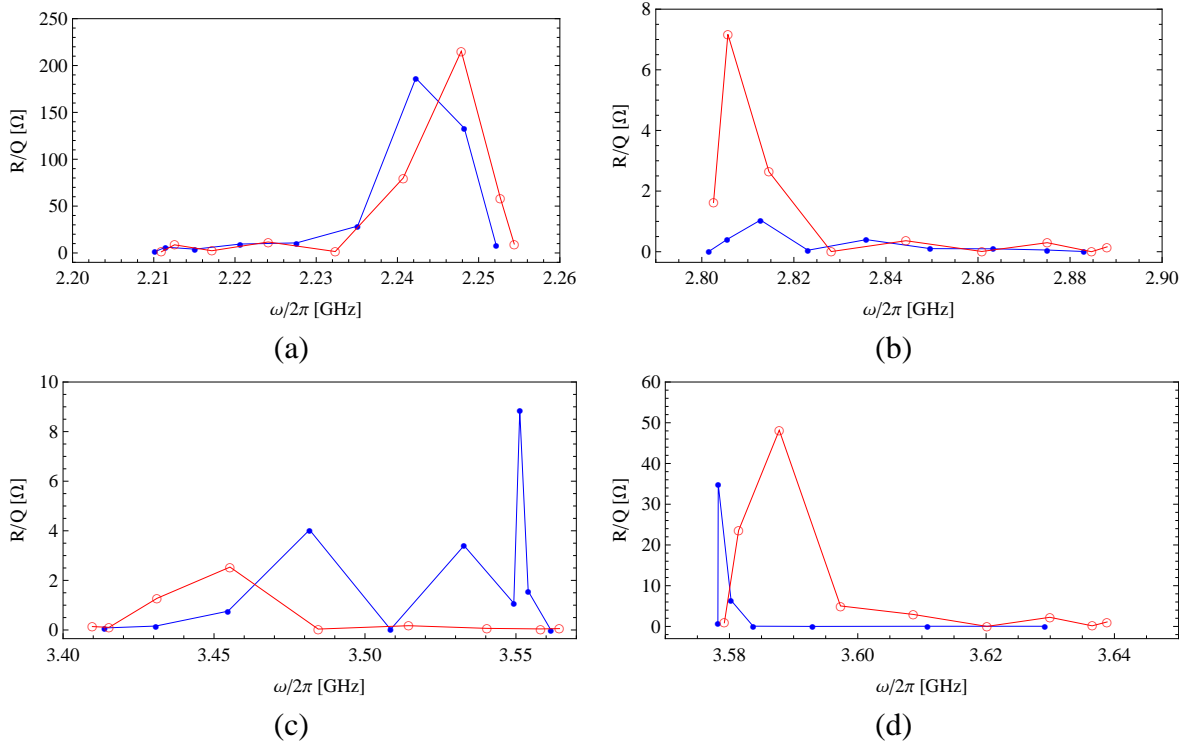
Figure 7.8: Analysis of the R/Qs of the higher monopoles, comparing a circuit model (red circles) and a nine-cell cavity (blue dots), in which (a) is the second band, (b) is the third band, (c) is the fourth band and (d) is the fifth band.
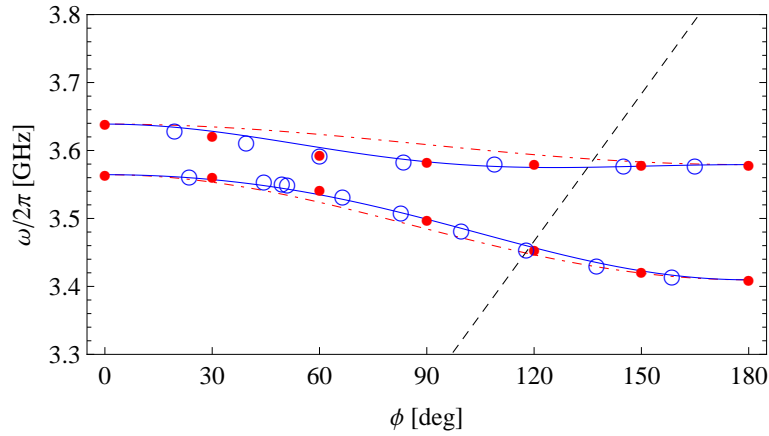
Figure 7.9: Dispersion diagram of the fourth and the fifth monopole, comparing a basic single chain circuit model (red dot-dash line) and the next nearest coupled model (blue line). The simulation results from a single-cell structure and a nine-cell cavity are indicated by red dots and blue circles, respectively.
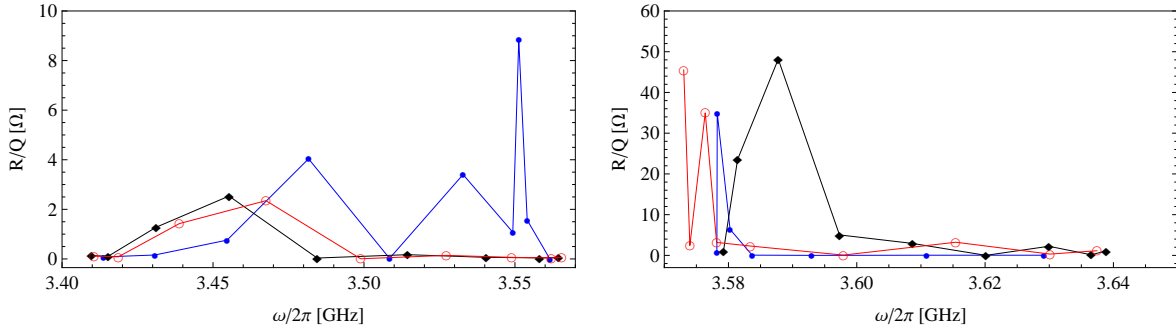
Figure 7.10: Comparison of the R/Qs of the higher monopole - the fourth band on the left and the fifth band on the right - with the next nearest coupled model (red circles), a basic single chain model (black diamonds) and a nine-cell cavity (blue dots).

Firstly, the model is employed to represent the two lowest dipole bands. Observing the field patterns from the simulations results in the input information and the calculated circuit parameters listed in Table 7.6. The two lowest dipole bands are well represented by a double chain circuit model in which the frequency discrepancy between the model and the simulation is less than 1 %. The frequency discrepancy between the model and the simulation are listed in Table 7.7 and Table 7.8 for a single-cell and a nine-cell cavity, respectively. A graphical comparison is illustrated by the dispersion curves in Fig. 7.11.

Table 7.6: Circuit model input information and a circuit model with calculated parameters for the two lowest dipoles.

	Input data				Circuit parameters	
	$\omega_0/2\pi$ [GHz]	$\omega_\pi/2\pi$ [GHz]	$\omega_s/2\pi$ [GHz]	K_s [V/pC/m/m]	$\omega_r/2\pi$ [GHz]	η [%]
TM chain	1.64954	1.85605	1.73956	17.67	1.74368	-11.74
TE chain	1.94421	1.79629	1.91546	23.00	1.86587	-7.90

Similar to the frequency, the R/Qs of both dipole bands are well predicted by the model, with a discrepancy appearing in the sum of the band's R/Qs, which are 4 and 6 Ω/cm^2 for the first and the second dipole bands, respectively. This comparison is illustrated by the R/Qs plot in Fig. 7.12.

Table 7.7: Results for the discrepancy between a circuit model and a single-cell structure for the first two dipoles.

| Band | ϕ [deg.] | $\omega/2\pi$ [GHz] | | $\Delta\omega/2\pi$ [MHz] | $\Delta\omega/2\pi$ [%] |
		Single cell	Circuit model		
	0	1.64954	1.64954	0.00	0.00
	30	1.65609	1.65612	0.03	0.00
	60	1.67500	1.67513	0.13	0.01
1st dipole	90	1.70406	1.70434	0.28	0.02
	120	1.73962	1.73998	0.36	0.02
	150	1.77578	1.77602	0.25	0.01
	180	1.79629	1.79629	0.00	0.00
	180	1.85605	1.85605	0.00	0.00
	150	1.87250	1.87216	0.34	0.02
	120	1.89771	1.89706	0.66	0.03
2nd dipole	90	1.91851	1.91785	0.66	0.03
	60	1.93305	1.93264	0.42	0.02
	30	1.94147	1.94135	0.12	0.01
	0	1.94421	1.94421	0.00	0.00

Secondly, with the successful implementation of a double chain circuit model on the first two dipole bands, the study is extended up to and including the eighth dipole band. As expected the discrepancy between the circuit model and simulation gets worse with higher frequencies. The maximum discrepancy in frequency between the circuit model and simulations are illustrated in Table 7.9. In this table, the subscript $1c$ is used for the result of the single-cell simulation, while the subscript $9c$ is used for the result of the nine-cell simulation. A dispersion diagram for the circuit model and simulations is illustrated in Fig. 7.13.

A potential reason for this large discrepancy is, in this high frequency region many modes are excited in the cavity, as can be seen from the dispersion diagram in Fig. 7.1. These modes, dipole and sextupole, can be mixed and separation can be complicated. The other issue is, that this circuit

Table 7.8: Results indicating the frequency discrepancy between a circuit model and a nine-cell structure for the first two dipoles.

Band	ϕ [deg.]	$\omega/2\pi$ [GHz]		$\Delta\omega/2\pi$ [MHz]	$\Delta\omega/2\pi$ [%]
		Nine-cell	Circuit model		
1st dipole	8.28	1.64789	1.65004	2.15	0.13
	14.66	1.65026	1.65112	0.86	0.05
	38.03	1.65925	1.66006	0.80	0.05
	59.22	1.67353	1.67449	0.96	0.06
	79.90	1.69245	1.69357	1.12	0.07
	100.26	1.71491	1.71604	1.13	0.07
	120.55	1.73952	1.74066	1.15	0.07
	140.71	1.76432	1.76538	1.06	0.06
	160.74	1.78584	1.78676	0.92	0.05
2nd dipole	171.23	1.85668	1.85787	1.19	0.06
	155.40	1.86699	1.86782	0.83	0.04
	136.30	1.88293	1.88372	0.79	0.04
	116.67	1.89877	1.89963	0.87	0.05
	97.33	1.91251	1.91330	0.80	0.04
	77.75	1.92359	1.92463	1.04	0.05
	58.38	1.93203	1.93326	1.23	0.06
	38.89	1.93787	1.93939	1.51	0.08
	19.68	1.94133	1.94298	1.65	0.09

Table 7.9: Results for the maximum frequency discrepancy between a circuit model and HFSS simulations for the dipole modes.

	Dipole band							
	1st	2nd	3rd	4th	5th	6th	7th	8th
$\Delta\omega_{1c}/2\pi$ [MHz]	0.36	0.66	0.49	2.19	1.57	9.50	56.27	11.18
$\Delta\omega_{9c}/2\pi$ [MHz]	2.15	1.65	2.10	8.10	3.58	16.11	55.25	13.01
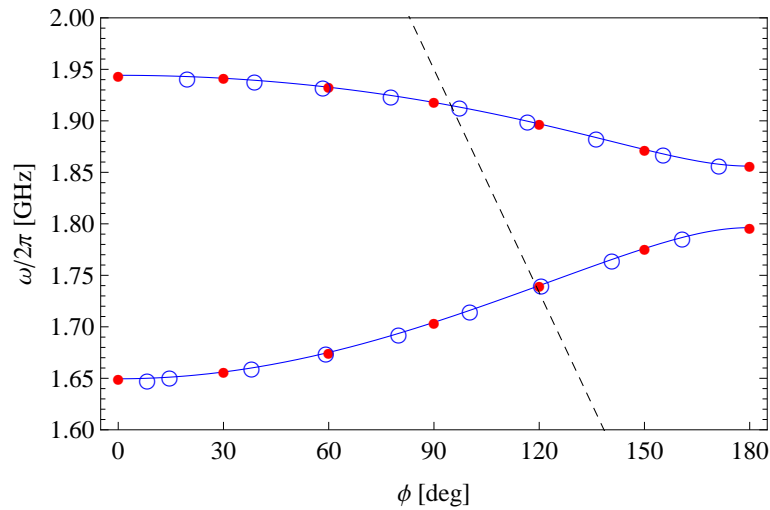
Figure 7.11: Dispersion diagram of the two lowest dipoles, comparing a double chain circuit model (blue line) with a simulations. The simulation results from a single-cell structure and a nine-cell cavity, are indicated by red dots and blue circles, respectively.
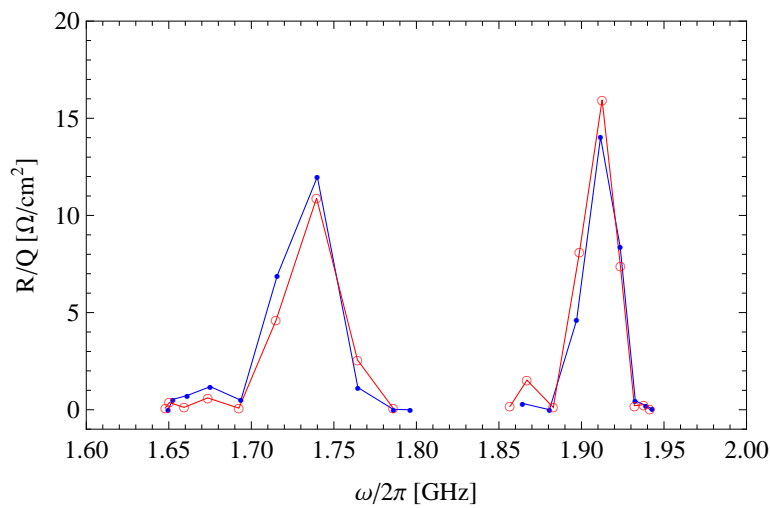
Figure 7.12: Comparing the R/Qs of the first two dipoles, i.e. a double chain circuit model (blue dots) and a nine-cell cavity (red circles).

model is developed from the assumption of the thin iris approximation and only the nearest cells are coupled. In an NLSF cavity, however, the iris is thick and, at the higher dipole band, excited modes become multicavity modes, which can propagate from one cavity to the others.

An additional parameter, corresponding to an iris of finite thickness may improve the agreement between the circuit model and HFSS simulations. The term is represented by the parameter h and the modified dispersion relation becomes:

$$\left(\frac{1 - \eta \cos \phi}{\omega_r^2} - \frac{1}{\omega^2}\right)\left(\frac{1 + \hat{\eta} \cos \phi}{\hat{\omega}_r^2} - \frac{1}{\omega^2}\right) - h\frac{\bar{\eta}^2}{\omega_r^2 \hat{\omega}_r^2} \sin^2 \phi = 0. \tag{7.1}$$

An additional point is needed from the dispersion curves to account for this parameter. The modified model is first tested with the two lowest dipoles to validate the model.

This modified model is particularly effective for higher dipole bands, in particular, the seventh dipole band, as can be observed from the comparison between Table 7.9 and Table 7.10. This improvement can be clearly seen from the comparison illustrated by the dispersion diagram in Fig. 7.14.

Table 7.10: Results for the maximum frequency discrepancy between a modified double chain circuit model and a dipole simulation.

	Dipole band							
	1st	2nd	3rd	4th	5th	6th	7th	8th
$\Delta\omega_{1c}/2\pi$ [MHz]	0.06	0.19	1.74	2.58	1.34	1.92	45.93	1.13
$\Delta\omega_{9c}/2\pi$ [MHz]	2.15	1.69	3.29	7.86	3.18	6.65	44.59	2.98

The modified double chain circuit model helps improve the frequency discrepancy for higher dipole bands, but the seventh dipole still suffers from a large discrepancy. A potential explanation for this
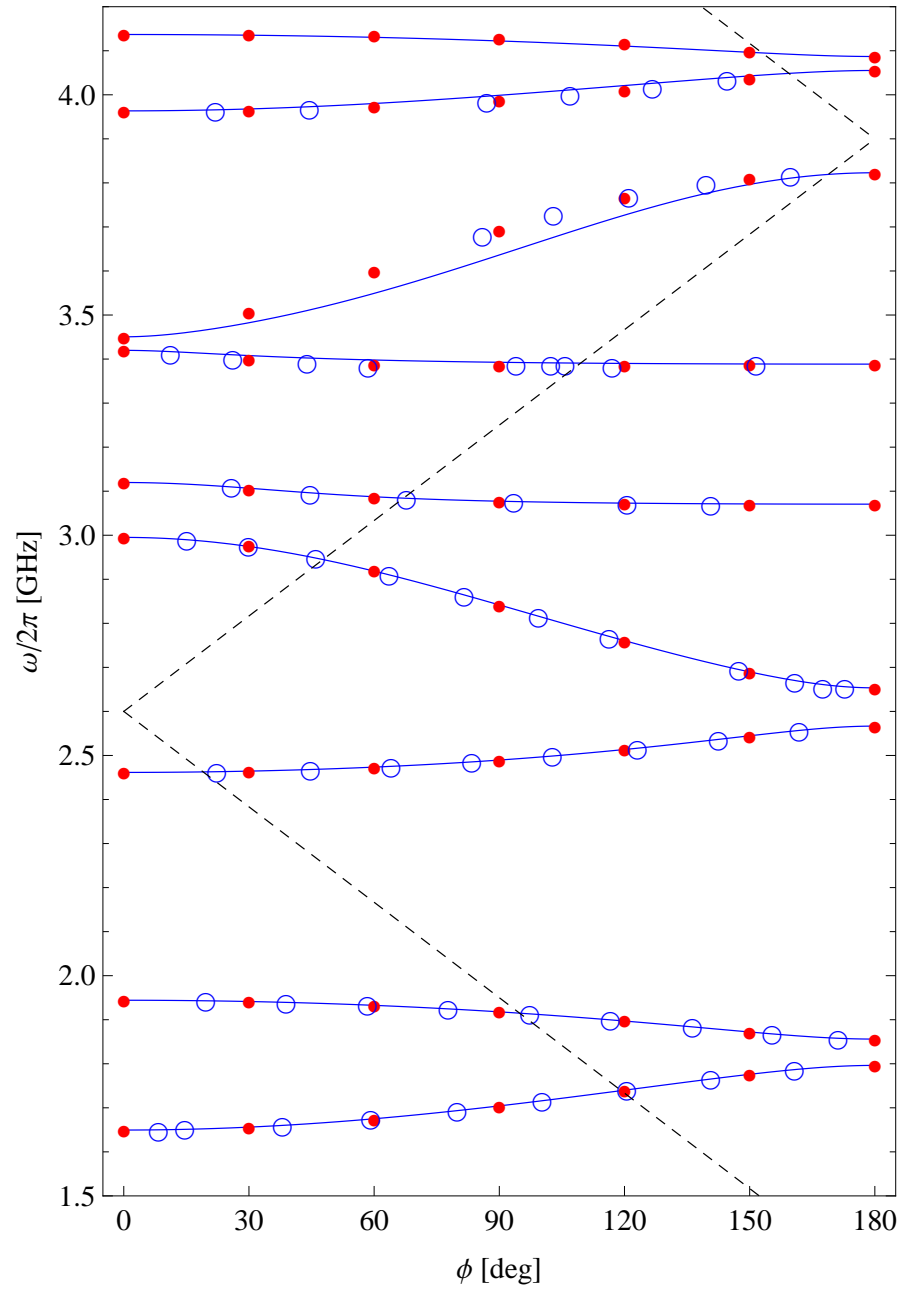
Figure 7.13: Circuit model dispersion curves (blue line) up to the ninth dipole band compared with the results from an infinite periodic structure simulation (red dots) and a nine-cell cavity simulation (blue circles).
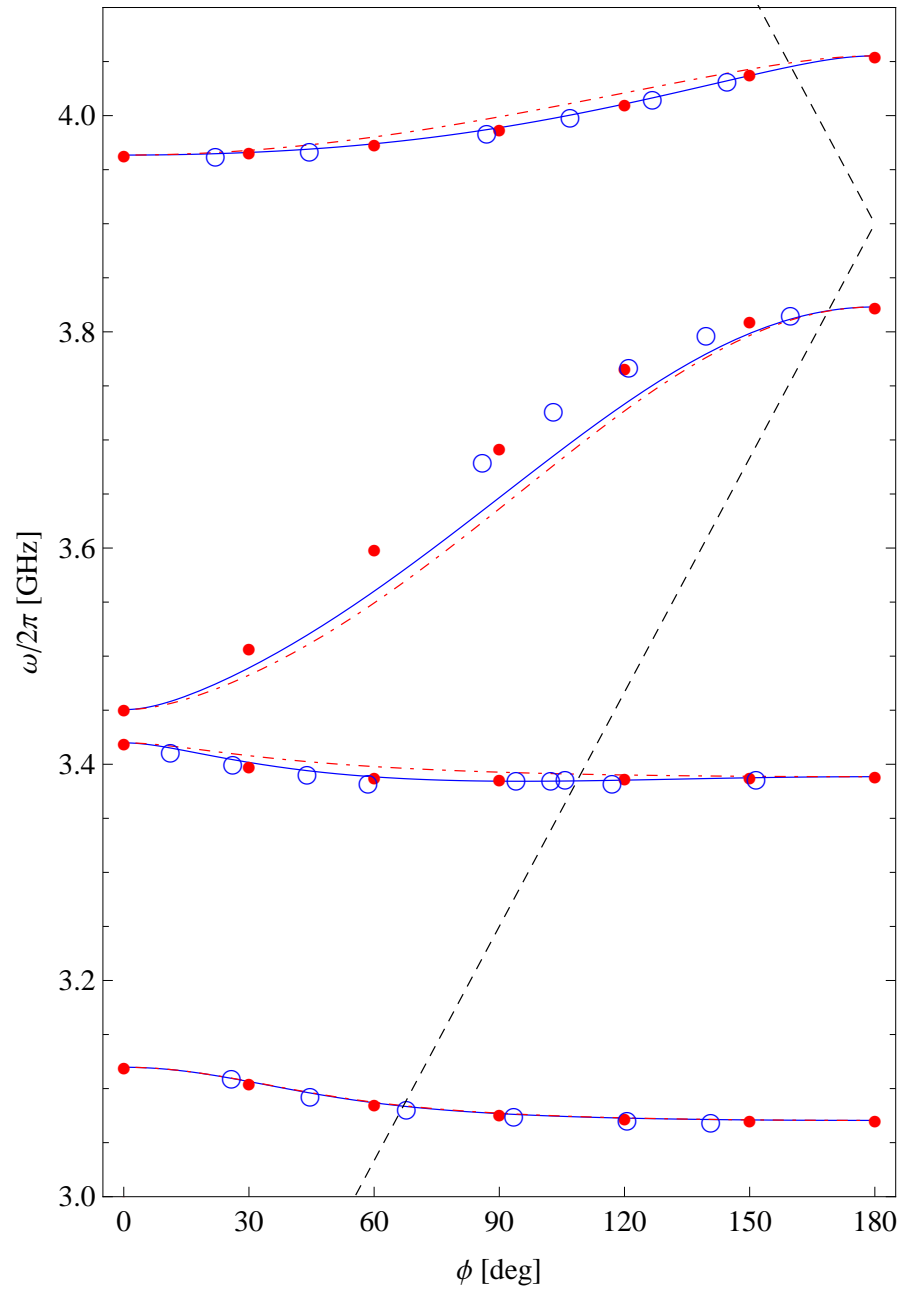
Figure 7.14: Dispersion diagram of the fifth to the eighth dipole, illustrating a comparison between a basic double chain circuit model (red dot-dash line) and a modified model (blue line). The simulation results from a single-cell structure and a nine-cell cavity are indicated by red dots and blue circles respectively.

nature is that this frequency region has multicavity modes and has several modes excited which can be mixed. Furthermore, the model is still based on the assumption that only the nearest cells are coupled, as discussed previously.

Finally, the prediction of the R/Qs for a NLSF cavity by using a double chain circuit model is presented for comparison with the simulation results in Fig. 7.15. This prediction uses a standard model up to the fourth dipole band and then a modified model is used.
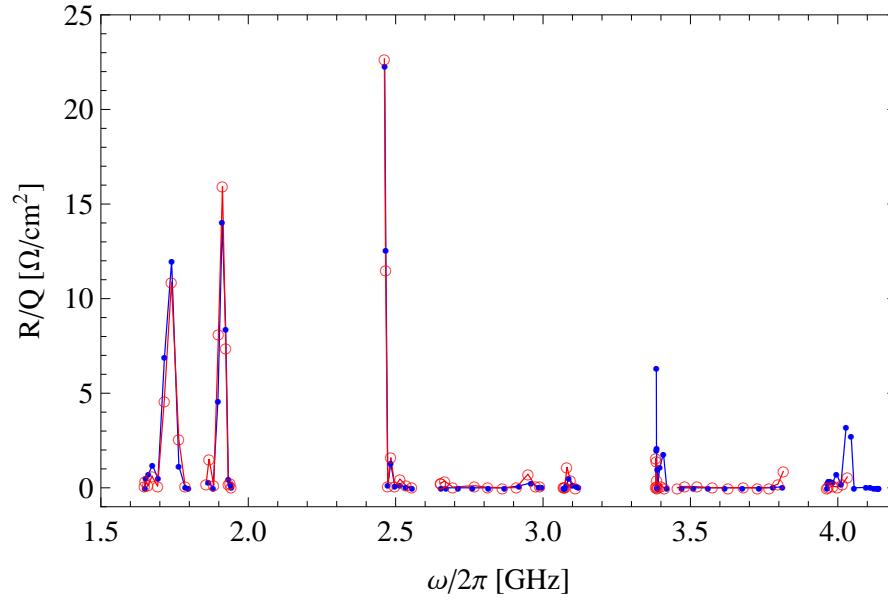
Figure 7.15: Dipole mode R/Qs comparison between a circuit model prediction (blue dots) and a nine-cell NLSF cavity simulation (red circles).

The double chain circuit model can be employed to predict a dipole mode behaviour of a NLSF cavity up to the sixth band, but for the dipole bands higher than the sixth band, the R/Qs becomes smaller and these modes can be damped easily by a proper HOM coupler design, as the modes can propagate through a cavity.

In summary, a detailed study of the NLSF cavity has been performed. The first few dipole bands are reasonably well-predicted by the model.

In the next chapter, short-range wakefields, resulting from geometric effects are studied for the NLSF cavity.

Chapter 8

A Study of Short Range Wakefields in the NLSF Cavity

General aspects of wakefield effects have been discussed briefly in section 2.4 and higher order modes associated with the long-range wakefields were studied in the previous chapter. Here, short-range wakefields due to geometrical effects are focussed on. Detailed simulations are performed and these are also supported by analytical models.

8.1   Numerical Study

A direct method to compute wakefields is to solve Maxwell's equations in the time domain with a suitable mesh-based algorithm. The monopole wakefield can be calculated from the fields induced by a Gaussian charge particle bunches passing on-axis through the structure. By discretising Maxwell's equations on a mesh of a particular geometry, these fields can be obtained. Weiland has developed a code for calculating the transverse interaction between a bunch of charged particles in cylindrically symmetric accelerating structures and this code is referred as a TBCI [61–63]. In the same time period, Chin also developed a wakefield and impedance code known as ABCI [64,65].

137

These codes use similar techniques to discretise Maxwell's equations [66, 67]. However ABCI has some internal differences. For example, it is capable of incorporating a larger mesh. Different mesh sizes may be specified in the transverse and longitudinal directions. ABCI includes Napoly's integration method [68] to calculate wake potentials in a structure, where parts of the structure extend to radii smaller than the radius of the beam tube. It also uses a moving mesh technique to reduce the number of mesh points and hence is capable of calculating very long structures and short bunches. This is because a moving mesh technique generates a mesh only for a part of the structure inside a defined window length. This mesh moves along with the charged particle bunch.

Igor Zagorodnov has recently developed a code, ECHO [69, 70], which is based on splitting the transverse e.m. field components in a time-based scheme. This scheme was proposed to overcome the numerical Cherenkov radiation effects in standard finite difference time domain methods used to model wakefields. Dispersion effects are thus minimised in this code.

The codes ABCI and ECHO, have been provided on a non-profit basis by their respective developers. The validation of these codes has been carried out by comparison for four cavities: TESLA, Ichiro, Re-entrant and NLSF cavity. An NLSF cavity geometry input for these simulations is illustrated in Fig. 8.1.
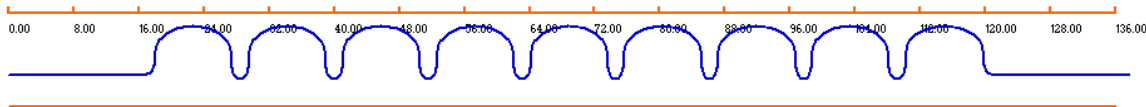
Figure 8.1: A NLSF cavity geometry input for ECHO numerical simulation, where dimension is in cm.

The wakefield results in terms of their loss and kick factors for one cavity structure, listed in Table 8.1, show that these results are reasonably consistent with one another (a maximum discrepancy of

5% is observed). The ABCI code requires more mesh points to give consistent mesh-stable results

Table 8.1: Comparison of loss and kick factors between two solvers on four accelerating cavities.

		$\sigma = 1\text{mm}$			$\sigma = 700\mu\text{m}$			$\sigma = 300\mu\text{m}$		
		ECHO	ABCI	$\triangle(\%)$	ECHO	ABCI	$\triangle(\%)$	ECHO	ABCI	$\triangle(\%)$
TESLA	$k_L[\text{V/pC}]$	9.89	10.04	1.52	11.56	11.82	2.25	17.72	18.46	4.18
($R_i = 35\text{mm}$)	$k_T[\text{V/pC/m}]$	18.36	18.52	0.87	15.41	15.61	1.30	10.38	10.57	1.83
Re-entrant	$k_L[\text{V/pC}]$	11.01	11.15	1.27	13.08	13.34	1.99	21.25	21.91	3.11
($R_i = 33\text{mm}$)	$k_T[\text{V/pC/m}]$	21.17	21.30	0.61	17.96	18.14	1.00	12.70	12.85	1.28
NLSF	$k_L[\text{V/pC}]$	11.32	11.36	0.35	13.28	13.35	0.45	20.84	21.03	0.91
($R_i = 32\text{mm}$)	$k_T[\text{V/pC/m}]$	23.47	23.55	0.21	19.81	19.90	0.45	13.65	13.82	1.25
Ichiro	$k_L[\text{V/pC}]$	12.89	13.03	1.09	15.32	15.57	1.63	25.19	25.77	2.30
($R_i = 30\text{mm}$)	$k_T[\text{V/pC/m}]$	28.14	28.26	0.43	23.94	24.06	0.50	17.03	17.12	0.53

and hence the computing time is longer. ABCI results also have a large variation for a short bunch. The method used to calculate the field has more numerical noise for short bunches and small mesh steps.
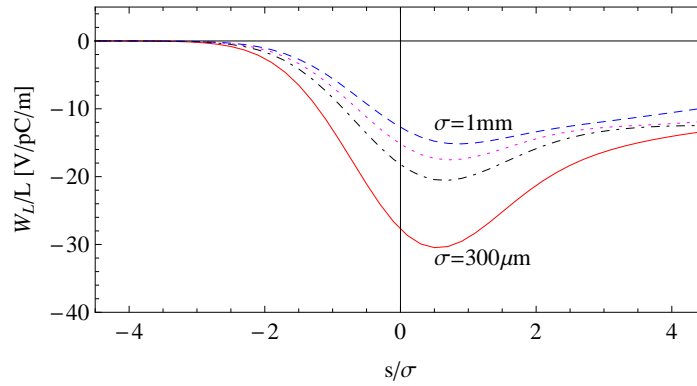
Figure 8.2: Normalised longitudinal wake function of a NLSF cavity for several bunch lengths: red line - 300 μm, black dot-dashed line - 500 μm, magenta dotted line - 700 μm, and blue dashed line - 1 mm.

In my NLSF cavity case, the normalised wake functions for Gaussian bunches, with varying rms length σ, to the structure length (L) from an ECHO simulation are plotted in Fig. 8.2 and Fig. 8.3 for longitudinal and transverse wakes, respectively. These results show that the longitudinal loss

factor (k_L) increases as the bunch length is reduced. The converse is the case for the transverse kick factor (k_T). This is a reflection of the definitions of the loss factor and kick factor. The longitudinal loss factor is defined as the bunch energy loss per unit charge squared and the transverse wake function defined as a change in transverse momentum kick per unit charge squared per unit offset from the cavity centre. Conversely a smaller particle bunch imparts a smaller transverse kick. These relationships between wakefields and geometric properties of a structure are discussed in the next section.
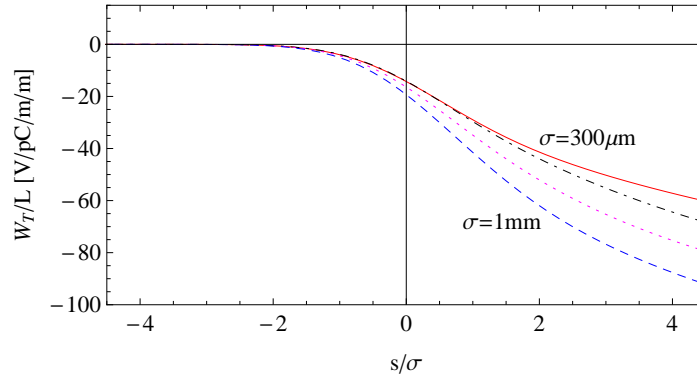
Figure 8.3: Normalised transverse wake function of a NLSF cavity with various bunch lengths: red line - 300 μm, black dot-dashed line - 500 μm, magenta dotted line - 700 μm, and blue dashed line - 1 mm.

These simulations have been based on a single cavity consisting of nine cells. In order to understand the periodic nature of the wakefield a string of cavities have been studied. Simulations have been carried out using one to eight cavities. All wakefields are normalised with respect to structure length in order to explicitly remove this dependence. These wake functions are illustrated in Fig. 8.4 and Fig. 8.5. As expected, until a sufficient number of cavities is used, there is a dependence of the wakefields on the number of cavities in the chain. Shorter bunches require more cavities in order to converge on the correct short-range wakefields. As stated in [71], the field reaches a steady state only after $N = 2a^2/(\sigma L_c)$ cells, where a is an iris radius and L_c is the cell length. In the NLSF cavity
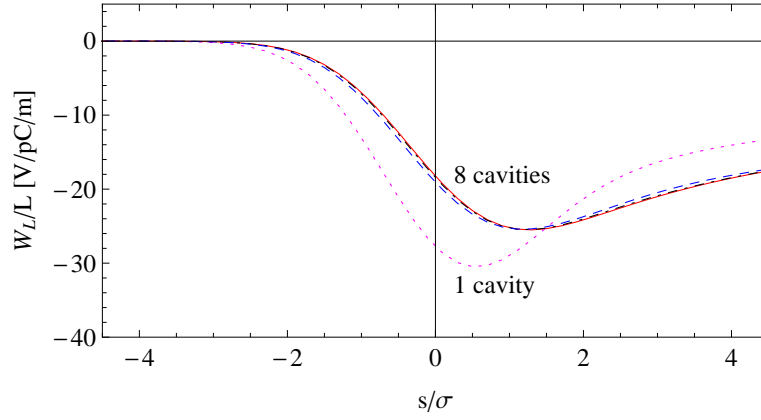
Figure 8.4: Normalised longitudinal wake function for various number of NLSF cavities: red line - 8 cavities, black dot-dashed line - 7 cavities, blue dashed line - 5 cavities, and magenta dotted line - 1 cavity, for a bunch length of $300\,\mu$m.

case, it is found that the wakefield converges provided $N \sim 60$ cells or 7 cavities for a 300 μm bunch length. A bunch length of 100 μm requires 20 cavities. For a 300 μm bunch the normalised loss
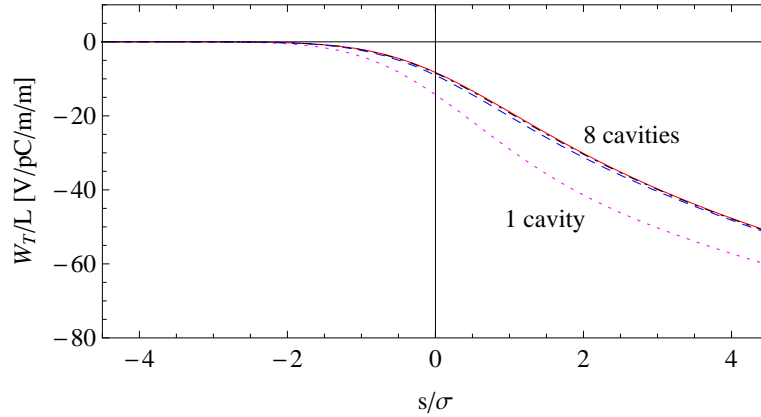
Figure 8.5: Normalised transverse wake function for various number of NLSF cavities: red line - 8 cavities, black dot-dashed line - 7 cavities, blue dashed line - 5 cavities, and magenta dotted line - 1 cavity, for a bunch length of $300\,\mu$m.

factor in this case is 16.52 V/pC/m and the normalised kick factor is 10.18 V/pC/m/m. The single cavity kick factor differs from the multi-cavity result by $\sim 20\%$.

The short-range wakefields can also been described by various analytical models for X-band and L-

band cavities [58, 59, 71–75]. These approximate models are useful in providing a rapid assessment of the impact of parameter variation on the wakefields. The direct application of these analytical models to my NLSF structure is discussed in the next section. Careful parametrisation is needed in order to properly account for the wakefields.

8.2   Analytical Study

In 1968 the British physicist, Lawson, suggested a diffraction model for calculating the energy loss of a point charge traversing a single cavity [76]. This model suggested a slow falloff of the real part of a beam-resonator coupling longitudinal impedance at high frequency as $\omega^{-1/2}$. This was also confirmed by the French physicist, Dome, with additional analytical approximations [77]. Dome's result was also confirmed with an iteration method by the Russian physicists, Heifets and Kheifets, in 1987 [78]. The American physicist, Gluckstern, studied the high frequency behaviour of this longitudinal impedance for a general shape cavity and a periodic structure in 1988 [79, 80], and the pillbox cavity results confirmed the results of Dome's impedance. In 1998, the Japanese physicist, Yokoya, and the American physicist, Bane, derived a more general result for longitudinal impedance in terms of the geometric properties of a structure.
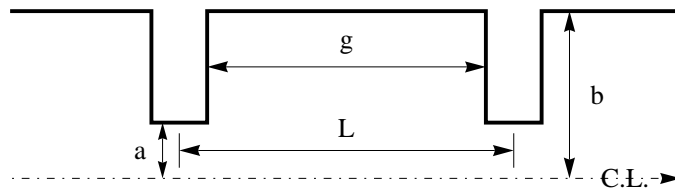
Figure 8.6: Cell geometry of 2D periodic pillbox structure.

Yokoya and Bane have studied short-range wakefields in a general periodic pillbox cavity focusing on accelerating structures for the NLC, and obtained an analytical short-range wake models for a

pillbox cavity [59,81], which is used widely as a basic approximation for parameterising short-range wakes in terms of the geometric properties of an accelerating structure over a range of parameters. The geometrical parametrisation used in the study are sketched in Fig. 8.6.

The Fourier transform of the wake provides the longitudinal and transverse impedances, Z_L and Z_T, respectively. Considering the structure in Fig. 8.6, Gluckstern derived the high frequency longitudinal impedance, with later modifications by Yokoya and Bane as [80, 81]:

$$Z_L(k) = \frac{iZ_0}{\pi k a^2} \left[1 + (1+i)\frac{\alpha(g/L)L}{a}\sqrt{\frac{\pi}{kg}} \right]^{-1} \qquad [k \text{ large}], \qquad (8.1)$$

where k is the wave number and $Z_0 = 120\pi$ is the impedance of free space. The parameter α is a function of geometric parameters and can be obtained approximately from [81]

$$\alpha(\gamma) \approx 1 - \alpha_1 \sqrt{\gamma} - (1 - 2\alpha_1)\gamma, \qquad (8.2)$$

with $\alpha_1 = 0.4648$. Taking the inverse Fourier transform of eq. 8.1 allows the longitudinal short-range wake function of a point-like charge to be obtained:

$$w_l(s) \approx \frac{Z_0 c}{\pi a^2}\text{erfc}\left(\sqrt{\frac{\pi s}{4 s_{00}}}\right)\exp\left(\frac{\pi s}{4 s_{00}}\right)\phi(s) \qquad [s \text{ small}], \qquad (8.3)$$

where $\phi(s)$ is the unit step function and

$$s_{00} = \frac{g}{8}\left(\frac{a}{\alpha(g/L)L}\right)^2. \qquad (8.4)$$

By making a series expansion of eq. 8.3 and focussing on the leading order dependence on s up to

the $\sqrt{s}$ term, the longitudinal short-range wake can be written as [59]:

$$w_l(s) \approx \frac{Z_0 c}{\pi a^2} \exp\left(-\sqrt{\frac{s}{s_{00}}}\right)\phi(s) \qquad [s \text{ small}]. \tag{8.5}$$

Fedotov, *et al*, studied the transverse impedance of a periodic array of cavities at high frequency and found a relationship between the transverse impedance and the longitudinal impedance [82]:

$$Z_T = \frac{2}{ka^2}Z_L \qquad [k \text{ large}]. \tag{8.6}$$

This allows the transverse wake function at short distances to be obtained as:

$$w_t(s) = \frac{2}{a^2} \int_0^s w_l(s')\,ds' \qquad [s \text{ small}]. \tag{8.7}$$

Combining eq. 8.5 and eq. 8.7 the transverse wake is given by:

$$w_t(s) = \frac{4Z_0 c s_{00}}{\pi a^4}\left[1 - \left(1 + \sqrt{\frac{s}{s_{00}}}\right)\exp\left(-\sqrt{\frac{s}{s_{00}}}\right)\right]\phi(s). \tag{8.8}$$

Bane applied these analytical formulae to periodic NLC structures [59, 83]. These structures have geometric parameters in the range $0.34 \le a/L \le 0.69$ and $0.54 \le g/L \le 0.89$. The fit is reasonably good over the range $0 \le s/L \le 0.16$ provided s_{00} is replaced with s_0 in eq. 8.5:

$$s_0 = 0.41\frac{a^{1.8}g^{1.6}}{L^{2.4}}. \tag{8.9}$$

Also for the transverse wakefield, s_{00} is replaced with s_1 in the fitting procedure. Here s_1 is:

$$s_1 = 0.169 \frac{a^{1.79} g^{0.38}}{L^{1.17}}. \tag{8.10}$$

Under these conditions the relationship between transverse and longitudinal wakefields still remain valid provided one is close to the head of the bunch:

$$\frac{d}{ds} w_t(0) = \frac{2}{a^2} w_l(0). \tag{8.11}$$

These formulae were derived based on periodic pillbox cavities. These cavities naturally have sharp irises. Nonetheless, they have been used widely to estimate the short-range wakefields for practical accelerating structures, which have rounded irises. They are also valid for an SRF cavity, which has a markedly rounded iris and this has been studied intensively by Zagorodnov on various SRF cavities [71–74].

These techniques are now applied to my NLSF cavity. Bane's original parametrisation is explored, subsequently improved by including finite structure effects.

8.2.1 Bane Model and Short-Range Wakefields

The method entails replacing all constants in eq. 8.5 and eq. 8.8 with the fit parameters: A, B, s_0, and s_1. This allows the wake functions to be re-parameterised as:

$$w_l(s) = \phi(s) \left[A e^{-\sqrt{s/s_0}} \right], \tag{8.12a}$$

$$w_t(s) = \phi(s) \left[B \left(1 - (1 + \sqrt{s/s_1}) e^{-\sqrt{s/s_1}} \right) \right]. \tag{8.12b}$$

Convolution of these wakes with a Gaussian bunch is compared with numerical simulations using the code ECHO. The fit parameters are varied in order to minimise the discrepancy between the model and simulation. For example, to obtain the longitudinal wake potentials of my NLSF cavity, the wake function is convolved with a Gaussian bunch, with $\sigma = 300\mu$m, and fit parameters, A, s_0, are varied in order to fit to ECHO simulations. A similar procedure is followed for the transverse wake function. This allows the NLSF cavity to be characterised with the following parameters: $A = 52.0$ and $s_0 = 1.10 \times 10^{-3}$ for the longitudinal wake function and $B = 110.0$ and $s_1 = 5.40 \times 10^{-4}$ for the transverse wake function.
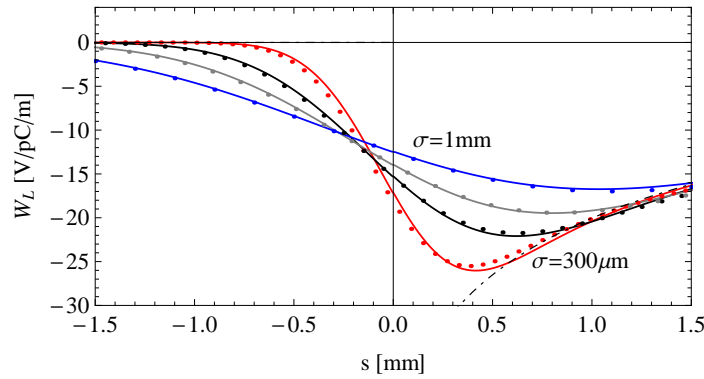
Figure 8.7: Application of Bane model to NLSF cavity. The Bane model predictions (lines) are shown along with numerical results (dots) of the longitudinal wake potential for various bunch lengths: red - $300\,\mu$m, black - $500\,\mu$m, gray - $700\,\mu$m and blue - 1mm, with the prediction for longitudinal short-range wake function indicated by a dot-dashed line.

The geometric parameters calculated from eq. 8.9 and eq. 8.10 are $A = 35.1$, $s_0 = 3.41 \times 10^{-3}$, $B = 249.8$ and $s_1 = 1.82 \times 10^{-3}$. These are quite different from the fit values because the original Bane parameters are for sharp iris transitions, but the NLSF cavity consists of decidedly rounded irises. This analytical model is applied over a range of bunch lengths and compared to ECHO simulations. The results of these validations simulations are illustrated in Fig. 8.7 and Fig. 8.8. It is clear that the analytical predictions are also in good agreement with ECHO simulations for bunch lengths in the range 300 μm to 1 mm. These results suggest that the wake function is effectively an

envelope function. The predictions for the corresponding loss factors and kick factors are listed in Table 8.2. The discrepancy between the analytical model and numerical simulations is exacerbated by short bunches. From the perspective of numerical simulations of short bunches, they may not be in a steady state condition and are affected by numerical noise. Also, the NLSF cavity has $a/L = 0.28$, which is below the range of validity allowed in the Bane formulae (this discrepancy was also observed in [75]).
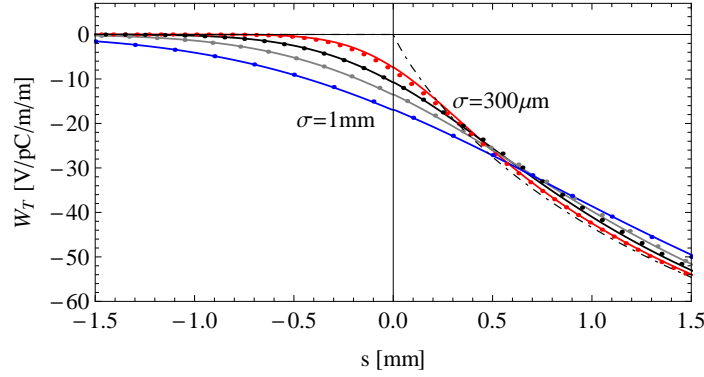
Figure 8.8: Application of Bane model to NLSF cavity. The transverse wake potential from the Bane model predictions (lines) are shown along with numerical results (dots) for various bunch lengths: red - $300\,\mu$m, black - $500\,\mu$m, gray - $700\,\mu$m and blue - 1mm, with the predictions for transverse short-range wake function indicated by a dot-dashed line.

Table 8.2: Comparison of loss and kick factors between the analytical Bane model predictions and the numerical results for the NLSF cavity.

σ[mm]	k_L[V/pC/m]			k_T[V/pC/m/m]		
	Numerical	Analytical	$\triangle(\%)$	Numerical	Analytical	$\triangle(\%)$
0.3	16.52	15.93	4.15	10.18	9.53	6.39
0.5	13.97	13.93	0.29	13.47	13.56	0.67
0.7	12.60	12.53	0.56	16.66	16.77	0.66
1.0	11.15	11.00	1.35	20.69	20.62	0.34

8.2.2   Modified Bane Model

Zagorodnov, *et al*, have applied the modified Bane formulae to characterise the LOLA-IV structure, the transverse deflecting cavity used for measuring the bunch length in the TTF-II project, and to a third harmonic cavity [72]. These formulae include finite effects of the structure, which lead to a high frequency dependence of the impedance of $\omega^{-1/2}$. This differs from an infinite periodic structure, which has a $\omega^{-3/2}$ dependence [80]. As my NLSF cavity has a finite length there is a transition region where the impedance behaviour changes from $\omega^{-3/2}$ to $\omega^{-1/2}$. This explains the oscillatory behaviour in the longitudinal wake potentials for the very short bunches. A cosine factor is added into a model to describe an oscillated behaviour. The modified analytical model for the longitudinal wake function is

$$w_l(s) = \phi(s) \left[A\, e^{-\sqrt{s/s_0}} + B\, \frac{\cos \omega s^\alpha}{\sqrt{s} + C s^\beta} \right], \tag{8.13}$$

where the first term describes periodic behaviour and the second term describes finite structure behaviour. The parameter A can be estimated from eq. 8.5 as

$$A = \frac{Z_0 c}{\pi a^2}, \tag{8.14}$$

which is normalised to the total structure length (L_{tot}). Also, s_0 can be obtained from eq. 8.9 and coefficient B can be estimated from [58]:

$$B = \frac{Z_0 c}{\sqrt{2L_{tot}}\, \pi^2 a}. \tag{8.15}$$

Other coefficients, α, β, C and ω, are obtained from a numerical fit to simulations of the wake potentials. The coefficients A and B from the expressions above can be ascribed as initial values in the fitting process. The final fit values may differ after the process is complete.

In a similar manner, the transverse wake parameter is obtained, including both the finite structure behaviour and the periodic nature:

$$w_t(s) = \phi(s)\left[D\left(1 - (1 + \sqrt{s/s_1})e^{-\sqrt{s/s_1}}\right) + E\sqrt{s}\right].\tag{8.16}$$

Here the coefficient s_1 is estimated from the expression in eq. 8.10 and the coefficient D is

$$D = \frac{4Z_0c}{\pi a^4}s_1.\tag{8.17}$$

As stated in [58], the coefficient E is estimated by

$$E = \frac{2\sqrt{2}Z_0c}{\pi^2 a^3 \sqrt{L_{tot}}},\tag{8.18}$$

where coefficients D, and E, are , as usual, normalised to the total structure length.

Once again, the convolution of these functions with a Gaussian distribution is compared to that of numerical simulations obtained with ECHO. The fitting parameters are varied in order to minimise the discrepancy between both methods. Applying this to my NLSF cavity results in:

$$
\begin{aligned}
w_l(s) &= \phi(s)\left[36.5\,e^{-\sqrt{s/2.44\times10^{-3}}} + 0.35\frac{\cos 1030s}{\sqrt{s} + 320s}\right], &(8.19a)\\
w_t(s) &= \phi(s)\left[90\left(1 - (1 + \sqrt{s/9.5\times10^{-4}})e^{-\sqrt{s/9.5\times10^{-4}}}\right) + 555\sqrt{s}\right], &(8.19b)
\end{aligned}
$$

for the longitudinal and the transverse wake functions, respectively. The initial estimated coefficients are: $A = 35.1$, $B = 0.09$, $s_0 = 3.41 \times 10^{-3}$, $D = 249.8$, $E = 343.1$ and $s_1 = 1.82 \times 10^{-3}$. These approximations are consistent with the final fit values. A comparison between the prediction and modified analytical model are illustrated in Fig. 8.9 and Fig. 8.10 for the longitudinal and the transverse wake functions, respectively. The corresponding loss factors and kick factors are also
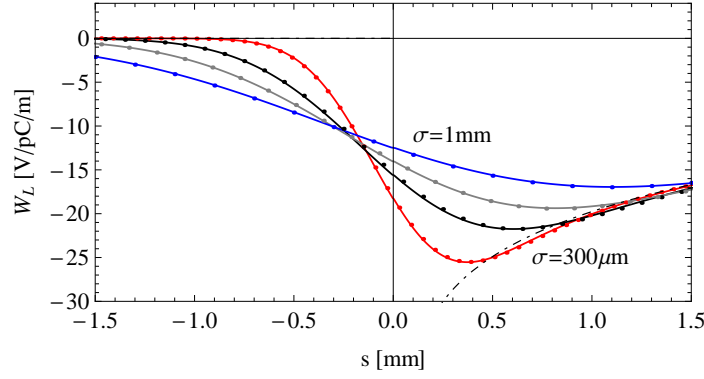
Figure 8.9: Application of modified Bane model to NLSF cavity. Results from the modified Bane model predictions (lines) are compared to numerical results (dots) of the longitudinal wake potential for various bunch lengths: red - $300\,\mu$m, black - $500\,\mu$m, gray - $700\,\mu$m and blue - 1mm, with the predictions for longitudinal short-range wake function indicated by a dot-dashed line.

calculated from these modified models and are listed Table 8.3. These modified models are in a good agreement with numerical results, with a maximum discrepancy of 4% for a short bunch. It is worth bearing in mind that shorter bunches require many cavities to be simulated and it may well be the case that the solution has not converged to the steady state for a 300 μm bunch.
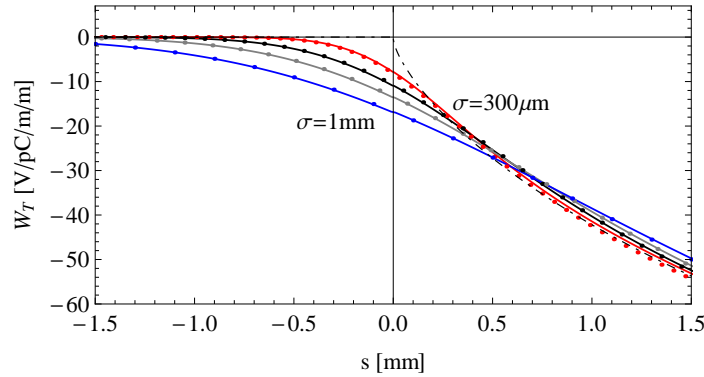
Figure 8.10: Application of modified Bane model to NLSF cavity. The transverse wake potential from modified Bane model predictions (lines) are shown along with numerical results (dots) for various bunch lengths: red - $300\,\mu$m, black - $500\,\mu$m, gray - $700\,\mu$m and blue - 1mm, with the prediction transverse short-range wake function indicated by a dot-dashed line.

These analytical studies show that the short-range wakefields can be estimated and predicted from the geometric properties of a structure in conjunction with one or two numerical simulations with

Table 8.3: Comparison of loss and kick factors for the NLSF cavity.

σ[mm]	k_L[V/pC/m]			k_T[V/pC/m/m]		
	Numerical	Analytical	$\triangle$(%)	Numerical	Analytical	$\triangle$(%)
0.3	16.52	16.51	0.66	10.18	9.80	3.73
0.5	13.97	14.06	0.64	13.47	13.57	0.74
0.7	12.60	12.59	0.08	16.66	16.70	0.24
1.0	11.15	11.11	0.36	20.69	20.65	0.19

different bunch lengths. It is useful for designing structures in a timely manner. All models presented in this context have been shown to be valid for the NLSF cavity for bunch rms lengths in the range from 300μm to 1mm. The maximum discrepancy from the numerical results is $\sim$ 7%. From these studies, the wake functions tend to be an envelope function. This provides an estimate of the maximum amplitude of short-range wakes for short bunches.

This concludes a study of the properties of the main body of the cavity. Means of coupling in power to the cavity, together with methods to damp the higher order modes, are considered in the next chapter.

Chapter 9

FP and HOM Coupler Design for the NLSF Cavity

To minimise wall losses superconducting cavities are used in the ILC design. The cavities of the ILC are maintained at 2K in a liquid Helium (He) vessel. All vessels are contained within a cryostat. RF power is transmitted into the cavities through couplers. These fundamental power (FP) couplers can either be waveguide or coaxial in nature. The relative merits of each have been discussed in section 1.5.2. The ILC design uses a coaxial type coupler. This is because it is compact and tuning the external quality factor (Q_e) is easily facilitated.

Similarly, the higher beam-excited modes must be coupled out of the cavity in order to reduce wall losses and to ensure the beam properties are preserved. A brief overview of the HOM coupler has been presented in section 1.5.3. The design process, together with detailed simulations for my NLSF cavity are described in this chapter.

9.1 Fundamental Power Coupler

The role of the FP coupler is to transfer rf power from the source system to the cavity. This is achieved by providing an impedance match between the source system and the combined cavity-beam system. The objective being, to minimise the reflected power. For an SRF cavity, the coupling hole is located on the beam pipe, just outside the end cell, where the fields are lower than in the cell. Even though the fields are significantly higher in the equator of cells, situating a coupling hole in this region will enhance the magnetic field and may lead to a quench. Moreover, it would also enhance the electric field in the cell wall, which can give rise to field emission if it is present near the iris.

In this section, the overall design process to obtain a coupler with a Q_e sufficient to satisfy the ILC project is discussed. Only the cold section of the coupler, the antenna and the size of the coupler, are studied in this context. Design of the window, the tuning mechanism and others issues associated with the warm section are excluded.

9.1.1 Optimal Coupling for a Beam-Loaded Cavity

Considering a beam-loaded cavity operating on resonance, the reflected power is obtained by invoking the conservation of energy from the generator power (P_g), transferring it to the beam (P_b) and dissipating it into a cavity wall (P_c) [10]:

$$P_r = P_g - P_b - P_c$$
$$= P_g \left(\frac{\beta - 1 - 2K \sqrt{\beta}}{\beta + 1} \right)^2, \tag{9.1}$$

where

$$K = \frac{I_0}{2} \sqrt{\frac{R_a}{P_g}} \tag{9.2}$$

is the dimensionless beam loading parameter, which relates the power transferred to the beam to the power dissipated in the cavity. R_a is the shunt impedance and I_0 is the time-average beam current. $\beta = P_e/P_c = Q_0/Q_e$ is the coupling coefficient, which is the ratio of power dissipated in the cavity to that dissipated in the input source (P_e).

In the unloaded case, $K = 0$, and zero reflection is achieved for $\beta = 1$. In the presence of beam loading, and if most of the power is transferred to the beam rather than is dissipated in the cavity wall (i.e., $K \gg 1$), then zero reflection is achieved when $\beta = P_g/P_c = 1 + P_b/P_c$. This yields the relation for the external quality factor

$$Q_e = \frac{Q_0}{1 + P_b/P_c}. \tag{9.3}$$

For a heavy beam loading in an SRF cavity case ($P_b \gg P_c$), the external quality factor required for operation with zero reflection is:

$$Q_e = \frac{V_c^2}{P_b(R/Q_0)}. \tag{9.4}$$

For the ILC, the average Q_e is 3.5×10^6 as stated in Table 1.4.

In order to understand the coupling mechanism from the coaxial coupler to the main accelerating cavity it is helpful to consider the modes excited. The next section investigates the nature of the coupler based on Slater's pioneering work in this area.

9.1.2 Kroll-Yu Method to Determine External Quality Factor

One of the earliest analytical studies of the behaviour of a combined cavity and waveguide system was performed by Slater, using a terminating short plane at the waveguide end. The relation between

the line resonant frequency and the cavity resonant frequency of the structure was found to be [84]:

$$\tan\left(2\pi l_g/\lambda_g\right) = \sum \frac{1}{Q_e}\left(\frac{\omega}{\omega_r} - \frac{\omega_r}{\omega}\right), \tag{9.5}$$

where l_g is the length of waveguide, λ_g the guide wavelength, and ω_r the resonant frequency. The Q_e of the system can be obtained by a curve-fitting process with various coupling lengths l_g and corresponding frequency ω data. Due to the transcendental nature of the equation there is no convenient form suitable for a direct calculation of Q_e.

Kroll and Yu suggested an alternate method to evaluate Q_e directly from computer simulation data [85]. This approach is similar to Slater's method but is better suited to direct computation. The Kroll-Yu method studies the reflection coefficient $R(\omega)$ near the cavity resonant frequency to calculate the Q_e of a waveguide-loaded cavity. This method is described in Appendix C together with the validations on various coupling systems. My calculation procedure used in these validations gives consistent results to those obtained by Kroll and Lin [85, 86].

The Kroll-Yu method has been extended to the weak coupling system [87] (high Q_e) which is the case in an SRF cavity, where the results are strongly affected by the choice of the data points. However, choosing data points near a cavity resonance does give consistent results.

Validations on a simplified system provides confidence in the accuracy of the Kroll-Yu method. This is then applied to a single-cell from my NLSF cavity. In this simulation the coaxial coupler is located 45 mm away from the entrance of the cavity. The antenna tip is located at the same vertical level as the iris radius and is illustrated in Fig. 9.1. Both MWS and HFSS have been used in these simulations. The coupler length was varied and the eigenmodes were studied. The frequency versus position along the terminating places are illustrated in Fig. 9.2.
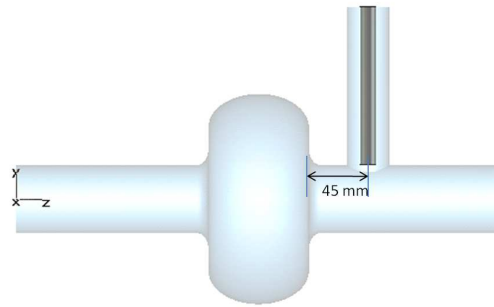
Figure 9.1: Single-cell cavity used in detailed finite element and finite difference e.m. simulations.
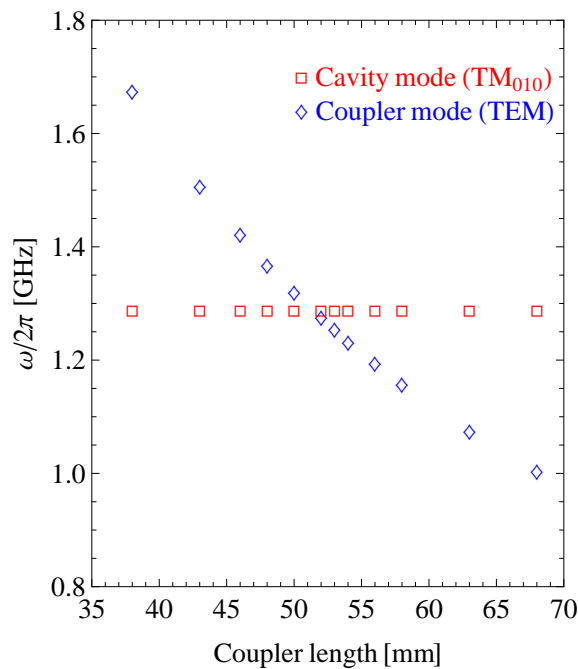
Figure 9.2: Mode frequencies versus the position of the terminating plane along the coupler.

The cavity frequency does not change whilst the coupler mode frequency changes when the position of the short varies. The fitted results are listed in Table 9.1. The results are however inconsistent between MWS and HFSS and have a large variation from the $Q_e \sim 4.7 \times 10^6$, calculated from a built-in module in MWS, on both solvers. They are strongly sensitive to the particular data sets chosen. This is because the avoided crossing region is very narrow and this gives a very sharp $\phi - \omega$

behaviour. This sharp corner makes the fitting process very sensitive.

Table 9.1: Comparison of fitted parameters using different data sets from two solver codes.

| No. | D [cm] | CST MWS results | | |
| | | $\omega/2\pi$ [GHz] | fitted parameters | |
			$\omega/2\pi$ [GHz]	Q_e [$\times 10^6$]
1	4.8, 5.3, 5.8	1.287 496 00, 1.287 492 55, 1.287 500 65	1.287 50	2.442
2	5.3, 5.4, 5.6, 5.8	1.287 492 55, 1.287 101 49, 1.287 409 81, 1.287 500 65	1.287 49	3.072
3	4.3, 4.8, 5.3, 5.8	1.287 658 64, 1.287 496 00, 1.287 492 55, 1.287 500 65	1.287 50	2.222
4	4.8, 5.0, 5.2, 5.4	1.287 496 00, 1.287 451 45, 1.287 131 30, 1.287 101 49	1.287 25	0.038
No.	D [cm]	Ansoft HFSS results		
		$\omega/2\pi$ [GHz]	fitted parameters	
			$\omega/2\pi$ [GHz]	Q_e [$\times 10^6$]
1	4.8, 5.3, 5.8	1.289 010 71, 1.289 022 33, 1.289 022 04	1.289 02	9.011
2	5.3, 5.4, 5.6, 5.8	1.289 022 33, 1.289 013 34, 1.289 023 67, 1.289 022 04	1.289 02	67.115
3	4.3, 4.8, 5.3, 5.8	1.289 041 48, 1.289 010 71, 1.289 022 33, 1.289 022 04	1.289 02	5.327
4	4.8, 5.0, 5.2, 5.4	1.289 010 71, 1.288 996 53, 1.289 028 88, 1.289 013 34	1.289 01	6.151

The Kroll-Yu method is accurate and straightforward to apply for sufficiently low external Q systems. However, It is difficult to reliably obtain the Q_e of weakly coupled cavities. Another method to compute the external Q, which overcomes these limitations, is discussed in the next section.

9.1.3   Balleyguier Method to Determine External Quality Factor

In order to overcome the limitations of the Kroll-Yu method, another method is considered. The Balleyguier method [88, 89] allows the Q_e to be obtained from eigensolutions of a cavity-coupler system with closed boundaries. The method relies on two standing wave solutions in the coupler line. Each of these standing waves is obtained using two possible coupler termination boundary conditions. This allows the system to be described by the superposition of the two time-inverted travelling wave solutions of the open system, as illustrated in Fig. 9.3. The Q_e of the system is obtained from the sum of the Q_e from the two standing wave solutions, provided that the coupler line is sufficiently long such that an unperturbed field pattern persists in the terminating plane.
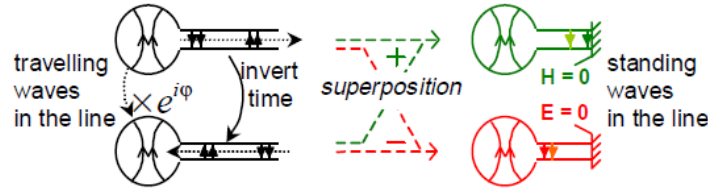
Figure 9.3: Superposition of two time-inverted travelling wave solutions of the open system results in the standing wave solutions of the closed system (adapted from [88]).

The method starts by considering a lossless cavity with some rf energy stored, U, at its resonant frequency, ω. If this cavity is weakly coupled to an infinite line, the cavity loses power, P, into this line. If only one mode is considered to travel along the line. P can be computed from either the electric or magnetic field amplitude by integrating over the line cross-section:

$$P = \frac{1}{2\eta} \iint |E|^2 dS \;=\; \frac{\eta}{2} \iint |H|^2 dS, \tag{9.6}$$

where $\eta = \sqrt{\mu_0/\epsilon_0}$ is the mode impedance for a TEM wave in vacuum. The stored energy U in the

cavity is the integral of the field amplitude over the cavity volume:

$$U = \frac{1}{2} \iiint \epsilon_0 |E|^2 dV = \frac{1}{2} \iiint \mu_0 |H|^2 dV.$$

(9.7)

From the definition of $Q_e = \omega U / P$, it can be expressed as

$$Q_e = \frac{\omega \iiint |F|^2 dV}{c \iint |F|^2 dS},$$

(9.8)

for the TEM mode in a line, which is assumed to be under vacuum, where F is either the electric or magnetic field. The line mode impedance, η, should be taken into account if the line is not under vacuum or if the mode is not TEM.

Inside the line, two travelling waves drive P in opposite directions, and they interfere to form a standing wave. Let us consider the terminating plane at an electric field maximum: the standing wave field amplitude is twice that of the individual travelling waves. The two fields inside the cavity have a phase difference, ϕ, so the amplitude of the resulting field is $\left| 1 + e^{j\phi} \right|$ larger than the original field. From eq. 9.8 we can define the quantity Q_1 as

$$Q_1 = \frac{\omega \iiint_{\text{cavity}} |E_1|^2 \, dV}{c \iint_{\text{ref. plane}} |E_1|^2 \, dS} = \frac{\left| 1 + e^{j\phi} \right|^2}{4} Q_e,$$

(9.9)

where the reference plane is the plane that has the standing wave field amplitude twice that of the travelling waves, with the perfect magnetic wall boundary condition at the terminating plane. This plane is the reference plane and computable by a suitable rf e.m. eigenmode code.

Let us consider the reference plane that has a magnetic field amplitude twice that of the travelling waves. The resulting field amplitude inside the cavity is now $\left| 1 - e^{j\phi} \right|$ times the original field and we

can define Q_2 as

$$Q_2 = \frac{\omega \iiint_{\text{cavity}} |H_2|^2 \, dV}{c \iint_{\text{ref. plane}} |H_2|^2 \, dS} = \frac{|1 - e^{j\phi}|^2}{4} Q_e. \tag{9.10}$$

A terminating plane with perfect electric wall boundary condition is considered as the reference plane in this case. The Q_e of this cavity-coupler system can be obtained from the sum of these two:

$$Q_e = Q_1 + Q_2. \tag{9.11}$$

This is independent of ϕ since: $|1 + e^{j\phi}|^2 + |1 - e^{j\phi}|^2 = 4$. Thus two rf solver runs are adequate to predict the external Q of the system. This method was developed for arbitrary coaxial lines with an assumption of only single mode TEM wave propagation along the line. The method has been extended to arbitrary rectangular waveguides by Shemelin *et. al* [90].

To validate this method, firstly, it is applied to a single-cell NLSF cavity equipped with a coaxial coupler as illustrated in Fig. 9.1. Two simulations have been carried out with different terminating plane boundary conditions in both MWS and HFSS. Additionally, one eigensolution is conducted using MWS and with the external Q calculation module selected. These simulation results are compared in Table 9.2.

Table 9.2: Comparison of the external Q produced using two rf e.m. codes on a single cell NLSF cavity (in Fig. 9.1) using the Balleyguier method and a built-in module within MWS.

Parameter	HFSS(A)	MWS(B)	MWS (built-in)(C)	|A-B|/A [%]	|A-C|/A [%]
$Q_1[\times 10^6]$	3.28	3.38	-	3.0	-
$Q_2[\times 10^6]$	1.18	1.13	-	4.2	-
$Q_e[\times 10^6]$	4.46	4.51	4.66	1.1	4.5
$\omega/2\pi[\text{GHz}]$	1.289	1.287	1.287	-	-

There is reasonable agreement between the independent codes on the Q_es. Indeed, the maximum

discrepancy between the two is approximately 5%. In order to allow the simulations from the in-dependent codes to converge a large mesh was necessary. In HFSS 1.2×10^6 tetrahedra were used and 1.0×10^6 mesh cells in MWS. The method has also been applied to a full nine-cell NLSF cavity with a standard coaxial coupler located at the same distance as applied to the Kroll-Yu method. The full cavity is illustrated in Fig. 9.4. The mode frequency and Q_es which result from this analysis are displayed in Table 9.3. Here the maximum discrepancy is no more than $\sim 6\%$.
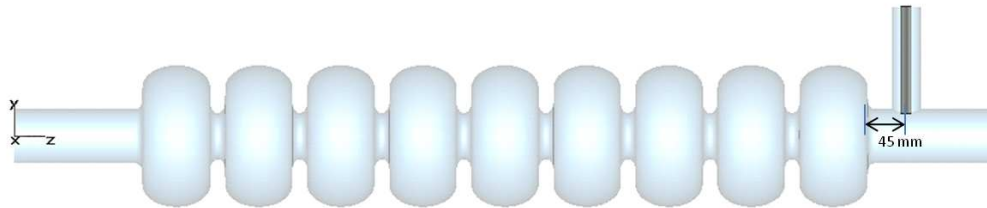
Figure 9.4: A nine-cell NLSF cavity with coaxial coupler placed 45 mm away from the cavity entrance and an antenna penetrating 6 mm into the beam pipe.

Table 9.3: Balleyguier external Q calculation from two rf solver codes and also a built-in module in MWS on a nine-cell NLSF cavity (in Fig. 9.4).

Parameter	HFSS(A)	MWS(B)	MWS (built-in)(C)	$|A\text{-}B|/A$ [%]	$|A\text{-}C|/A$ [%]
$Q_1[\times 10^6]$	2.95	2.76	-	6.4	-
$Q_2[\times 10^6]$	0.88	0.91	-	3.4	-
$Q_e[\times 10^6]$	3.83	3.86	3.77	0.8	1.6
$\omega/2\pi$[GHz]	1.300	1.296	1.296	-	-

Simulations made with MWS indicate a 4 MHz discrepancy with HFSS. This frequency difference is consistent with the accuracy of the simulations: 1.6×10^6 tetrahedra used with HFSS and 1.2×10^6 mesh cells used in MWS. The beam dynamics criterion specifies the cavity Q_e should be 3.5×10^6. Careful positioning of the coupler will allow this Q_e to be obtained. The penetration depth can be modified experimentally to obtain the requisite Q_e.

This coupler is non-optimal. Stronger coupling with a larger bandwidth can be obtained with other couplers. These are investigated in the next section.

9.1.4   FP Coupler for the NLSF Cavity

Various types of coaxial couplers are studied within this section with a view to optimising the coupling. The coupler is parameterised as indicated in Fig. 9.5.
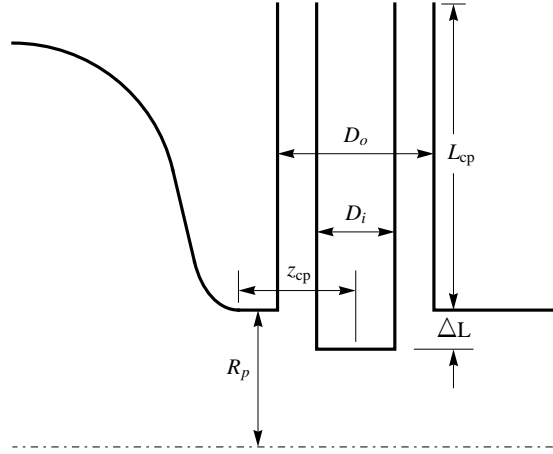
Figure 9.5: Schematic of the fundamental power coupler.

The main accelerating cavities for the ILC project are based on TESLA cavity with a TTF-III coupler [91]. In this study, for the NLSF cavity, the TTF-III coupler is investigated along with a series of other couplers. To begin with, a coaxial coupler equipped with an unmodified antenna tip is studied. This is illustrated in Fig. 9.6, where D_o = 40 mm, D_i = 15 mm, and L_{cp} = 180 mm. R_p is 38 mm. Varying the coupler position and penetration depth of the inner conductor allows a series of power couplings to be obtained. This coupler was modelled using MWS with the Q_e evaluated using the built-in module of the software.

front view

bottom view   side view
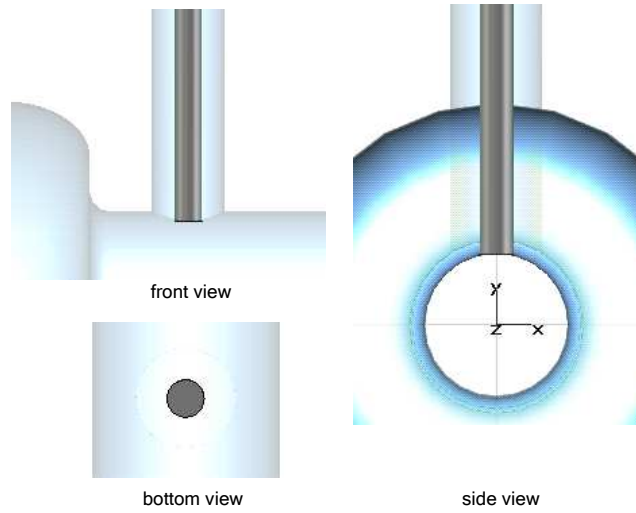
Figure 9.6: Sectional views of the coaxial power coupler.

Here z_{cp} is fixed at 45 mm to study the effect of the antenna penetration depth, ΔL, and its influence on the accelerating field flatness and Q_e. The results show that there is less perturbation to the accelerating field when ΔL is between 4 and 8 mm. The minimum perturbation is at 6 mm. The power coupling is very weak when the antenna is withdrawn into the coupler, $\Delta L < 0$. For a ΔL between 4 and 8 mm, Q_e is in the range of 3×10^6 to 6×10^6, which corresponds to the baseline range for the ILC.

In another simulation z_{cp} is varied while ΔL is held at a fixed value (at the lowest perturbation point of 6 mm). The accelerating field is affected slightly when the coupler position is close to the cavity entrance. This effect is very slight compared to that which occurs when the antenna penetration is varied. Choosing z_{cp} between 40 and 50 mm allows acceptable Q_es to be obtained, illustrated in Fig. 9.7.

In addition, the influence of a modified antenna tip was also studied. A 5 mm thick circular disc with a diameter of 18 mm was attached to the coaxial antenna. This is indicated in Fig. 9.8. Simulations carried out with this coupler on the NLSF cavity with a fixed antenna penetration of 6 mm, in order
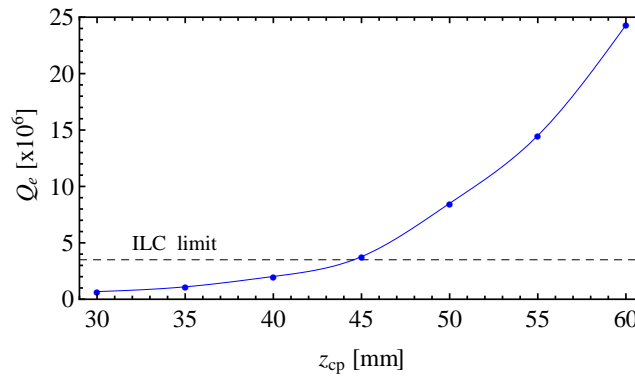
Figure 9.7: Q_e versus coupler position for a simple coaxial power coupler, where the blue dots are simulation results and the ILC requirement is indicated by a dashed line.

to ensure the perturbation on the accelerating field is minimised. This new design results in an enhanced coupling. This is because the antenna tip enhances the electric field in the vicinity of the tip and it facilitates a strong coupling to the accelerating field. A summary of simulations on Q_e versus penetration depth is presented in Fig. 9.9.
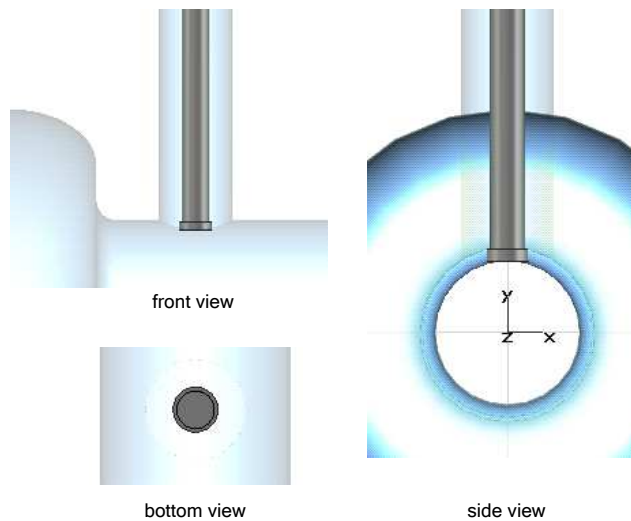
Figure 9.8: Sectional views of the disc-type power coupler.

The third design considered is based on the input coupler used for the ERL injector cavity at Cornell [92]. This design has a 5 mm-thick, curved rectangular plate with 20×20 mm size attached to
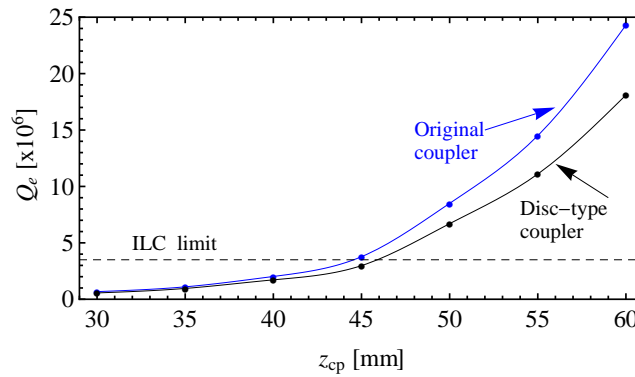
Figure 9.9: Q_e versus coupler position comparison between a simple coaxial coupler (blue dots) and a disc-type coupler (black dots), where the ILC requirement is indicated by a dashed line.

an antenna tip. The D_i and D_o are 12.5 mm and 40 mm, respectively. Various sectional views of this coupler are illustrated in Fig. 9.10. The large tip allows an enhancement in the electric field. Simulations have been carried out with various coupler positions at a fixed penetration depth of 6 mm. The results of these simulations are displayed in Fig. 9.11. The Q_e of this design is similar to a disc-type design. A slightly more complex fabrication process is involved however, compared to that of a disc-type coupler.
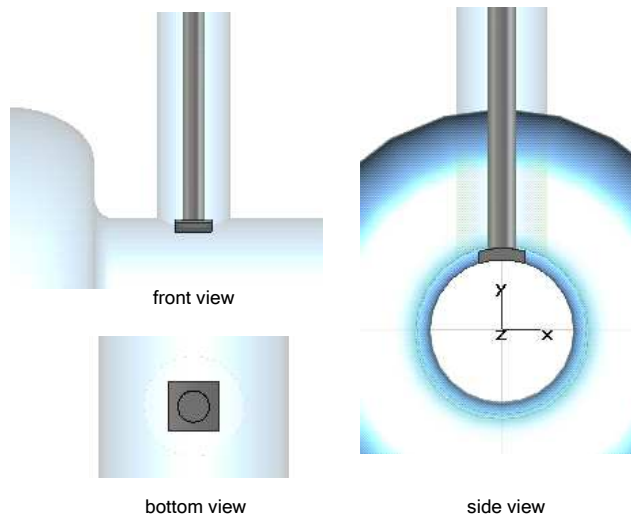
Figure 9.10: Sectional views of the "curve-type" coupler.
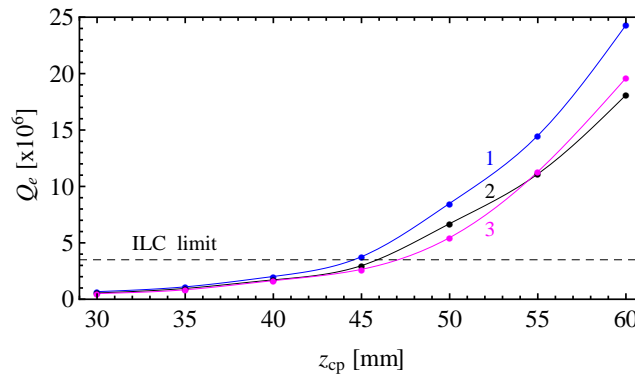
Figure 9.11: Q_e versus coupler position comparison between a curve-type coupler (3-indicted by magenta dots) and the first two designs: a disc-type coupler (2-indicated by black dots), and a simple coaxial coupler (1-indicated by blue dots), where the ILC requirement is indicated by a dashed line.

Finally, the TTF-III baseline coupler was modelled and simulated with the nine-cell NLSF cavity to validate the power coupling of the coupled system. This coupler has an D_i of approximately 12.5 mm and the tip is rounded, as the cut views illustrate in Fig. 9.12. Simulations have been carried out
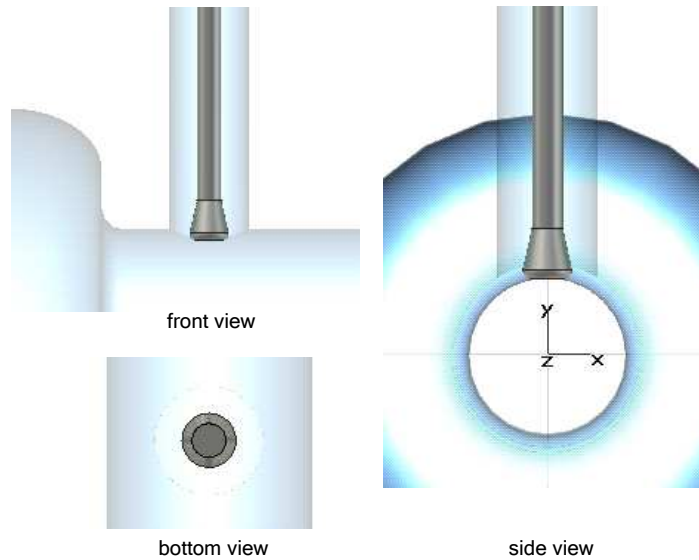
Figure 9.12: Sectional views of the TTF-III coupler.

at a fixed ΔL of 6 mm to maintain the perturbation effect. The coupler position was varied. The Q_e results of this coupler, illustrated in Fig. 9.13, have a similar behaviour to a simple coaxial coupler.

In fact, this coupler has mixed properties of both a simple coaxial type and a disc-type. It has a smaller tip area compared to a disc-type antenna, and thus reduces the coupling. The shape of the TTF-III coupler has been designed with a view to reducing multipacting within the coupler.
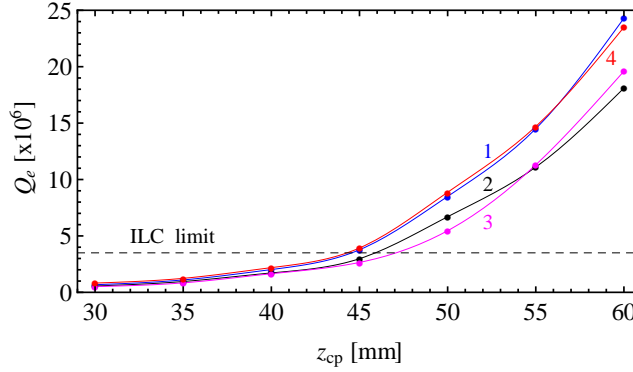
Figure 9.13: Q_e versus coupler position for various designs: a simple coaxial coupler (1-indicated by blue dots), a disc-type coupler (2-indicated by black dots), a curve-type coupler (3-indicated by magenta dots), and a TTF-III coupler (4-indicated by red dots), where the ILC requirement is indicated by a dashed line.

Simulations show that this TTF-III coupler, used as the baseline power coupler for the ILC, is also a candidate for a power coupler for my NLSF cavity. The coupler for the ILC is situated 45 mm away from the cavity entrance and has an antenna penetration depth of 6 mm. This ensures a Q_e of 3.5×10^6 is achieved. This configuration also minimises the perturbation on the accelerating field. Other designs may enhance the multipacting in this region and hence are less favoured.

Another important issue is that of suppressing the higher order modes excited by the beam. The design of a suitable HOM coupler for my NLSF cavity is the subject of the next section.

9.2   HOM Coupler for the NLSF Cavity

If left undamped, beam-excited HOMs can dilute the emittance of the beam and can also cause a BBU instability to occur. In practise the HOMs are damped down to a level prescribed by beam dynamics simulations. Here, the TESLA-style TTF-III coupler is attached to my NLSF nine-cell cavity and the damping properties are investigated.
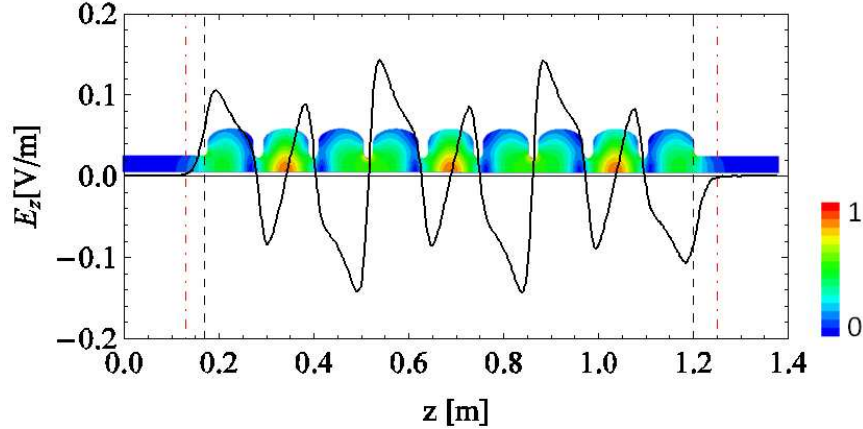
Figure 9.14: Electric field of 1.740 GHz HOM taken at 15 mm offset from a cavity axis. HOM coupler positions are indicated by red dot-dashed lines, whilst black dashed lines represent the cavity entrance and exit.

Prior to designing the couplers the distribution of the modes for the first three highest R/Qs is investigated. These three modes have significantly larger R/Qs than the other modes. These are located at 1.740 GHz, 1.913 GHz, and 2.462 GHz. The corresponding R/Qs are 10.89, 15.95, and 22.68 Ω/cm^2 respectively. These modes are illustrated in Fig. 9.14 through 9.16. It is evident that very small fields exist in the regions of the couplers and hence a careful design is needed which maximises the coupling.

In order to obtain rapid results only one and a half cells are retained from the nine-cell cavity. The inherently 3D nature of the problem necessitates a large mesh density. Hence even this reduced ge-
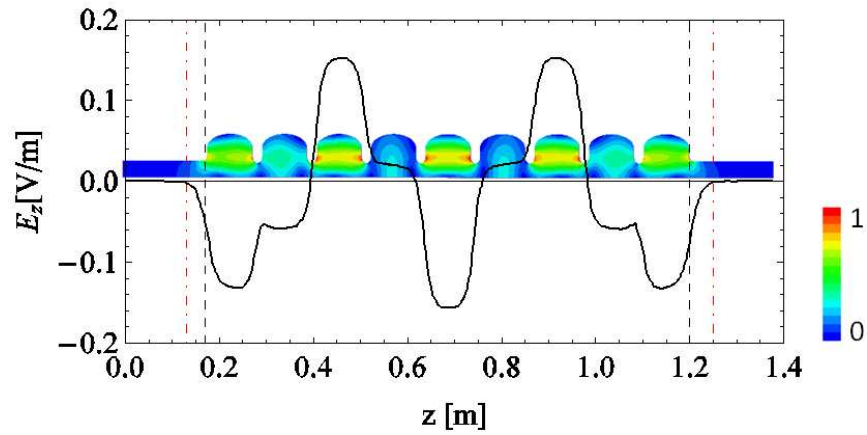
Figure 9.15: Electric field of 1.913 GHz HOM taken at 15 mm offset from a cavity axis. HOM coupler positions are indicated by red dot-dashed lines, whilst black dashed lines represent the cavity entrance and exit.

ometry requires significant computational resources to allow adequate modelling of the e.m. fields.
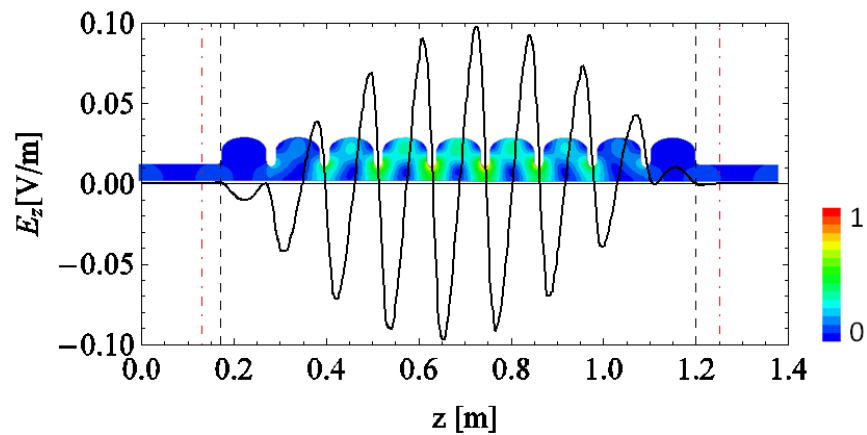
Figure 9.16: Electric field of 2.462 GHz HOM taken at 15 mm offset from a cavity axis. HOM coupler positions are indicated by red dot-dashed lines, whilst black dashed lines represent the cavity entrance and exit.

The HOM couplers are similar to those presented in [93–95], illustrated in Fig. 9.17. It is important to note that this configuration does not interfere with the accelerating mode (no field is coupled between the cavity and a HOM coupler). This is illustrated in Fig. 9.18. The simulations provide

evidence of HOM field coupling in all three dipole bands. This is illustrated in Fig. 9.19. However, in order to obtain the practical cavity Q_e a full nine-cell geometry is needed for modelling. This requires large computational resources.
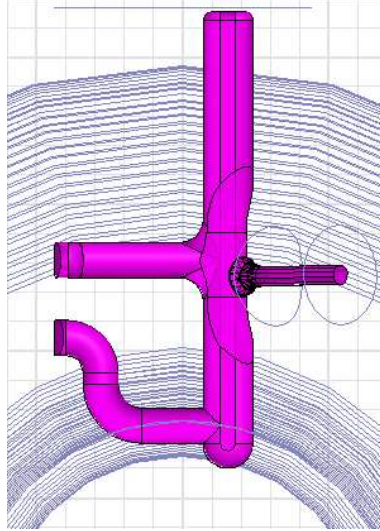
Figure 9.17: HOM coupler antenna simulation model.
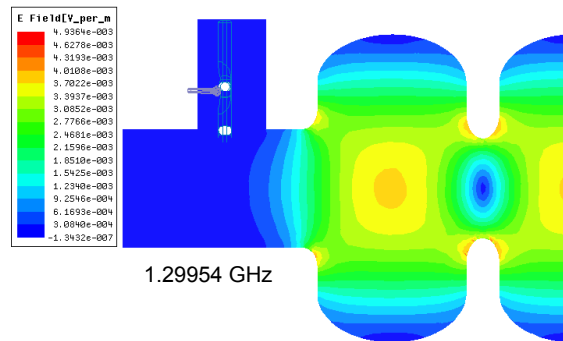
Figure 9.18: Accelerating mode field in presence of HOM coupler.

The HOM couplers were placed at 115 degrees with respect to each other, as indicated in Fig. 9.20. Simulations were performed to obtain the Q_es of the first three dipole bands using both MWS and HFSS. Q_es are obtained and displayed in Fig. 9.21 using the built-in module in MWS and using the
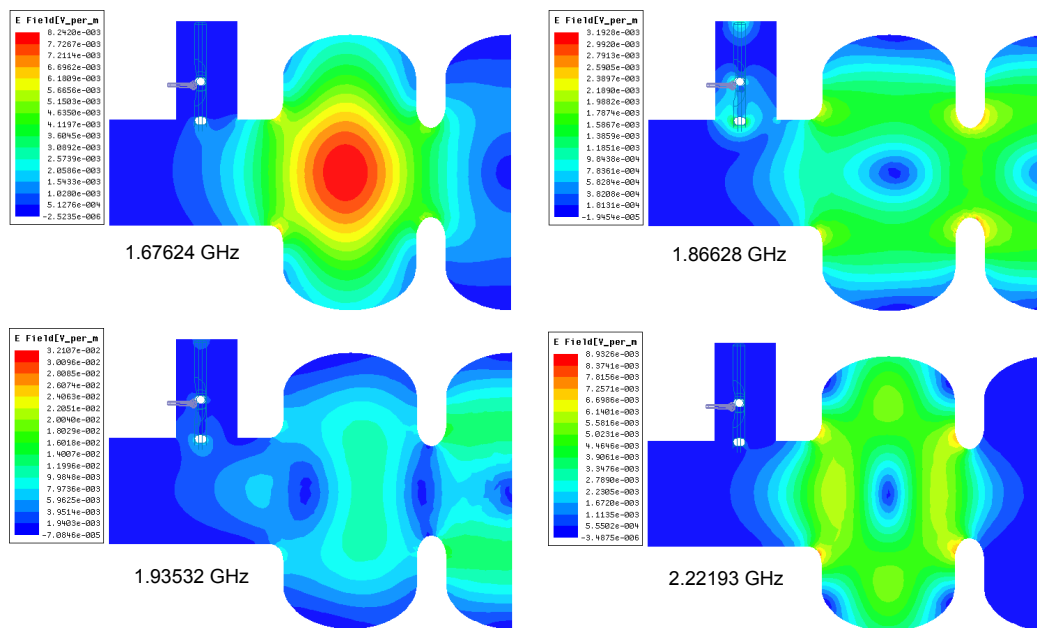
Figure 9.19: Electric field coupling in the vicinity of HOM coupler of the lower three dipole bands.
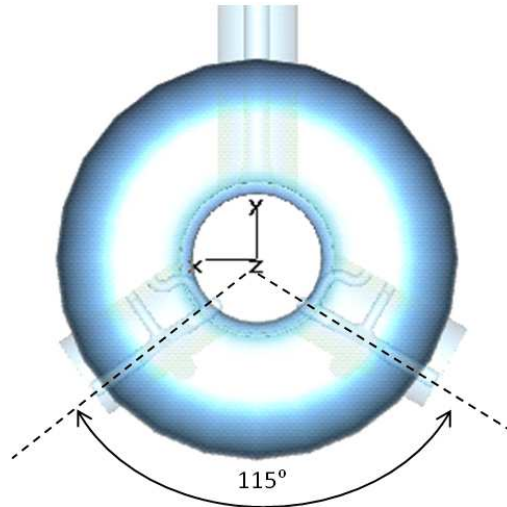
Figure 9.20: Couplers configuration in the NLSF cavity.
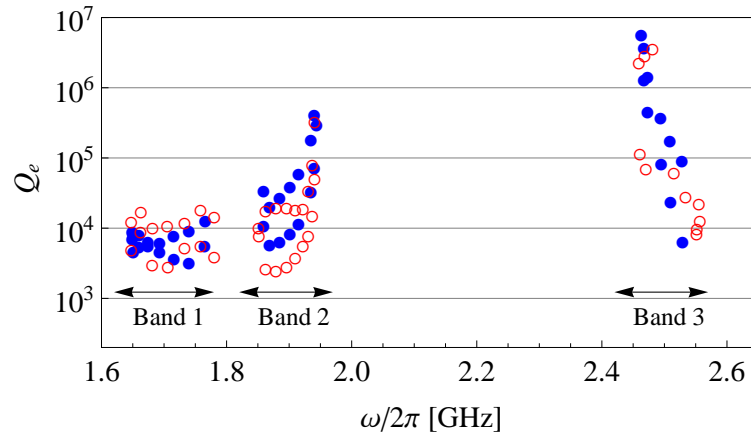
Figure 9.21: HOM damping Qs results calculated using HFSS (blue dots) and MWS (red circles).

Balleyguier method in HFSS. In the HFSS simulations 2×10^6 tetrahedra were used and 1.6×10^6 mesh cells in MWS. The majority of the Q_es of these modes are located in the range 10^3 - 10^6. However, some are above the beam dynamics imposed value of 10^6. These will not satisfy the ILC requirements [20].
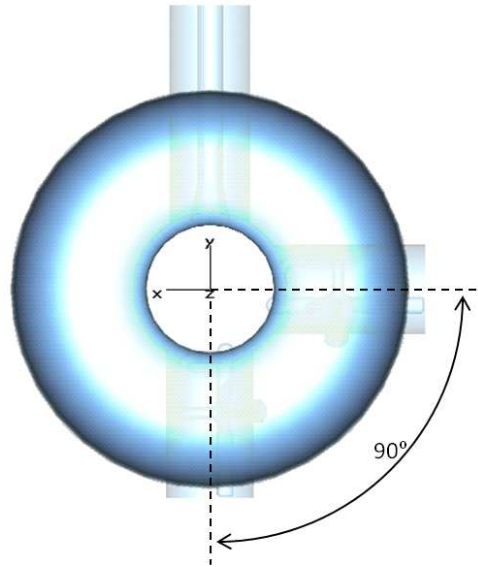
Figure 9.22: Improved HOMs damping couplers configuration in the NLSF cavity.

A new configuration of HOM couplers has been investigated to improve the HOM damping. These HOM couplers were placed at 90 degrees with respect to each other. This is illustrated in Fig 9.22. Simulations were performed using HFSS and a similar analysis has been performed to obtain the Q_e. The modes are well-damped in this configuration as the Q_es of the first six dipole bands are below 10^6. This is illustrated in Fig 9.23. The couplers in this orientation are better targeted to couple to the e.m. fields.
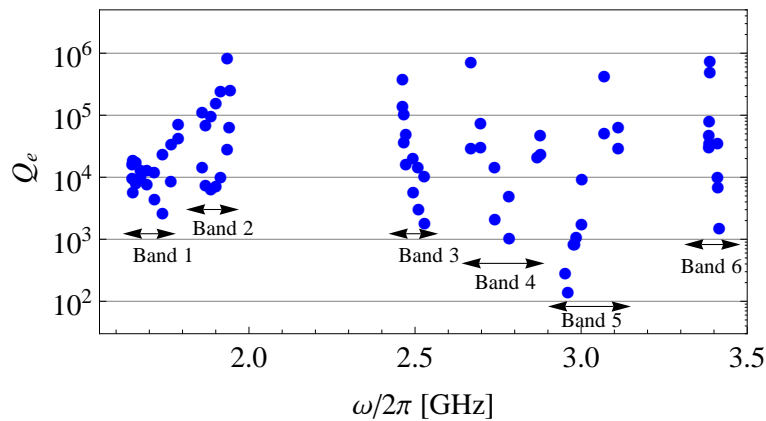
Figure 9.23: HOM damping Qs results of new HOM couplers configuration calculated using HFSS.

This new configuration has the potential to be utilised in my NLSF cavity. Additional details on a study of the FP and HOM couplers are provided elsewhere [96]. However, to ensure the beam quality is preserved during acceleration a detailed investigation of HOMs damping effects is needed. This is a potential subject for future beam dynamics studies.

Chapter 10

Discussion and Conclusion

The ILC project is based on a superconducting linear accelerator. The present baseline design prescribes a working accelerating gradient of 31.5 MV/m. Each cavity is qualified to work at 35MV/m. My initial work was concerned with understanding the behaviour of the baseline ILC cavity design, the TESLA cavity, and the methodology of rf simulation and an equivalent circuit representation. I then focussed on searching for an alternative cavity design which can handle a higher working accelerating gradient. I have presented here, my new cavity design, the New Low Surface Field (NLSF) cavity, which has optimally low surface e.m. fields. The bandwidth of the accelerating mode has also been maximised, constrained by HOM excitation.

A complete nine-cell design of my NLSF cavity has the potential to achieve an accelerating gradient of 47 MV/m, with the maximum surface magnetic field 180 mT and surface electric field 99 MV/m. With this low surface electric field, the risk from electron field emission is diminished. The NLSF cavity has a 9% larger R/Q compared to that of the TESLA cavity. This allows for increased efficiency.

The manufacture of an NLSF cavity is not expected to present problems. Similar fabrication pro-

cesses used for the TESLA shape can also be employed on the NLSF cavity.

The fundamental mode and higher order modes have been represented with a circuit model. This allows a rapid determination of the influence of fabrication errors.

A complete design for my NLSF cavity, including the fundamental power coupler and HOM couplers has been presented. The input power coupler is based on the TTF-III type coupler. This configuration meets the required Q_e of the ILC at 3.5×10^6. Furthermore, the baseline TESLA HOM coupler design is used for the NLSF cavity to damp the HOMs. An accurate calculation of the Q_es of the HOM couplers is obtained through a complete nine-cell cavity. The results of these simulations indicate that the Q_es lay in the range 10^3 to 10^6. These are sufficiently well damped to satisfy the ILC requirements. Other configurations of the HOM couplers are a potential subject for further study as it may allow for improved HOM suppression.

Collective effects, resulting from geometric short-range wakefields of the NLSF cavity have been studied from both numerical simulations and analytical models. The analytical formulae provide estimates of both longitudinal and transverse wakefields. This is useful for designing cavities and linacs with limited time and computing resources. In particular, the Bane formulae allow the short-range wakefields of the NLSF cavity to be computed.

The NLSF cavity has been designed to potentially work at a higher accelerating gradient. The cavity is proposed as an alternative design for the ILC project, since the community has been searching for a way to reduce the overall cost of the ILC. However, the NLSF cavity can also be utilised in other superconducting accelerators such as the energy recovery linac, and the free electron laser linac. In practise, there are other factors to limit the gradient of a cavity such as the material properties, the

cell fabrication process, the surface treatment used and cleaning, and also the cleanliness of the work place environment. All of these need to be taken into account and carefully controlled.

This completes a study of the rf properties of a new cavity for the ILC. There exists the opportunity for further work on a beam dynamics study in particular, and on an analysis of the engineering tolerances.

Bibliography

[1] S.Y. Lee, *Accelerator Physics*, 2nd ed. World Scientific, 2004.

[2] "LEP Design Report. Vol I and II," CERN-LEP-TH-83-29,1983.

[3] "LEP Design Report. Vol III," CERN-AC/96-01 (LEP2),1996.

[4] M. Tigner, "CESR-An electron Positron Colliding Beam Facility at Cornell," *IEEE Trans. Nucl. Sci.*, vol. 24, pp. 1849–1853, 1977.

[5] D. J. Holder, N. G. Wyles, and P. D. Quinn, "The SRS at Daresbury Laboratory: a Eulogy to the World's First Dedicated High-energy Synchrotron Radiation Source," in *the Proceedings of 11th European Particle Accelerator Conference (EPAC08)*, Genoa, Italy, June 2008.

[6] O. S. Bruning *et al.*, "LHC Design Report. Vol. I: The LHC Main Ring," CERN-2004-003-V-1.

[7] R. Brinkman *et al.*, "The TESLA technical design report," DESY-2001-33.

[8] "International linear collider reference design report," http://www.linearcollider.org/cms/?pid= 1000437, August 2007.

[9] T. O. Raubenheimer, "The Preservation of low emittance flat beams," in *the Proceedings of Particle Accelerator Conference (PAC 93)*, Washington, DC, May 1993.

[10] H. Padamsee, J. Knobloch, and T. Hays, *RF Superconductivity for Accelerators*, 2nd ed. Wiley-VCH, 2008.

[11] S. Dobert, "Status and Future Prospects of CLIC," CERN, Geneva, Tech. Rep. CERN-BE-2009-001. CLIC-Note-768, January 2009.

[12] "ITRP Recommendation," http://www.fnal.gov/directorate/icfa/ITRP_Report_Final.pdf, 2004.

[13] "A superconducting TESLA cavity image," http://www.interactions.org/imagebank/search_detail.php?image_no=DE0083.

[14] R. Geng, "Review of new shapes for higher gradients," *Physica C: Superconductivity*, vol. 441, no. 1-2, pp. 145 – 150, 2006, proceedings of the 12th International Workshop on RF Superconductivity. [Online]. Available: http://www.sciencedirect.com/science/article/B6TVJ-4JT3S57-7/2/45edde1e465c992ad689d331f12027c5

[15] T. Saeki, F. Furuta, Y. Higashi, T. Higo, S. Kazakov *et al.*, "Series test of high-gradient single-cell superconducting cavity for the establishment of KEK recipe," in *the Proceedings of 10th European Particle Accelerator Conference (EPAC 06)*, Edinburgh, Scotland, June 2006.

[16] R. Wanzenberg, "Monopole, dipole and quadrupole passbands of the TESLA 9- cell cavity," DESY-TESLA-2001-33.

[17] S. Belomestnykh, M. Liepe, H. Padamsee, V. Shemelin, and V. Veshcherevich, "High Average Power Fundamental Input Couplers for the Cornell University. ERL: Requirements, Design Challenges and First Ideas," ERL-02-8.

[18] A. Dhavale and K. Mittal, "Design of input coupler for the superconducting cavity," *Nuclear Instruments and Methods in Physics Research Section A: Accelerators, Spectrometers, Detectors and Associated Equipment*, vol. 604, no. 3, pp. 443 – 448, 2009.

[Online]. Available: http://www.sciencedirect.com/science/article/B6TJM-4W0SJVX-1/2/
0a2e71dfc4affa4cf2df0d90dff88875

[19] W. D. Moeller for the TESLA Collaboration, "High power coupler for the TESLA test facility,"
in *the Proceedings of 9th Workshop on RF Superconductivity*, Los Alamos National Lab, USA,
November 1999.

[20] J. Sekutowicz, *Multi-cell Superconducting Structures for High Energy e+-e- Colliders and
Free Electron Laser Linacs*. Publishing Office of Warsaw University of Technology, Poland,
2008.

[21] T. Weiland, "On the computation of resonant modes in cylindrically symmetric cavities," *Nu-
clear Instruments and Methods in Physics Research*, vol. 216, no. 3, pp. 329 – 348, 1983.

[22] P. B. Wilson, "Introduction to Wake Fields and Wake Potentials," *AIP Conf. Proc.*, vol. 184,
pp. 525–564, 1989.

[23] L. Palumbo, V. G. Vaccaro, and M. Zobov, "Wake fields and impedance," http://www.citebase.
org/abstract?id=oai:arXiv.org:physics/0309023, p. 95, 1995.

[24] E. U. Condon, "Forced oscillations in cavity resonators," *Journal of Applied Physics*, vol. 12,
no. 2, pp. 129–132, 1941. [Online]. Available: http://link.aip.org/link/?JAP/12/129/1

[25] W. K. H. Panofsky and W. Wenzel, "Some considerations concerning the transverse deflection
of charged particles in radiofrequency fields," *Rev. Sci. Instrum.*, vol. 27, p. 967, 1956.

[26] A. Chao, *Physics of Collective Beam Instabilities in High Energy Accelerators*. Wiley and
Sons, 1993.

[27] V. E. Balakin, A. V. Novokhatsky, and V. P. Smirnov, "VLEPP: TRANSVERSE BEAM DY-NAMICS," Batavia, Illinois, August 1983, pp. 119 – 120, the Proceedings of 12th International Conference on High-Energy Accelerators.

[28] K. Saito, "Fundamental RF Critical Field Overview," in *the Proceedings of Pushing the limits of RF superconductivity Workshop*, Argonne, USA, September 2004.

[29] J. R. Delayen and K. W. Shepard, "Tests of a superconducting rf quadrupole device," *Applied Physics Letters*, vol. 57, no. 5, pp. 514–516, 1990. [Online]. Available: http://link.aip.org/link/?APL/57/514/1

[30] J. Graber, C. Crawford, J. Kirchgessner, H. Padamsee, D. Rubin, and P. Schmueser, "Reduction of field emission in superconducting cavities with high power pulsed rf," *Nuclear Instruments and Methods in Physics Research Section A: Accelerators, Spectrometers, Detectors and Associated Equipment*, vol. 350, no. 3, pp. 572 – 581, 1994. [Online]. Available: http://www.sciencedirect.com/science/article/B6TJM-473FHWB-1X/2/dee60fab7405cac78bc30f8c0a77000e

[31] R. Geng, A. Seaman, V. Shemelin, and H. Padamsee, "World record accelerating gradient achieved in a superconducting niobium RF cavity," in *the Proceedings of Particle Accelerator Conference (PAC 05)*, Knoxville, Tennessee, May 2005.

[32] D. Moffat, T. Flynn, J. Kirchgessner, H. Padamsee, D. Rubin *et al.*, "Superconducting Niobium RF Cavities Designed to Attain High Surface Electric Fields," in *the Proceedings of 4th Workshop on RF Superconductivity*, KEK, Tsukuba, Japan, August 1989.

[33] V. D. Shemelin, "Optimized shape of cavity cells for apertures smaller than in TESLA geometry," in *the Proceedings of Particle Accelerator Conference (PAC 05)*, Knoxville, Tennessee, May 2005.

[34] J. Sekutowicz, P. Kneisel, G. Ciovati, and H. Wang, "Low Loss Cavity for the 12 GeV. CEBAF Upgrade," JLAB, Newport News,Virginia, Tech. Rep. TN-02-023, June 2002.

[35] J. Sekutowicz, L. Ge, K. Ko, L. Lee, Z. Li *et al.*, "Design of a low loss SRF cavity for the ILC," in *the Proceedings of Particle Accelerator Conference (PAC 05)*, Knoxville, Tennessee, May 2005.

[36] J. Sekutowicz, P. Kneisel, T. Higo, Y. Morozumi, K. Saito *et al.*, "Optimization of the Low Loss SRF Cavity for the ILC," in *the Proceedings of Particle Accelerator Conference (PAC07)*, Albuquerque, New Mexico, June 2007.

[37] Z. Li and C. Adolphsen, "A New SRF Cavity Shape with Minimized Surface Electric and Magnetic Fields for the ILC ," in *the Proceedings of 24th Linear Accelerator Conference (LINAC08)*, Victoria, Canada, October 2008.

[38] V. Shemelin, H. Padamsee, and R. L. Geng, "Optimal cells for tesla accelerating structure," *Nuclear Instruments and Methods in Physics Research Section A: Accelerators, Spectrometers, Detectors and Associated Equipment*, vol. 496, no. 1, pp. 1 – 7, 2003. [Online]. Available: http://www.sciencedirect.com/science/article/B6TJM-46XH6VT-2/2/ 1e6c76b218f479d92764d19ed1121660

[39] T. I. Smith, "Standing Wave Modes in a Superconducting Linear Accellerator," HEPL-437.

[40] T. Saeki, "Latest Results of High Gradient Cavities at KEK," in *Presentation given at the SMTF Collaboration Meeting, Fermilab, Battavia, IL, USA*, October 2005.

[41] T. Grimm and other, "New directions in superconducting radio frequency cavities for accelerators," *Applied Superconductivity, IEEE Transactions on*, vol. 15, no. 2, pp. 2393–2396, June 2005.

[42] M. Meidlinger, T. Grimm, and W. Hartung, "Design of Half-Reentrant SRF Cavities," in *the Proceedings of 12th International Conference on RF Superconductivity (SRF2005)*, New York, USA, July 2005.

[43] F. Furuta, K. Saito, and T. Konomi, "S0 Tight Loop Studies on Ichiro 9-Cell Cavities," in *the Proceedings of 14th International Conference on RF Superconductivity (SRF2009)*, Berlin, Germany, September 2009, THPPO082.

[44] N. Juntong, R. M. Jones, and I. R. R. Shinton, "SRF cavity geometry optimization for the ILC with minimized surface e.m. fields and superior bandwidth," in *the Proceedings of 23rd Particle Accelerator Conference (PAC09)*, Vancouver, Canada, May 2009.

[45] N. Juntong and R. M. Jones, "High-Gradient SRF Cavity with Minimized Surface E.M. Fields and Superior Bandwidth for The ILC," in *the Proceedings of 14th International Conference on RF Superconductivity (SRF2009)*, Berlin, Germany, September 2009.

[46] D. E. Nagle, E. A. Knapp, and B. C. Knapp, "Coupled Resonator Model for Standing Wave Accelerator Tanks," *Review of Scientific Instruments*, vol. 38, no. 11, pp. 1583–1587, 1967. [Online]. Available: http://link.aip.org/link/?RSI/38/1583/1

[47] S. O. Schriber, "Characteristics of full-cell terminated RF structures: Results of analogue studies," CERN-PS-2001-067.

[48] S. O. Schriber, "Analog analysis of pi-mode structures: Results and implications," *Phys. Rev. ST Accel. Beams*, vol. 4, p. 122001, 2001.

[49] K. L. Bane and R. L. Gluckstern, "The Transverse wake field of a detuned x band accelerator structure," *Part. Accel.*, vol. 42, pp. 123–169, 1993.

[50] M. McAshan and R. Wanzenberg, "RF design of a transverse mode cavity for kaon separation," FERMILAB-TM-2144.

[51] N. Juntong, R. M. Jones, I. R. R. Shinton, C. Beard, and G. Burt, "RF Coupler Kicks and Wake-fields in SC Accelerating Cavities," in *the Proceedings of 11th European Particle Accelerator Conference (EPAC08)*, Genoa, Italy, June 2008.

[52] B. Szczesny, I. R. R. Shinton, and R. M. Jones, "Third Harmonic Cavity Modal Analysis," in *the Proceedings of 14th International Conference on RF Superconductivity (SRF2009)*, Berlin, Germany, September 2009.

[53] N. Juntong and R. M. Jones, "High Gradient Superconducting Cavity with Low Surface EM Fields and Well-Suppressed HOMS for the ILC," in *the Proceedings of 1st International Particle Accelerator Conference (IPAC10)*, Kyoto, Japan, May 2010.

[54] "ANSOFT HFSS, 3D Full-wave Electromagnetic Field Simulation," http://www.ansoft.com/products/hf/hfss/.

[55] "Wolfram Mathematica," http://www.wolfram.com/products/mathematica.

[56] K. Halbach and R. F. Holsinger, "Superfish-a Computer Program for Evaluation of RF Cavities with Cylindrical Symmetry," *Part. Accel.*, vol. 7, pp. 213–222, 1976.

[57] M. Dohlus and V. Kaljuzhny, "Relative Nonuniformity in the Amplitude of the Accelerating Field Along the M x N-cell TESLA Supercavities," TESLA-1998-26.

[58] K. L. Bane and M. Sands, "WAKE FIELDS OF VERY SHORT BUNCHES IN AN ACCEL-ERATING CAVITY," *Part. Accel.*, vol. 25, p. 73, 1990.

[59] K. L. F. Bane, "Short range dipole wakefields in accelerating structures for the NLC," SLAC-PUB-9663.

[60] T. P. Wangler, *Principles of RF Linear Accelerators*, 1st ed.   John Wiley and Sons, 1998.

[61] T. Weiland, "Transverse Beam Cavity Interaction. Part 1. Short Range Forces," DESY 82-015.

[62] T. Weiland, "Transverse beam cavity interaction. part i: Short range forces," *Nuclear Instruments and Methods in Physics Research*, vol. 212, no. 1-3, pp. 13 – 21, 1983. [Online]. Available: http://www.sciencedirect.com/science/article/B73DP-46YSR0B-Y/2/ 4b9f46e96445f43dfc4d82e12dd35902

[63] T. Weiland, "Transverse Beam Cavity Interaction Part. 2. Long Range Forces (On The Computation Of Resonant Modes In Cylindrically Symmetric Cavities)," DESY 83-005.

[64] Y. H. Chin, "User's guide for new ABCI version 6.1 (azimuthal beam cavity interaction)," CERN-SL-92-49-AP.

[65] Y. Shobuda, Y. H. Chin, and K. Takata, "ABCI Progresses and Plans: Parallel Computing and Transverse Napoly Shobuda Integral," in *the Proceedings of 22nd Particle Accelerator Conference (PAC07)*, Albuquerque, New Mexico, June 2007.

[66] T. Weiland, "A discretization model for the solution of Maxwell's equations for six-component fields," *Archiv Elektronik und Uebertragungstechnik*, vol. 31, pp. 116–120, Mar. 1977.

[67] K. S. Yee, "Numerical solution of initial boundary value problems involving maxwell's equations in isotropic media," *Antennas and Propagation, IEEE Transactions on*, vol. 14, no. 3, pp. 302 –307, May 1966.

[68] O. Napoly, Y. H. Chin, and B. Zotter, "A generalized method for calculating wake potentials," *Nuclear Instruments and Methods in Physics Research Section A: Accelerators, Spectrometers, Detectors and Associated Equipment*, vol. 334, no. 2-3, pp. 255 – 265, 1993. [Online]. Available: http://www.sciencedirect.com/science/article/B6TJM-472T1VV-DM/2/ 47cc12485ea199dcc8332a1e5f918d6b

[69] I. Zagorodnov and T. Weiland, "TE/TM field solver for particle beam simulations without numerical Cherenkov radiation," *Phys. Rev. ST Accel. Beams*, vol. 8, p. 042001, 2005.

[70] I. Zagorodnov, "Indirect methods for wake potential integration," *Phys. Rev. ST Accel. Beams*, vol. 9, p. 102002, 2006.

[71] I. Zagorodnov and T. Weiland, "The Short Range Transverse Wakefields in TESLA Accelerating Structure," in *the Proceedings of Particle Accelerator Conference (PAC 03)*, Portland, Oregon, May 2003.

[72] I. Zagorodnov, T. Weiland, and M. Dohlus, "Wake fields generated by the LOLA-IV structure and the 3rd harmonic section in TTF-II," DESY-TESLA-2004-01.

[73] I. Zagorodnov, M. Dohlus, and T. Weiland, "Wakefield Calculations for TTF-II," in *the Proceedings of the 9th European Particle Accelerator Conference (EPAC 2004)*, Lucerne, Switzerland, July 2004.

[74] I. Zagorodnov and N. Solyak, "Wakefields effects of new ILC cavity shapes," in *the Proceedings of European Particle Accelerator Conference (EPAC 06)*, Edinburgh, Scotland, June 2006.

[75] R. Zennaro, "Study of the Validity of K. Bane's Formulae for the CLIC Accelerating Structure," in *the Proceedings of 11th European Particle Accelerator Conference (EPAC08)*, Genoa, Italy, June 2008.

[76] J. D. Lawson, "Radiation from a ring charge passing through a resonator," *Part. Accel.*, vol. 25, pp. 107–112, 1990, Originally issued at Rutherford High Energy Laboratory, Report No. RHEL/M 144, 1968.

[77] G. Dome, "Wake Potentials of a Relativistic Point Charge Crossing a Beam Pipe Gap: An Analytical Approximation," *IEEE Trans. Nucl. Sci.*, vol. 32, pp. 2531–2534, 1985.

[78] S. A. Heifets and S. A. Kheifets, "High Frequency Limit Of The Longitudinal Impedance," *Part. Accel.*, vol. 25, p. 61, 1990.

[79] R. L. Gluckstern, "High Frequency Behavior Of The Longitudinal Impedance For A Cavity Of General Shape," *Phys. Rev.*, vol. D39, pp. 2773–2779, 1989.

[80] R. L. Gluckstern, "Longitudinal Impedance Of A Periodic Structure At High Frequency," *Phys. Rev.*, vol. D39, pp. 2780–2783, 1989.

[81] K. Yokoya and K. L. F. Bane, "The longitudinal high-frequency impedance of a periodic accelerating structure," in *the Proceedings of IEEE Particle Accelerator Conference (PAC 99)*, New York, March 1999.

[82] A. V. Fedotov, R. L. Gluckstern, and M. Venturini, "Transverse impedance of a periodic array of cavities," *Phys. Rev. ST Accel. Beams*, vol. 2, no. 6, p. 064401, Jun 1999.

[83] K. L. F. Bane, A. Mosnier, A. Novokhatsky, and K. Yokoya, "Calculations of the short-range longitudinal wakefields in the NLC linac," SLAC-PUB-7862, Talk given at 6th European Particle Accelerator Conference (EPAC 98), Stockholm, Sweden, 22-26 Jun 1998 and at ICAP '98, Monterey, California, 14-18 Sep 1998.

[84] J. C. Slater, *Microwave electronics*, ser. Bell Telephone Laboratories series.   Van Nostrand, 1950.

[85] N. M. Kroll and D. U. L. Yu, "Computer Determination of the External Q and Resonant Frequency of Waveguide Loaded Cavities," *Part. Accel.*, vol. 34, pp. 231–250, 1990, SLAC-PUB-5171.

[86] X. Lin, "Transverse wake field of waveguide damped structures and beam dynamics," Ph.D. dissertation, University of California, San Diego, 1995.

[87] A. S. Dhavale and K. C. Mittal, "Evaluation of external Q of the superconducting cavity using Kroll-Yu method," *Review of Scientific Instruments*, vol. 77, no. 6, p. 066101, 2006. [Online]. Available: http://link.aip.org/link/?RSI/77/066101/1

[88] P. Balleyguier, "External Q Studies for APT SC-Cavity Couplers," in *the Proceedings of 19th Linear Accelerator Conference (LINAC98)*, Chicago, IL, August 1998.

[89] P. Balleyguier, "A straightforward method for cavity external Q computation," *Part. Accel.*, vol. 57, pp. 113–127, 1997.

[90] V. Shemelin and S. Belomestnykh, "Calculation of the B-Cell Cavity External Q with MAFIA and Microwave Studio," SRF-020620-03.

[91] T. Gravey, "The TTF-III Power Coupler," in *Presentation given at the first ILC Workshop, KEK, Japan*, November 2004.

[92] V. Veshcherevich *et al.*, "Input Coupler for ERL Injector Cavities," in *the Proceedings of Particle Accelerator Conference (PAC 03)*, Portland, Oregon, May 2003.

[93] C. Ng, R. M. Jones, K. Bane, and N. Solyak, Eds., *Wake Fest 07 - ILC Wakefield Workshop at SLAC*, 2007.

[94] V. Yakovlev, private communications, March 2008.

[95] Z. Rihua and T. Zhao, private communications, March 2010.

[96] N. Juntong and R. M. Jones, "HOM and FP Coupler Design for the NLSF High Gradient SC Cavity," to be submitted to the 2nd International Particle Accelerator Conference (IPAC11), Kursaal, San Sebastian, Spain, September, 2011.

[97] N. Marcuvitz, *Waveguide Handbook*.   P. Peregrinus on behalf of the Institution of Electrical Engineers, London, UK :, 1986.

Appendix A

Frequency Scaling of Cavity Parameters

Using Maxwell's equations it is possible to show that for alternating fields, $\mathbf{E} = \mathbf{E}_0 e^{i\omega t}$ with $\mathbf{j} = \sigma \mathbf{E}$ and for a good conductor ($\omega \epsilon \ll \sigma$):

$$\nabla^2 \mathbf{E} = \tau_n^2 \mathbf{E} \tag{A.1}$$

with $\tau_n = \sqrt{i\omega\sigma\mu_0}$. Similar equations can be ontained for current $\mathbf{j}$ and magnetic field $\mathbf{H}$. For example, considering a plane of conductor in x, assume that the electric field is in the z direction and that there are no variations with y or z. A solution for E_z field is

$$E_z = E_0 e^{-\tau_n x} \tag{A.2}$$

which can be written as

$$E_z = E_0 e^{-x/\delta} e^{-ix/\delta} \tag{A.3}$$

where δ is ac penetration thickness or skin depth

$$\delta = \sqrt{\frac{2}{\omega\mu_0\sigma}} \propto \omega^{-1/2} \tag{A.4}$$

With similar treatment, the ac current density and magnetic field are given by

$$j_z = j_0 e^{-\tau_n x}, H_y = H_0 e^{-\tau_n x} \tag{A.5}$$

The total current is obtained from the integration

$$I = \int_0^\infty j_z(x) dx = \int_0^\infty j_0 e^{-\tau_n x} dx = \frac{j_0}{\tau_n} \tag{A.6}$$

Using the relation $j_0 = \sigma E_0$, we get the surface impedance

$$Z_s = \frac{E_0}{I} = \frac{E_0}{j_0/\tau_n} = \frac{\tau_n}{\sigma} = \sqrt{\frac{i\omega\mu_0}{\sigma}} \tag{A.7}$$

The impedance has an imaginary part because the surface field is not in phase with the total current in the conductor, due to the rate of change of magnetic flux in the conductor. The microwave surface resistance of a conductor is

$$R_s = \sqrt{\frac{\omega\mu_0}{2\delta}} = \frac{1}{\delta\sigma} \propto \omega^{1/2} \tag{A.8}$$

In superconductor [10] there are two components of the current: the normal component and the super-current component. The total current is the sum of the two components. The normal component of the current is $j_n = \sigma_n E$ where

$$\sigma_n = \frac{n_n q^2 \tau}{m} \tag{A.9}$$

here n_n is the number of unpaired electrons and τ is the relaxation time. For the super-current component we get $j_s = -i\sigma_s E$ where

$$\sigma_s = \frac{n_s q^2 \tau}{m\omega} \tag{A.10}$$

The total two fluid current becomes

$$j = j_n + j_s = (\sigma_n - i\sigma_s)E \tag{A.11}$$

In analogy with the treatment for the normal conductor we can show that

$$\nabla^2 \mathbf{E} = \tau_{tot}^2 \mathbf{E} \tag{A.12}$$

with $\tau_{tot} = \sqrt{i\mu_0\omega(\sigma_n - i\sigma_s)}$. Similar to the normal conductor, the surface impedance of a supercon-ductor is given by

$$Z_s = \sqrt{\frac{i\omega\mu_0}{\sigma_n - i\sigma_s}} = R_s + iX_s \tag{A.13}$$

At temperature lower than the transition temperature ($T \ll T_c$) the n_n is very much smaller then the n_s and for the normal conducting electrons, the relaxation time ($\approx 10^{-14}$ s) between collision is very much smaller than the rf period ($\approx 10^{-9}$ s), i.e., $\tau \ll 1/\omega$. With these two reasons the $\sigma_n \ll \sigma_s$, the simpler expression for Z_s is obtained with the surface resistance and reactance as:

$$R_s = \frac{1}{2}\sigma_n\omega^2\mu_0^2\lambda_L^3 \propto \omega^2 \tag{A.14}$$

$$X_s = \omega\mu_0\lambda_L \tag{A.15}$$

with a constant $\lambda_L = \sqrt{m/(n_s q^2 \mu_0)}$. From equation A.8 and A.14 it is clearly seen that the SC is preferred to be operated at low frequency with an opposite direction in the NC.

Considering a cavity with fixed accelerating field E_0 and fixed total energy gain $\triangle W$, the cavity resonant frequency is inversely proportional to the cavity dimension, b or $b \propto \omega^{-1}$. The transit time factor and the fields are independent of frequency. We scale other cavity parameters with

frequency. The power dissipated in the cavity walls is given by

$$P_d = \frac{1}{2} R_s \int_S |\mathbf{H}|^2 dS \tag{A.16}$$

For the sake of comparison we scale the power dissipated per unit length in which the relation in NC case is

$$P'_d \propto R_s |\mathbf{H}|^2 b \propto \omega^{1/2} \cdot \omega^{-1} \propto \omega^{-1/2} \tag{A.17}$$

and

$$P'_d \propto R_s |\mathbf{H}|^2 b \propto \omega^2 \cdot \omega^{-1} \propto \omega \tag{A.18}$$

for SC case.

The total energy stored in the cavity is given by

$$U = \frac{1}{2} \epsilon_0 \int_V |\mathbf{E}|^2 dV = \frac{1}{2} \mu_0 \int_V |\mathbf{H}|^2 dV \tag{A.19}$$

The energy stored per unit length in NC and SC has the same frequency scaling as

$$U' \propto |\mathbf{E}|^2 b^2 \propto |\mathbf{H}|^2 b^2 \propto \omega^{-2} \tag{A.20}$$

The cavity quality factor, which is related to the stored energy and the power dissipation is defined as

$$Q_0 = \frac{\omega U}{P_d} \tag{A.21}$$

In NC case it is scaled as

$$Q_0 \propto \frac{\omega \cdot \omega^{-2}}{\omega^{-1/2}} \propto \omega^{-1/2} \tag{A.22}$$

and for SC case is

$$Q_0 \propto \frac{\omega \cdot \omega^{-2}}{\omega} \propto \omega^{-2} \tag{A.23}$$

The parameter R/Q_0 is obtained from

$$\frac{R}{Q_0} = \frac{V_c^2}{\omega U} \tag{A.24}$$

This parameter per unit length has the same frequency scaling in both cases as

$$\frac{R'}{Q_0} \propto \frac{|\mathbf{E}|^2}{\omega \cdot \omega^{-2}} \propto \omega \tag{A.25}$$

This leads to the frequency scaling of cavity shunt impedance per unit length in NC case to be obtained as

$$R' \propto Q_0 \cdot \omega \propto \omega^{-1/2} \cdot \omega \propto \omega^{1/2} \tag{A.26}$$

and

$$R' \propto Q_0 \cdot \omega \propto \omega^{-2} \cdot \omega \propto \omega^{-1} \tag{A.27}$$

in SC cavity. The geometry factor of the cavity is defined as

$$G = \frac{\omega \mu_0 \int_V |\mathbf{H}|^2 dV}{\int_S |\mathbf{H}|^2 dS} \propto \frac{\omega \cdot \omega^{-3}}{\omega^{-2}} \propto \omega^0 \tag{A.28}$$

This parameter is independent of frequency since this is a figure of merit that depends only on the cavity shape. The longitudinal loss factor per unit length is defined as

$$k_L' = \frac{V_c^2}{4U} \propto \frac{|\mathbf{E}|^2}{\omega^{-2}} \propto \omega^2 \tag{A.29}$$

This is the same for NC and SC cavities. The transverse dipole kick factor is defined as

$$k_T = \frac{k_L^{(1)}(r)}{\omega_1 r^2/c} \tag{A.30}$$

where $k_L^{(1)}(r)$ is the longitudinal loss factor of the dipole mode and r, the beam offset from the cavity

axis, which is $\propto \omega^2$, and ω_1 is the dipole frequency, which is $\propto \omega$. We scale this factor with the fundamental mode frequency as

$$k_T \propto \frac{\omega^2}{\omega \cdot \omega^{-2}} \propto \omega^3 \tag{A.31}$$

This is the same in both types of cavity. The longitudinal and transverse wakefields are proportional to their loss factors. We can scale these effects as

$$W_L \propto \omega^2 \tag{A.32}$$

and

$$W_T \propto \omega^3 \tag{A.33}$$

The summary of frequency scaling of cavity parameters are listed in Table A.1 in comparison between SC and NC cavities.

Table A.1: Comparison between normal and superconducting cavities on frequency scaling of cavity parameters.

Parameter	Super conducting	Normal conducting
Cavity dimension (b)	ω^{-1}	ω^{-1}
Surface resistance (R_s)	ω^2	$\omega^{1/2}$
Power dissipation (P'_d)	ω^1	$\omega^{-1/2}$
Stored energy (U')	ω^{-2}	ω^{-2}
Quality factor (Q_0)	ω^{-2}	$\omega^{-1/2}$
Shunt impedance (R')	ω^{-1}	$\omega^{1/2}$
Geometric factor (G)	ω^0	ω^0
R over Q (R'/Q_0)	ω^1	ω^1
Longitudinal lost factor (k'_L)	ω^2	ω^2
Transverse kick factor (k'_T)	ω^3	ω^3

Appendix B

Application of Circuit Model to Compute Modal Momentum Kicks

In order to find the kick factors of the cavity we first take the voltage drop across the capacitor in loop m of the circuit model (see figure 4.1) to represent the longitudinal voltage the beam loses in cell m of the cavity. So the value of this capacitor is

$$C_m = \frac{1}{2\mathcal{K}_s^m z_e z L} \tag{B.1}$$

where $\mathcal{K}_s^m = \omega_s^m K_s^m / c$ is the loss factor for the periodic structure of cell m, K_s^m is the kick factor, z_e is the driving charge offset, z is the test charge offset, and L is the cell length. Assume the cavity is empty at time $t = 0$ the driving charge enters the cavity at time $t = L/2c$ and reaches the center of cell m at $t = mL/c$. In addition, in each loop m we add the current source $-q_e \delta(t - mL/c)$ in parallel with the capacitor. Since we know the Fourier transform of the eigenfunctions of the system we obtain the time evolution of the currents in the circuit by performing the inverse Fourier transform and the finally we obtain the kick factors.

From equation 4.2 the eigenvalue equation can be written as

$$M\mathbf{f}^{(p)} = \lambda_p \mathbf{f}^{(p)} \tag{B.2}$$

where M is the system matrix, $\mathbf{f}^{(p)}$ is the pth eigenfunction and $\lambda_p = 1/v_p^2$ is the pth eigenvalue. We want to solve the system by adding the driving terms

$$h_m = \frac{q_e}{v^2 \sqrt{C_m}} e^{-i\omega L/c} \tag{B.3}$$

in our matrix equation, where m^{th} element of vector gives the value of the parameter in cell m. The new eigenvalue equation is written as

$$M\mathbf{g} - \lambda\mathbf{g} = \mathbf{h} \tag{B.4}$$

with $\lambda = 1/v^2$ for the vector $\mathbf{g}$. Expanding $\mathbf{g}$ and $\mathbf{h}$ in terms of the eigenfunctions leads to

$$\mathbf{g} = \sum_p \frac{\mathbf{f}^{(p)}}{\lambda_p - \lambda} \left[\frac{\mathbf{f}^{(p)} \cdot \mathbf{h}}{|f^{(p)}|^2} \right] \tag{B.5}$$

We have used the orthogonality of the eigenfunctions, which holds because our matrix is real and symmetric. We have also assumed the system is non-degenerate.

In time domain, in loop m of the circuit

$$
\begin{aligned}
G_m(t) &= \int_{-\infty}^{\infty} g_m(v) e^{i2\pi v t}\, dv \\
&= q_e \sum_p \frac{f_m^{(p)} v_p^2}{|f^{(p)}|^2} \sum_n \frac{f_n^{(p)}}{\sqrt{C_n}} \int_{-\infty}^{\infty} \frac{e^{i2\pi v(t-nL/c)}}{v^2 - v_p^2}\, dv
\end{aligned} \tag{B.6}
$$

This equation has two poles, at $v = \pm v_p$. Adding a small positive imaginary part to these poles to solve this equation. If $(t - nL/c) > 0$ using the close integration loop in the upper half plane, else in

the lower half plane. We got this result

$$G_m(t) = -2\pi q_e \sum_p \frac{f_m^{(p)} v_p}{|f^{(p)}|^2} \sum_n \Theta(t - nL/c) \frac{f_n^{(p)}}{\sqrt{C_n}} \sin 2\pi v_p(t - nL/c) \tag{B.7}$$

where $\Theta(t) = 0$ for $t < 0$, $\Theta(t) = 1$ for $t > 0$. From the definition of $f_m \equiv i_m v_m \sqrt{L_m} = i_m/\sqrt{C_m}$, the inductor current in loop m is given by $I_m = \sqrt{C_m} G_m(t)$. Adding the driving current to this we get the capacitor current and then results the voltage drop across the capacitor

$$\begin{aligned} V_{zm}(t) &= \frac{1}{C_m} \int_0^t I_m(t') \, dt' + \frac{q_e}{C_m} \Theta(t - mL/c) \\ &= \frac{q_e}{C_m} \sum_p \frac{f_m^{(p)}}{|f^{(p)}|^2} \sum_n \Theta(t - nL/c) \frac{f_n^{(p)}}{\sqrt{C_n}} \cos 2\pi v_p(t - nL/c) \end{aligned} \tag{B.8}$$

The capacitor voltage represents the energy loss of a test charge to the dipole modes of the cavity. Using the Panofsky-Wenzel theorem [25] we obtain the transverse kick from the longitudinal, i.e. the transverse kick $V_m(t) = (c/x) \int^t V_{zm}(t') \, dt'$. Thus the transverse kick in cell m is given by

$$V_m(t) = 2q_e x_e L \sum_p \frac{f_m^{(p)} \sqrt{K_s^{(m)} v_s^{(m)}}}{v_p |f^{(p)}|^2} \sum_n \Theta(t - nL/c) f_n^{(p)} \sqrt{K_s^{(n)} v_s^{(n)}} \sin 2\pi v_p(t - nL/c) \tag{B.9}$$

This equation is valid for all time and implies that the amplitudes and phases of the modes after the driving charge has left the cavity are given by

$$V_m(t) = \sum_p V_m^{(p)} \sin(2\pi v_p t - \theta_p) \quad t > NL/c \tag{B.10}$$

with

$$V_m^{(p)} = \frac{2q_e x_e L f_m^{(p)} \sqrt{K_s^{(m)} v_s^{(m)}}}{v_p |f^{(p)}|^2} \left| \sum_n f_n^{(p)} \sqrt{K_s^{(n)} v_s^{(n)}} e^{in\varphi_p} \right|$$

$$\tan \theta_p = \frac{\sum_n f_n^{(p)} \sqrt{K_s^{(n)} v_s^{(n)}} \sin(n\varphi_p)}{\sum_n f_n^{(p)} \sqrt{K_s^{(n)} v_s^{(n)}} \cos(n\varphi_p)}$$

(B.11)

and $\varphi_p = 2\pi v_p L / c$.

Equation B.9 can be utilized to obtain the total voltage a test charge, following a distance s behind the driving charge, experiences in cell m of the cavity, $\tilde{V}_m(s)$, as

$$\tilde{V}_m(s) = V_m \left(\frac{mL + s}{c} \right)$$

(B.12)

The total kick felt by the test charge can be obtained by summing up the contributions of all the cavity cells

$$\tilde{V}(s) = \sum_m \tilde{V}_m(s)$$

(B.13)

Assume that the couplings η are small so that the effects of any precursor voltages can be ignored, then we can approximate $\tilde{V}(s) = 0$ for $s < 0$, i.e. ahead of driving charge. This relation combined with equations B.9, B.12, and B.13 leads to

$$\tilde{V}(s) \approx 2q_e x_e NL \sum_p K_p \sin \frac{2\pi v_p s}{c} \quad s > 0$$

(B.14)

with the kick factor for mode p given by

$$K_p = \frac{\left| \sum_n f_n^{(p)} \sqrt{K_s^{(n)} v_s^{(n)}} e^{in\varphi_p} \right|^2}{N v_p |f^{(p)}|^2} \tag{B.15}$$

For any dipole mode of a cavity p the loss factor $\mathcal{K}_p = 2\pi v_p K_p / c$ is given by the ratio of the square of the maximum voltage gained by a test charge to the product $4 x_e x N L$ times the energy stored in the mode. Form this physics we see that equation B.15 gives approximately the proper ratio of the maximum voltage squared and the energy stored in the modes of circuit chain.

For a double chain circuit model, the derivations of the time development of the fields, wakefields and the kick factors are in similar fashion as the single chain model and the results is also similar as the kick factor for the double chain model is given by

$$K_p = \frac{\left| \sum_n f_n^{(p)} \sqrt{\epsilon^{(n)} K_s^{(n)} v_s^{(n)}} e^{in\varphi_p} \right|^2}{N v_p (|f^{(p)}|^2 + |\hat{f}^{(p)}|^2)} \tag{B.16}$$

with $\epsilon^{(n)}$ is a fitting parameter given by $1 + (|\hat{f}^{(p)}|^2 / |f^{(p)}|^2)$, where p is the mode nearest the synchronous point, and $\varphi_p = 2\pi v_p L / c$ is the phase shift per cell. Note that only the f_m's appear in the numerator of this equation, since only the TM_{110} component of the fields (not the TE_{111} component) will kick the beam.

Appendix C

Validation of Kroll-Yu Method

A summary of some investigation validating the Kroll-Yu method on various coupling systems are presented here. The Kroll-Yu method studies the reflection coefficient $R(\omega)$ near the cavity resonant frequency to calculate the Q_e of a waveguide-loaded cavity.

The method begins by considering the field in a waveguide region between the waveguide origin and the shorting plane. This is of the form of an outgoing and a reflected wave:

$$e^{jkz} + Re^{-jkz} \tag{C.1}$$

where $k = 2\pi/\lambda_g$, and z is distance along the waveguide. At the shorting plane at $z = D$, the field must vanish, thus $e^{jkD} + Re^{-jkD} = 0$, and

$$R = -e^{j2kD} = -e^{j2\phi}. \tag{C.2}$$

The Kroll-Yu method utilises the observation that the eigenfrequency of the cavity-waveguide system without the shorting plane corresponds to a situation in which there is an outgoing wave but

199

no incoming wave. This is in conjunction with the fact that the reflection coefficient must have an absolute value of one for a real frequency ω, so we can write:

$$R(\omega) = -e^{j2\phi} = -\frac{\omega - u + jv}{\omega - u - jv}e^{-j2\chi(\omega)} \tag{C.3}$$

where $\chi(\omega)$ is a real analytic function in the vicinity of the pole. By taking the logarithm of both sides, we obtain:

$$\phi(\omega) = \tan^{-1}\left(\frac{v}{\omega - u}\right) - \chi(\omega) + n\pi. \tag{C.4}$$

Differentiating and using the first two terms of a Taylor series expansion around u for $\chi(\omega)$, $\chi(\omega) \approx \chi(u) + \chi'(u)(\omega - u)$, we obtain:

$$-\frac{1}{2}\frac{d\phi}{d\omega} = \frac{1}{2}\frac{u}{(\omega - u)^2 + v^2} + \frac{1}{2}\chi'(u). \tag{C.5}$$

This is a typical Breit-Wigner resonant form with peak at $\omega = u$. This equation, when multiplied by v, will have a peak value of $Q + \frac{1}{2}v\chi'(u)$, where $Q = \frac{u}{2v}$.

Four $\phi - \omega$ pairs are required to determine the Q from eq. C.4. These $\phi - \omega$ pairs can be obtained using an rf e.m. solver on the cavity-waveguide system in which D is varied. Inspecting the field plot, if one branch near the resonance (avoided crossing) can be identified, four runs with different lengths will provide enough information. If two branches near avoided crossings are identified, two values of D are sufficient.

Each point is designated by the subscript $i \in \{1, 2, 3, 4\}$. The following equations are readily obtained [85]:

$$u = \frac{\omega_2 + AB_{12} + \omega_1 A^2}{1 + A^2}, \tag{C.6}$$

$$v = (u - \omega_1)A - B_{12}, \tag{C.7}$$

$$\chi(u) = \tan^{-1}\left(\frac{v}{\omega_i - u}\right) - \phi_i - \chi'(u)(\omega_i - u), \tag{C.8}$$

where

$$A \equiv \frac{B_{12} - B_{23}}{\omega_3 - \omega_1}, \tag{C.9}$$

$$B_{12} \equiv -v - \frac{(\omega_1 - u)(\omega_2 - u)}{v} = (\omega_1 - \omega_2)\cot(\phi_1 - \phi_2 + \chi'(u)(\omega_1 - \omega_2)), \tag{C.10}$$

$$B_{23} \equiv -v - \frac{(\omega_2 - u)(\omega_3 - u)}{v} = (\omega_2 - \omega_3)\cot(\phi_2 - \phi_3 + \chi'(u)(\omega_2 - \omega_3)). \tag{C.11}$$

The expression for $\chi(u)$ in eq. C.8 can be evaluated at any of the three points. From the remaining three data sets and assuming in the vicinity of a resonance that $\chi'(u) = 0$, we can obtain an explicit three-parameter formula. This allows Q_e to be obtained. The $\chi'(u)$ can be obtained from a fourth data point since it is a root of

$$\omega_4 - u - v\cot(\phi_4 - \chi(u) + \chi'(u)(\omega_4 - u)) = 0. \tag{C.12}$$

To validate this method, a series of tests have been carried out using MWS on a straightforward coupled cavity-waveguide system as illustrated in Fig. C.1. The uncoupled cavity consists of a
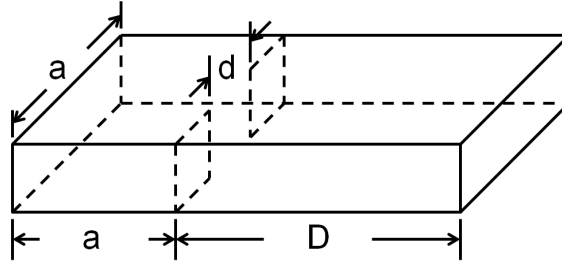
Figure C.1: The waveguide-cavity system. The cavity is a shorted rectangular waveguide of dimension $a \times a$. It is coupled to another rectangular waveguide through an iris of aperture d. The waveguide has a terminating plane at distance D from the iris.

closed rectangular waveguide. The mode frequency of this waveguide is calculated analytically

from:

$$\left(\frac{\omega_{n0p}}{c}\right)^2 = \left(\frac{n\pi}{a}\right)^2 + \left(\frac{p\pi}{a}\right)^2, \tag{C.13}$$

where $n = 1, p = 1$ for TE_{101} mode, which defines $f_0 = \omega_{101}/2\pi = c/a\sqrt{2}$ and half the cutoff wavelength is equal to a. Let us define the normalised waveguide length to a cavity dimension, $r = D/a$, and the normalised frequency

$$\frac{f}{f_0} = \frac{1}{\sqrt{2}} \sqrt{1 + \left(\frac{p}{r}\right)^2}, \tag{C.14}$$

for a TE_{10p} mode in the waveguide. This relationship is for an uncoupled waveguide mode. When an iris is introduced, these two waveguides become coupled. This can be represented by the equivalent circuit in Fig. C.2.
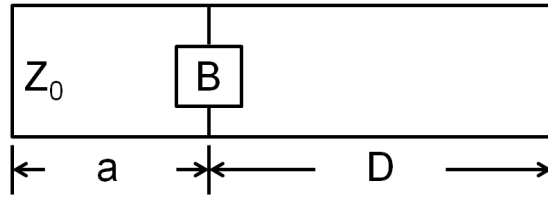
Figure C.2: Equivalent circuit for the cavity-waveguide model with a terminating short at a distance D from the iris.

The shunt susceptance B, normalised to the characteristic admittance of the waveguide, is given as [85, 97]:

$$B = -\frac{2\pi}{ka} \cot^2\left(\frac{\pi d}{2a}\right), \tag{C.15}$$

where k is a propagation constant. Using the circuit model [85] and searching for resonances in the system are obtained:

$$\cot(\pi x) + \frac{2}{x} \cot^2\left(\frac{\pi d}{2a}\right) + \cot(\pi xr) = 0, \tag{C.16}$$

with $x = \sqrt{2(\omega/u_0)^2 - 1}$ and u_0 is the real part of the cavity cutoff frequency. This provides a rela-

tionship between the mode frequency as a function of the shorting place distance r.

Validation was performed on three different systems involving the detailed dimensions in [85, 86]. The first system is the strong coupled system, which has $Q_e \sim 38$. The cavity has a dimension $a = 150$ mm and the iris $d = 67.4$ mm. Simulations have been carried out with varying shorting distances. Consulting the field pattern, we can separate the mode frequencies into a group, which is clearly illustrated in Fig. C.3. The eigenfrequency results are plotted in comparison with the

| mode 1 | mode 2 | mode 3 | mode 4 |
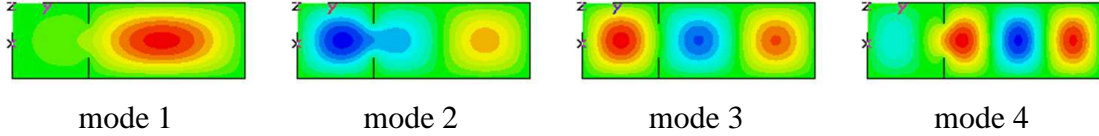
Figure C.3: Field amplitude plots of a cavity-waveguide system of the first four eigenmodes (red represents the maximum amplitude whilst the minimum is indicated in blue.

uncoupled waveguide mode and the coupled waveguide mode in Fig. C.4. The simulation results are in good agreement with analytical results obtained from the transmission line equivalent circuit. The phase change along the waveguide is given by $2\pi D/\lambda_g$. These $\phi - \omega$ points from various waveguide lengths are plotted in Fig. C.5 and are used as the inputs for determining the Q_e of the system.

Four data points are chosen near a region of avoided crossing, which is the region near $r = 1$ or $r = 2$. Carefully fitting selected data points to eq. C.4 allows the Q_e values presented in Table C.1 to be obtained. The two-branch data set is relatively straightforward to fit and has less variation compared to the one-branch data set, as seen in the frequency and Q_e variations plotted versus the data set in Fig. C.6 and Fig. C.7, respectively.

The second validation has been carried out with a moderate coupling system, $Q_e \sim 1600$. The cavity has a dimension $a = 150$ mm and the iris $d = 27.67$ mm. A similar analysis has been performed. The
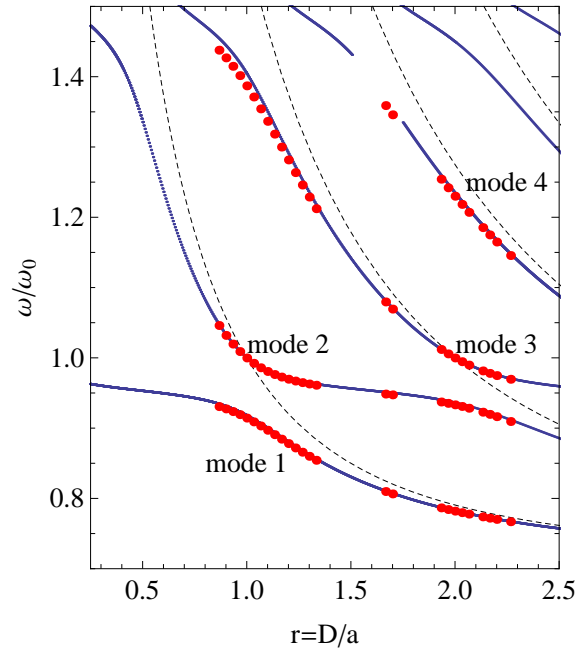
Figure C.4: Normalised frequency as a function of normalised length, *r*. Red dots indicate the results from MWS simulation, blue dots represent analytical solutions from an equivalent circuit, and dashed lines are the uncoupled waveguide resonances.
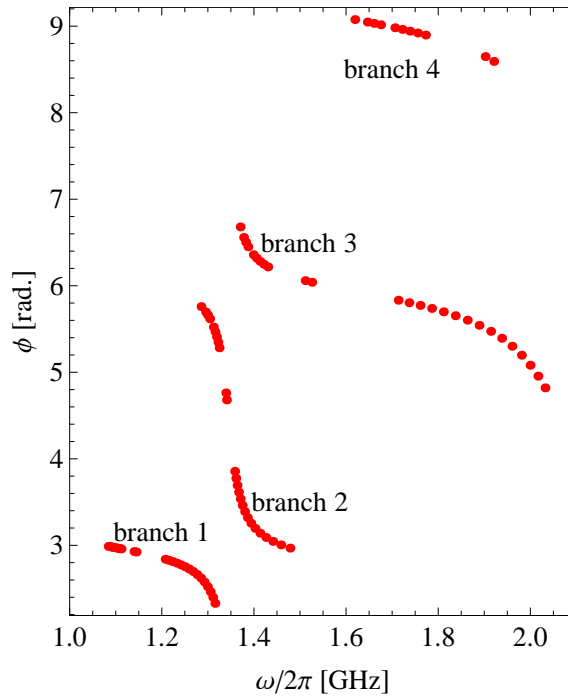
Figure C.5: Phase ϕ as a function of frequency for a low Q system.

Table C.1: Comparison of fitted parameters using different data sets for a low Q system.

No.	Branches	D [cm]	$\omega/2\pi$ [MHz]	Q_e
1	1, 2	15.5, 16.0	1344.57	34.37
2	1	14.0, 14.5, 15.5, 16.0	1344.68	33.81
3	2	14.5, 15.5, 16.5, 17.5	1344.62	34.82
4	2, 3	32.5, 33.0	1344.56	34.45
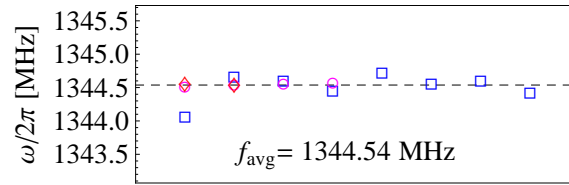
Figure C.6: Frequency variation with a varying data set: red diamonds and magenta circles are the two-branch data with a low phase and high phase avoided crossing region, respectively, while blue rectangles are the one-branch data. The dashed line indicates the average value.
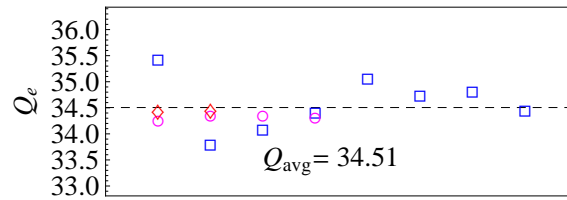
Figure C.7: Q_e variation with a varying data set: red diamonds and magenta circles are the two-branch data with a low phase and high phase avoided crossing region, respectively, while blue rectangles are the one-branch data. The dashed line indicates the average value.

average Q_e is 1613, comparable to the analytical one. The avoided crossing region is very narrow as can be observed from Fig. C.8 and Fig. C.9. The selected fitted results are listed in Table C.2.
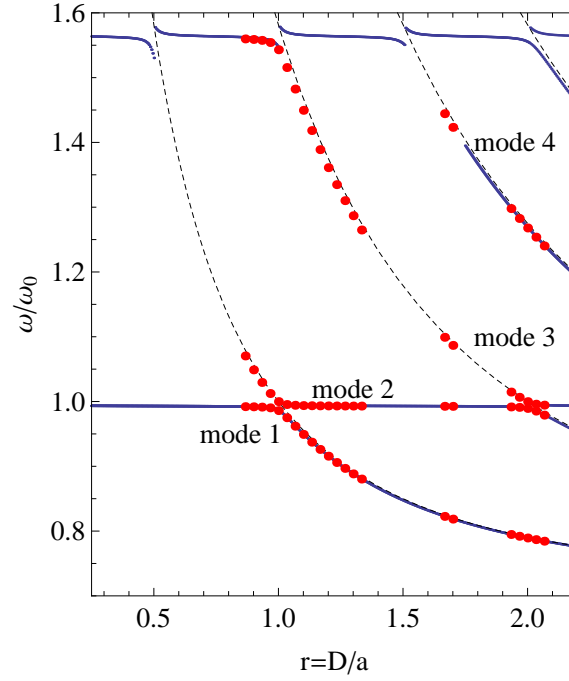
Figure C.8: Normalised frequency plotted as a function of normalised length, r. Red dots indicate the results from MWS simulation, blue dots represent an analytical solutions from an equivalent circuit, and dashed lines are the uncoupled waveguide resonances.

Table C.2: Comparison of fitted parameters using different data sets for a moderate Q system.

No.	Branches	D [cm]	$\omega/2\pi$ [MHz]	Q_e
1	1, 2	15.0, 15.5	1403.05	1605.26
2	1	14.5, 15.0, 15.5, 16.0	1403.05	1604.64
3	2	14.5, 15.0, 15.5, 16.0	1403.05	1605.75
4	2, 3	30.0, 30.5	1403.00	1620.95

A third validation is performed on a high coupled system (as was also performed by Lin [86]). The calculation procedure used with the previous systems gives consistent results compared to the results
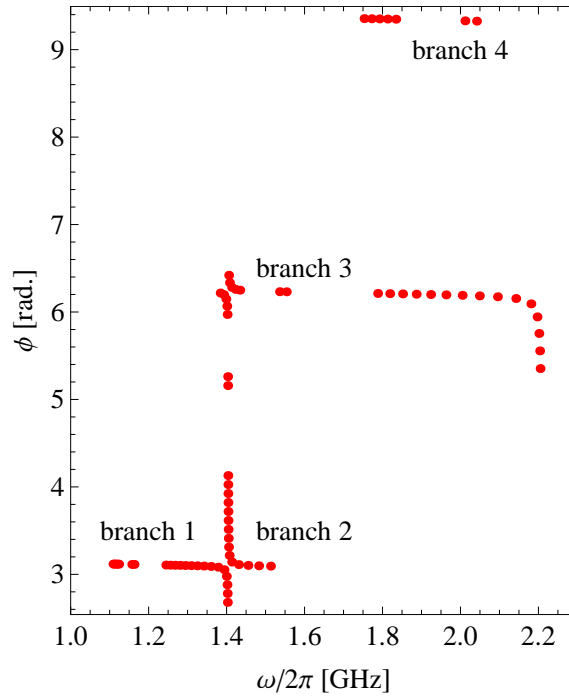
Figure C.9: The phase variable ϕ as a function of frequency for a moderate Q system.

presented in [86] as listed in Table C.3.

Table C.3: Comparison of fitted parameters using different data sets.

d/a	Lin thesis		my attempt	
	$\omega/2\pi$ [MHz]	Q_e	$\omega/2\pi$ [MHz]	Q_e
0.50	8768.98	34.57	8768.10	34.51
0.65	8405.65	10.38	8407.31	10.51
0.70	8266.90	7.50	8258.71	8.01
0.75	8111.05	5.53	8103.93	5.92

Appendix D
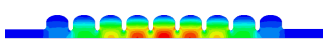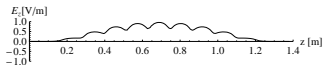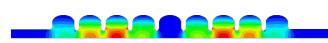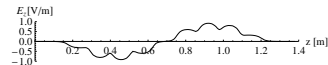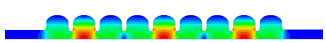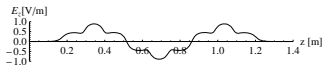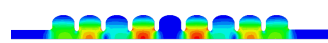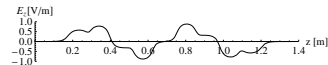
Detailed Mode Compendium
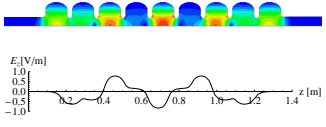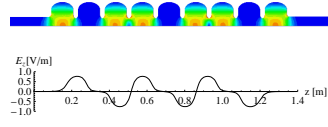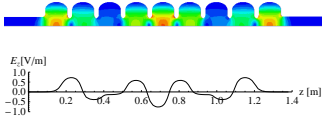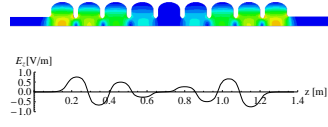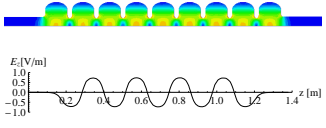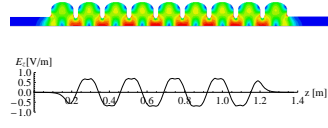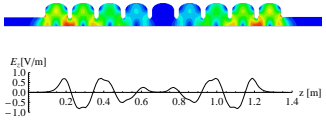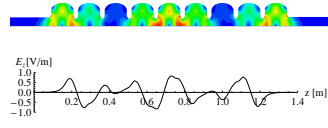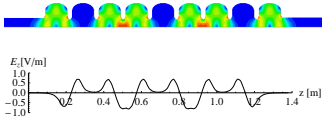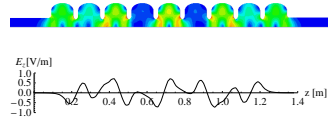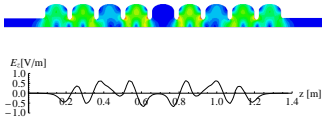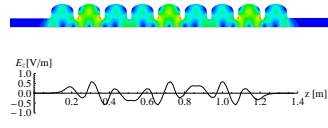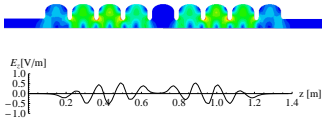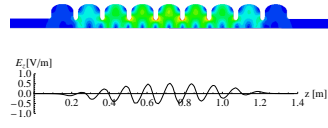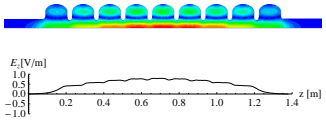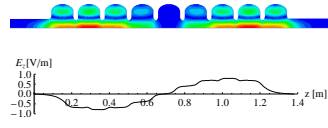
Future work, concerned with HOM diagnostics and the influence of the wakefield on beam dynamics will all profit from a knowledge of the modal distribution. This compendium serves as a guide to the modes in my NLSF cavity.
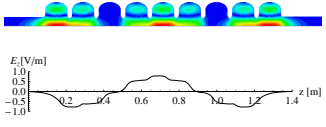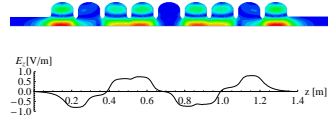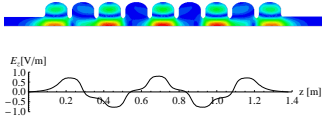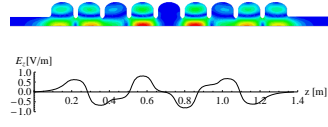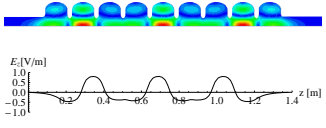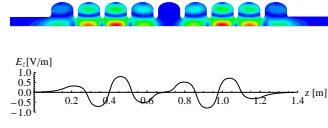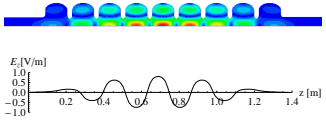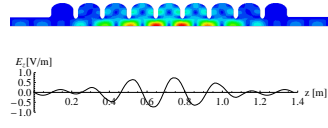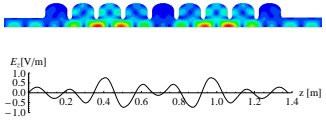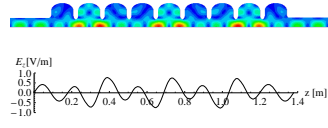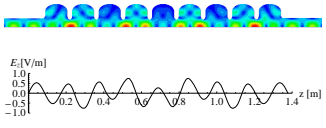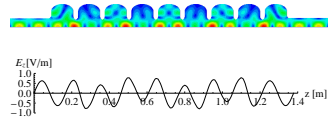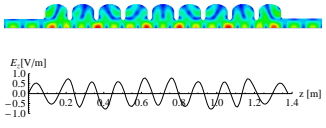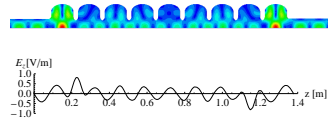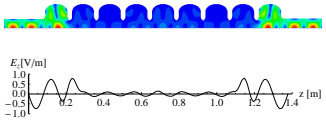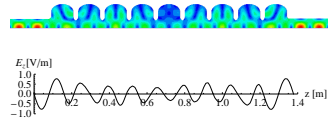
D.1   Monopole Mode with MM Boundary Condition
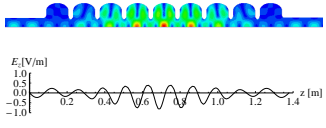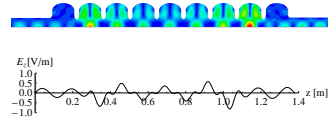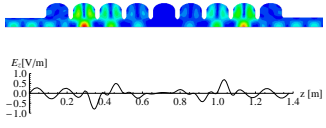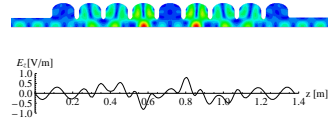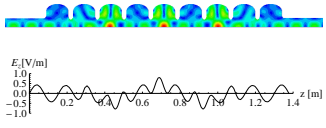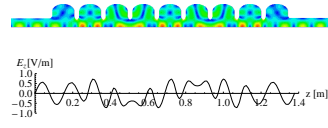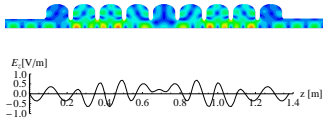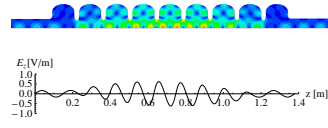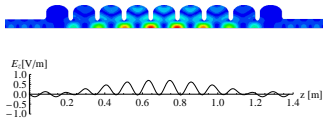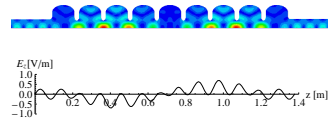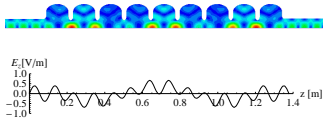
The longitudinal electric field plot (E_z) is taken at 15 mm offset from the cavity axis.

Table D.1: Monopole mode with MM boundary condition

MP-MM-001 f=1.2791 GHz, R/Q =0.00 Ω	MP-MM-002 f=1.2808 GHz, R/Q =0.01 Ω
MP-MM-003 f=1.2835 GHz, R/Q =0.03 Ω	MP-MM-004 f=1.2868 GHz, R/Q =0.02 Ω

MP-MM-005 f=1.2904 GHz, R/Q =0.07 Ω	MP-MM-006 f=1.2938 GHz, R/Q =0.03 Ω
MP-MM-007 f=1.2965 GHz, R/Q =0.01 Ω	MP-MM-008 f=1.2983 GHz, R/Q =0.01 Ω
MP-MM-009 f=1.2989 GHz, R/Q =1126.78 Ω	MP-MM-010 f=2.2102 GHz, R/Q =1.39 Ω
MP-MM-011 f=2.2115 GHz, R/Q =6.17 Ω	MP-MM-012 f=2.2151 GHz, R/Q =4.06 Ω
MP-MM-013 f=2.2207 GHz, R/Q =9.52 Ω	MP-MM-014 f=2.2276 GHz, R/Q =10.74 Ω
MP-MM-015 f=2.2351 GHz, R/Q =28.66 Ω	MP-MM-016 f=2.2423 GHz, R/Q =186.53 Ω
MP-MM-017 f=2.2482 GHz, R/Q =133.07 Ω	MP-MM-018 f=2.2522 GHz, R/Q =7.96 Ω
MP-MM-019 f=2.8015 GHz, R/Q =0.01 Ω	MP-MM-020 f=2.8056 GHz, R/Q =0.41 Ω
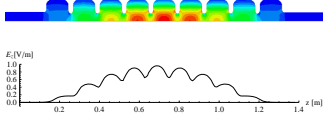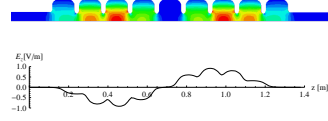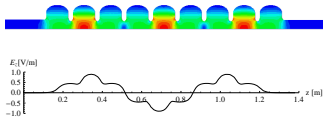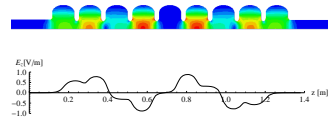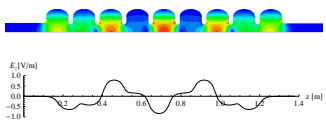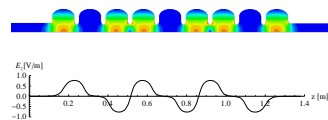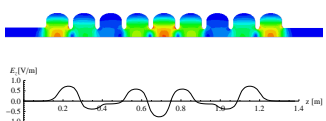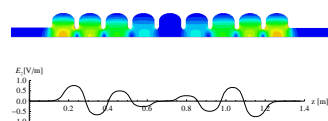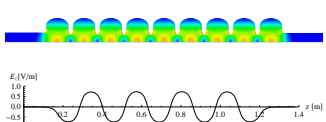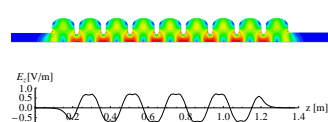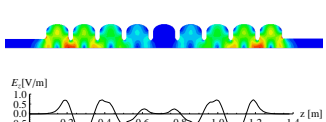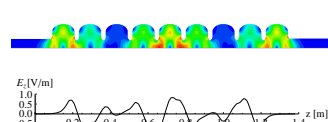
	MP-MM-021 f=2.8128 GHz, R/Q =1.04 Ω		MP-MM-022 f=2.8231 GHz, R/Q =0.05 Ω
	MP-MM-023 f=2.8357 GHz, R/Q =0.40 Ω		MP-MM-024 f=2.8497 GHz, R/Q =0.10 Ω
	MP-MM-025 f=2.8633 GHz, R/Q =0.10 Ω		MP-MM-026 f=2.8750 GHz, R/Q =0.06 Ω
	MP-MM-027 f=2.8830 GHz, R/Q =0.01 Ω		MP-MM-028 f=3.4137 GHz, R/Q =0.08 Ω
	MP-MM-029 f=3.4307 GHz, R/Q =0.16 Ω		MP-MM-030 f=3.4546 GHz, R/Q =0.76 Ω
	MP-MM-031 f=3.4817 GHz, R/Q =4.04 Ω		MP-MM-032 f=3.5085 GHz, R/Q =0.02 Ω
	MP-MM-033 f=3.5328 GHz, R/Q =3.40 Ω		MP-MM-034 f=3.5493 GHz, R/Q =1.08 Ω
	MP-MM-035 f=3.5513 GHz, R/Q =8.84 Ω		MP-MM-036 f=3.5541 GHz, R/Q =1.57 Ω
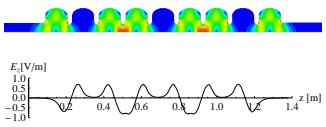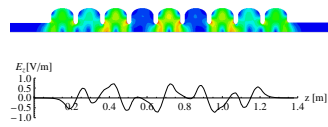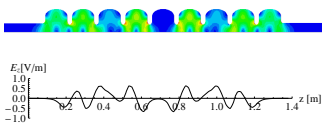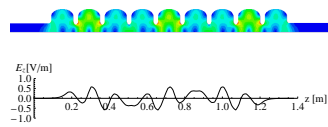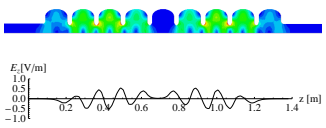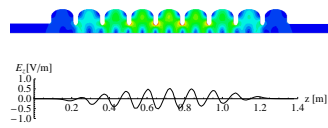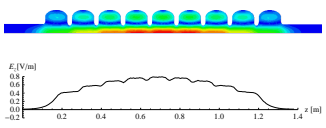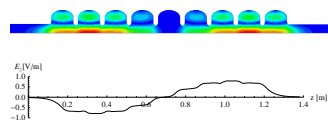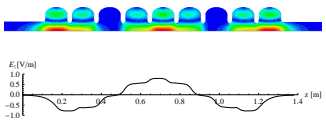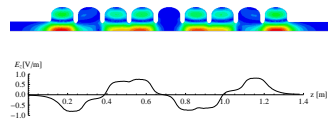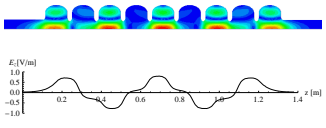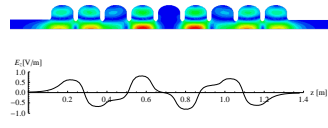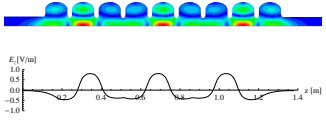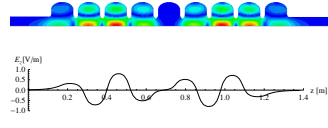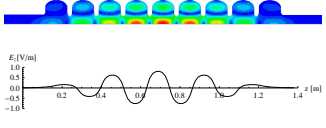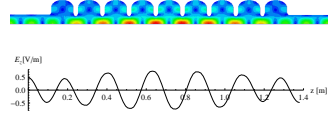
	MP-MM-037 f=3.5616 GHz, R/Q =0.00 Ω		MP-MM-038 f=3.5782 GHz, R/Q =0.69 Ω
	MP-MM-039 f=3.5783 GHz, R/Q =34.90 Ω		MP-MM-040 f=3.5803 GHz, R/Q =6.39 Ω
	MP-MM-041 f=3.5837 GHz, R/Q =0.06 Ω		MP-MM-042 f=3.5930 GHz, R/Q =0.01 Ω
	MP-MM-043 f=3.6109 GHz, R/Q =0.04 Ω		MP-MM-044 f=3.6292 GHz, R/Q =0.04 Ω
	MP-MM-045 f=4.0217 GHz, R/Q =0.02 Ω		MP-MM-046 f=4.0522 GHz, R/Q =0.89 Ω
	MP-MM-047 f=4.0919 GHz, R/Q =0.57 Ω		
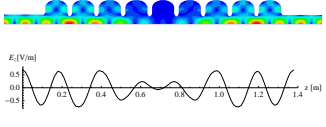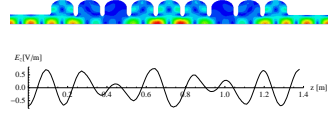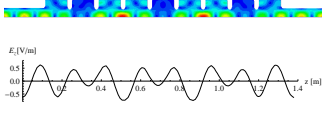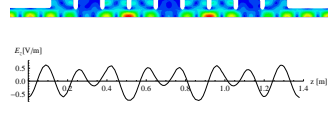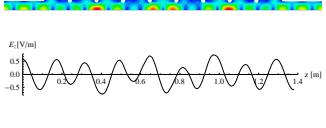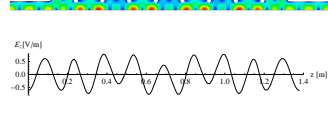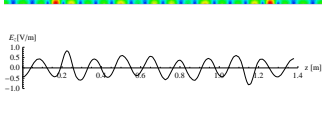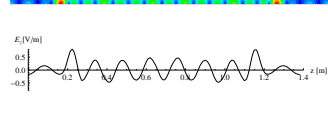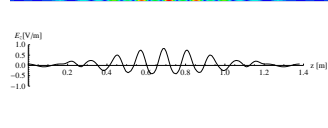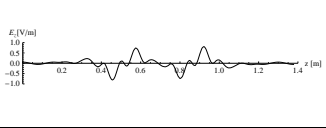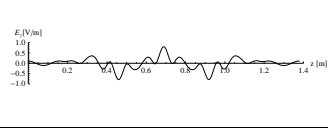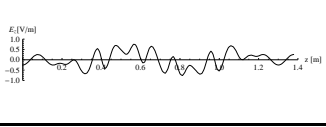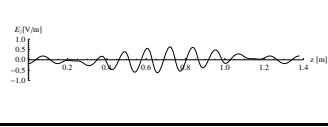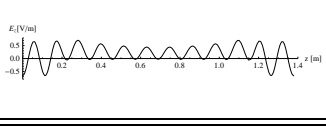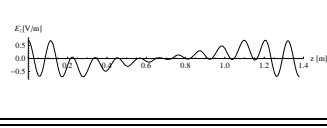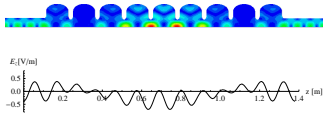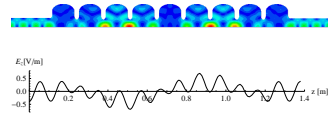
D.2   Monopole Mode with EE Boundary Condition

The longitudinal electric field plot (E_z) is taken at 15 mm offset from the cavity axis.

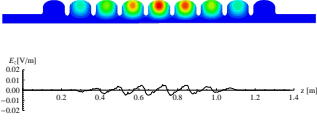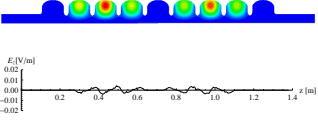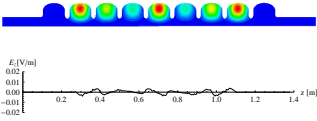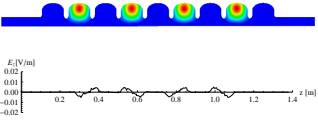Table D.2: Monopole mode with EE boundary condition

	MP-EE-001 f=1.2791 GHz, R/Q =0.00 Ω		MP-EE-002 f=1.2808 GHz, R/Q =0.01 Ω
	MP-EE-003 f=1.2835 GHz, R/Q =0.03 Ω		MP-EE-004 f=1.2868 GHz, R/Q =0.02 Ω
	MP-EE-005 f=1.2904 GHz, R/Q =0.07 Ω		MP-EE-006 f=1.2938 GHz, R/Q =0.03 Ω
	MP-EE-007 f=1.2965 GHz, R/Q =0.01 Ω		MP-EE-008 f=1.2983 GHz, R/Q =0.01 Ω
	MP-EE-009 f=1.2989 GHz, R/Q =1126.79 Ω		MP-EE-010 f=2.2102 GHz, R/Q =6.98 Ω
	MP-EE-011 f=2.2115 GHz, R/Q =6.16 Ω		MP-EE-012 f=2.2151 GHz, R/Q =4.06 Ω

	MP-EE-013 f=2.2207 GHz, R/Q =9.51 Ω		MP-EE-014 f=2.2276 GHz, R/Q =10.74 Ω
	MP-EE-015 f=2.2351 GHz, R/Q =28.64 Ω		MP-EE-016 f=2.2423 GHz, R/Q =186.53 Ω
	MP-EE-017 f=2.2482 GHz, R/Q =133.09 Ω		MP-EE-018 f=2.2522 GHz, R/Q =7.96 Ω
	MP-EE-019 f=2.8015 GHz, R/Q =0.01 Ω		MP-EE-020 f=2.8056 GHz, R/Q =0.35 Ω
	MP-EE-021 f=2.8128 GHz, R/Q =1.03 Ω		MP-EE-022 f=2.8230 GHz, R/Q =0.08 Ω
	MP-EE-023 f=2.8357 GHz, R/Q =0.36 Ω		MP-EE-024 f=2.8496 GHz, R/Q =0.14 Ω
	MP-EE-025 f=2.8633 GHz, R/Q =0.07 Ω		MP-EE-026 f=2.8750 GHz, R/Q =0.07 Ω
	MP-EE-027 f=2.8830 GHz, R/Q =0.00 Ω		MP-EE-028 f=3.4090 GHz, R/Q =1.12 Ω
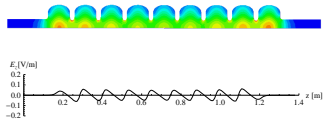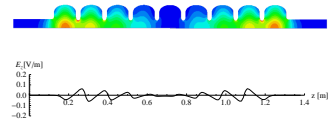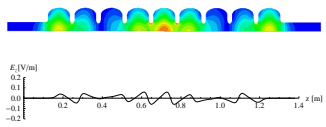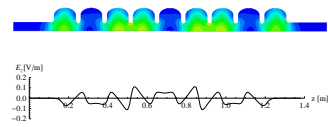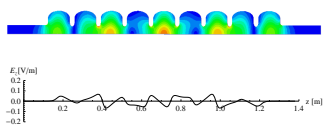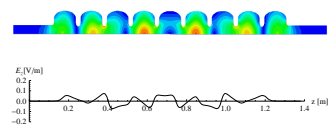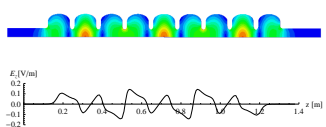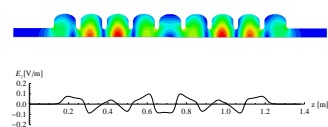
	MP-EE-029 f=3.4151 GHz, R/Q =3.49 Ω		MP-EE-030 f=3.4276 GHz, R/Q =6.78 Ω
	MP-EE-031 f=3.4473 GHz, R/Q =4.89 Ω		MP-EE-032 f=3.4500 GHz, R/Q =4.53 Ω
	MP-EE-033 f=3.4728 GHz, R/Q =1.74 Ω		MP-EE-034 f=3.5002 GHz, R/Q =2.42 Ω
	MP-EE-035 f=3.5223 GHz, R/Q =3.39 Ω		MP-EE-036 f=3.5367 GHz, R/Q =8.52 Ω
	MP-EE-037 f=3.5504 GHz, R/Q =0.03 Ω		MP-EE-038 f=3.5608 GHz, R/Q =0.79 Ω
	MP-EE-039 f=3.5794 GHz, R/Q =33.10 Ω		MP-EE-040 f=3.5816 GHz, R/Q =4.56 Ω
	MP-EE-041 f=3.5883 GHz, R/Q =1.06 Ω		MP-EE-042 f=3.6267 GHz, R/Q =0.20 Ω
	MP-EE-043 f=4.0009 GHz, R/Q =4.96 Ω		MP-EE-044 f=4.0051 GHz, R/Q =1.07 Ω
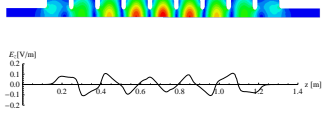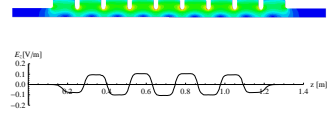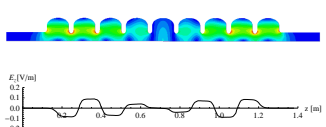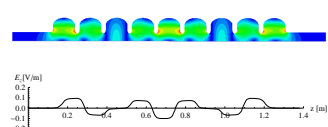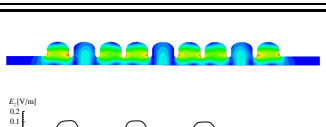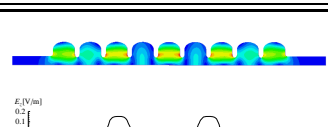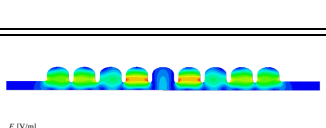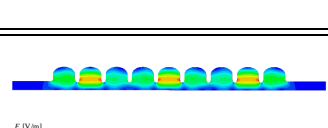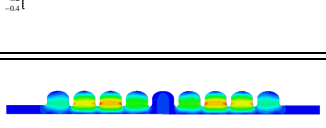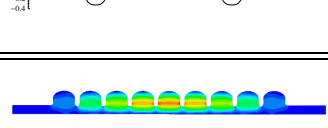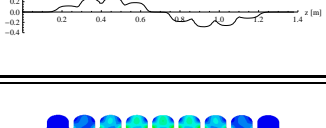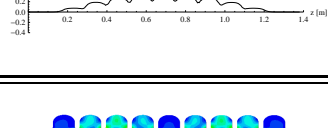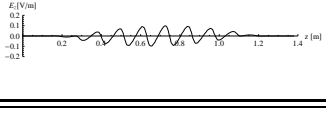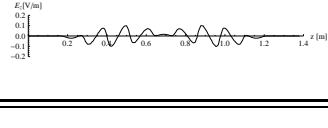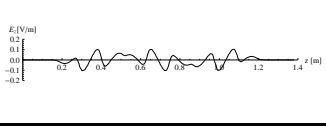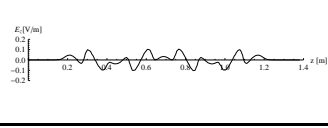
	MP-EE-045 f=4.0353 GHz, R/Q =3.64 Ω		MP-EE-046 f=4.0752 GHz, R/Q =1.71 Ω
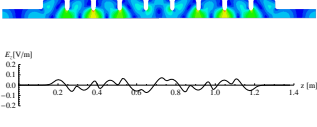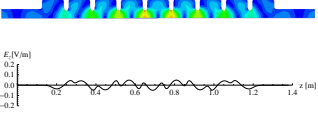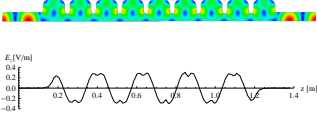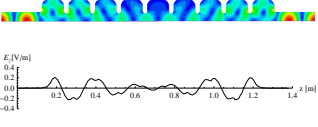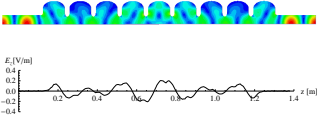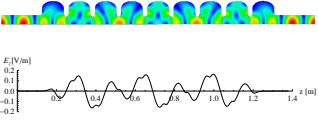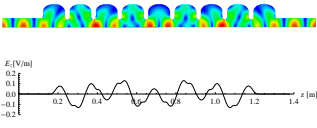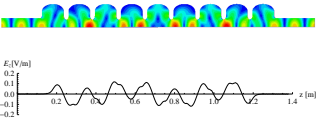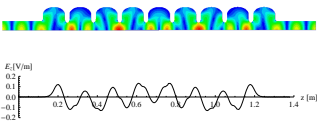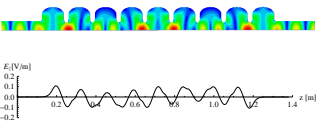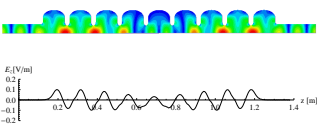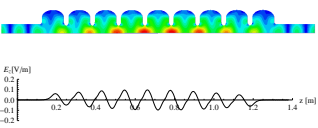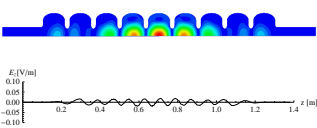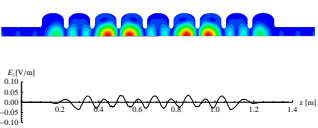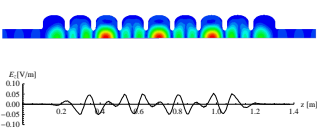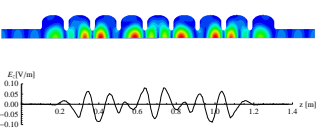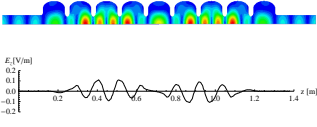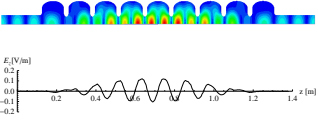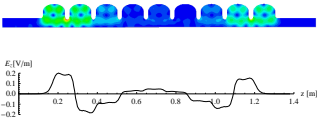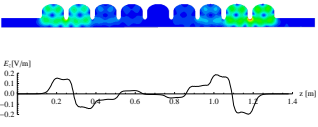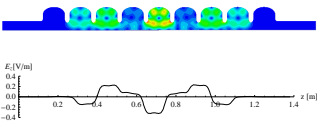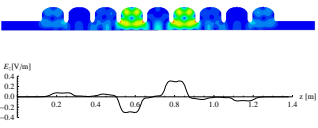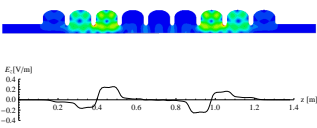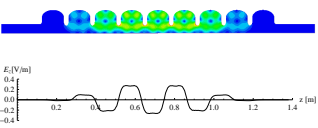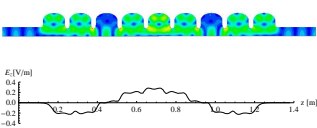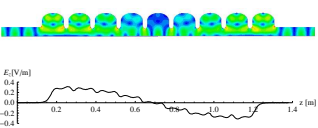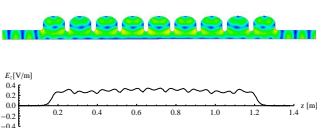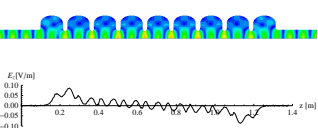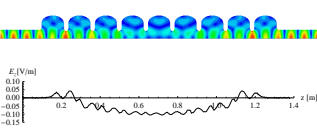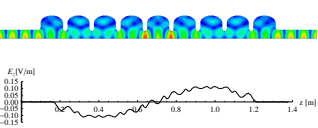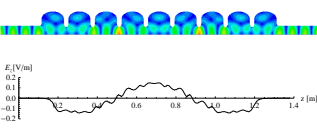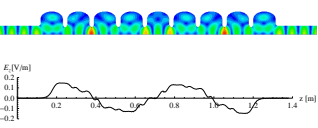
D.3   Dipole Mode with MM Boundary Condition

The longitudinal electric field plot (E_z) is taken at 15 mm offset from the cavity axis.
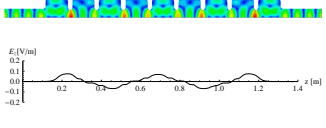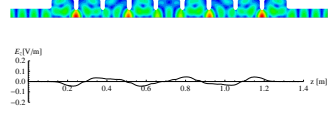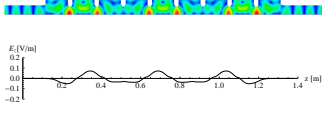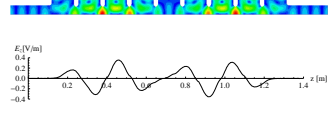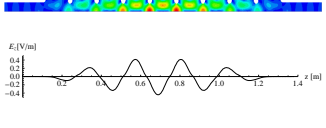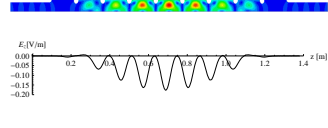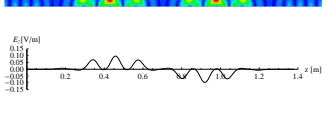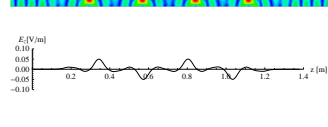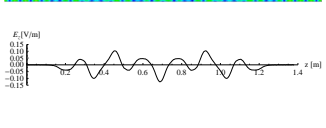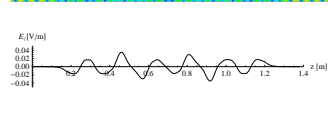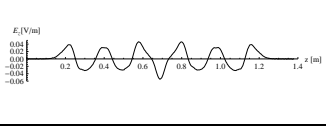
Table D.3: Dipole mode with MM boundary condition

	DP-MM-001 f=1.6479 GHz, R/Q =0.09 Ω/cm^2		DP-MM-002 f=1.6503 GHz, R/Q =0.37 Ω/cm^2
	DP-MM-003 f=1.6593 GHz, R/Q =0.12 Ω/cm^2		DP-MM-004 f=1.6735 GHz, R/Q =0.61 Ω/cm^2
	DP-MM-005 f=1.6925 GHz, R/Q =0.08 Ω/cm^2		DP-MM-006 f=1.7149 GHz, R/Q =4.59 Ω/cm^2
	DP-MM-007 f=1.7395 GHz, R/Q =10.89 Ω/cm^2		DP-MM-008 f=1.7643 GHz, R/Q =2.56 Ω/cm^2

	DP-MM-009 f=1.7858 GHz, R/Q =0.09 Ω/cm^2		DP-MM-010 f=1.8567 GHz, R/Q =0.17 Ω/cm^2
	DP-MM-011 f=1.8670 GHz, R/Q =1.52 Ω/cm^2		DP-MM-012 f=1.8829 GHz, R/Q =0.12 Ω/cm^2
	DP-MM-013 f=1.8988 GHz, R/Q =8.10 Ω/cm^2		DP-MM-014 f=1.9125 GHz, R/Q =15.95 Ω/cm^2
	DP-MM-015 f=1.9236 GHz, R/Q =7.40 Ω/cm^2		DP-MM-016 f=1.9320 GHz, R/Q =0.21 Ω/cm^2
	DP-MM-017 f=1.9379 GHz, R/Q =0.26 Ω/cm^2		DP-MM-018 f=1.9413 GHz, R/Q =0.02 Ω/cm^2
	DP-MM-019 f=2.4616 GHz, R/Q =22.68 Ω/cm^2		DP-MM-020 f=2.4660 GHz, R/Q =11.50 Ω/cm^2
	DP-MM-021 f=2.4732 GHz, R/Q =0.11 Ω/cm^2		DP-MM-022 f=2.4835 GHz, R/Q =1.60 Ω/cm^2
	DP-MM-023 f=2.4973 GHz, R/Q =0.07 Ω/cm^2		DP-MM-024 f=2.5145 GHz, R/Q =0.46 Ω/cm^2

DP-MM-025 f=2.5348 GHz, R/Q =0.12 Ω/cm^2	DP-MM-026 f=2.5549 GHz, R/Q =0.05 Ω/cm^2
DP-MM-027 f=2.6529 GHz, R/Q =0.24 Ω/cm^2	DP-MM-028 f=2.6664 GHz, R/Q =0.36 Ω/cm^2
DP-MM-029 f=2.6936 GHz, R/Q =0.04 Ω/cm^2	DP-MM-030 f=2.7671 GHz, R/Q =0.11 Ω/cm^2
DP-MM-031 f=2.8128 GHz, R/Q =0.03 Ω/cm^2	DP-MM-032 f=2.8618 GHz, R/Q =0.00 Ω/cm^2
DP-MM-033 f=2.9093 GHz, R/Q =0.01 Ω/cm^2	DP-MM-034 f=2.9486 GHz, R/Q =0.72 Ω/cm^2
DP-MM-035 f=2.9748 GHz, R/Q =0.09 Ω/cm^2	DP-MM-036 f=2.9887 GHz, R/Q =0.06 Ω/cm^2
DP-MM-037 f=3.0690 GHz, R/Q =0.02 Ω/cm^2	DP-MM-038 f=3.0707 GHz, R/Q =0.01 Ω/cm^2
DP-MM-039 f=3.0742 GHz, R/Q =0.03 Ω/cm^2	DP-MM-040 f=3.0808 GHz, R/Q =1.10 Ω/cm^2
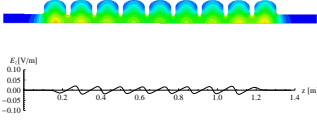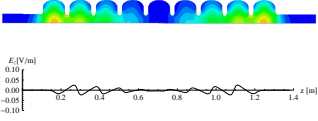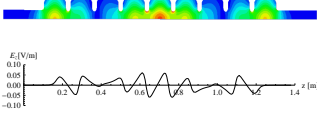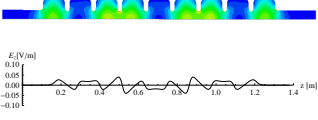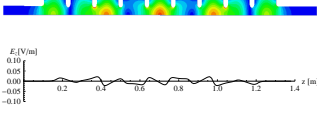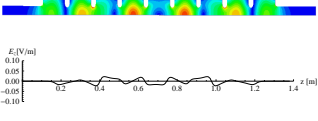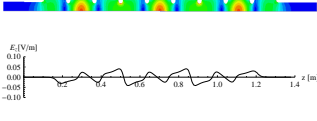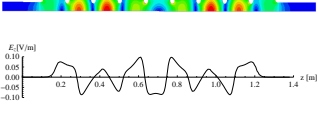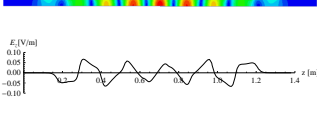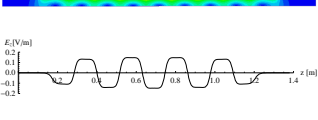
DP-MM-041 f=3.0927 GHz, R/Q =0.41 Ω/cm^2	DP-MM-042 f=3.1092 GHz, R/Q =0.00 Ω/cm^2
DP-MM-043 f=3.3821 GHz, R/Q =0.03 Ω/cm^2	DP-MM-044 f=3.3822 GHz, R/Q =1.58 Ω/cm^2
DP-MM-045 f=3.3850 GHz, R/Q =1.42 Ω/cm^2	DP-MM-046 f=3.3855 GHz, R/Q =0.42 Ω/cm^2
DP-MM-047 f=3.3860 GHz, R/Q =0.09 Ω/cm^2	DP-MM-048 f=3.3865 GHz, R/Q =0.00 Ω/cm^2
DP-MM-049 f=3.3904 GHz, R/Q =0.05 Ω/cm^2	DP-MM-050 f=3.3998 GHz, R/Q =0.11 Ω/cm^2
DP-MM-051 f=3.4112 GHz, R/Q =0.00 Ω/cm^2	DP-MM-052 f=3.4556 GHz, R/Q =0.00 Ω/cm^2
DP-MM-053 f=3.4808 GHz, R/Q =0.07 Ω/cm^2	DP-MM-054 f=3.5228 GHz, R/Q =0.06 Ω/cm^2
DP-MM-055 f=3.5739 GHz, R/Q =0.01 Ω/cm^2	DP-MM-056 f=3.6275 GHz, R/Q =0.00 Ω/cm^2
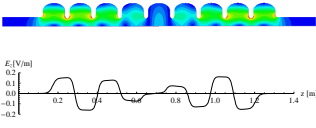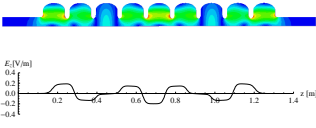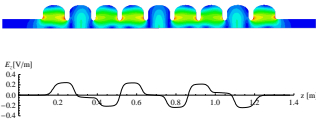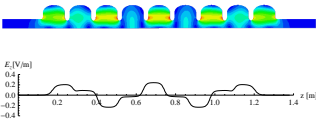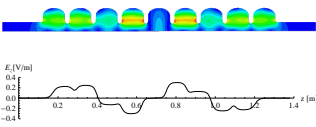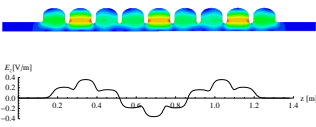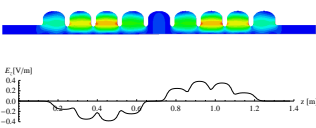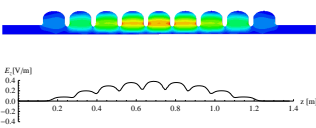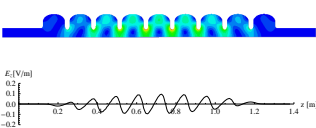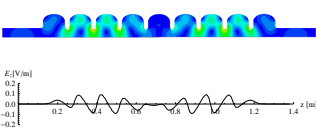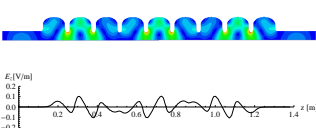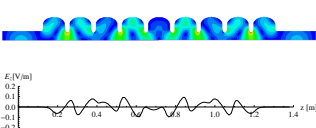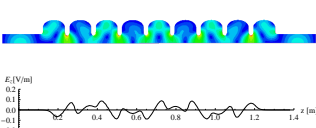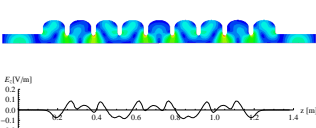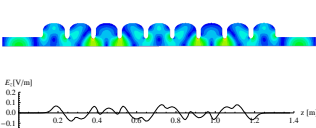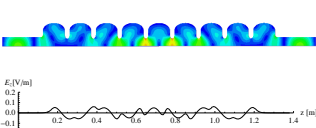
	DP-MM-057 f=3.6793 GHz, R/Q =0.01 Ω/cm^2
	DP-MM-058 f=3.7267 GHz, R/Q =0.00 Ω/cm^2
	DP-MM-059 f=3.7669 GHz, R/Q =0.00 Ω/cm^2
	DP-MM-060 f=3.7970 GHz, R/Q =0.20 Ω/cm^2
	DP-MM-061 f=3.8151 GHz, R/Q =0.86 Ω/cm^2
	DP-MM-062 f=3.9629 GHz, R/Q =0.00 Ω/cm^2
	DP-MM-063 f=3.9668 GHz, R/Q =0.02 Ω/cm^2
	DP-MM-064 f=3.9840 GHz, R/Q =0.09 Ω/cm^2
	DP-MM-065 f=3.9982 GHz, R/Q =0.04 Ω/cm^2
	DP-MM-066 f=4.0152 GHz, R/Q =0.17 Ω/cm^2
	DP-MM-067 f=4.0321 GHz, R/Q =0.57 Ω/cm^2
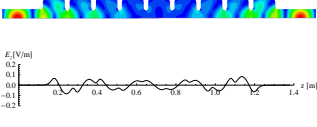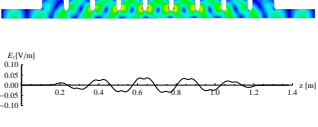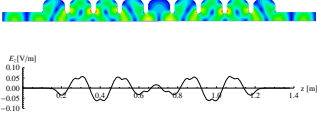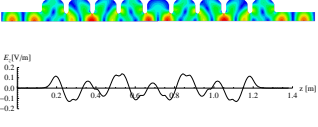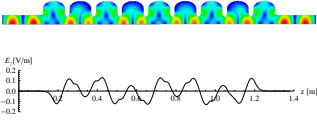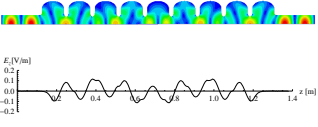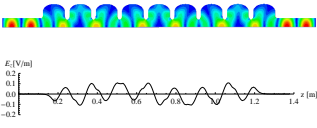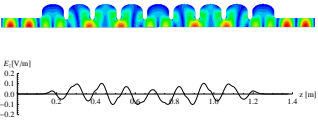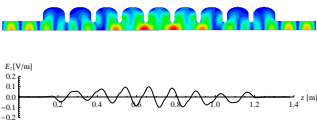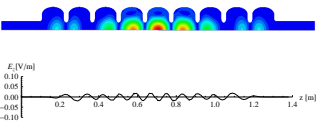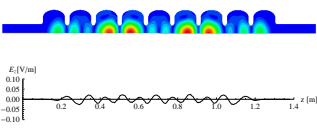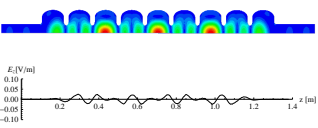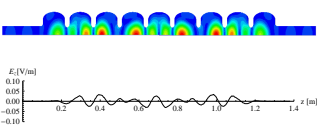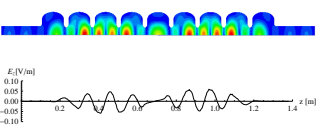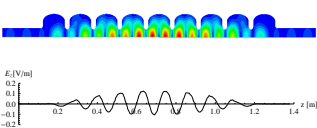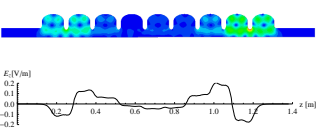
D.4 Dipole Mode with EE Boundary Condition
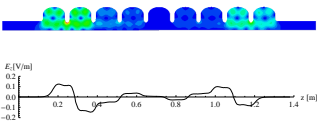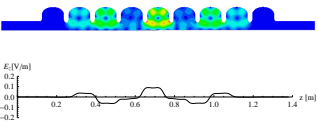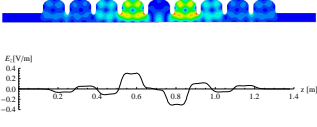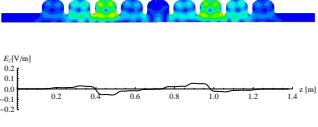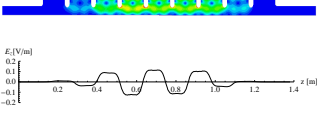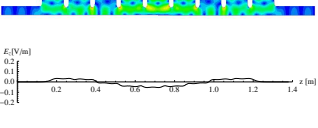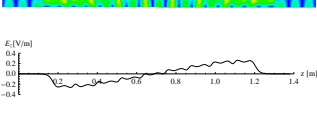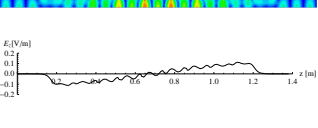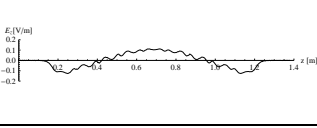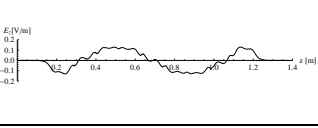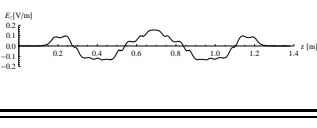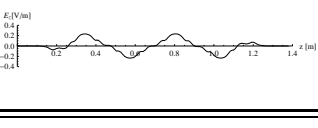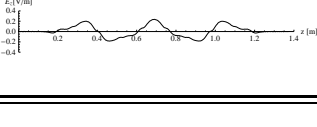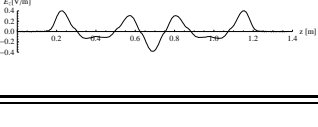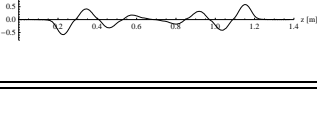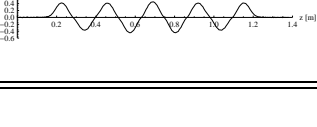
The longitudinal electric field plot (E_z) is taken at 15 mm offset from the cavity axis.
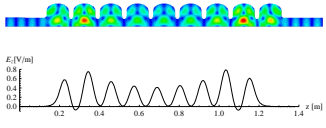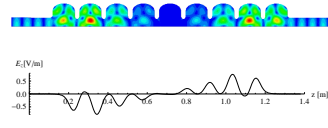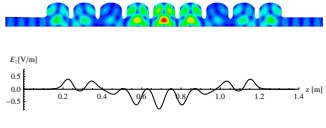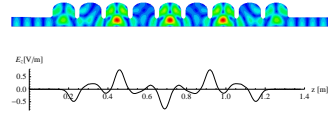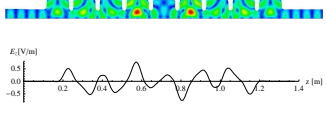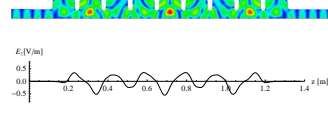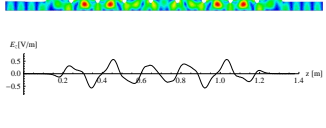
Table D.4: Dipole mode with EE boundary condition

	DP-EE-001 f=1.6479 GHz, R/Q =0.09 Ω/cm^2		DP-EE-002 f=1.6502 GHz, R/Q =0.37 Ω/cm^2
	DP-EE-003 f=1.6593 GHz, R/Q =0.12 Ω/cm^2		DP-EE-004 f=1.6735 GHz, R/Q =0.61 Ω/cm^2
	DP-EE-005 f=1.6924 GHz, R/Q =0.08 Ω/cm^2		DP-EE-006 f=1.7149 GHz, R/Q =4.59 Ω/cm^2
	DP-EE-007 f=1.7395 GHz, R/Q =10.89 Ω/cm^2		DP-EE-008 f=1.7643 GHz, R/Q =2.56 Ω/cm^2
	DP-EE-009 f=1.7858 GHz, R/Q =0.09 Ω/cm^2		DP-EE-010 f=1.8566 GHz, R/Q =0.17 Ω/cm^2

DP-EE-011 f=1.8669 GHz, R/Q =1.53 Ω/cm^2	DP-EE-012 f=1.8829 GHz, R/Q =0.12 Ω/cm^2
DP-EE-013 f=1.8988 GHz, R/Q =8.14 Ω/cm^2	DP-EE-014 f=1.9126 GHz, R/Q =16.00 Ω/cm^2
DP-EE-015 f=1.9237 GHz, R/Q =7.38 Ω/cm^2	DP-EE-016 f=1.9321 GHz, R/Q =0.22 Ω/cm^2
DP-EE-017 f=1.9380 GHz, R/Q =0.25 Ω/cm^2	DP-EE-018 f=1.9414 GHz, R/Q =0.02 Ω/cm^2
DP-EE-019 f=2.4612 GHz, R/Q =24.33 Ω/cm^2	DP-EE-020 f=2.4647 GHz, R/Q =15.84 Ω/cm^2
DP-EE-021 f=2.4708 GHz, R/Q =0.05 Ω/cm^2	DP-EE-022 f=2.4800 GHz, R/Q =1.79 Ω/cm^2
DP-EE-023 f=2.4925 GHz, R/Q =0.18 Ω/cm^2	DP-EE-024 f=2.5084 GHz, R/Q =0.37 Ω/cm^2
DP-EE-025 f=2.5269 GHz, R/Q =0.33 Ω/cm^2	DP-EE-026 f=2.5465 GHz, R/Q =0.00 Ω/cm^2

DP-EE-027 f=2.5656 GHz, R/Q =0.27 Ω/cm^2	DP-EE-028 f=2.6653 GHz, R/Q =0.05 Ω/cm^2
DP-EE-029 f=2.6972 GHz, R/Q =0.02 Ω/cm^2	DP-EE-030 f=2.7842 GHz, R/Q =0.25 Ω/cm^2
DP-EE-031 f=2.8301 GHz, R/Q =0.13 Ω/cm^2	DP-EE-032 f=2.8729 GHz, R/Q =0.02 Ω/cm^2
DP-EE-033 f=2.9120 GHz, R/Q =0.43 Ω/cm^2	DP-EE-034 f=2.9483 GHz, R/Q =0.02 Ω/cm^2
DP-EE-035 f=2.9783 GHz, R/Q =0.10 Ω/cm^2	DP-EE-036 f=3.0691 GHz, R/Q =0.03 Ω/cm^2
DP-EE-037 f=3.0709 GHz, R/Q =0.00 Ω/cm^2	DP-EE-038 f=3.0745 GHz, R/Q =0.46 Ω/cm^2
DP-EE-039 f=3.0817 GHz, R/Q =1.17 Ω/cm^2	DP-EE-040 f=3.0945 GHz, R/Q =0.25 Ω/cm^2
DP-EE-041 f=3.1110 GHz, R/Q =0.00 Ω/cm^2	DP-EE-042 f=3.3824 GHz, R/Q =0.07 Ω/cm^2
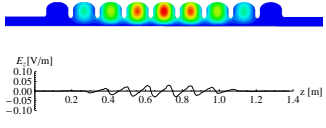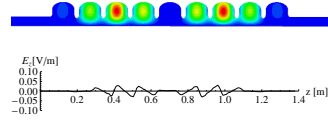
DP-EE-043 f=3.3825 GHz, R/Q =1.49 Ω/cm^2	DP-EE-044 f=3.3850 GHz, R/Q =1.38 Ω/cm^2
DP-EE-045 f=3.3855 GHz, R/Q =0.43 Ω/cm^2	DP-EE-046 f=3.3862 GHz, R/Q =0.03 Ω/cm^2
DP-EE-047 f=3.3865 GHz, R/Q =0.00 Ω/cm^2	DP-EE-048 f=3.3924 GHz, R/Q =0.08 Ω/cm^2
DP-EE-049 f=3.4082 GHz, R/Q =0.13 Ω/cm^2	DP-EE-050 f=3.4827 GHz, R/Q =0.05 Ω/cm^2
DP-EE-051 f=3.5331 GHz, R/Q =0.05 Ω/cm^2	DP-EE-052 f=3.5872 GHz, R/Q =0.01 Ω/cm^2
DP-EE-053 f=3.6422 GHz, R/Q =0.00 Ω/cm^2	DP-EE-054 f=3.6950 GHz, R/Q =0.01 Ω/cm^2
DP-EE-055 f=3.7416 GHz, R/Q =0.03 Ω/cm^2	DP-EE-056 f=3.8010 GHz, R/Q =0.00 Ω/cm^2
DP-EE-057 f=3.8132 GHz, R/Q =0.15 Ω/cm^2	DP-EE-058 f=3.8192 GHz, R/Q =1.14 Ω/cm^2
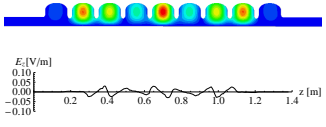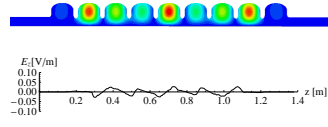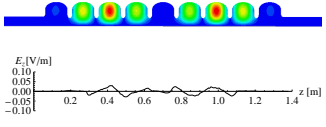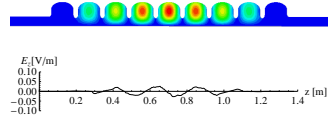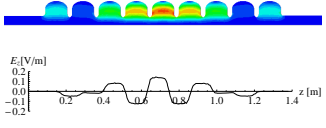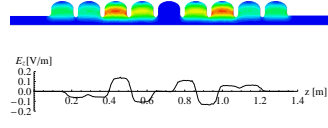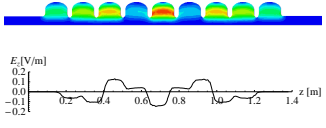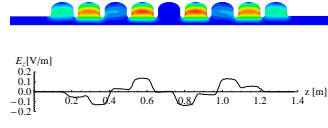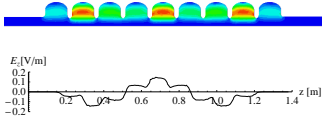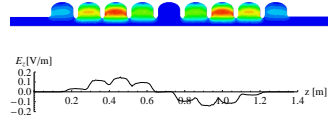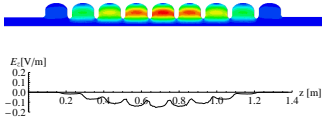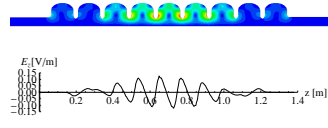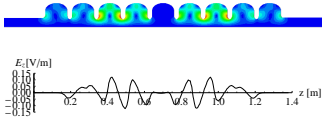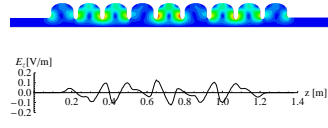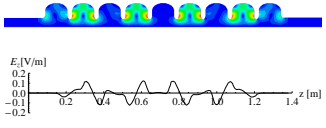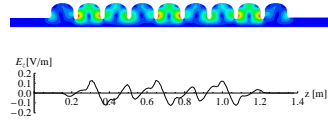
	DP-EE-059 f=3.9603 GHz, R/Q =0.03 Ω/cm^2		DP-EE-060 f=3.9608 GHz, R/Q =0.03 Ω/cm^2
	DP-EE-061 f=3.9652 GHz, R/Q =0.02 Ω/cm^2		DP-EE-062 f=3.9828 GHz, R/Q =0.03 Ω/cm^2
	DP-EE-063 f=3.9972 GHz, R/Q =0.21 Ω/cm^2		DP-EE-064 f=4.0143 GHz, R/Q =0.00 Ω/cm^2
	DP-EE-065 f=4.0318 GHz, R/Q =2.22 Ω/cm^2		
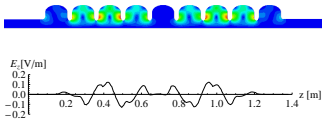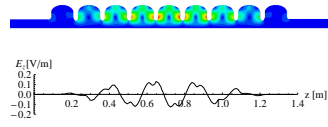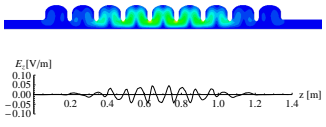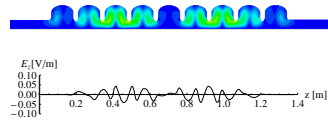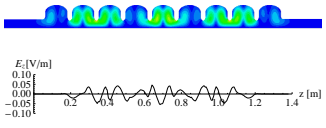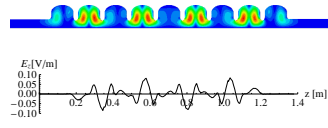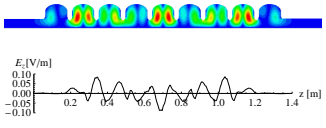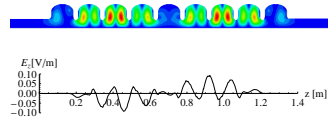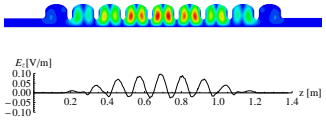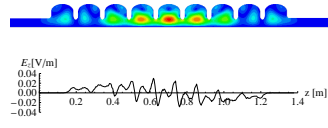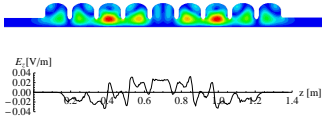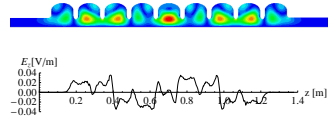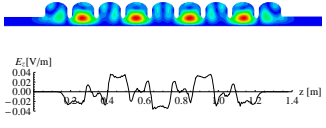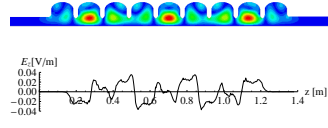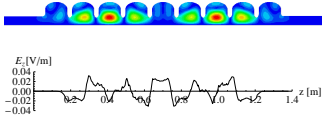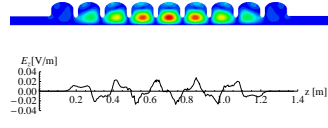
D.5 Quadrupole Mode with MM Boundary Condition
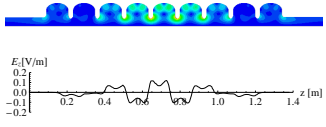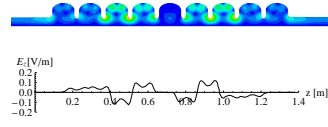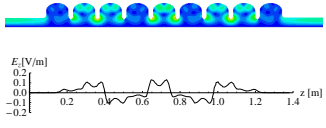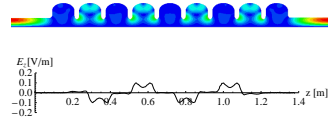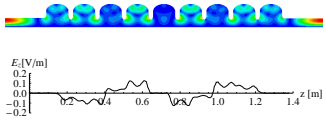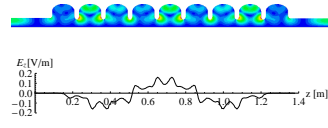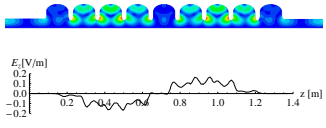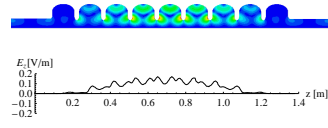
The longitudinal electric field plot (E_z) is taken at 15 mm offset from the cavity axis.

Table D.5: Quadrupole mode with MM boundary condition

	QP-MM-001 f=2.2437 GHz, R/Q =0.01 Ω/cm^4		QP-MM-002 f=2.2449 GHz, R/Q =0.05 Ω/cm^4

QP-MM-003 f=2.2467 GHz, R/Q =0.04 Ω/cm^4	QP-MM-004 f=2.2507 GHz, R/Q =0.00 Ω/cm^4
QP-MM-005 f=2.2524 GHz, R/Q =0.00 Ω/cm^4	QP-MM-006 f=2.2535 GHz, R/Q =0.00 Ω/cm^4
QP-MM-007 f=2.5747 GHz, R/Q =0.00 Ω/cm^4	QP-MM-008 f=2.5771 GHz, R/Q =0.00 Ω/cm^4
QP-MM-009 f=2.5802 GHz, R/Q =0.00 Ω/cm^4	QP-MM-010 f=2.5834 GHz, R/Q =0.00 Ω/cm^4
QP-MM-011 f=2.5865 GHz, R/Q =0.01 Ω/cm^4	QP-MM-012 f=2.5891 GHz, R/Q =0.00 Ω/cm^4
QP-MM-013 f=2.5907 GHz, R/Q =0.10 Ω/cm^4	QP-MM-014 f=3.1560 GHz, R/Q =0.00 Ω/cm^4
QP-MM-015 f=3.1633 GHz, R/Q =0.22 Ω/cm^4	QP-MM-016 f=3.1735 GHz, R/Q =0.88 Ω/cm^4
QP-MM-017 f=3.1853 GHz, R/Q =0.59 Ω/cm^4	QP-MM-018 f=3.1974 GHz, R/Q =0.05 Ω/cm^4
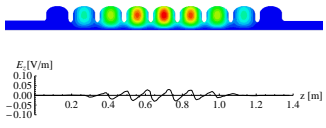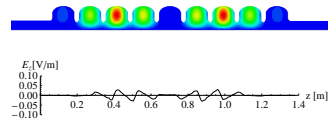
QP-MM-019 f=3.2082 GHz, R/Q =0.01 Ω/cm^4	QP-MM-020 f=3.2157 GHz, R/Q =0.00 Ω/cm^4
QP-MM-021 f=3.5037 GHz, R/Q =0.03 Ω/cm^4	QP-MM-022 f=3.5145 GHz, R/Q =0.16 Ω/cm^4
QP-MM-023 f=3.5284 GHz, R/Q =0.09 Ω/cm^4	QP-MM-024 f=3.5431 GHz, R/Q =0.00 Ω/cm^4
QP-MM-025 f=3.5566 GHz, R/Q =0.00 Ω/cm^4	QP-MM-026 f=3.5675 GHz, R/Q =0.00 Ω/cm^4
QP-MM-027 f=3.5750 GHz, R/Q =0.00 Ω/cm^4	QP-MM-028 f=3.6471 GHz, R/Q =0.00 Ω/cm^4
QP-MM-029 f=3.6518 GHz, R/Q =0.00 Ω/cm^4	QP-MM-030 f=3.6574 GHz, R/Q =0.00 Ω/cm^4
QP-MM-031 f=3.6632 GHz, R/Q =0.00 Ω/cm^4	QP-MM-032 f=3.6689 GHz, R/Q =0.00 Ω/cm^4
QP-MM-033 f=3.6739 GHz, R/Q =0.00 Ω/cm^4	QP-MM-034 f=3.6773 GHz, R/Q =0.00 Ω/cm^4
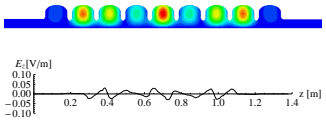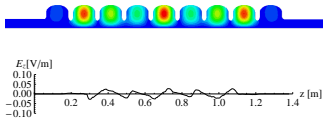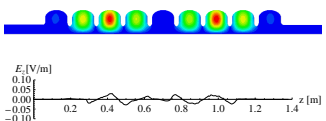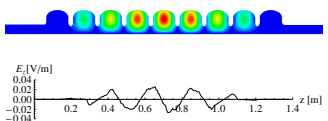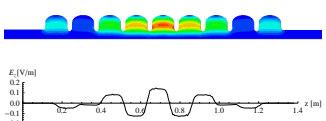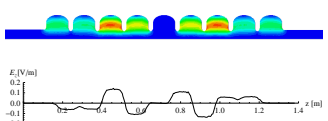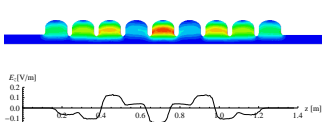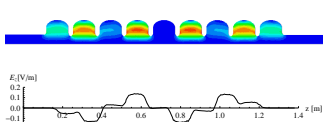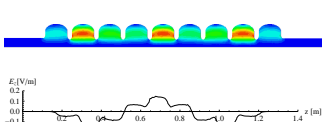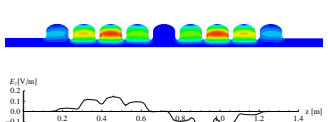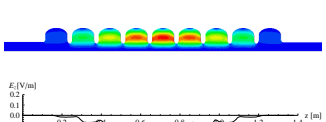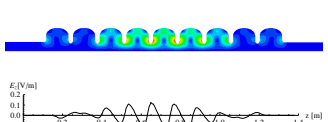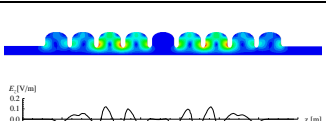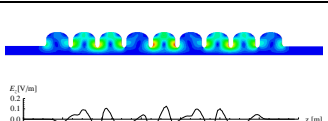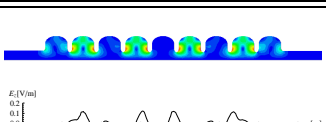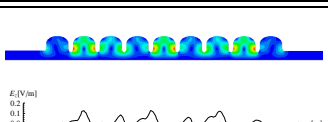
	QP-MM-035 f=3.8020 GHz, R/Q =0.54 Ω/cm^4		QP-MM-036 f=3.8161 GHz, R/Q =0.06 Ω/cm^4
	QP-MM-037 f=3.8346 GHz, R/Q =0.03 Ω/cm^4		QP-MM-038 f=3.8514 GHz, R/Q =0.01 Ω/cm^4
	QP-MM-039 f=3.8662 GHz, R/Q =0.00 Ω/cm^4		QP-MM-040 f=3.8872 GHz, R/Q =0.00 Ω/cm^4
	QP-MM-041 f=3.9104 GHz, R/Q =0.00 Ω/cm^4		QP-MM-042 f=3.9288 GHz, R/Q =0.00 Ω/cm^4
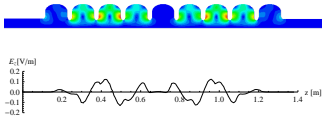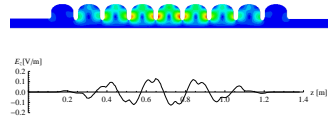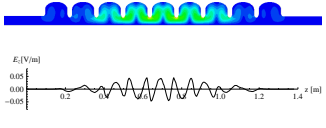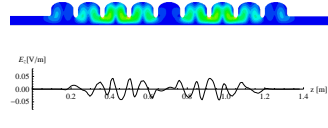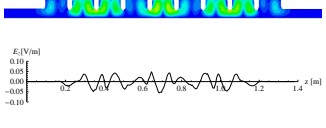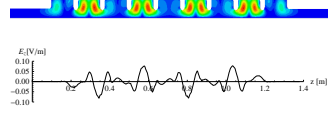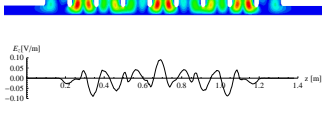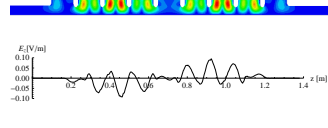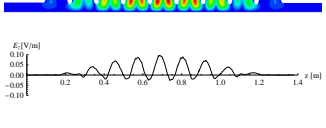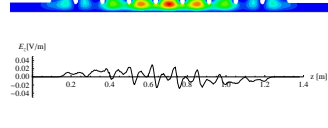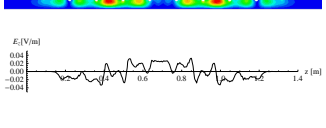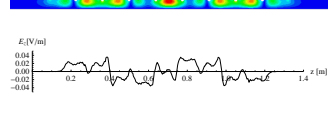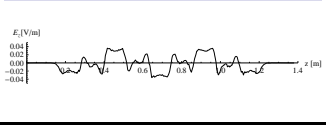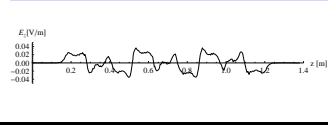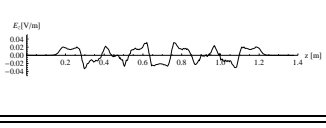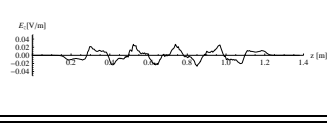
D.6 Quadrupole Mode with EE Boundary Condition
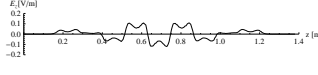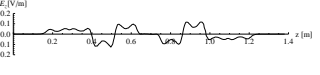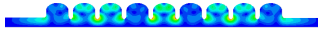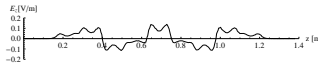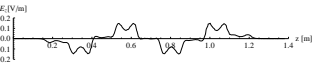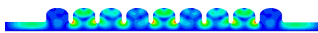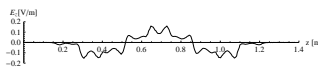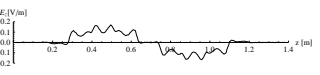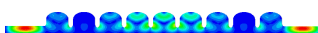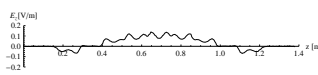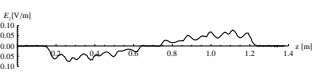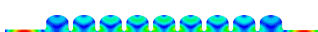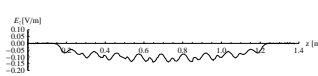
The longitudinal electric field plot (E_z) is taken at 15 mm offset from the cavity axis.

Table D.6: Quadrupole mode with EE boundary condition

	QP-EE-001 f=2.2437 GHz, R/Q =0.01 Ω/cm^4		QP-EE-002 f=2.2449 GHz, R/Q =0.05 Ω/cm^4

QP-EE-003 f=2.2467 GHz, R/Q =0.03 Ω/cm^4		QP-EE-004 f=2.2507 GHz, R/Q =0.00 Ω/cm^4	
QP-EE-005 f=2.2524 GHz, R/Q =0.00 Ω/cm^4		QP-EE-006 f=2.2535 GHz, R/Q =0.00 Ω/cm^4	
QP-EE-007 f=2.5747 GHz, R/Q =0.00 Ω/cm^4		QP-EE-008 f=2.5771 GHz, R/Q =0.00 Ω/cm^4	
QP-EE-009 f=2.5802 GHz, R/Q =0.00 Ω/cm^4		QP-EE-010 f=2.5834 GHz, R/Q =0.00 Ω/cm^4	
QP-EE-011 f=2.5865 GHz, R/Q =0.01 Ω/cm^4		QP-EE-012 f=2.5891 GHz, R/Q =0.00 Ω/cm^4	
QP-EE-013 f=2.5907 GHz, R/Q =0.10 Ω/cm^4		QP-EE-014 f=3.1560 GHz, R/Q =0.00 Ω/cm^4	
QP-EE-015 f=3.1633 GHz, R/Q =0.22 Ω/cm^4		QP-EE-016 f=3.1735 GHz, R/Q =0.88 Ω/cm^4	
QP-EE-017 f=3.1853 GHz, R/Q =0.59 Ω/cm^4		QP-EE-018 f=3.1974 GHz, R/Q =0.05 Ω/cm^4	
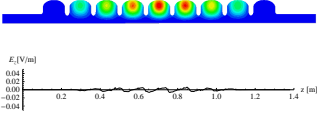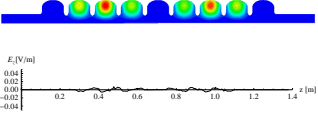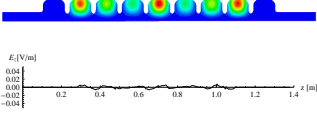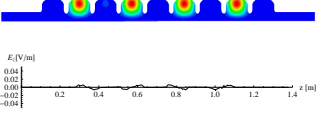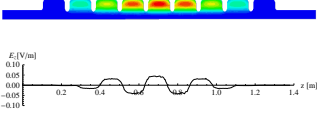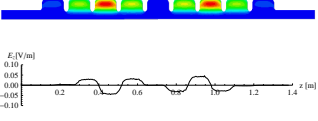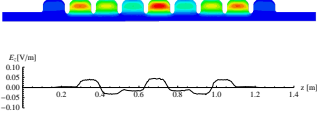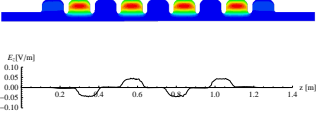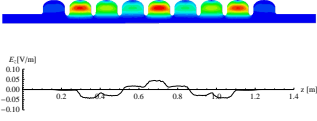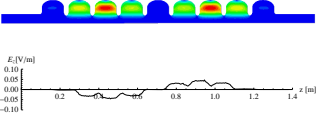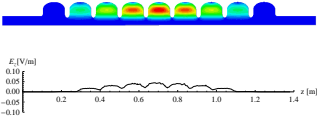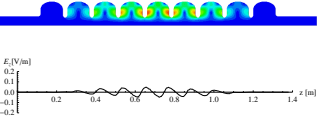
	QP-EE-019 f=3.2082 GHz, R/Q =0.01 Ω/cm^4		QP-EE-020 f=3.2157 GHz, R/Q =0.00 Ω/cm^4
	QP-MM-021 f=3.5037 GHz, R/Q =0.03 Ω/cm^4		QP-MM-022 f=3.5145 GHz, R/Q =0.16 Ω/cm^4
	QP-EE-023 f=3.5284 GHz, R/Q =0.09 Ω/cm^4		QP-EE-024 f=3.5430 GHz, R/Q =0.00 Ω/cm^4
	QP-EE-025 f=3.5566 GHz, R/Q =0.00 Ω/cm^4		QP-EE-026 f=3.5675 GHz, R/Q =0.00 Ω/cm^4
	QP-EE-027 f=3.5750 GHz, R/Q =0.00 Ω/cm^4		QP-EE-028 f=3.6471 GHz, R/Q =0.00 Ω/cm^4
	QP-EE-029 f=3.6518 GHz, R/Q =0.00 Ω/cm^4		QP-EE-030 f=3.6574 GHz, R/Q =0.00 Ω/cm^4
	QP-EE-031 f=3.6632 GHz, R/Q =0.00 Ω/cm^4		QP-EE-032 f=3.6689 GHz, R/Q =0.00 Ω/cm^4
	QP-EE-033 f=3.6738 GHz, R/Q =0.00 Ω/cm^4		QP-EE-034 f=3.6773 GHz, R/Q =0.00 Ω/cm^4
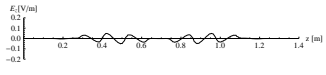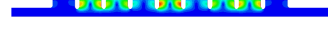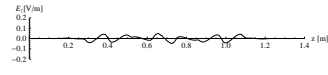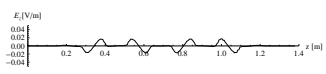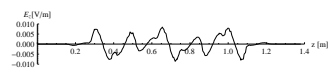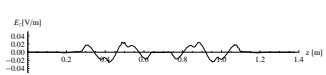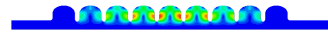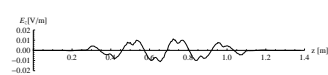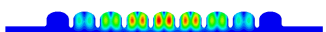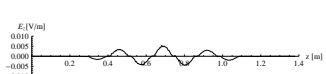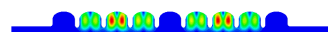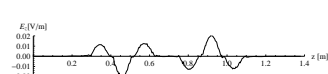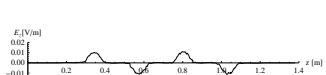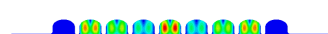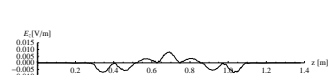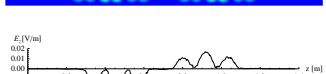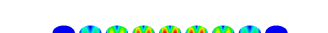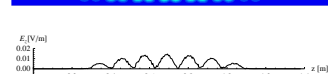
	QP-EE-035 f=3.8022 GHz, R/Q =0.52 Ω/cm^4		QP-EE-036 f=3.8166 GHz, R/Q =0.06 Ω/cm^4
	QP-EE-037 f=3.8360 GHz, R/Q =0.02 Ω/cm^4		QP-EE-038 f=3.8588 GHz, R/Q =0.01 Ω/cm^4
	QP-EE-039 f=3.8833 GHz, R/Q =0.01 Ω/cm^4		QP-EE-040 f=3.9062 GHz, R/Q =0.00 Ω/cm^4
	QP-EE-041 f=3.9227 GHz, R/Q =0.01 Ω/cm^4		QP-EE-042 f=3.9296 GHz, R/Q =0.00 Ω/cm^4
	QP-EE-043 f=3.9333 GHz, R/Q =0.00 Ω/cm^4		

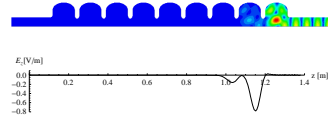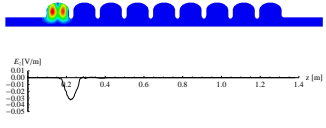# D.7   Sextupole Mode with MM Boundary Condition

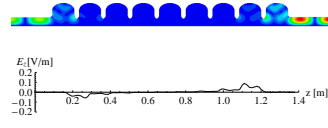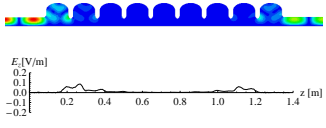The longitudinal electric field plot (E_z) is taken at 15 mm offset from the cavity axis.

Table D.7: Sextupole mode with MM boundary condition
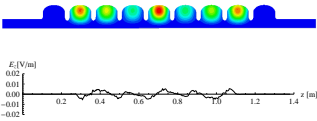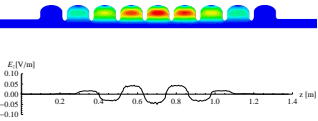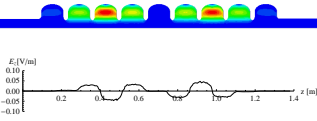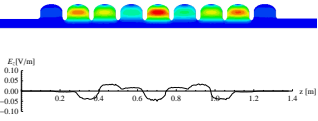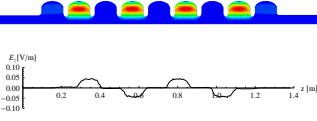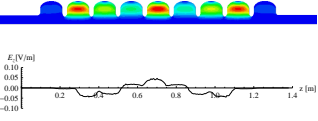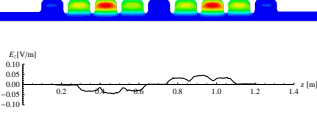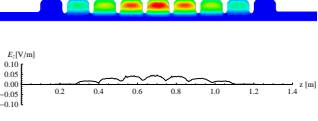
	SP-MM-001 f=2.7107 GHz, R/Q =0.00 Ω/cm^6		SP-MM-002 f=2.7108 GHz, R/Q =0.00 Ω/cm^6
	SP-MM-003 f=2.7109 GHz, R/Q =0.00 Ω/cm^6		SP-MM-004 f=2.7111 GHz, R/Q =0.00 Ω/cm^6
	SP-MM-005 f=3.2002 GHz, R/Q =0.00 Ω/cm^6		SP-MM-006 f=3.2006 GHz, R/Q =0.00 Ω/cm^6
	SP-MM-007 f=3.2011 GHz, R/Q =0.00 Ω/cm^6		SP-MM-008 f=3.2016 GHz, R/Q =0.00 Ω/cm^6
	SP-MM-009 f=3.2022 GHz, R/Q =0.00 Ω/cm^6		SP-MM-010 f=3.2027 GHz, R/Q =0.00 Ω/cm^6
	SP-MM-011 f=3.2030 GHz, R/Q =0.00 Ω/cm^6		SP-MM-012 f=3.7981 GHz, R/Q =0.00 Ω/cm^6

	SP-MM-013		SP-MM-014
	f=3.7995 GHz,		f=3.8015 GHz,
	R/Q =0.00 Ω/cm^6		R/Q =0.00 Ω/cm^6
	SP-MM-015		SP-MM-016
	f=3.8038 GHz,		f=3.8061 GHz,
	R/Q =0.00 Ω/cm^6		R/Q =0.00 Ω/cm^6
	SP-MM-017		SP-MM-018
	f=3.8080 GHz,		f=3.8093 GHz,
	R/Q =0.00 Ω/cm^6		R/Q =0.01 Ω/cm^6
	SP-MM-019		SP-MM-020
	f=3.9689 GHz,		f=3.9692 GHz,
	R/Q =0.00 Ω/cm^6		R/Q =0.00 Ω/cm^6
	SP-MM-021		SP-MM-022
	f=3.9701 GHz,		f=3.9705 GHz,
	R/Q =0.00 Ω/cm^6		R/Q =0.00 Ω/cm^6
	SP-MM-023		SP-MM-024
	f=3.9709 GHz,		f=3.9711 GHz,
	R/Q =0.00 Ω/cm^6		R/Q =0.00 Ω/cm^6

D.8   Sextupole Mode with EE Boundary Condition

The longitudinal electric field plot (E_z) is taken at 15 mm offset from the cavity axis.

Table D.8: Sextupole mode with EE boundary condition
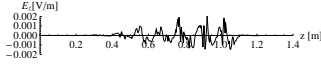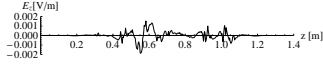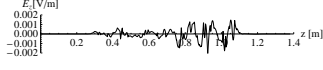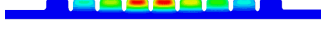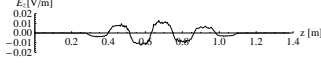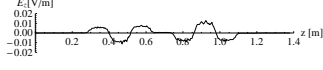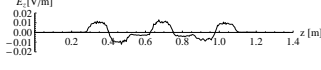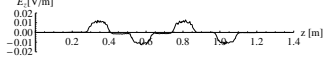
	SP-EE-001 f=2.7107 GHz, R/Q =0.00 Ω/cm^6		SP-EE-002 f=2.7108 GHz, R/Q =0.00 Ω/cm^6
	SP-EE-003 f=2.7109 GHz, R/Q =0.00 Ω/cm^6		SP-EE-004 f=2.7110 GHz, R/Q =0.00 Ω/cm^6
	SP-EE-005 f=2.7112 GHz, R/Q =0.00 Ω/cm^6		SP-EE-006 f=3.2003 GHz, R/Q =0.00 Ω/cm^6
	SP-EE-007 f=3.2006 GHz, R/Q =0.00 Ω/cm^6		SP-EE-008 f=3.2011 GHz, R/Q =0.00 Ω/cm^6
	SP-EE-009 f=3.2017 GHz, R/Q =0.00 Ω/cm^6		SP-EE-010 f=3.2022 GHz, R/Q =0.00 Ω/cm^6
	SP-EE-011 f=3.2027 GHz, R/Q =0.00 Ω/cm^6		SP-EE-012 f=3.2030 GHz, R/Q =0.00 Ω/cm^6

	SP-EE-013 f=3.7981 GHz, R/Q =0.00 Ω/cm^6		SP-EE-014 f=3.7995 GHz, R/Q =0.00 Ω/cm^6
	SP-EE-015 f=3.8014 GHz, R/Q =0.00 Ω/cm^6		SP-EE-016 f=3.8061 GHz, R/Q =0.00 Ω/cm^6
	SP-EE-017 f=3.8080 GHz, R/Q =0.00 Ω/cm^6		SP-EE-018 f=3.8093 GHz, R/Q =0.01 Ω/cm^6
	SP-EE-019 f=3.9689 GHz, R/Q =0.00 Ω/cm^6		SP-EE-020 f=3.9702 GHz, R/Q =0.00 Ω/cm^6
	SP-EE-021 f=3.9707 GHz, R/Q =0.00 Ω/cm^6		SP-EE-022 f=3.9710 GHz, R/Q =0.00 Ω/cm^6
	SP-EE-023 f=3.9712 GHz, R/Q =0.00 Ω/cm^6		

D.9 Octupole Mode with MM Boundary Condition

The longitudinal electric field plot (E_z) is taken at 15 mm offset from the cavity axis.
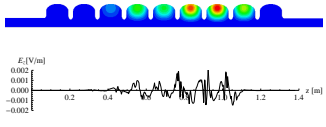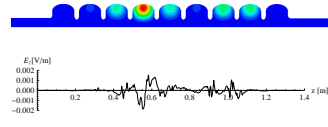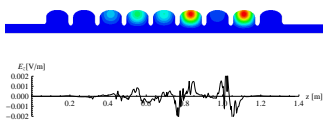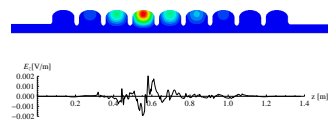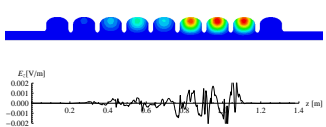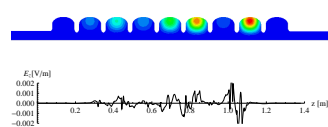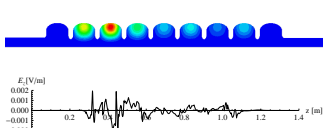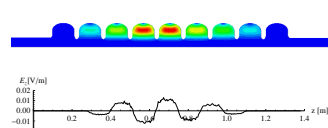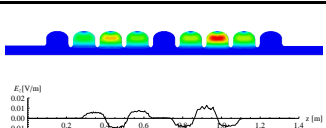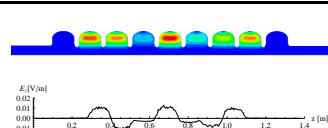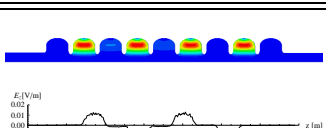
Table D.9: Octupole mode with MM boundary condition

	OP-MM-001 f=3.18271 GHz, R/Q =0.00 Ω/cm^8		OP-MM-002 f=3.18272 GHz, R/Q =0.00 Ω/cm^8
	OP-MM-003 f=3.18274 GHz, R/Q =0.00 Ω/cm^8		OP-MM-004 f=3.18274 GHz, R/Q =0.00 Ω/cm^8
	OP-MM-005 f=3.77752 GHz, R/Q =0.00 Ω/cm^8		OP-MM-006 f=3.77758 GHz, R/Q =0.00 Ω/cm^8
	OP-MM-007 f=3.77765 GHz, R/Q =0.00 Ω/cm^8		OP-MM-008 f=3.77775 GHz, R/Q =0.00 Ω/cm^8

D.10   Octupole Mode with EE Boundary Condition

The longitudinal electric field plot (E_z) is taken at 15 mm offset from the cavity axis.
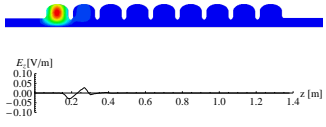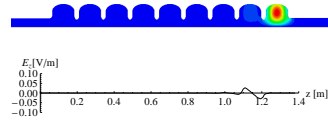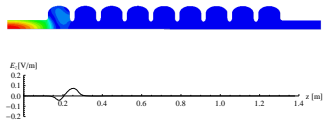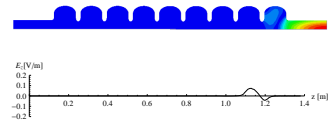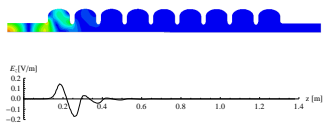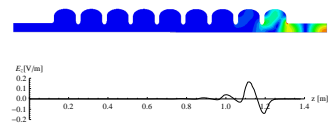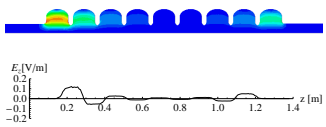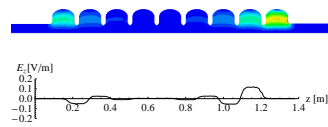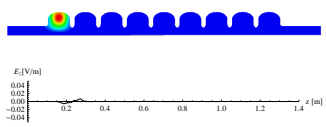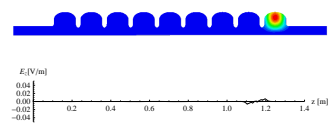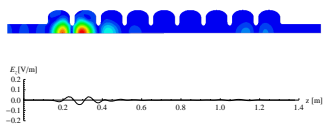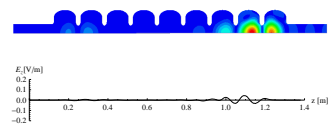
Table D.10: Octupole mode with EE boundary condition
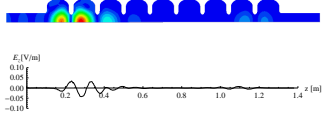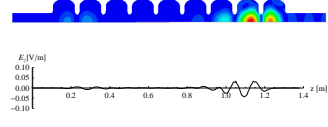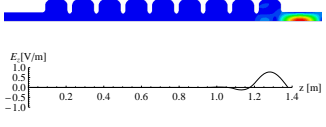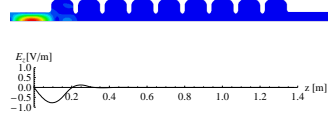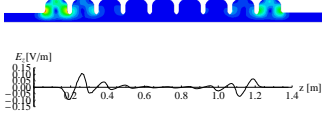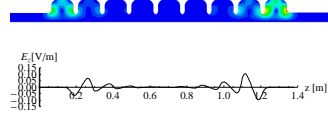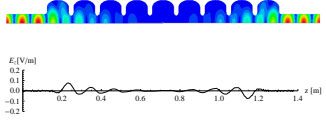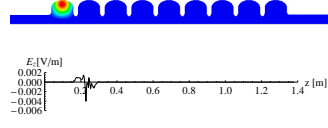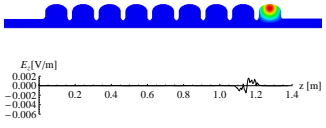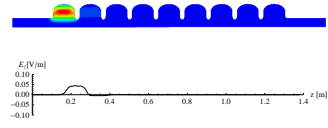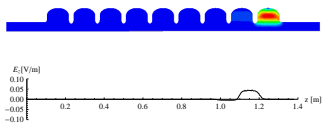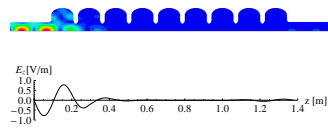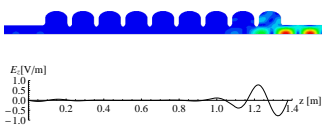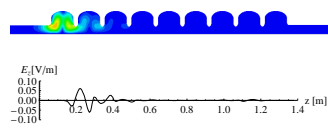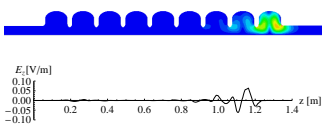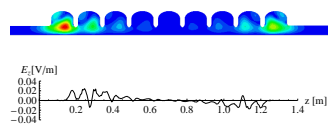
	OP-EE-001 f=3.18271 GHz, R/Q =0.00 Ω/cm^8		OP-EE-002 f=3.18272 GHz, R/Q =0.00 Ω/cm^8
	OP-EE-003 f=3.18274 GHz, R/Q =0.00 Ω/cm^8		OP-EE-004 f=3.18277 GHz, R/Q =0.00 Ω/cm^8
	OP-EE-005 f=3.18279 GHz, R/Q =0.00 Ω/cm^8		OP-EE-006 f=3.18281 GHz, R/Q =0.00 Ω/cm^8
	OP-EE-007 f=3.18282 GHz, R/Q =0.00 Ω/cm^8		OP-EE-008 f=3.77752 GHz, R/Q =0.00 Ω/cm^8
	OP-EE-009 f=3.77758 GHz, R/Q =0.005 Ω/cm^8		OP-EE-010 f=3.77765 GHz, R/Q =0.00 Ω/cm^8
	OP-EE-011 f=3.77775 GHz, R/Q =0.00 Ω/cm^8		
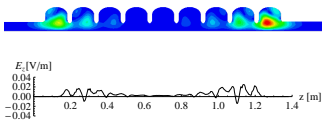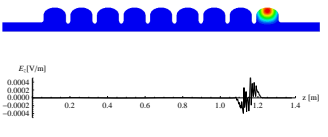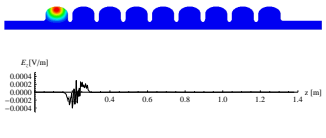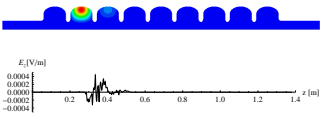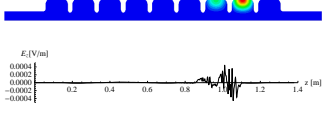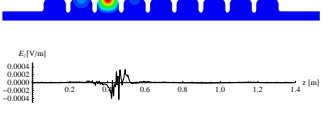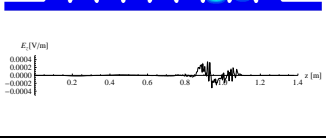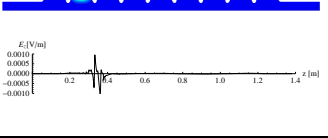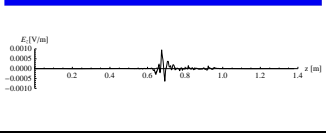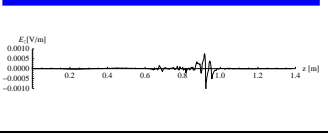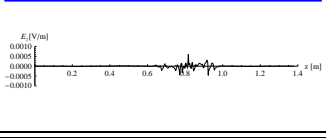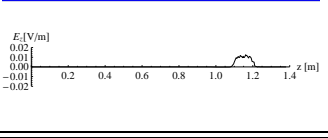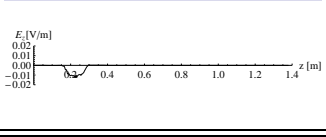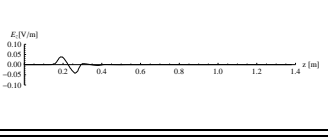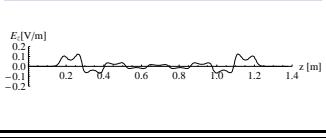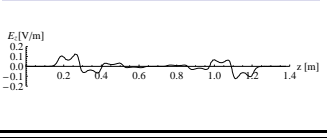
D.11 Beam Pipe Mode with MM Boundary Condition
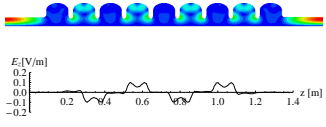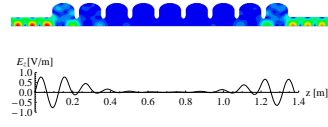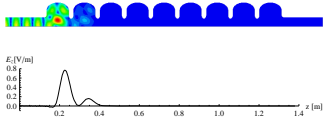
The longitudinal electric field plot (E_z) is taken at 15 mm offset from the cavity axis.

Table D.11: Beam pipe mode with MM boundary condition

	BP-MM-001 f=2.2255 GHz, R/Q =0.03 Ω/cm^2		BP-MM-002 f=2.2255 GHz, R/Q =0.03 Ω/cm^2
	BP-MM-003 f=2.3271 GHz, R/Q =0.28 Ω/cm^2		BP-MM-004 f=2.3272 GHz, R/Q =0.28 Ω/cm^2
	BP-MM-005 f=2.4429 GHz, R/Q =3.87 Ω/cm^2		BP-MM-006 f=2.4430 GHz, R/Q =3.91 Ω/cm^2
	BP-MM-007 f=2.5710 GHz, R/Q =0.01 Ω/cm^2		BP-MM-008 f=2.5711 GHz, R/Q =0.00 Ω/cm^2
	BP-MM-009 f=2.6951 GHz, R/Q =0.00 Ω/cm^2		BP-MM-010 f=2.6951 GHz, R/Q =0.00 Ω/cm^2
	BP-MM-011 f=3.0666 GHz, R/Q =0.12 Ω/cm^2		BP-MM-012 f=3.0666 GHz, R/Q =0.07 Ω/cm^2

	BP-MM-013 f=3.0666 GHz, R/Q =0.11 Ω/cm^2	BP-MM-014 f=3.0666 GHz, R/Q =0.07 Ω/cm^2
	BP-MM-015 f=3.1156 GHz, R/Q =0.54 Ω/cm^2	BP-MM-016 f=3.1157 GHz, R/Q =0.53 Ω/cm^2
	BP-MM-017 f=3.1410 GHz, R/Q =0.04 Ω/cm^2	BP-MM-018 f=3.1410 GHz, R/Q =0.60 Ω/cm^2
	BP-MM-019 f=3.1414 GHz, R/Q =0.19 Ω/cm^2	BP-MM-020 f=3.1692 GHz, R/Q =0.00 Ω/cm^2
	BP-MM-021 f=3.1692 GHz, R/Q =0.00 Ω/cm^2	BP-MM-022 f=3.1942 GHz, R/Q =0.00 Ω/cm^2
	BP-MM-023 f=3.1942 GHz, R/Q =0.00 Ω/cm^2	BP-MM-024 f=3.3373 GHz, R/Q =0.83 Ω/cm^2
	BP-MM-025 f=3.3373 GHz, R/Q =0.75 Ω/cm^2	BP-MM-026 f=3.4622 GHz, R/Q =0.18 Ω/cm^2
	BP-MM-027 f=3.4623 GHz, R/Q =0.15 Ω/cm^2	BP-MM-028 f=3.6374 GHz, R/Q =0.00 Ω/cm^2
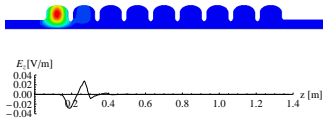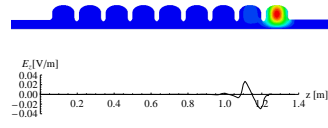
	BP-MM-029 f=3.6375 GHz, R/Q =0.00 Ω/cm^2		BP-MM-030 f=3.6529 GHz, R/Q =0.00 Ω/cm^2
	BP-MM-031 f=3.6529 GHz, R/Q =0.00 Ω/cm^2		BP-MM-032 f=3.6654 GHz, R/Q =0.00 Ω/cm^2
	BP-MM-033 f=3.6654 GHz, R/Q =0.00 Ω/cm^2		BP-MM-034 f=3.6654 GHz, R/Q =0.00 Ω/cm^2
	BP-MM-035 f=3.6654 GHz, R/Q =0.00 Ω/cm^2		BP-MM-036 f=3.6654 GHz, R/Q =0.00 Ω/cm^2
	BP-MM-037 f=3.6654 GHz, R/Q =0.00 Ω/cm^2		BP-MM-038 f=3.6654 GHz, R/Q =0.00 Ω/cm^2
	BP-MM-039 f=3.6654 GHz, R/Q =0.00 Ω/cm^2		BP-MM-040 f=3.7717 GHz, R/Q =0.00 Ω/cm^2
	BP-MM-041 f=3.7717 GHz, R/Q =0.15 Ω/cm^2		BP-MM-042 f=3.7746 GHz, R/Q =0.00 Ω/cm^2
	BP-MM-043 f=3.7837 GHz, R/Q =0.85 Ω/cm^2		BP-MM-044 f=3.7840 GHz, R/Q =0.71 Ω/cm^2

	BP-MM-045 f=3.8555 GHz, R/Q =0.63 Ω/cm^2		BP-MM-046 f=3.8555 GHz, R/Q =1.27 Ω/cm^2
	BP-MM-047 f=3.9277 GHz, R/Q =0.36 Ω/cm^2		BP-MM-048 f=3.9277 GHz, R/Q =0.36 Ω/cm^2
	BP-MM-049 f=3.9342 GHz, R/Q =0.00 Ω/cm^2		BP-MM-050 f=4.0145 GHz, R/Q =0.03 Ω/cm^2
	BP-MM-051 f=4.0145 GHz, R/Q =0.02 Ω/cm^2		
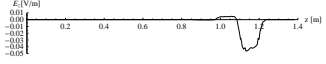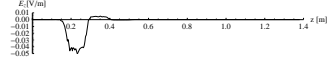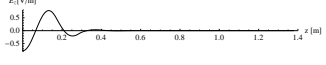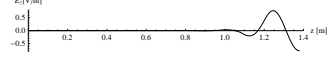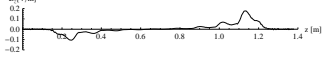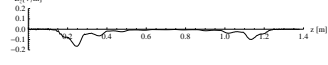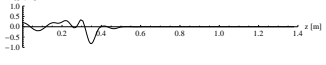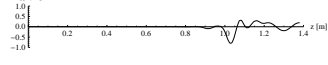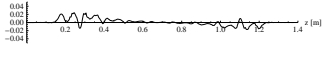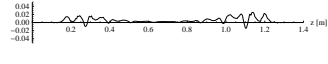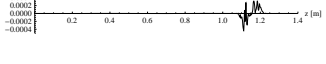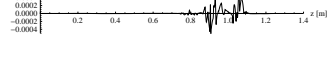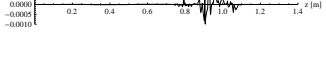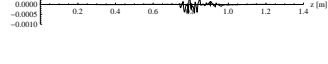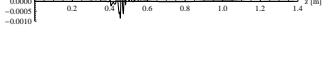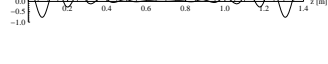
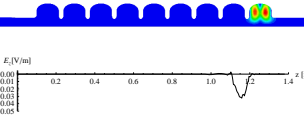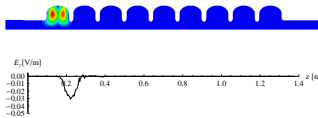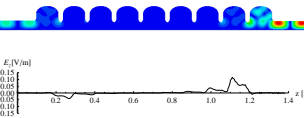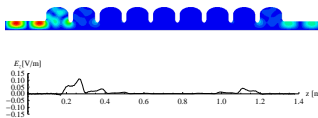## D.12   Beam Pipe Mode with EE Boundary Condition
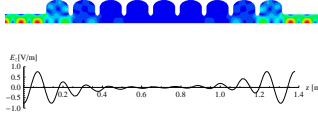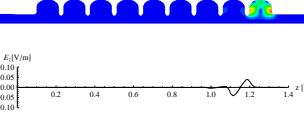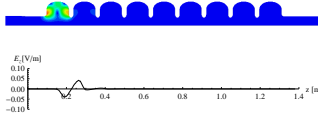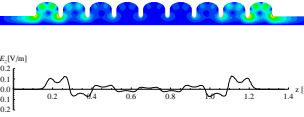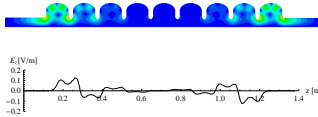
The longitudinal electric field plot (E_z) is taken at 15 mm offset from the cavity axis.

Table D.12: Beam pipe mode with EE boundary condition

	BP-EE-001 f=2.2255 GHz, R/Q =0.03 Ω/cm^2		BP-EE-002 f=2.2255 GHz, R/Q =0.03 Ω/cm^2

BP-EE-003 f=2.3742 GHz, R/Q =1.08 Ω/cm^2	BP-EE-004 f=2.3742 GHz, R/Q =1.07 Ω/cm^2
BP-EE-005 f=2.5710 GHz, R/Q =0.01 Ω/cm^2	BP-EE-006 f=2.5711 GHz, R/Q =0.00 Ω/cm^2
BP-EE-007 f=2.6950 GHz, R/Q =0.00 Ω/cm^2	BP-EE-008 f=2.6950 GHz, R/Q =0.00 Ω/cm^2
BP-EE-009 f=3.0031 GHz, R/Q =0.06 Ω/cm^2	BP-EE-010 f=3.0042 GHz, R/Q =0.35 Ω/cm^2
BP-EE-011 f=3.0429 GHz, R/Q =7.31 Ω/cm^2	BP-EE-012 f=3.0429 GHz, R/Q =7.38 Ω/cm^2
BP-EE-013 f=3.0670 GHz, R/Q =0.12 Ω/cm^2	BP-EE-014 f=3.0671 GHz, R/Q =0.07 Ω/cm^2
BP-EE-015 f=3.1410 GHz, R/Q =0.04 Ω/cm^2	BP-EE-016 f=3.1410 GHz, R/Q =0.60 Ω/cm^2
BP-EE-017 f=3.1692 GHz, R/Q =0.00 Ω/cm^2	BP-EE-018 f=3.1692 GHz, R/Q =0.00 Ω/cm^2

	BP-EE-019 f=3.1942 GHz, R/Q =0.00 Ω/cm^2
	BP-EE-020 f=3.1943 GHz, R/Q =0.00 Ω/cm^2
	BP-EE-021 f=3.2221 GHz, R/Q =5.35 Ω/cm^2
	BP-EE-022 f=3.2221 GHz, R/Q =5.34 Ω/cm^2
	BP-EE-023 f=3.3117 GHz, R/Q =0.09 Ω/cm^2
	BP-EE-024 f=3.3117 GHz, R/Q =0.02 Ω/cm^2
	BP-EE-025 f=3.5739 GHz, R/Q =4.55 Ω/cm^2
	BP-EE-026 f=3.5739 GHz, R/Q =4.57 Ω/cm^2
	BP-EE-027 f=3.6375 GHz, R/Q =0.00 Ω/cm^2
	BP-EE-028 f=3.6375 GHz, R/Q =0.00 Ω/cm^2
	BP-EE-029 f=3.6529 GHz, R/Q =0.00 Ω/cm^2
	BP-EE-030 f=3.6653 GHz, R/Q =0.00 Ω/cm^2
	BP-EE-031 f=3.6653 GHz, R/Q =0.00 Ω/cm^2
	BP-EE-032 f=3.6654 GHz, R/Q =0.00 Ω/cm^2
	BP-EE-033 f=3.6654 GHz, R/Q =0.00 Ω/cm^2
	BP-EE-034 f=3.6902 GHz, R/Q =0.00 Ω/cm^2

	BP-EE-035 f=3.6904 GHz, R/Q =5.82 Ω/cm^2		BP-EE-036 f=3.7746 GHz, R/Q =0.00 Ω/cm^2
	BP-EE-037 f=3.7746 GHz, R/Q =0.01 Ω/cm^2		BP-EE-038 f=3.7843 GHz, R/Q =0.90 Ω/cm^2
	BP-EE-039 f=3.7846 GHz, R/Q =0.73 Ω/cm^2		BP-EE-040 f=3.9343 GHz, R/Q =0.00 Ω/cm^2
	BP-EE-041 f=3.9344 GHz, R/Q =0.15 Ω/cm^2		BP-EE-042 f=4.1134 GHz, R/Q =0.05 Ω/cm^2
	BP-EE-043 f=4.1134 GHz, R/Q =0.01 Ω/cm^2		